# Dynamic characterization of the wetting and drying states of DTI (Deep Trench Isolation) structures using high frequency ultrasonic waves

Abbas Salhab

**Thèse de doctorat**

**Pour obtenir le grade de Docteur de**

**l'UNIVERSITÉ POLYTECHNIQUE HAUTS-DE-FRANCE**

**et l'INSA HAUTS-DE-FRANCE**

**Micro-nano systèmes et capteurs**

**Présentée et soutenue par Abbas SALHAB.**

**Le 04/02/2022, à VALENCIENNES**

**École doctorale :**

École Doctorale Polytechnique Hauts-de-France (ED PHF)

**Unité de recherche :**

Institut d'Electronique de Microélectronique et de Nanotechnologie - Département Opto-Acousto-Electronique (IEMN DOAE – UMR 8520)

# Caractérisation dynamique de l'état de mouillage et de séchage de structures DTI (Deep Trench Isolation) par ondes ultrasonores haute fréquence

## JURY

**Président du jury**

- Le Clézio, Emmanuel. Professeur. IES UMR CNRS 5214 - Université de Montpellier.

**Rapporteurs**

- Dejous, Corinne. Professeure. IMS UMR CNRS 5218, Université de Bordeaux.
- Le Clézio, Emmanuel. Professeur. IES UMR CNRS 5214 - Université de Montpellier.

**Examinateurs**

- Tiron, Raluca. Ingénieur de recherche. CEA Leti, technology research institute, Grenoble.
- Xu, Xiumei. Ingénieur de recherche. IMEC, Leuven, Belgique.
- Toubal, Malika. Ingénieur de recherche. UPHF – IEMN UMR CNRS 8520 – DOAE, Valenciennes.

**Co-directeur de thèse** :

- Carlier, Julien. Professeur. UPHF – IEMN UMR CNRS 8520 – DOAE, Valenciennes.
- Thomy, Vincent. Professeur. Université Lille – IEMN – UMR CNRS 8520, Villeneuve d'Ascq.

**Co-encadrant**: Campistron, Pierre. Maître de conférence. UPHF – IEMN UMR CNRS 8520 – DOAE, Valenciennes.

**Membres invités**

- Neyens, Marc. Ingénieur de recherche. STMicroelectronics, Crolles (Co-encadrant).
- Nongaillard, Bertrand. Professeur (retraité). UPHF – IEMN UMR CNRS 8520 – DOAE, Valenciennes

# PhD Thesis

## Submitted for the degree of Doctor of Philosophy from

## UNIVERSITÉ POLYTECHNIQUE HAUTS-DE-FRANCE

## And INSA HAUTS-DE-FRANCE

**Micro-nano systems and sensors**

**Presented and defended by Abbas SALHAB.**

**On 04/02/2022, Valenciennes**

**Doctoral school:**

Doctoral School Polytechnique Hauts-de-France

**Research unit:**

Institute of Electronics Microelectronics and Nanotechnology – Department of Opto-Acousto-Electronics (IEMN DOAE – UMR 8520)

# Dynamic characterization of the wetting and drying states of DTI (Deep Trench Isolation) structures using high frequency ultrasonic waves.

## JURY

**President of jury**

- Le Clézio, Emmanuel. Professor. IES UMR CNRS 5214 - Université de Montpellier.

**Reviewers**

- Dejous, Corinne. Professor. IMS UMR CNRS 5218, Université de Bordeaux.
- Le Clézio, Emmanuel. Professor. IES UMR CNRS 5214 - Université de Montpellier.

**Examiners**

- Tiron, Raluca. Research engineer. CEA Leti, technology research institute, Grenoble.
- Xu, Xiumei. Research engineer. IMEC, Leuven, Belgium.
- Toubal, Malika. Research engineer. UPHF – IEMN UMR CNRS 8520 – DOAE, Valenciennes.

**Thesis co-director**:

- Carlier, Julien. Professor. UPHF – IEMN UMR CNRS 8520 – DOAE, Valenciennes.
- Thomy, Vincent. Professor. Université Lille – IEMN – UMR CNRS 8520, Villeneuve d'Ascq.

**Co-supervisor**: Campistron, Pierre. Associate professor. UPHF – IEMN UMR CNRS 8520 – DOAE, Valenciennes.

**Invited members**

- Neyens, Marc. Research engineer. STMicroelectronics, Crolles (co-supervisor).
- Nongaillard, Bertrand. Professor (retired). UPHF – IEMN UMR CNRS 8520 – DOAE, Valenciennes

**"The secret of happiness, you see, is not found in seeking more, but in developing the capacity to enjoy less"**

**— Socrates, Greek philosopher, 470 – 399 BC.**

# Acknowledgements

Well then, after 3 years and 5 months, a chapter in my life (well, four chapters in the PhD) is (are) finished.

First of all, I would like to thank the jury members for accepting the invitation to evaluate this PhD. I would like to thank Pr. Corine Dejous and Pr. Emmanuel Le Clézio for accepting to be reviewers and for their remarks in improving this thesis manuscript. Also, I like to thank Mme. Raluca Tiron, Mme. Xiumei Xu and Mme. Malika Toubal for accepting to be examiners in the PhD defense.

Secondly, I would like to thank my PhD co-directors and supervisors who accepted me to be recruited for this PhD subject and accompanied me along this journey:
Pr. Julien Carlier, who was one of my co-directors, for his guidance and availability from the first day I arrived at the IEMN laboratory until the last day. I really appreciated our almost daily discussions and his advice to various problems we encountered in the PhD.
More than a supervisor, a sort of a mentor, I would like to give special thanks to Pr. Betrand Nongaillard for his help in making the experimental measurements possible, his guidance and advice in the discussions we had each morning. Even after his retirement he continued to participate in the discussions and didn't hesitate to come to the laboratory in the case where we had some technical problems with the measurement bench which I really appreciated and I will be thankful forever.
I would like to also thank Dr. Pierre Campistron for his help in the numerical simulation, Python programming and his help in explaining the various aspects of interactions and propagations of acoustic waves. He is highly competent person that I had the honor to meet and learn a lot from.
I like to also thank my co-director Pr. Vincent Thomy for his guidance and help in the establishing the micro-channel design and fabrication process also, for his deep knowledge and competence in explaining the wetting phenomenon inside textured surfaces. Throughout our different discussions and the resources he provided I learned a lot about the wetting physics inside textured surfaces.
Last but not least, I would like to thank my industrial supervisor Mr. Marc Neyens for his help in managing this PhD, whether in providing data and samples from different sources at ST to his advice on the technical difficulties we encountered. He was the first person I met on the first day of starting the PhD and I really appreciated his warm welcome, management approach, and his help in guiding me through the site of ST / Crolles during the different visits that I carried out.

In the IEMN laboratory, special thanks to the research engineer Mme. Malika Toubal for helping in the acoustic measurements which were never possible without her and also, for her continuous participation in the different discussions and finally her positivity throughout the different obstacles we faced.
Also, special thanks go to Karim Dogheche (research engineer / IEMN) and Paul Moustiez (PhD student / IEMN) for their help in taking SEM images that were used in this work.

Thanks also go to all the IEMN engineers at Valenciennes and inside the clean room at Villenueve d'ascq who contributed to the work done in this PhD.

I like to also thank Mr. Philippe Garnier from the Wet-3Di R&D team at ST, for his great help in providing the samples, technical data and also, his time in explaining the wet and etch processes included in the samples preparations at ST.
I would like to also thank Mme. Claire Richard and all the members of the Wet-3Di R&D team for their warm welcome during the time I passed at the site of Crolles.
I like to also thank Mme Lucile Broussous from ST / Crolles for her tremendous help during the recruitment process at ST. I will be always grateful for the opportunity she presented to take on this PhD.

Finally, I'm thankful for all my friends specifically Marwa, Hassan and Wissam for their continuous support throughout the past four years.
Also, I'm eternally grateful for my **family**, for the support and love they have shown throughout the difficult times. I'm thankful for my parents for their time and effort in raising me and the love they gave and continue to show, I would like to dedicate this work to them.

The utmost thanks go to **God** for all the blessing he gave me and without **God** none of this work would be possible.

# Table of Contents

## List of Main Symbols

$\gamma$ : Liquid surface tension

$\Delta P_{laplace}$ : Laplace pressure

$\theta_A$ : Advancing contact angle

$\theta_R$ : Receding contact angle

$\Delta\theta$ : Contact angle hysteresis

$\theta^*$ : Apparent contact angle

$P_{liquid}$ : Pressure of suspended liquid

$P_{air}$ : Pressure of trapped air

$\Delta P_{cap}$ : Capillary pressure

$\eta$ : Dynamic viscosity

$c_0$ : Speed of sound

$f$ : Frequency

$\omega$ : Angular frequency

$\lambda$ : Wavelength

$K$ : Wave number

$S_{ij}$ : Strain tensor component

$\sigma_{ij}$ : Stress tensor component

$\rho$ : Density

$V_L$ : Longitudinal velocity

$V_T$ : Transverse velocity

$Z$ : Acoustic impedance

$Z_t$ : Electrical impedance of the transducer

$R_{bottom}$ : Acoustic reflection coefficient on the bottom surface of textures

$S_{11}$ : Electrical reflection coefficient of the transducer

$A_{11}$ : Bottom surface echo

$A_{12}$ : Top surface echo

$h$ : Fluid film thickness

$Q$ : Flow rate

$\omega$ : Rotational speed

$v$ : Kinematic viscosity

$r$ : Radius of the silicon wafer

$u_r$ : Radial velocity of the fluid

$D$ : Hydraulic diameter

$R_e$ : Reynolds number

$f$ : Friction coefficient

$\Delta P$ : Pressure loss inside the micro-channel

$R_{top}$ : Acoustic reflection coefficient on the top surface of textures

$r_{Si/liquid}$ : Reflection coefficient between smooth silicon surface and a liquid

$c_{Si}$ : Longitudinal velocity of sound in silicon

$|r_1|$ : Reflection coefficient on the bottom surface of DTI

$|r_2|$ : Reflection coefficient on the top surface of DTI

$S_w$ : Unit area fraction of wetted surface

## General Introduction

The study of fluids had its fair share of interest throughout history from ancient civilizations (like Phoenicians, Romans and Greeks) that used their fair knowledge of fluid solid interactions to build basic sail ships designs. Many notable figures throughout history made their marks on explaining the fluids interactions, including Archimedes who is famously know in the fluidics domain for his Archimedes principle describing the buoyant force of a submerged object. There is Leonardo da Vinci (1452-1519) who derived the mass conservation equation in one-dimensional steady flow and described the turbulent flow created behind objects (Figure.1). Forward to the Nineteenth century with the introduction of Navier-Stokes equations which described the motion of fluids that are used up to this day in many fluidic applications. However, theoretical solutions to Navier-Stokes equations remain incomplete. Nowadays, with the help of computers, Computational Fluid Dynamics (CFD) is a popular branch of fluid mechanics which uses numerical methods and algorithms to solve complex problems which includes fluid flows.

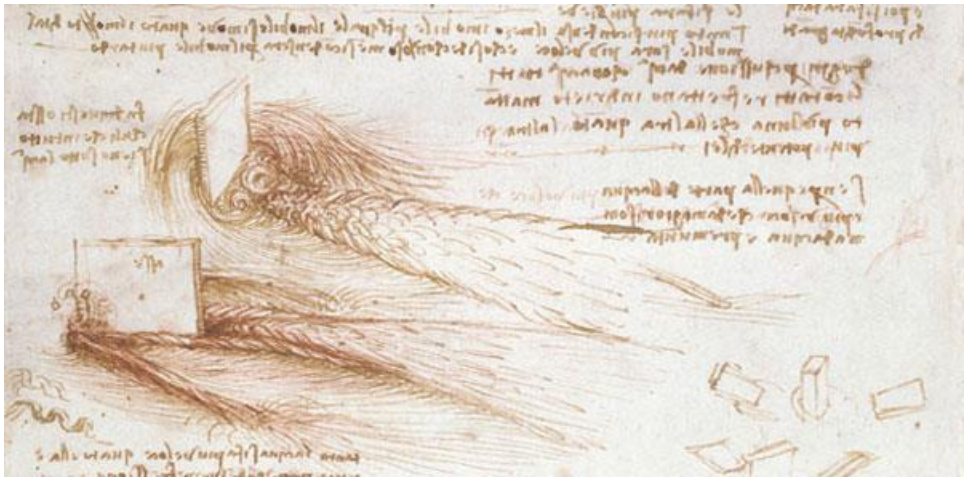

Figure.1 Sketch by Da Vinci describing turbulence created behind an object [1]

The fluid-solid interaction is also an important aspect of understanding the different interactions that result at macroscopic scales and could be investigated and explained at micro or even nanometric scales. One famous phenomenon depicting this aspect is the famous Lotus leaf effect (Figure.2). When a drop of water is placed on a Lotus leaf, the liquid remains in equilibrium on the micro / nanometric asperities of the leaf and the air contained between these asperities stays trapped expelled. This phenomenon was studied in detail from the 1970s thanks to the development of electron microscopy, it allows water to glide over the leaf which then becomes "non-wetted" and gives it a self-cleaning power. This type of surface is said to be superhydrophobic.


Figure.2 Liquid droplets suspended on lotus leaf (a), SEM image of micro-textured surface of the leaf (b) and (c) micro/nanostructure of the lotus leaf surface [2]

At micro / nano-metric scales, the gravitational forces are negligible and the capillary forces generated by physicochemical interactions of electrostatic origin are the dominant forces at the liquid interface. In the case of the Lotus leaf, the intensity of the capillary forces is governed by the chemical nature of the surface coating of the leaf (epicuticular wax) which prevents water from spreading on the surface rendering it hydrophobic and by the physical texturing of the surface which amplifies this effect, making the surface superhydrophobic. In nature, different superhydrophobic surfaces exist where the wetting state of the liquid is not complete due to gas being trapped inside the surface textures between the liquid and the solid surface. These superhydrophobic structures have been extensively studied until this day for a lot of potential applications. For example, the floating leaves of the plant *Melilotus siculus* which are able to retain gas underwater [3]. In the animal kingdom many forms of hydrophobic surfaces exist including the wings flies and moths [4].
Many practical applications have emerged from the study of superhydrophobic surfaces. For example, surperhydrophobic protective coatings on sub-marines, marine vessels and oil rigs to protect them from harsh saline environment [5]. superhydrophobic paper for the making of currency bills to increase their longevity from the sweat of people using them [6].

In some applications the superhydrophobic character had its advantages as we saw in the previous paragraph. In the microelectronics industry and for STMicroelectronics specifically, the fabrication of micro / nanometric silicon structures of high aspect ratios (ratio of height to lateral length of the structure) can create structures with characteristics similar to those of superhydrophobic structures in a sense that they create wetting defects by trapping air inside the textures, leading to difficulty for the liquids during the cleaning process to penetrate these structures and creating a “non-wetting” behavior. In addition to the problems related to cleaning, the high aspect ratio structures can induce high capillary forces during the drying phase of the structures at nanometric scales in which the liquid films pulls on the surface as it evaporates and deforms the material until it bends creating “pattern collapse” of these silicon structures. Inefficient cleaning coupled with structures deformation lead to low quality electronic products. As we will see in this work, the consequences of wetting behavior on STMicroelectronics nanostructures will be studied, from wetting default, structure deformation to the impact of the drying process. These consequences are more significant as the structures are increasingly small in size.

The pathway for the semiconductor industry was first paved through a paper written by Gordon Moore in 1965 in which he introduced the famous Moore's law stating that the number of electronic components ( for example transistors) which can fit into an integrated circuit would increase over time [7]. With the increase in number of components per electronic chip, the total size of the chip has to be contained within practical and economic limits which leads to downscaling the dimensions of the various chip's components. Through the process of scaling down transistors, the semiconductor industry was able to accomplish better performance per cost ratio which leads to market growth and attracted more investments in new technologies (Figure.3).

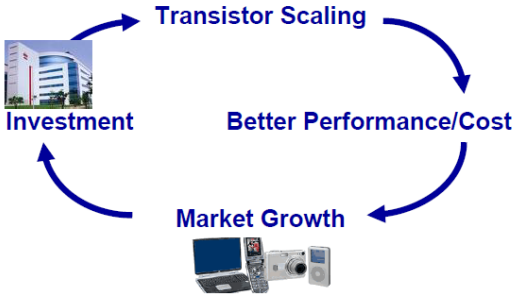


Figure.3 Schematic of the virtuous cycle of the semiconductor industry [8]

The international Technology Roadmap for Semiconductors introduced a new concept which does not focus on miniaturization but on other aspect such as functional diversity of the electronic products, built with different technologies and materials, such as photonic components for example. The Moore's law focused on the miniaturization of transistors namely Complementary Metal-Oxide-Semiconductor (CMOS) which are the building block for digital components, the new trend focuses on also non-digital products. Strong aspect ratios can then also appear for the micro / nanostructures of these components. This approach was called "More Than Moore" (Figure.4).

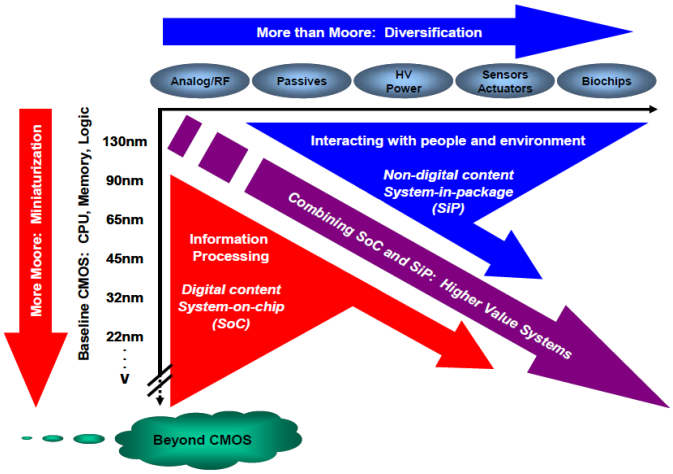


Figure.4 Schematic of the evolution of systems following Moore's Law and the "More Than Moore" approach. The combined needs for digital and non-digital functions in integrated systems follow a dual trend: miniaturization of digital functions ("More Moore") and diversification of functions ("More Than Moore") [8]

The etching process (Figure.5) generally consists of many steps including: deposition the material in which the structures are formed, optical lithography to define the zones of etch and plasma or wet etching to transfer the patterns into the material and finally a cleaning process after the plasma etching to remove the resist and other contaminants that maybe present.

During the cleaning process, different chemical solutions and liquids are used and between each cleaning cycle, the drying process takes place to remove the liquid chemicals.

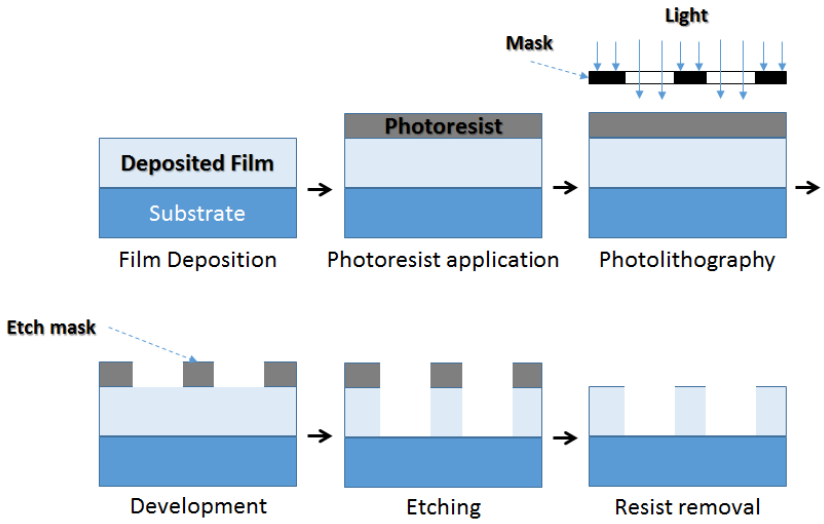


Figure.5 Schematic of the etching process in the fabrication of structures in microelectronics [9]

Some of the problems that arise during the wet etching or cleaning steps are related to the inability of the liquid to penetrate inside the micro / nanostructures. The result being the liquid not wetting the textured surface like a drop of water on the Lotus leaf, reducing the cleaning efficiency and the chip could end up being defective. Thus, knowledge of the wetting state during wet process is a crucial issue in the microelectronics industry.
Other types of problems arise during the drying of the structures. At the micro /nanometric scale, the capillary forces of the liquids can reach high values. When the liquid evaporates, it exerts capillary forces on the micro / nanostructures which can cause the pattern to deform and even collapse, ultimately affecting the overall quality of the fabricated chip.

Different methods of wetting characterization exist. At IEMN, a method using high frequency acoustic waves in order of gigahertz has been developed to characterize the wetting of droplet of liquid on STMicroelectronics structures [10]. The use of frequencies of the order of gigahertz makes it possible to bring together different surface properties and to determine the physicochemical nature of the interfaces within the textured layers: solid - liquid or solid - air.

The choice of the frequency and the geometry of the active acoustic element will be determining parameters of the sensitivity of the method to the presence or absence of liquid inside the micro / nanostructures.

In the previous study of wetting characterization for STMicroelectronics, the use of a droplet of liquid on the textured surface is adopted (no movement of liquid). Nonetheless, in the actual industrial process, the cleaning is done using a liquid dispensed on a spinning wafer which involves fluid hydrodynamics (includes movement of cleaning liquid).

The thesis work will be then a continuation of the previous work of wetting characterization, but the scope of the work will be centered on approaching the actual industrial cleaning process which involves the use of micro-channel to allow the movement of liquid. In addition, the use of such a confined structure will enable us to study the drying process along with its connection to pattern collapse. The entire study was carried out as part of a partnership between STMicroelectronics and IEMN for its expertise in acoustics and microsystems manufacturing in the frame work of CIFRE thesis. This work therefore takes place within the framework of the Joint Laboratory IEMN-ST.

In Chapter I, we will present the basic concepts of the physics behind the wetting and drying phenomenon, the main methods of characterization of wetting and some principles of hydrodynamic flow in channels bounded by a textured surface.

In Chapter II, the basic theoretical notions of acoustics will be introduced in order to understand how an acoustic wave propagates in a fluid or solid medium and how it behaves at an interface between two different mediums. In addition, the bibliographical study of the different models reflecting the behavior of an acoustic wave in a micro / nanostructured layer will be presented. We will also introduce the finite difference model (FDTD: Finite Difference Time Domain) which will allow us to better understand the fluid / textured surface interaction and then use it to interpret the experimental measurements.

Chapter III will present the acoustic method of high frequency reflectometry to characterize the wetting of micro / nanostructured surfaces, the modification of the acoustic transducer technical fabrication to produce transversal waves and the PolyDiMethySiloxane (PDMS) micro-channel which will allow us to create a movement of the liquid on the STMicroelectronics structures. The entire experimental set-up and measurement methods will also be presented.

Finally, in chapter IV, the results of the study of the wetting of micro / nanostructured surfaces from STMicroelectronics will be presented. The relationship between the experimental and theoretical results of the models introduced in Chapter II will be presented. A new technique of following the wetting and drying processes in real-time will be introduced enabling us to conclude on the wetting states, the pattern collapse phenomena and to provide answers to the questions of STMicroelectronics.

# I. Wetting Phenomenon

The work presented in this thesis governs the problematic of cleaning silicon wafers at STMicroelectronics and it concerns mainly two aspects: the study of wetting phenomenon over etched silicon wafers and the characterization of wetting state using acoustic waves at ultra-high frequency.

The first chapter presents a theoretical study of the wetting phenomenon to understand the work done to characterize the wetting at etched silicon interface. It also presents the different notions of fluidic flow inside a micro channel used to approach the industrial cleaning process to finally characterize the wetting state using ultra-high frequency acoustic reflectometry and compare the acoustic experimental results to a simulation model.

The theory of surface/liquid interaction on smooth surface will be presented first and then it will be presented over a structured (etched) surface. Secondly we will present the fluid flow inside a micro channel and make a link for the use of fluid flow in the study of wettability to approach the industrial cleaning and drying process used at STMicroelectronics. Finally, different wetting characterization methods will be presented to at last introduce the acoustic characterization method and its convenience for our study.

## I.A. Surface/Liquid Interaction

### I.A.1. Surface Tension

The fluid molecules within a fluid are exposed to attractive forces between each other. If we consider a free surface between a liquid and gas for example water and air, the water molecules at the interface are exposed to less attractive forces compared to the molecules in the water. This makes the surface molecules having higher potential energy in an energetically unbalanced state thus, the fluid will tend to minimize the surface areas, turning the fluid molecules into spheres hence, the existence of surface tension.

The *surface tension* ($\gamma$) is defined as the ratio of potential energy at the interface to the interface area and its unit given SI in N/m.

### I.A.2. Contact Angle and Wetting Phenomenon

Considering a sessile liquid droplet on a solid homogeneous surface (perfectly smooth without impurities) as illustrated in Figure I.1. The dimensions of the liquid droplet are small enough in order to neglect the gravitational effect. This dimension is called the capillary length and is defined as $\lambda_{cap} = \frac{\gamma}{\rho g}$ with $\rho$ the density of the fluid and $g$ the gravitational acceleration. In the case of water at 20$^{O}$C, $\lambda_{cap} = 2.71mm$.

The contact angle (or Young's angle "θ") is defined as the angle formed between the liquid/vapor interface and the liquid/solid interface; we can obtain this angle geometrically by drawing a tangent line from the contact point (point where the three interfaces co-exist) along

the liquid/vapor interface. The line where the three interfaces (Liquid, solid and vapor) co-exist is called the contact line.

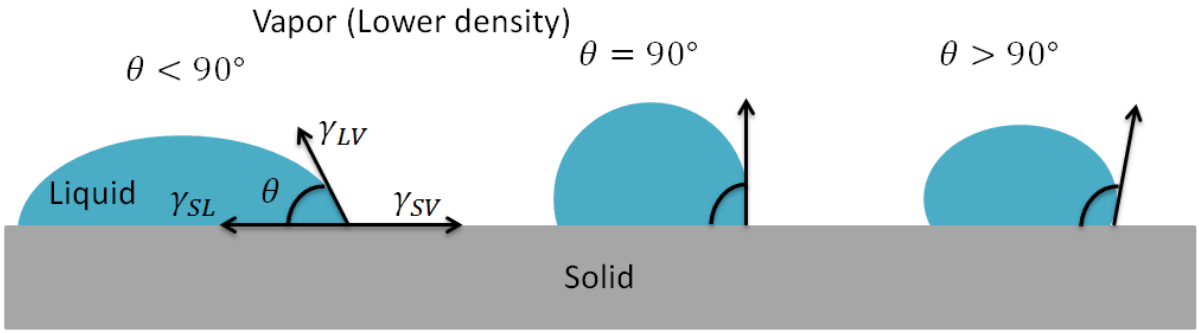


Figure I.1 Diagram showing Young's angle formed by a drop of liquid deposited on a solid

As described by Thomas Young in 1805 [11], the contact angle is obtained at mechanical equilibrium of the interfacial force on the horizontal axis:

$$\gamma_{LV} \cos\theta = \gamma_{SV} - \gamma_{SL} \quad \text{Eq I-1}$$

where, $\Upsilon_{LV}$, $\Upsilon_{SV}$ and $\Upsilon_{SL}$ are the interfacial tensions across the liquid/vapor, solid/vapor and solid/liquid interfaces, respectively.

There are different values that the contact angle can take when a liquid droplet is deposited on a surface:

- $\theta = 0^{\circ}$: The liquid turns into a flat film and we have complete wetting
- $\theta = 180^{\circ}$: There is no wetting at all
- $90^{\circ} < \theta < 180^{\circ}$: We have a partial wetting and we say the wetting is favorable for $\theta < 90^{\circ}$ and unfavorable wetting for $\theta > 90^{\circ}$

### I.A.3. Pressure difference across an Interface

Another consequence of the surface tension is the pressure difference across the interface. This pressure is created by the surface tension force normal to the direction of the interface. This pressure is important on the concave side of the interface and it's dependent on the radii of curvature and the surface tension. The expression of the pressure difference is given by the Young-Laplace equation:

$$\Delta P_{Laplace} = \gamma\left(\frac{1}{R_1} + \frac{1}{R_2}\right) \quad \text{Eq I-2}$$

where, $\Upsilon$ is the surface tension and $R_1$, $R_2$ are the principal radii of curvature (minimal and maximal) of the interface.

If we consider a liquid-gas interface, $\Delta P = P_L - P_V$ when the interface curves into the gas phase (rain droplet in air) and $\Delta P = P_V - P_L$ when the interface curves into the liquid phase (air bubble in liquid); $P_L$ and $P_V$ are respectively the liquid and gas pressures.

In a specific case where we have a spherical droplet of radius *R*, the two radii of curvature become equal to *R*. Eq I-2 is reduced to:

$$\Delta P_{Laplace} = \frac{2\gamma}{R}. \qquad \text{Eq I-3}$$

### I.A.4. Advancing and Receding Contact Angle

In reality the single value contact angle defined by Young's equation Eq I-1 does not exit due to the fact that there is no ideal smooth surface. When a liquid is deposited on a solid surface, the movement of the liquid to wet the fresh solid surface coupled with the liquid movement during the deposition leads the contact angle to be comprised a range scale and not a single value as described by Eq I-1. This range is defined by a minimum and maximum value, called receding and advancing contact angles respectively. The difference between these values is called contact angle hysteresis. There are two methods illustrated in Figure I.2 to measure the dynamic contact angle. The first method called the tilting plate method consists of depositing a liquid droplet (with diameter below the capillary length) on a surface inclined by a critical angle to cause the movement of the droplet and then the advancing and receding contact angles are measured as the downhill and uphill angles. The second method consists of changing the volume of the liquid droplet, when the droplet is inflated (expand) the contact line moves away from the center of the droplet, we get the advancing contact angle $\theta_A$, and when the droplet is contracted by removing liquid progressively for example, the contact line moves towards the center of the droplet and we get the receding contact angle $\theta_R$. The contact angle hysteresis is given as:

$$\Delta\theta = \theta_A - \theta_R . \qquad \text{Eq I-4}$$

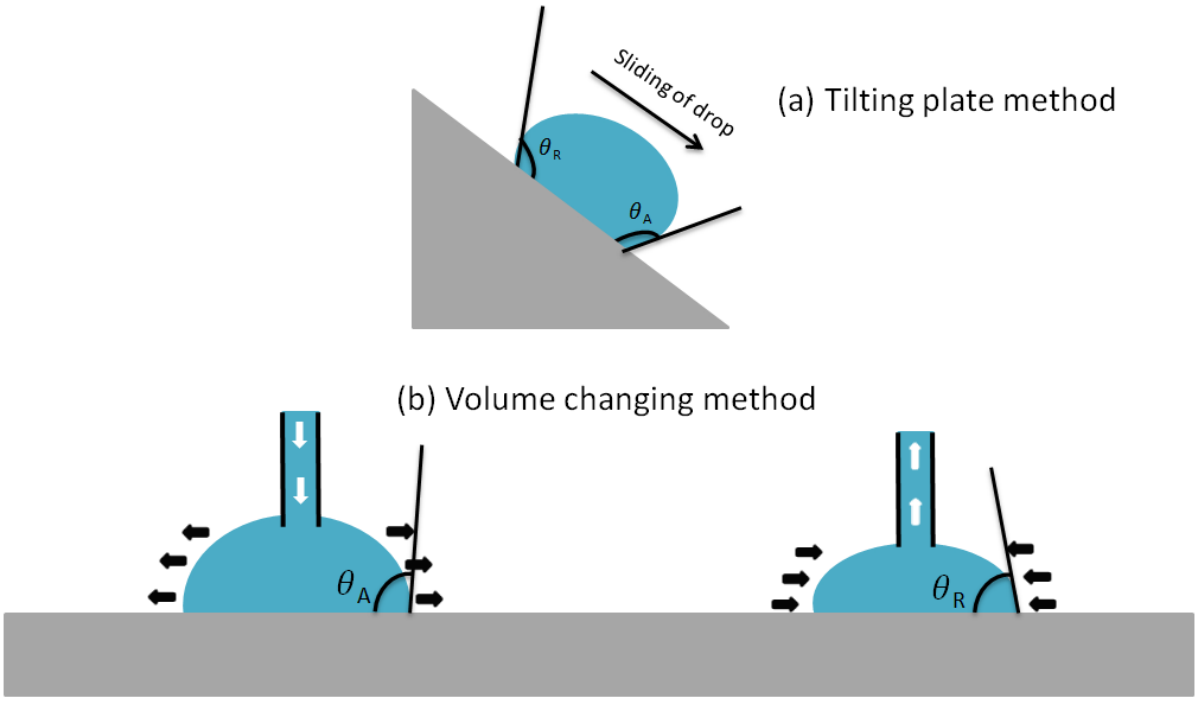


Figure I.2 Diagram showing the advancing and receding angles using tilting plate method (a) and volume changing method (b)

Contact angle hysteresis arises from different factors namely surface roughness and impurities (heterogeneous surface). For example, hydrophobic heterogeneous surface with trenches (roughness) will hold the movement of the contact line. These trenches on the surface can prevent the spreading of the liquid and therefore lead to increase the apparent contact angle. In the same manner the trenches will hold back the contracting motion of the liquid droplet leading to decrease the apparent contact angle. In this context, an ideal surface is only present in theory. In practical terms, the contact angle presented by the Young's equation is therefore not fully representative of its wetting properties. Nevertheless, the advancing contact angle $\theta_A$ on smooth heterogeneous surfaces is found experimentally to be a good approximation of Young's contact angle $\theta$ [12], while the receding contact angle $\theta_R$ is unstable due to liquid sorption and solid swelling [13]. On rough surfaces, all the contact angles differ from the contact angle given by the Young's equation [14].

## I.B. Liquid/Solid Interaction: Textured surface

### I.B.1. Wetting States:

In our work studying wetting, we will deal with structured surfaces which are used at STMicroelectronics by etching micro/nanostructures on silicon wafers. In what follows we will be dealing with the wetting on physically and or chemically heterogeneous surfaces.

When a liquid droplet is deposited on a structured interface, the form of the droplet is no longer a perfect sphere and the triple contact line is no longer necessarily a circle. The contact angle given in Eq I-1 is no longer valid except if we look at a very local scale of the

structuration, meaning that we look at the contact angle of the individual micro / nanometric structure. So, different contact angles depending on the scale taken can be considered.

There exist different wetting states: Wenzel, Cassie-Baxter and Wet Cassie states (Figure I.3) possible on a structured surface with each giving rise to an apparent contact angle $\theta^*$. In what follows we will present the relation between the apparent contact angle $\theta^*$ and Young's angle $\theta$.

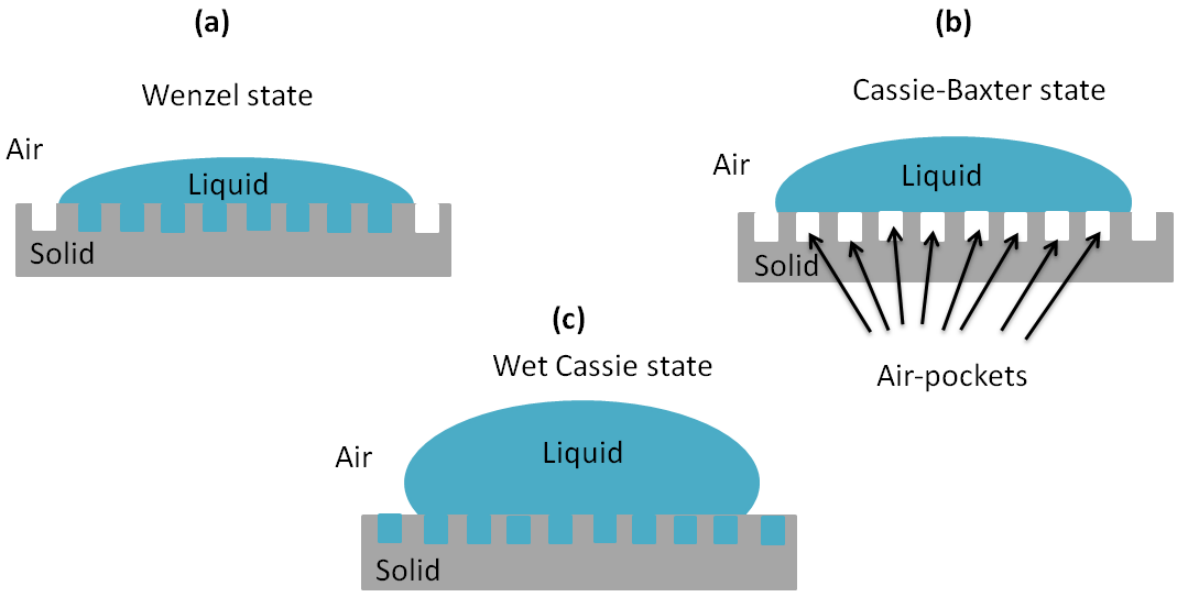


Figure I.3 Different Wetting states on structured surface: (a) Wenzel, (b) Cassie-Baxter and (c) Wet Cassie or hemi-wicking.

### *I.B.1.a. Wenzel State*

When a liquid droplet is deposited on a rough solid, a Wenzel state is obtained when the liquid penetrates the space between the roughness structuration of the solid (Figure I.3.a). This state has been described by Wenzel [15] and it is characterized by an apparent contact angle $\theta^*$. Let's consider a rough surface of roughness factor $r$, which is the ration between the real surface area and the equivalent flat or smooth surface area ($r > 1$). The apparent contact angle is evaluated by taking an infinitesimal displacement $dx$ of the contact line as shown in Figure I.4.


Figure I.4 Infinitesimal displacement of the contact line in Wenzel case

This small displacement causes a change in the surface energy *dE* given as:

$$dE = r(\gamma_{SV} - \gamma_{SL})dx + \gamma_{LV}dx\cos\theta^* . \quad \text{Eq I-5}$$

With $\theta^*$ the apparent contact angle. At equilibrium the surface energy *E* is minimal (*dE* = 0), coupled with Young's equation (Eq I-1) we can obtain the Wenzel's relation:

$$\cos\theta^* = r\cos\theta . \quad \text{Eq I-6}$$

From Eq I-6 above we can deduce that: $\theta^* < \theta < 90^\circ$ and $\theta^* > \theta > 90^\circ$ ($r > 1$). So, with a structured surface hydrophilicity and hydrophobicity are amplified.

***I.B.1.b. Cassie-Baxter State***

The Cassie-Baxter state is obtained when the liquid droplet deposited does penetrate the interior of the surface texturing and remains in equilibrium at top. In that case, air pockets are present in these within these textures (Figure I.3.b).

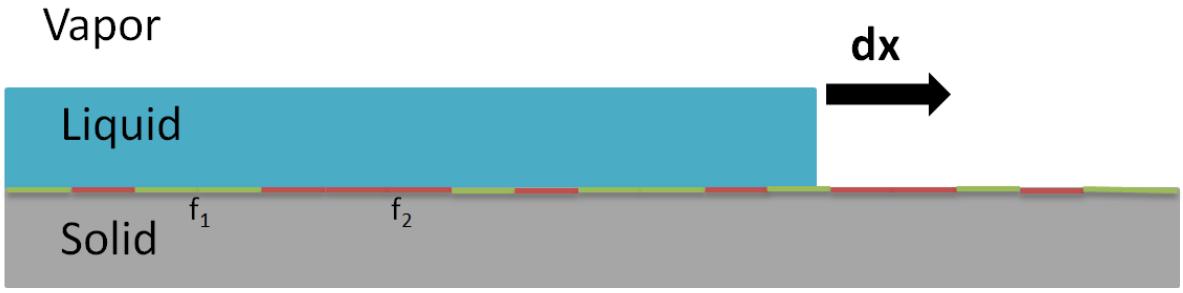


Figure I.5 Infinitesimal displacement of the contact line in Cassie-Baxter case

To find the apparent contact angle for the Cassie-Baxter state we consider a liquid droplet on a heterogeneous solid made up of two chemical species (one of them could be air to represent the Cassie-Baxter surface) and each with surface fraction $f_1$ and $f_2$ ($f_1 + f_2 = 1$). In the same manner as done for the Wenzel state, taking an infinitesimal displacement of the contact line (Figure I.5). The change in surface energy is:

$$dE = f_1(\gamma_{SV1} - \gamma_{SL1})dx + f_2(\gamma_{SV2} - \gamma_{SL2})dx + \gamma_{LV}dx\cos\theta^* \quad \text{Eq I-7}$$

where, indices 1 and 2 refer to the two species that the solid is composed of.

At equilibrium, the surface energy E is minimal (*dE* = 0). Eq I-7 is reduced to:

$$\cos\theta^* = f_1\cos\theta_1 + f_2\cos\theta_2 . \quad \text{Eq I-8}$$

For a micro/nanostructured surface, the two species are the solid and air since the Cassie-Baxter state creates air-pockets which are trapped in the surface texturing. The contact angle of a liquid droplet in air is 180° ($\theta_2 = 180^\circ$). Eq I-8 is then reduced to:

$$\cos\theta^* = f(1 + \cos\theta) - 1 \quad \text{Eq I-9}$$

where, *f* is the area fraction of the solid-liquid interface.

### *I.B.1.c. Hemi-Wicking State:*

The Hemi-Wicking (also called Wet Cassie) state is obtained when a liquid film is formed that penetrates the surface texturing and at the same time a formed droplet sits on top of this film. The liquid droplet doesn't cover the all area of the liquid film which covers the entire textured surface. Note also that the formation of the liquid droplet isn't necessarily; Hemi-Wicking state could exist with just the formation of the liquid film.

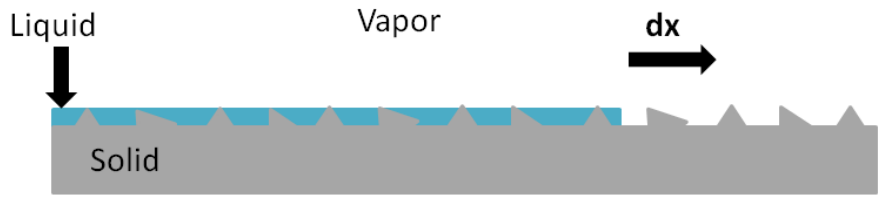


Figure I.6 Infinitesimal propagation of the liquid film in the surface texturing (features)

To find the apparent contact angle, let us consider the model presented in Figure I.6, let's take $\Phi_S$ as the ratio of surface area of the top features to the total surface area of the sample ($\Phi_S$ < 1). In the same manner as done previously for the Wenzel's and Cassie-Baxter states, the infinitesimal displacement leads to a change in the surface energy:

$$dE = (r - \emptyset_S)(\gamma_{SL} - \gamma_{SV})dx + \gamma_{LV}(1 - \emptyset_S)dx \, . \qquad \text{Eq I-10}$$

The factor ($r$ - $\Phi_S$) is due to the penetration of the liquid inside the surface features. The second term in Eq I-10 is due to the creation of the liquid/vapor interface as the liquid film moves. Hemi-Wicking state occurs when $dE < 0$, coupled with the Young's equation we get the following condition:

$$\theta < \theta_c \;\; with \;\; \cos\theta_c = \frac{1 - \emptyset_S}{r - \emptyset_S} \, . \qquad \text{Eq I-11}$$

The condition states that the contact angle $\theta$ over a flat surface should be smaller than a critical angle $\theta_c$.

The contact angle for the Hemi-Wicking state can be found if we consider the formation of a droplet on top of the liquid film (Figure I.6), then following an infinitesimal displacement of the contact line [16] the change in surface energy is:

$$dE = (\gamma_{SL} - \gamma_{SV})\emptyset_S dx - \gamma_{LV}(1 - \emptyset_S)dx + \gamma_{LV}\cos\theta^* dx \qquad \text{Eq I-12}$$

At equilibrium, $dE = 0$. Using Young's equation (Eq I-1) we get:

$$\cos\theta^* = \emptyset_S \cos\theta + 1 - \emptyset_S \, . \qquad \text{Eq I-13}$$

### *I.B.1.d. Composite Wetting States*

In reality, when a liquid drop is deposited on a textured surface, the complete Wenzel or Cassie-Baxter states may exist, but we find composite states, a mix of both states locally at the surface's features. As presented in Figure I.7 there are three different composite states.

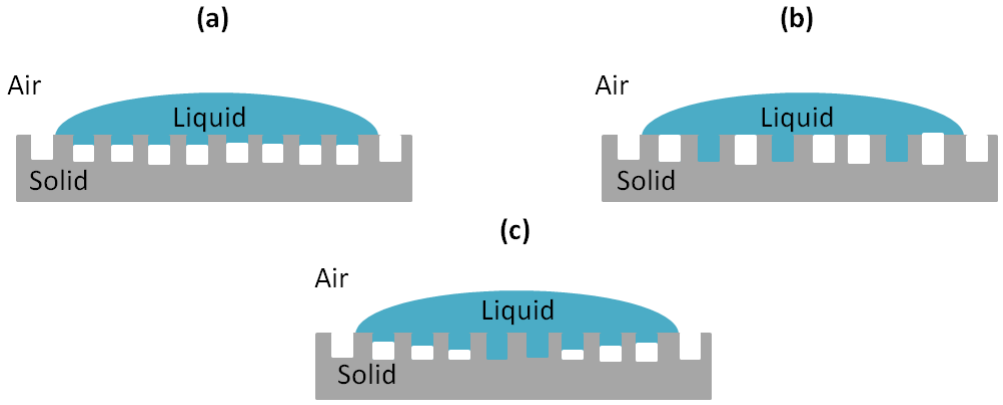


Figure I.7 Schematic of different composite wetting states: Partial penetration of liquid (a), Mix of Wenzel and Cassie-Baxter states (b), Impalement of the droplet with partial penetration of liquid

The apparent contact angle $\theta^*$ of these composite states is given by Marmur [17] as:

$$\cos\theta^* = f\emptyset_S \cos\theta + \emptyset_S - 1\,. \qquad \text{Eq I-14}$$

## I.B.2. Wetting States Transitions:

### *I.B.2.a. Three-phase contact line*

As presented previously (I.A.2), the three-phase contact line is an important characteristic of the solid-liquid interaction in defining the value of the contact angle [18]. It is defined as the locations where the solid, liquid and gas phases coexist. The measurement of the contact angle on a textured surface is thus more complicated than on a planar one because it depends on the localization of the measurement all long the triple line and in the experimental conditions. The locations can vary depending on the wetting state of a droplet deposited on a solid surface. In the case of Wenzel state, the three-phase contact line is located at the droplet periphery (Figure I.8.a). For the Cassie-Baxter state, multiple three-phase contact line exists. It can be formed on the periphery of the droplet which can be observed macroscopically and microscopically. We can also observe it below the droplet, what can be called an 'internal contact line' formed at the interface between the solid interface, the suspended liquid in the surface texture and the trapped air phase (Figure I.8.b).

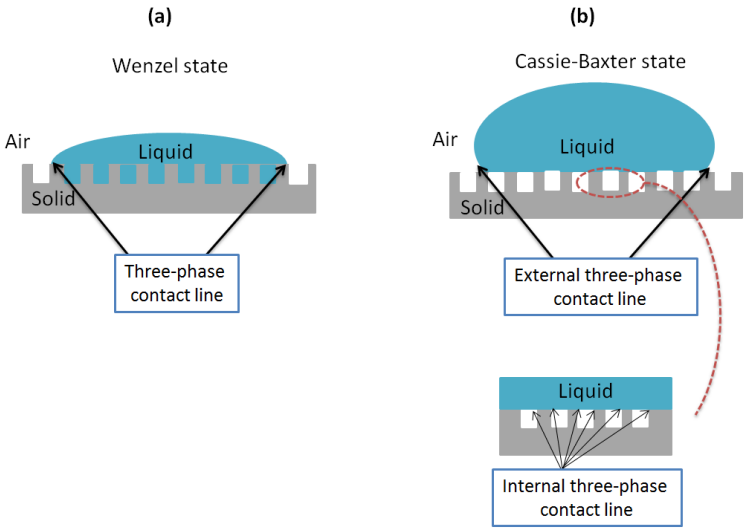


Figure I.8 Schematic of the three-phase contact line for the Wenzel state (a) and the Cassie-Baxter state (b)

### *I.B.2.b. Droplet deformation*

When a liquid droplet is deposited on a rough surface it can undergo some degree of local deformations. On a macroscopic scale the liquid can appear to have a quasi-perfect circular shape, but at microscopic view (some µm) of the contact between liquid and the surface reveals the level of deformations (Figure I.9). While one condition to a proper contact angle measurement is for the droplet to have a symmetrical shape, the deformations lead the droplet to have asymmetrical shape rendering the measurements of the contact angle not meaningful in a sense of obtaining a mean contact angle, but it can give us an idea of the local contact angle.

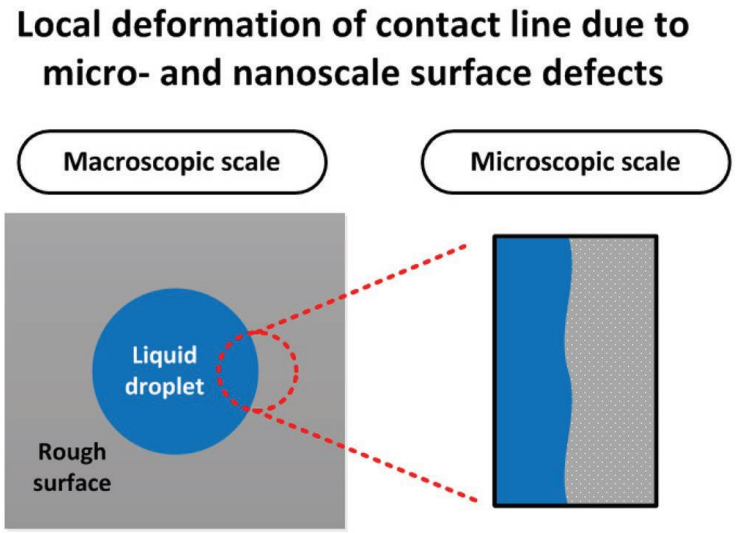


Figure I.9 Deformation of the three-phase contact line due to surface roughness leading to the asymmetrical droplet shape [19]

One solution to overcome this problem is the use of larger droplet size to reach more symmetrical shape since the larger the droplet the lesser it is impacted by surface roughness and chemical composition [20],[21]. Also, it has been proved mathematically that as the droplet size increases (always below the dimension of the capillary line), the better the prediction of the contact angle will be given by the Cassie-Baxter and Wenzel equations [22].

### *I.B.2.c. Gibbs Energy:*

The wetting states that were previously presented are the stable wetting states in term of thermodynamic equilibrium and each state presenting a minimum of Gibbs energy for the system (Figure I.10). The states which have a global minimum energy are called stable and the other states which have local minimum but high energy are called metastable. Due to their high energy, the Cassie-Baxter's and composite states are considered metastable and by passing an energy barrier the system could undergo a transition to the lower energy states like the Wenzel, Hemi-Wicking and composite states.

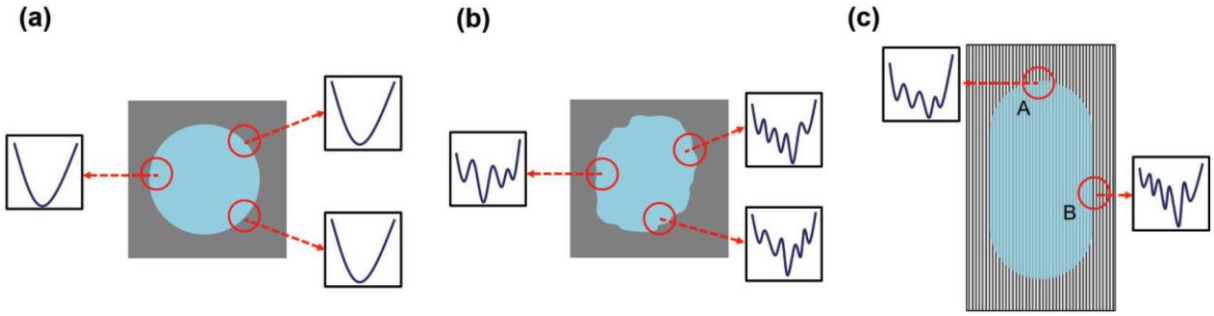


Figure I.10 Schematic of the Gibbs energy profile at different local sites for a sessile droplet on a) an ideal smooth surface, b) surface with uniform roughness and c) textured surface. [19]

By equating Eq I-6 and Eq I-9 we can determine theoretically the critical contact angle used to separate the two wetting states:

$$\cos\theta_C = \frac{f-1}{r-f}. \qquad \text{Eq I-15}$$

When $\theta_C > 90^\circ$ both the Cassie and Wenzel states exist. One homogeneous wetting state can exist when we have $\theta < \theta_C$, otherwise multiple states can exist theoretically [23]. There have been some observations noting that even when the Young's angle is smaller than the critical angle, the Cassie state can exist, meaning that both states Cassie and Wenzel can exist at the same time leading to a heterogeneous wetting state [8–12] .

### *I.B.2.d. Pressure induced wetting state transitions*

The transition from Cassie-Baxter to Wenzel state is governed by mechanical equilibrium at the liquid / air interface inside the surface textures. This mechanical equilibrium can be seen theoretically as pressure equilibrium which is the pressure difference between the suspended

liquid and the trapped air pockets inside the textures (Figure I.11). When a droplet in Cassie-Baxter state reaches a critical Laplace pressure (downwards acting liquid pressure), the liquid starts impaling into the surface textures. Thus, the liquid pressure exceeds the inside air pressure shifting the liquid / air interface and wetting transition may occur.

The maximum pressure difference that can be supported in the Cassie-Baxter state between the liquid and air is given as [29]:

$$\Delta P_{max} = P_{liquid} - P_{air} = -\frac{2\gamma \cos \theta_A}{w}$$

where, $\theta_A$ is the local advancing contact angle and $w$ the width of the surface texture (separation distance between the texture walls).

We can notice that the maximum pressure difference that can be supported by the Cassie-Baxter state decreases as the width of the texture increases. For textures with nanometric width, the maximum pressure difference is reported to be in the range of $O(10^5)$ Pa [30]. Shen *et al.* [31] showed that through a temperature decrease, induced contraction of the trapped air pockets occur causing the air pressure to decrease and the observation of wetting transition on superhydrophobic surface.

Fang *et al.* [32] also showed a Cassie-Baxter to Wenzel transition using droplet squeeze test on a surface composed of micropillar array. The transition occurred at a certain critical pressure which was higher than the theoretical prediction. This was due to errors in estimating the contact angle of the micropillars's sidewall.

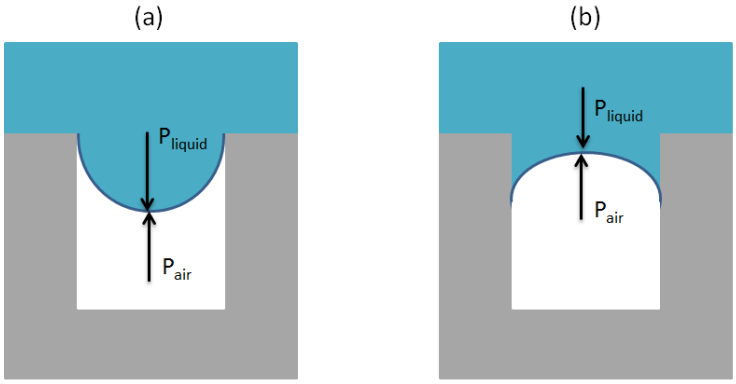


Figure I.11 Schematic of the pressures acting on the liquid / air interface for non-wettable liquid / solid contact surface (a) and wettable liquid / solid contact surface (b)

An increase in liquid pressure above trapped gas (air) can also lead to an increase in the diffusion rate of gas into the liquid thus, leading to shrinkage of the gas volume and a transition to the Wenzel state may occur. Ling *et al.* [33] monitored the diffusion rate of trapped gas in superhydrophobic textured surface as the pressure of the liquid flowing on top of the surface increases gradually from 1 to 1.9 atm (Figure I.12). The transition is composed of three stages where the second stage II ($60 < t < 320$s) is characterized by the depinning of the trapped gas and by the decrease of the volume of trapped gas under the liquid. At stage III ($320 < t < 350$s), the liquid interface touches the bottom of the groove and we can observe

two remaining gas pockets at the corners (Figure I.12.a). It is reported that beyond t = 350s, the gas pockets are no longer visible but most likely some residual nano-pockets of gas might be remaining.

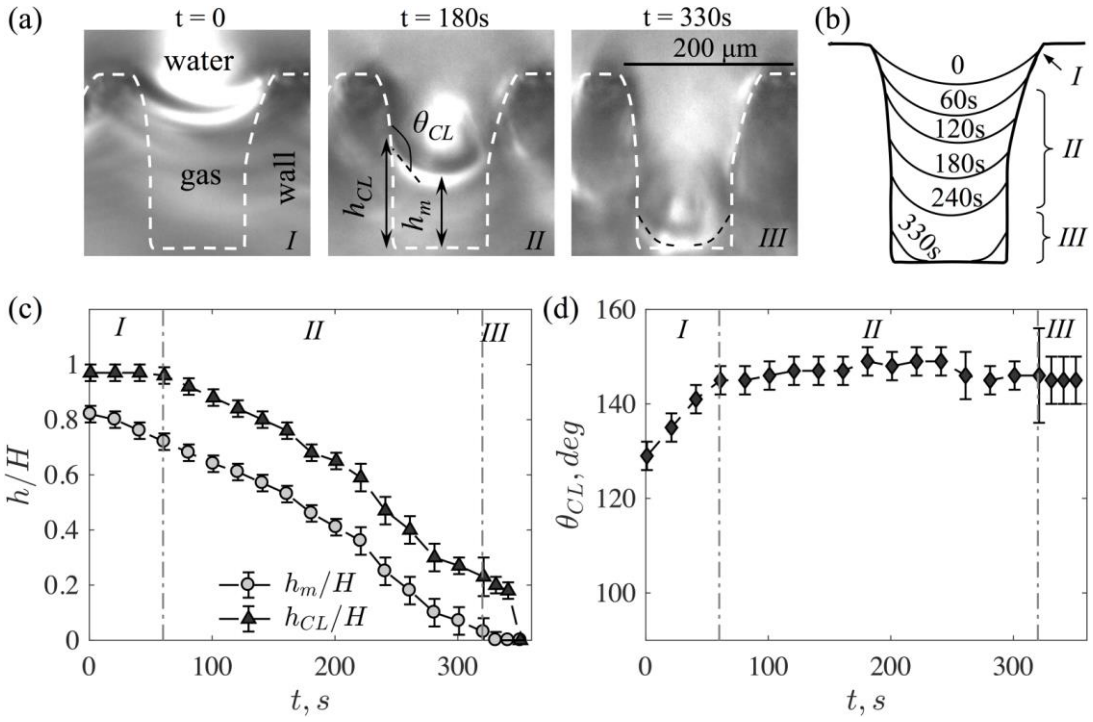


Figure I.12 Wetting transition due to gas diffusion at constant $\Delta P$ = 0.23 atm: (a) Images of the shrinkage of gas volume with time; (b) Schematic of the interface shape; (c) Average of the interface heights at the contact line and in the middle of the meniscus; (d) Average local contact angle [33]

### *I.B.2.e. Penetration Mechanism:*

As we saw before, the wetting transition of a droplet is possible when we give a certain amount of energy to the system. We present now two possible impalement scenarios for a droplet inside a textured surface [34], [35] (Figure I.13.a and Figure I.13.b).

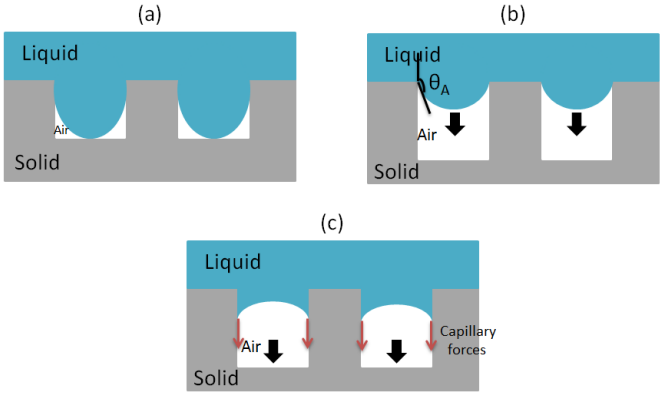


Figure I.13 Schematic representation of the wetting transition mechanisms: By "Touch down" (a), by "Sliding" (b). Liquid impalement inside solid textures in the case of hydrophilic surface (c).

In the case of a low aspect ratio of the textures, we have what is called a "Touch down" mechanism where the interface curvature increases, implying that the minimal height which

separates the liquid interface and the bottom of the surface texture diminishes. At higher aspect ratio of the surface textures, the local contact angle at the top of the textures attains the value of the advancing contact angle $\theta_A$. If the contact angle $\theta > \theta_A$, the contact line will slide in a continuous manner towards alone the walls of the texture to reach the bottom, and that what we call the "Sliding" mechanism.

In the case where the surface is hydrophilic, theoretically there's no energy needed to start the impalement of the droplet, therefore the droplet slides naturally undergoing capillary forces which act at the level of the local triple line consequently forcing the liquid towards the bottom of the texture (Figure I.13.c).

We note that all the previous considerations are valid when the air trapped can escape easily the network of the surface textures (open structures).

In the case of air being trapped inside the surface textures, a diffusion mechanism takes place where the air escapes the surface textures by diffusion into the penetrating liquid. If we consider liquid (for example water) suspended inside a surface groove under which gas is trapped, a plastron (gas + water vapor) trapped layer is formed. The mass flux for a two dimensional (2D) formed plastron is then given as [33]:

$$M = D(P_w + \frac{2\gamma \cos\theta_{CL}}{w} - P_v - P_\infty)/(k_H \delta_c) \quad \text{Eq I-16}$$

where, $D$ the diffusion coefficient, $P_w$ water pressure, $P_v$ water vapor pressure, $P_\infty = k_H c_\infty$ saturation pressure corresponding to gas pressure in the liquid bulk, $\delta_c$ gas diffusion length scale, w width of the groove, $\theta_{CL}$ local contact angle and $k_H$ is the Henry's law constant.

One condition to maintain the Cassie-Baxter state is when $M \leq 0$ [36]. An increase in $P_w$ to a level such that $M > 0$ will cause a wetting transition.

Whatever the mechanism for trapped gas escaping structured surface (escaping through open structures or diffusion through suspended liquid for closed structures), it is important to study the wetting dynamics at very small scales to better understand the wetting transition.

## I.C. Wetting Problems in Microelectronics

### I.C.1. Contaminations Problems

Several types of contaminations can be present on the surface of silicon wafer, and they can originate from dry etch process or just simply contact with air during storage. These contaminations if not properly removed can lead to defective chips during the next steps in the silicon wafer process. Multiple cleaning processes are developed for removing contaminations to better control the surface of the wafer without deforming the state of surface or adding new contaminations.

The surface contaminants can be present under different forms (particle, film, absorbed molecules) and its nature can also vary between (metallic, organic, ionic) (Figure I.14).

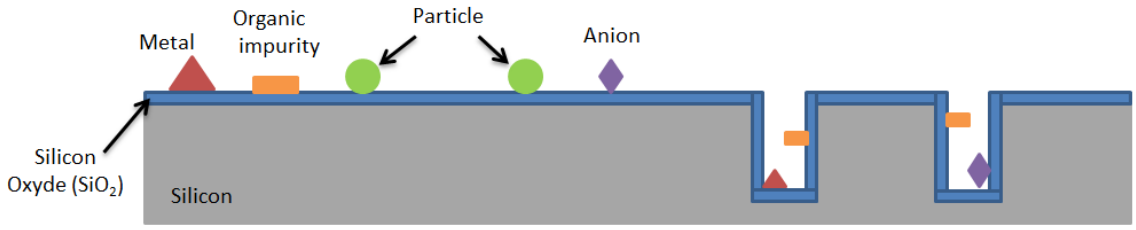


Figure I.14 Schematic of different contaminants that can be present on a structured silicon surface coated with oxide layer

The choice of the cleaning procedure is highly depends on the nature of contaminants present on the silicon surface and the exposed material.

### I.C.2. Liquids for cleaning

There are several cleaning solutions used in contaminants removal at the semiconductor industry (like STMicrolectronics) [37]:

1- Hydrofluoric acid solutions:

Solutions of diluted hydrofluoric acid (HF) are used to remove contaminants (metals, organic and inorganic particles) and etch the silicon dioxide ($SiO_2$) and silicon nitride ($Si_3N_4$) at ambient temperature. The thin native oxide film is completely removed after immersion of the silicon wafer in HF solution. One indication of the removal of this oxide layer is the wetting characteristic change of the silicon surface from hydrophilic to hydrophobic which is a direct effect of the H-passivated silicon surface. Typical mixture of HF solution is: 1:50 to 1:100 HF (49 wt%; wt: mass fraction) / $H_2O$ at room temperature.

2- Sulfuric acid ($H_2SO_4$)/hydrogen peroxide solutions:

The sulfur peroxide mixture (SPM) also known as “Piranha etch” or “Caros acid” because of their ability to remove large organic materials and some photoresist resists from the silicon surface. One down side to this cleaning process is that the silicon surface will be left contaminated with sulfur (S) residues from the $H_2SO_4$. Typical mixtures used: 2:1 to 4:1 volume ratios of $H_2SO_4$ (98 wt%) and $H_2O_2$ (30 wt%) at 100 – 130 ˚C.

3- RCA solutions:

The RCA cleaning process consists of applying hot solutions known as SC-1 and SC-2 (Standard Clean 1 and 2) to the Si wafers. The SC-1 solution is the first in the cleaning process and it is mixture of ammonium hydroxide ($NH_4OH$), hydrogen peroxide ($H_2O_2$) and distilled water ($H_2O$). It is used to remove oxide and quartz organic contaminants from the Si surface, the basic pH also makes it possible to limit the adhesion (or re-deposition) of particles on the surface dioxide ($SiO_2$) surface thanks to the stronger negative electrostatic interactions at these pHs. The SC-2 solution which comes second in the cleaning process consists of a hydrochloric acid (HCl), hydrogen peroxide ($H_2O_2$) and

distilled water ($H_2O$). The SC-2 solution is used to eliminate from Si surface alkali residues and traces of metals (Au and Ag) and also some metal hydroxides such as $Al(OH)_3$, $Fe(OH)_3$, $Mg(OH)_2$ and $Zn(OH)_2$. Typical mixtures used: 1:1:5 $NH_4OH$ (29 wt%) and $H_2O_2$ (30 wt%) at 70 ˚C for SC-1 solutions and 1:1:5 HCl (37 wt%) and $H_2O_2$ (30 wt%) at 70 ˚C for SC-2 solutions.

4- Deionized Water:

After each process of cleaning/etching, the Si wafers are rinsed with a bath of deionized water with controlled quantity of dissolved gases such as oxygen ($O_2$), nitrogen ($N_2$) and carbon dioxide ($CO_2$). The purpose of this process is to remove previous chemical solutions from the Si wafers surface before drying them. After passing through some cleaning processes (SPM, SC-1 and SC-2), the Si wafer surface will be hydrophilic and hydrophobic after HF cleaning process. Therefore it's an important step to control the wetting properties of the Si wafer after each process transition even for smooth Si surfaces (some defects can be added during the drying of droplets on hydrophobic surfaces).

## I.C.3. Industrial processes for cleaning

In the semiconductors industry, the wet cleaning processes represent around 40% of the total steps in the silicon wafer production. There are two main processes used in the industry for wafers cleaning, the "batch process" and the "single wafer" process "(Figure I.15). The batch process consists of immersing multiple wafers in a single bath of chemical solution while the single wafer process dispense a liquid jet on a single rotating wafer thus creating a liquid film on the wafer's surface.

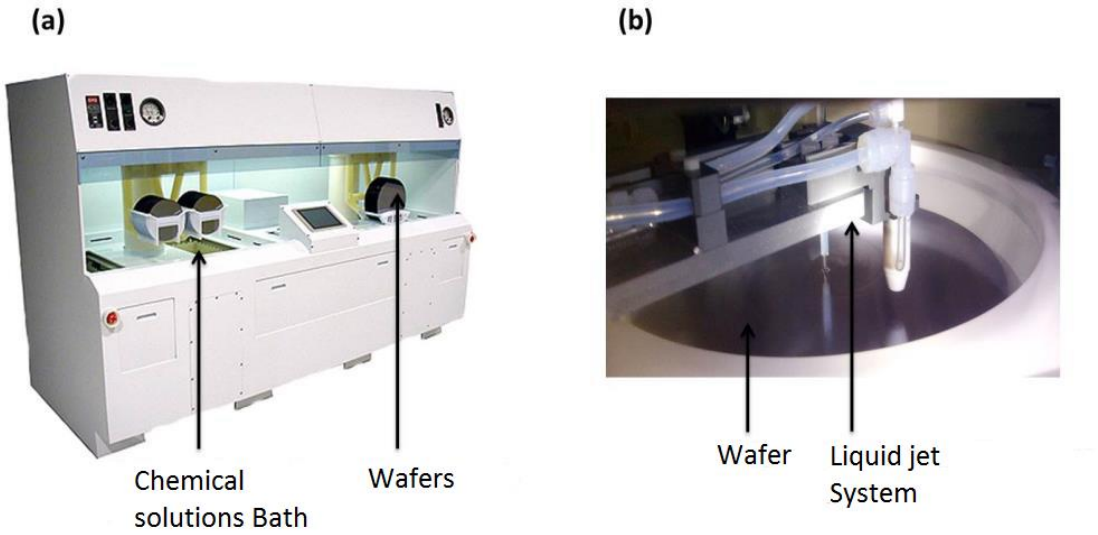


Figure I.15 Cleaning systems used at the microelectronics industry: Batch process (a) and single wafer process (b) [10].

Compared to the batch process, the single wafer process has shorter process time and better performance at room temperature [38]. For that reason, in the production of chips over 300

mm diameter wafer, the microelectronic industry is oriented more and more towards the single wafer process and therefore optimizing various parameters of this process.

The miniaturization of electronics components throughout the years subsequently lead to advanced technologies in the semiconductor industry (sensors, 3D integration, Full Depleted Silicon On Insulator), these technologies make use of high aspect ratio etched silicon structures. These high aspect ratio structures created problems in the cleaning, wet etching and drying processes due to the difficulty of the liquid to penetrate these structures and hence interact with the solid interface to achieve the desired chemical reaction.

Moreover, the wetting state of the silicon surface can be altered depending on the wet process that this surface has been exposed to. For example, the surface becomes hydrophobic (Cassie or composite wetting states) after HF cleaning or dry etching using fluorinated plasma.

As we can see, the state of wetting of silicon wafer surface is an important parameter to know in order to optimize the wet processes. In this thesis we will study the wetting and the drying processes on one type of silicon structures called Deep Trench Isolation (DTI) which is used in the production of sensors. We will study for different etch depth namely 4, 5, 6 and 7µm (aspect ratios of 20, 25, 30 and 35 respectively) of these trenches and conclude about their wetting and drying states.

## I.C.4. Micro/Nanometric Trenches (DTI)

### *I.C.4.a. Wetting*

The use of high aspect ratio trenches in the microelectronics industry is continuing to grow and advance throughout the years. These trenches are used in many technologies including DRAM memories, NAND 3D memories and image sensors. The continuing work on these technologies has led to trenches of width reaching to 18nm with an aspect ratio reaching 100.

In CMOS image sensors, Deep Trench Isolation (DTI) technology (with aspect ratio that could reach 50) is used to isolate pixel and eliminate electrical crosstalk [39], which gives better performing sensors (Figure I.16). Therefore the wet processes related to the DTI fabrication and cleaning are critical in obtaining good performing products.


Figure I.16 Cross-sectional SEM image of DTI (a), white pixels phenomenon appearing on defective sensor (b) [10].

To understand the cleaning of mechanism of "single process wafer" several 2D models have been developed [40], [41], [42] which give the duration of the cleaning of etched trenches. A complete model presented which takes into consideration the absorption, desorption, convection and diffusion of chemical species inside the trenches. It was found that the cleaning time for the trenches is in order of hundredth of seconds and it increases along with the increase aspect ratio of the trenches in consideration (Figure I.17).

The previous models take into account that the trenches are initially completely filled with the fluid. This assumption is valid when the filling time is very small compared to the cleaning time.

We need now to consider two situations. The first having a non-wetting case of the fluid on a homogeneous surface (the local contact angle on the trenches level stays constant), then the penetration of the fluid is impossible without applying external energy to the system as we saw in part I.B.2 of this chapter. The second case where the fluid wet the homogenous surface, then the penetration of the fluid inside the trenches is possible and the filling time can be calculated. For a trench of width $w_t$, the penetration distance of the fluid $z_p$ is related to time $t$ by Washburn law [43]:

$$z_p = \sqrt{\frac{w_t \, \Upsilon \cos\theta}{2\eta} . t} \qquad \text{Eq I-17}$$

where, $\Upsilon$ is the fluid surface tension, θ is the Young's contact angle and $\eta$ is the dynamic viscosity of the fluid.

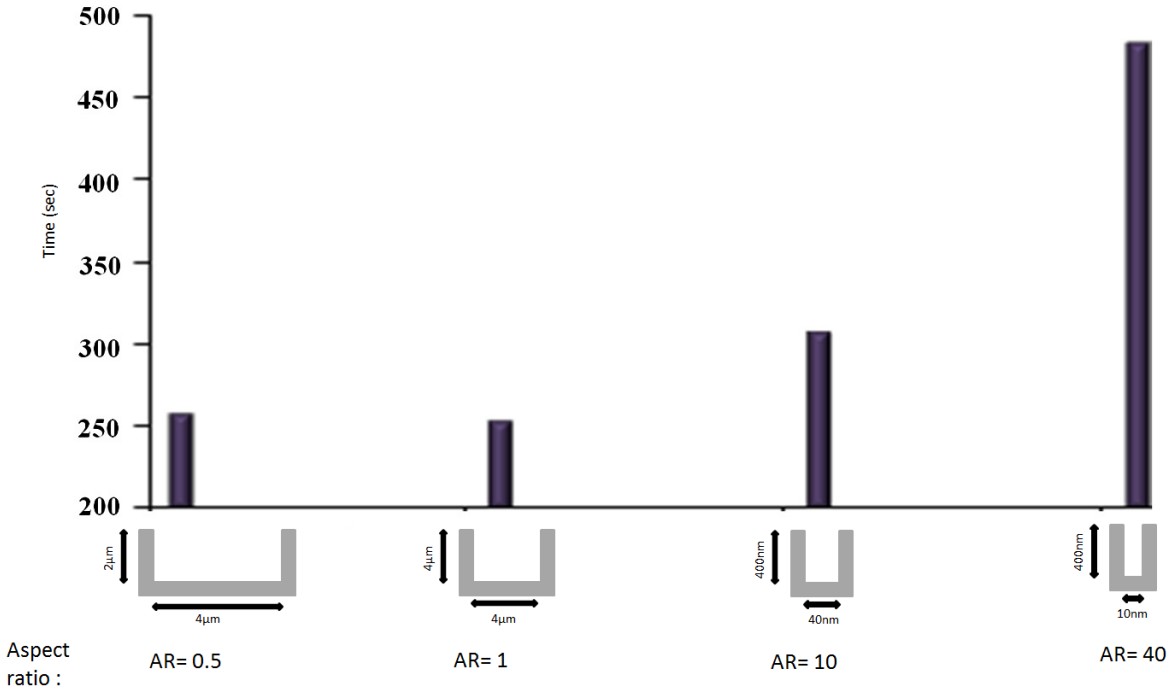


Figure I.17 Cleaning simulation time at 90% efficiency of trenches with different aspect ratio (AR) after being exposed to Hydrofluoric acid (HF) contamination (1:100 HF:$H_2O$). The liquid used for cleaning is water [44]

The filling time for micro/nano-metric DTI with hydrophilic surface has been shown to be in the order of milliseconds. For trenches of width in the order of tens of nanometers, it has been proven that the Washburn law could be modified [45] due to the formation of air nano-bubbles [46] which could increase the filling time.

For cases with a hydrophilic surface, it has been showed that for textured surfaces the total wetting is not always achievable. For example that's the case for nanopillars [47], nanoholes and nanometric porous materials [48]. The reason for having partial wetting associated to these cases being the presence of trapped air inside the textures.

One condition of filling the total surface of the trenches is the dissolution of gas pockets inside the fluid. The escape process of the gas takes place by diffusion through the fluid and as the fluid continues to advance along the length of the trench the volume of the gas is replaced by that of the fluid. The maximum time of the trench filling $\Delta T_{trench}$ could be estimated [49] by:

$$\Delta T_{trench} = \frac{k_H}{D_{gas} RT}\left(1 + \frac{w_t P_h}{2\Upsilon cos(\theta)}\right){h_t}^2 \qquad \text{Eq I-18}$$

with $k_H$ the Henry gas/liquid constant, $D_{gas}$ diffusion coefficient of gas in liquid, $T$ is the temperature, $P_h$ pressure at the bottom of trench filled by the liquid, $h_t$ is the depth of the trench and $R$ is the universal gas constant.

The complete wetting of DTI type trenches with water at 20˚C as the liquid and in presence of air and without applying any hydrostatic pressure lasts between one second ($\theta$ = 30°, $h_t$ =

4µm, $w_t$ = 200nm, AR = 20) and fifteen seconds for higher aspect ratios and contact angles close to 90° ($\theta$ = 85°, $h_t$ = 10µm, $w_t$ = 200nm, AR = 50).

For DTI trenches, the wetting is quasi instantaneous with water when air can escape the trenches. In the case of water droplet covering the whole network of the trenches, air pockets can easily be trapped. Both for the "batch process" and the "single wafer process" cases, it is difficult to predict if air will be trapped or not, because it can directly depend on the geometry of the trenches network. Therefore, experimental characterization of the wetting state at the bottom of the trenches as a function of time is necessary as well as the dynamics of liquid interaction with trapped air pockets.

### *I.C.4.b. Drying*

The drying of DTI is an important subject to consider after the cleaning process is completed. The nanometric trenches of DTI have high aspect ratio which can lead to mechanical deformations on the walls of these trenches [50]. The drying process of the trenches is done by applying a flow of nitrogen on a rotating silicon wafer after the cleaning process with chemical solutions and DI water is completed. During the process, drying is accomplished by the evaporation of the liquid inside the trenches which aren't necessarily all filled to the same level, so the capillary forces between two neighboring trenches don't cancel each other. The result is the bending and collapse "Pattern collapse" of the trenches walls.

There are different forces which act on nanometric structures during drying. These forces include van der Waals forces, hydrogen bonding, solid bridging, electrostatic forces, centrifugal forces and capillary forces. The main forces which act on the structures are the van der Waals, electrostatic and capillary forces and it was found that during the drying process the capillary forces are significantly dominant [51]. The capillary force is defined as the capillary pressure acting over a specific area:

$$F_{capp} = \Delta P_{cap} A \qquad \text{Eq I-19}$$

where, $A$ is the surface area and $\Delta P_{cap}$ is the pressure difference formed across a meniscus (Liquid-air interface). It is given by [51]:

$$\Delta P_{cap} = \frac{2\Upsilon_l \cos\alpha}{d} \qquad \text{Eq I-20}$$

with $\Upsilon_l$ being the liquid surface tension, $\alpha$ is the contact angle and $d$ is the width of the trench.

As shown in Figure I.18, the capillary forces generate from different filling heights and spacing between trenches.

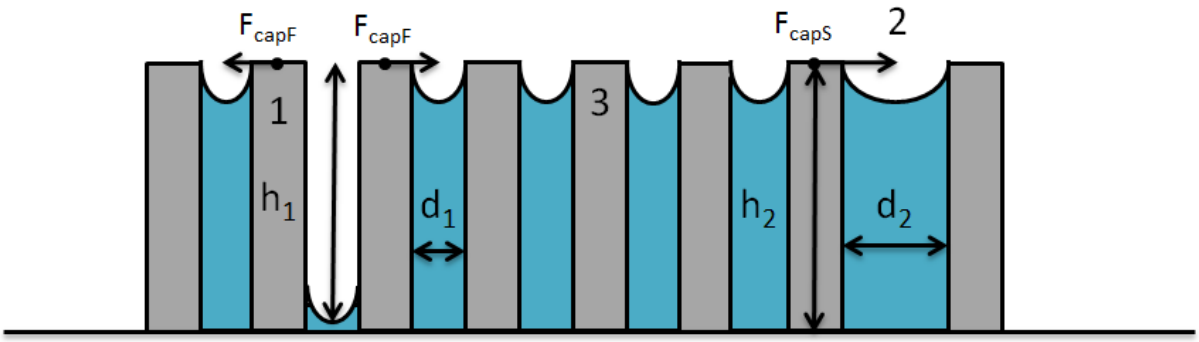


Figure I.18 Schematic of the capillary forces acting upon trenches with different filling height "1", different spacing distance "2" and balanced forces "3"

We will designate $F_{capF}$ as the capillary force generated due to different filling heights and $F_{capS}$ the capillary force generated due different trenches spacing. Both capillary forces are given as [51]:

$$F_{capF} = \frac{2\Upsilon_l \cos\alpha}{d_1} h_1 l \qquad \text{Eq I-21}$$

$$F_{capS} = 2\Upsilon_l \cos\alpha \, h_2 l \left(\frac{1}{d_1} - \frac{1}{d_2}\right) \qquad \text{Eq I-22}$$

where, $l$ is the length of the trench. All other parameters are listed in Figure I.18.

For our DTI structures, we have trenches of 200nm width, therefore the case of different spacing doesn't exist and $F_{capF}$ is the capillary force acting upon the trenches.

Additional horizontal force generated from the surface tension could be added to the capillary forces as shown in Figure I.19:

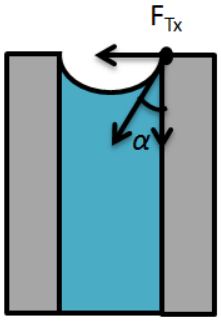


Figure I.19 Horizontal component of the surface tension

The horizontal component of the surface tension is given as:

$$F_{Tx} = \Upsilon_l l \sin\alpha \,. \qquad \text{Eq I-23}$$

If we consider the ratio between $F_{capF\ and}\ F_{Tx}$ :

$$\frac{F_{capF}}{F_{Tx}} = \frac{2h_1 \cos\alpha}{d_1 \sin\alpha}.$$ Eq I-24

In our case study, the lowest aspect ratio $h_1/d_1$ is 20 and if we consider low contact angles, we can see that the capillary force exceeds by at least an order of magnitude the surface tension force. Therefore, the surface tension force can be neglected.

After the drying process is completed it was found that capillary forces don't dominate anymore. The hydrophobic silicon structures are bonded by the action of van der Waals forces and for hydrophilic silicon structures the bonding hydrogen forces dominate [52].

The problems related to drying and "Pattern collapse" can be limited by several methods which reduce the value of capillary forces. Reducing the surface tension of the liquids used before drying is one solution, by addition of surfactants to rinsing water [53], or after the rinsing is done, the water is replaced by isopropyl alcohol (IPA) or fluorinated liquids [54]. Increasing the local contact angle on the walls of the structures without surpassing 90° to assure that wetting is favorable inside the structures is one solution to reduce the capillary forces. This is done by using mixtures of IPA and hexamethyldisilazane (HMDS) [55]. There exist other methods to reduce the collapse of the structures and allow the cleaning and drying in one single process. The HF vapor treatment at high temperature and reduced pressure is a good alternative used during the etching/cleaning of silicon wafers [56]. It has been shown also that the HF vapor could repair in some cases the collapse of the structures and allow the straightening of nanopillars elastic deformations [57].

To conclude, in the microelectronic industry we can see that the wetting and drying defaults can present a real challenge and affect the overall quality of the manufactured products. The more we go down in sizes, the more the impact of the phenomena (wetting, drying and pattern collapse). Therefore, the use of experimental techniques is necessary to observe the different phenomenon present.

## I.D. Wetting Characterization Methods

### I.D.1. Macroscopic Methods

#### *I.D.1.a. Contact angle measurements*

This method commonly called sessile drop goniometry consists of depositing a droplet of liquid on a solid surface (Figure I.20) and then recording a video of the droplet in order to determine visually the contact angle using the different set of taken images. The idea behind this method assumes that the droplet is in a global energy minimum thus, in a stable state which enables us to obtain a contact angle similar to the one given by the Young's equation. However, the droplet is in a metastable state and can have any local energy minimum. Thus, depending on each measurement and deposition of the droplet, the contact angle can take any value within the hysteresis range[58].

One technique using vibrations to enable the droplet to reach its most stable state can be found in literature [59]. However, this technique is still not available for commercial goniometers.

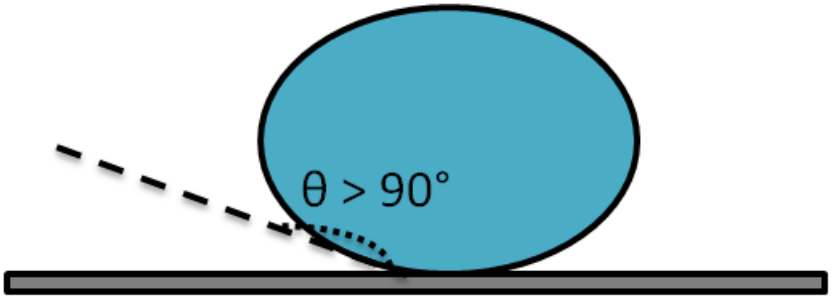


Figure I.20 Schematic of contact angle measurement on a hydrophobic surface

Therefore, in order to obtain information about the contact angle it is necessary to measure the hysteresis of the apparent contact angle to characterize the deformation of the triple line of the drop at the surface textures.

### *I.D.1.b. Contact angle hysteresis measurement*

As discussed before, when a liquid droplet is deposited on a solid surface, the contact angle varies within a hysteresis range. This range is given a minimum and maximum called receding and advancing contact angles respectively. Two main techniques are used to measure the advancing and receding contact angles.
The tilting plate technique consists of depositing a liquid droplet on solid surface while gradually increasing the tilt angle of the surface until the liquid droplet starts sliding. After that, the angles on the upper and lower sides of the droplet (receding and advancing angles respectively) are recorded.
The other technique often called needle method consists inflating / deflating the deposited liquid droplet in order to measure the contact angle changes. As the liquid droplet is deposited, a volume of liquid is gradually added with a needle (inflation), when the contact line start to move, advancing contact angle is recorded. Conversely, liquid volume is absorbed (deflation) from the droplet and the receding angle is recorded just before the movement of the contact line.

Some problem associated with the tilting technique is that the sliding angle is highly dependent on the droplet size while as we know, contact angle hysteresis is a surface property and is independent of the droplet size [60], [61]. As for the needle method, the use of the needle during the measurement may distort the shape of the droplet thus, creating error in contact angle observation, the other major issue is the difficulty in observing optically where the droplet ends and the surface begins as the contact angle approaches $0^{O}$ or $180^{O}$.

### *I.D.1.c. Wihelmy method:*

This method is a form of tensiometry that uses force balance to calculate the contact angles (advancing and receding) of liquids with known surface tension. The method consists of using a plate with specific dimensions, a container full of liquid and a force meter (Figure I.21). As the plate in submerged in the bulk of the liquid, the advanced contact angle can be calculated and when the plate emerges from the liquid, the receding angle is calculated. The contact angle measurements are averaged over the whole area immersed in the liquid thus, this method is suitable for thin objects [62].

To calculate the contact angle, one must balance the different forces acting on the plate. During the immersion, the force exerted on the plate is $\overrightarrow{F_w}$. Three different forces are exerted on the plate: capillary forces, the buoyant force and shear force. The shear force resulting from the viscosity is negligible for low immersion speeds $V_{im}$ around 0.05 mm/s to 5 mm/s.

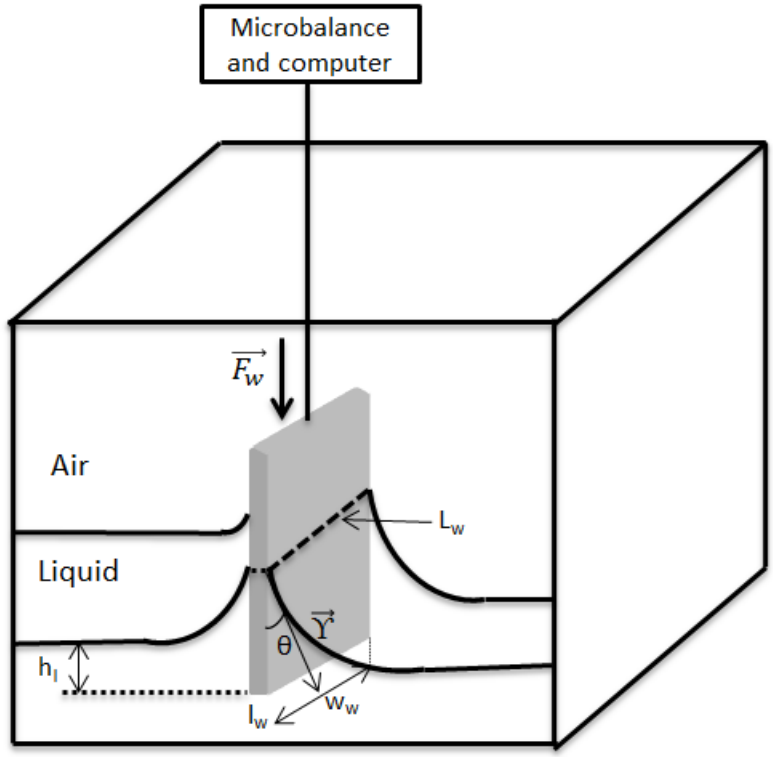


Figure I.21 Schematic of Wihelmy's setup for determination of the contact angle

The buoyant force has the following expression, $F_b = \Delta\rho V_w g$, with $\Delta\rho$ being the density difference between the liquid and air, $g$ is the gravitational acceleration and $V_w = h_l l_w w_w$ is the volume of the displaced liquid (Figure I.21). The capillary forces which act on the plate have the following formula, $F_c = \gamma L_w \cos(\theta)$ (when θ > 90° they act upwards on the plate and if θ < 90° they act downwards), with $L_w = 2l_w + 2w_w$ being the total perimeter of the plate on the level of the triple line. The total force measured on the microbalance $F_w$ is equal to $F_c - F_b$. We can then obtain the following relation for the contact angle:

$$\cos(\theta) = \frac{F_w + \Delta\rho V_w g}{\gamma L_w}. \qquad \text{Eq I-25}$$

The Wilhelmy method provides an indirect way of measuring the contact angle by a direct measurement of the force acting on the plate. However, the Wilhelmy method requires some restrictions on the dimension of the immersed sample. In general, the sample must be flat homogenous and of uniform cross section so that the wetted length $L_w$ is constant during the wetting process [63].

### I.D.2. Micro/Nanoscopic methods

In the previous part we saw how to characterize the wetting behavior based on finding the macroscopic contact angle using three different techniques which utilize optical imagery. As we know when a liquid droplet is placed on a micro / nanometric textured surface, it undergoes local deformation at the level of the contact line between the liquid and the surface feature thus, leading to a local contact angle. Therefore, it is interesting to look at the wetting behavior at a local scale to obtain useful information that helps us understand the wetting phenomenon. In this part we will present the microscopic characterization techniques which include optical and electronic microscopy, electrochemical techniques and infrared (IR) and acoustic reflection characterization methods, all used to characterize the wetting state.

#### *I.D.2.a. Static wetting visualization methods*

The utilization of X-ray scanning for the wetting visualization of a liquid drop can provide high spatial resolution images and details about the wetting behavior. Also, it's an alternative to optical microscopy which can be complicated to use because of the diffraction and reflection phenomena of the light passing through the liquid drop.

Santini *et al*. [64] implemented the X-ray micro-computed tomography (microCT) to visualize the multiphase (solid, liquid and gas) interface using 3D scan of the droplet. The 3D colored images of sessile water drop on gas diffusion layer (GDL) surface which is carbon fiber cloth with a hydrophobic agent to investigate the liquid-solid interaction are reconstructed (Figure I.22). Also, using microCT measurements of the drop volume could be obtained.

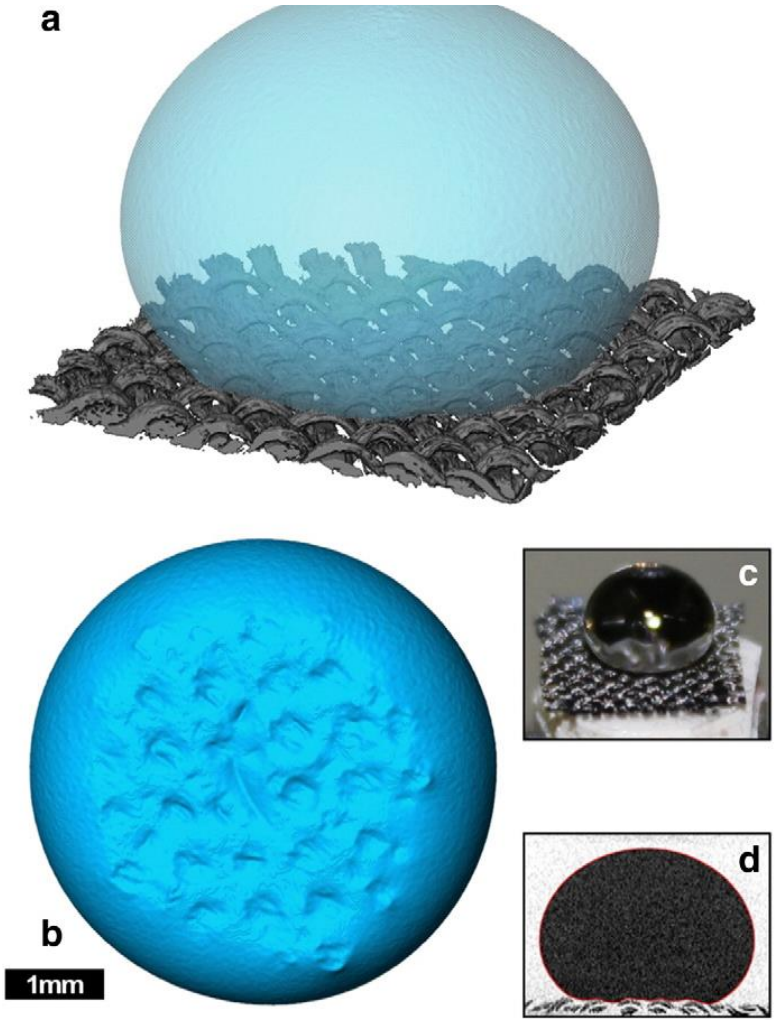


Figure I.22 X-ray microCT of GDL substrate and a sessile water drop. Segmented and rendered (with colors and transparencies) volume (a) the drop volume from the bottom (b) evidencing the topology of the real interface imprinted by the GDL in normal conditions (c); a slice extracted from the reconstructed volume, with the contour evidenced in red, to show how the drop is in a Cassie-Baxter wetting state (d) [64]

The X-ray microCT has a resolution suitable for the observation at the micrometric scale, but this method does not give us detailed information about the liquid impalement inside the structures thus, differentiation between the Wenzel and the composite states is difficult.

Another approach is to use scanning electron microscopy (SEM) to increase the resolution to better understand the state of wetting state in the structures network. For micrometric structures, the visualization of the high wettability (contact angle approaching zero) of molten liquid caesium iodine (CsI) through the pores network of solid uranium oxide is shown through SEM cross-sectional images [65] (Figure I.23).

The penetration of molten liquid CsI was found to penetrate up to several tens of micrometers below the surface of solid uranium dioxide ($UO_2$) through network of pores. Also, it was found that with low contact angle between CsI and $UO_2$ along with high fraction of pores (above a critical value), the infiltration depth increased in parabolic way with time.

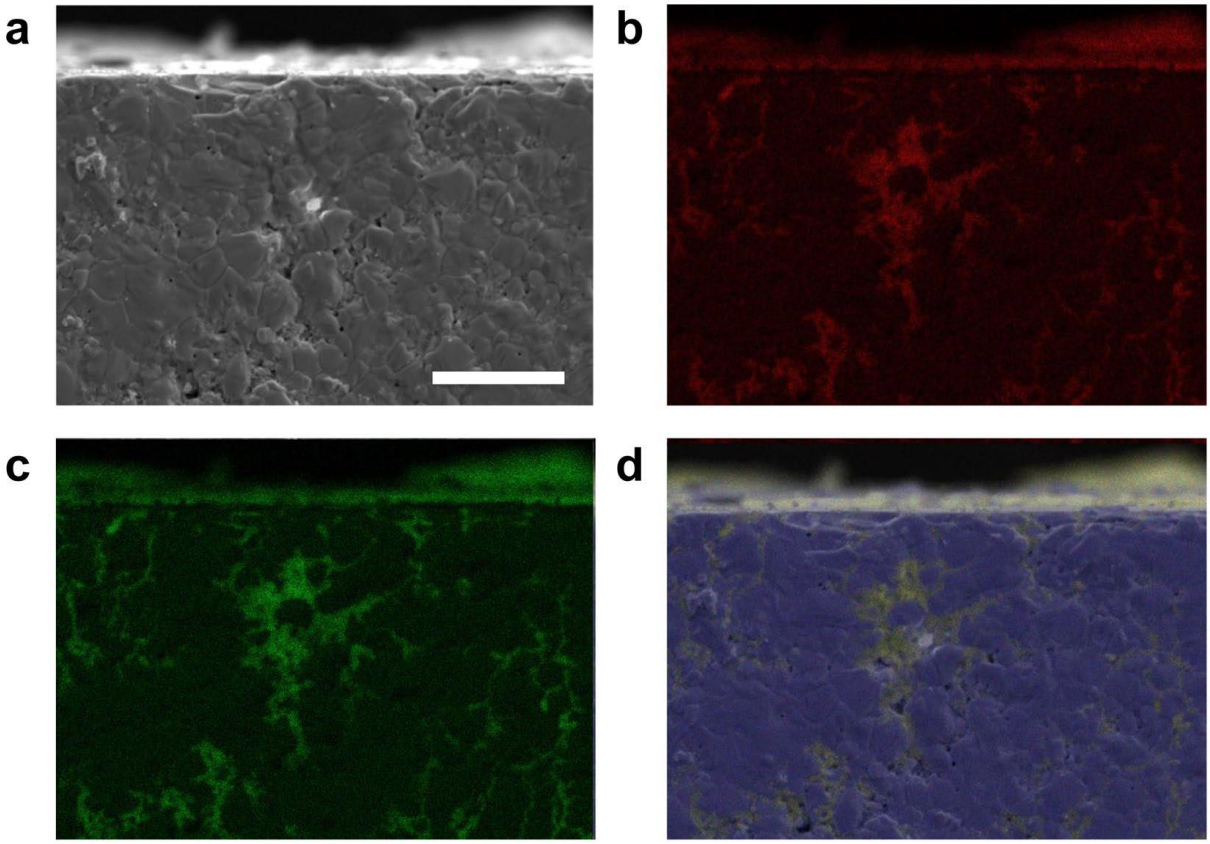


Figure I.23 Cross-sectional observation results following sessile drop method testing between solid uranium dioxide (UO2) and liquid caesium iodine (CsI). The sample was at the maximum temperature (T = 973 K) with liquid CsI for 1 minute in maximum. (a) SEM image and EDX mapping images of (b) I, (c) Cs and (d) U. Observations noted deep infiltration of liquid CsI into the solid $UO_2$ on a macroscopic scale through the pores network present in the polycrystalline structure. [65]

For nanometric structures, Park *et al*. used a method named cryogenic FIB "Focused Ion Beam" scanning electron microscopy to characterize the size-dependent wettability of sessile water droplets [66] (cryo-FIB / SEM). This method is generally used for the characterization of emulsions or biological cells. Here, the liquid condensed at room temperature on a patterned copper substrate, and then the droplets are frozen by submerging the substrate in liquid nitrogen for 1 sec. The different steps of the process are shown in Figure I.24.

This method allows us to obtain high resolution imagery of both the wetting state and the contact line (Figure I.24.b). Another advantage is decreasing the evaporation rate of the observed liquid droplet through the use of rapid freezing rate ($20000^{O}C/s$) [67], which will enable the observation of the droplet without any volumetric changes.

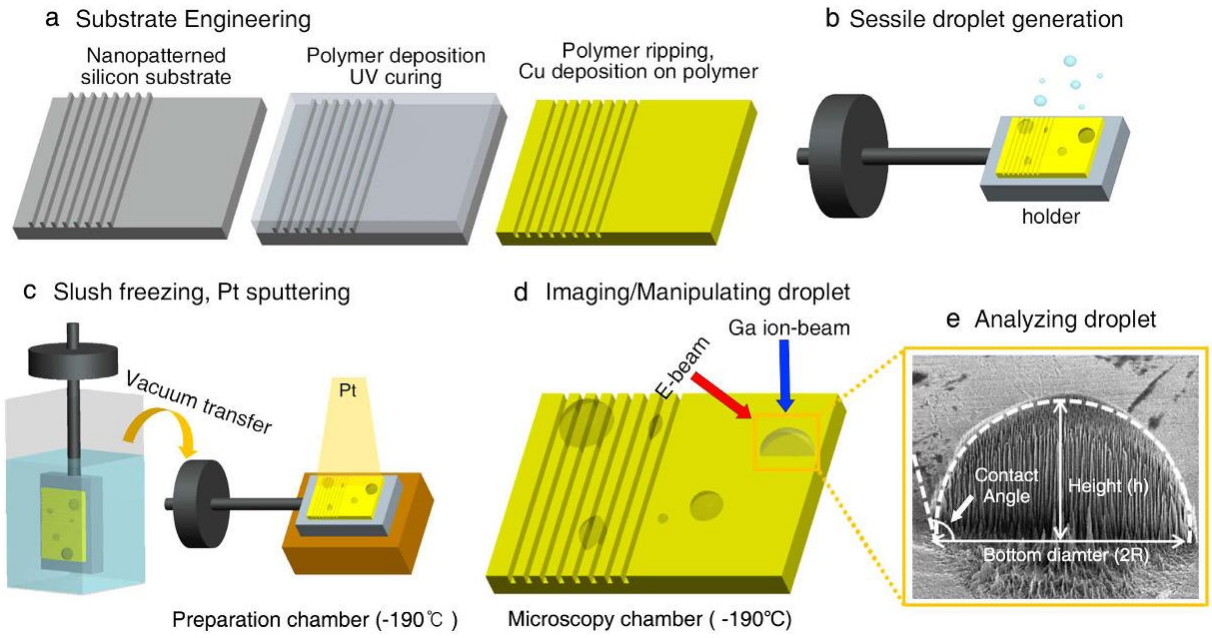


Figure I.24 Schematic of the droplet analysis using the cryo-FIB/SEM system. (a) Substrate made by Cu deposition on the patterned/non-patterned polymer substrate. (b) Sessile droplet generation on the engineered Cu substrate. (c) Rapid freezing of the droplet and c onsequent Pt sputtering (conductive layer) under a cryogenic temperature. (d) Electron and gallium ion beam integrated milling and imaging of the droplet under a cryogenic temperature. (e) Wettability analysis of the FIB-milled droplets [66]

The scanning electron microscopy methods can provide very good images of the wetting state. However, one drawback of this method is the evaporation of the liquid droplet under vacuum, making it impossible to observe the wetting changes of the droplet including contact angle hysteresis. Although some techniques are used to overcome this problem including increasing the pressure [68], other techniques are needed to observe wet specimens.

***I.D.2.b. Dynamic wetting visualization methods:***

The environmental scanning electron microscopy (ESEM) is a useful tool in visualizing contact angle hysteresis. It allows high magnification imaging without affecting the material. The use of this tool involves introducing liquids to a measuring chamber under vacuum (typical pressure hundreds of Pascals). The changes to liquid wetting state can therefore be observed, but the images resolution will be less than those obtained by a SEM.

The water droplet condensation on a hydrophobic surface made of nano-grains ranged from 22 to 49 nm was observed at different instants using ESEM [69] (Figure I.25). The liquid droplet initiated from inside the hydrophobic surface grew as the process of condensation advanced with time and it preserved its spherical shape as it didn’t penetrate into other hydrophobic cavities. Also we can see the coalescence of multiple small droplets in the Cassie-Baxter state, a transition to the Wenzel state is observed on the larger formed droplet (Figure I.26.b)

The ESEM could be less efficient for smaller structures at nanometric scales. One downward side of the ESEM is that the changes to the advancing and receding contact angle happen at a

faster rate than capturing images for measurement. Although, small incremental changes to pressure to grow and reduce the liquid drop size to measure the contact angle changes can be made, nevertheless, it is time consuming and is affected by beam heating, especially at higher magnifications.

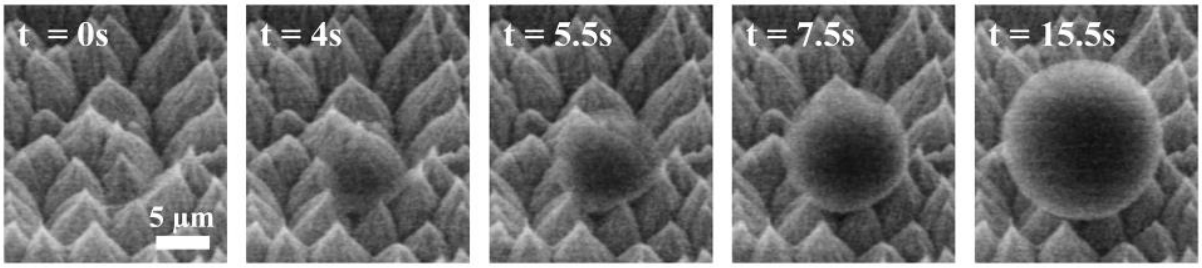


Figure I.25 Time-lapse ESEM images of single water droplet nucleation at different instants of time [69]

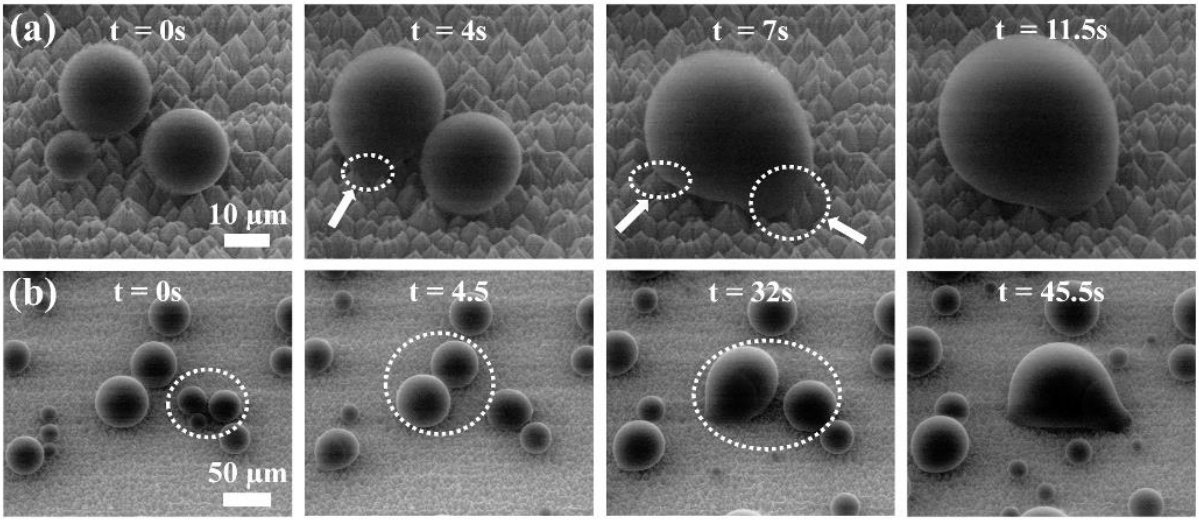


Figure I.26 (a) Time-lapse ESEM images of water droplet coalescence with a $40^{O}$ tilt angle. The arrows and dashed lines indicate droplet deformation. (b) By the process of coalescence of many droplets, A transition from Cassie-Baxter (with a small wetted region under the droplet) to a Wenzel state (with a large wetted region under the droplet) is observed. The dashed lines indicate the droplets before coalescence. [69]

Confocal microscopy makes it possible to obtain 3D images of the liquid droplet through the use of 3D scan at different axes [70]. Thus, it is possible to follow the wetting state over time. This method makes use of fluorescence optics to create sharp images on the plane of liquid drop and the surface features.

In Figure I.27, we can observe the transition from Cassie state to Wenzel state of a cylindrical micropores structured superhydrophobic surface (pores radius 25 µm and height $H$ = 40 µm) submerged in a water [71]. The transition was made by applying pressure on the water through the use of air pressure supply (up to 50 kPa). The liquid penetration profile allows detection of different composite wetting states until complete collapse of the liquid during the transition from Cassie state to Wenzel state (Figure I.27.g). The resolution of the images obtained is of the order of microns, also allowing measurements of contact angles at the level of the cylindrical pores by observation of the local triple line. In addition, the method also makes it possible to measure apparent contact angles.

The confocal microscopy technique is powerful in a sense that it provides 3D spatial resolution down to the sub-micron scale. However, it requires the use of transparent surfaces as well as the staining of the liquid and the micro-structures with fluorescent molecules [35].

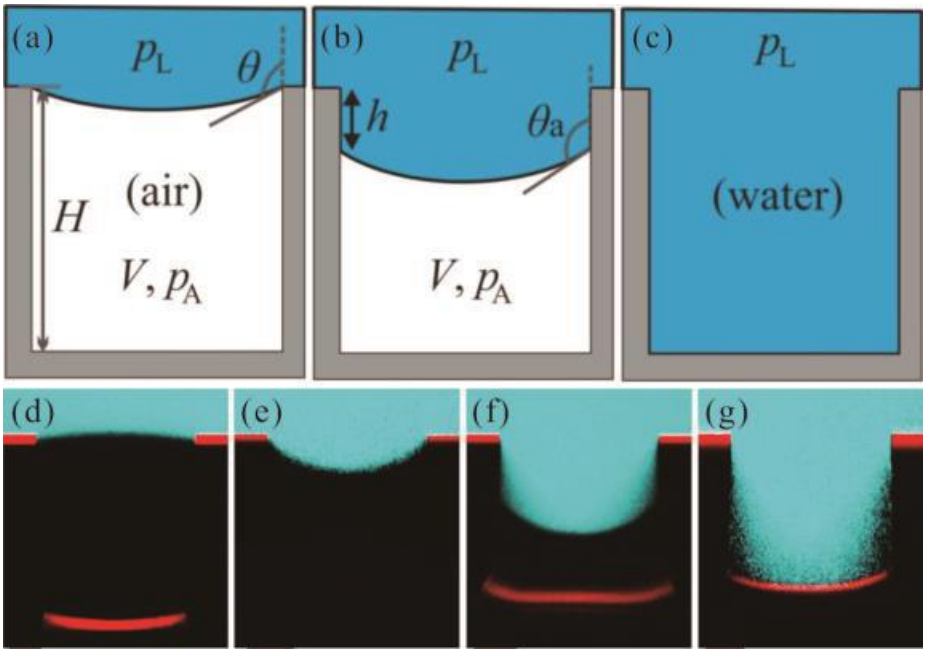


Figure I.27 Schematics of different wetting states (a-c) and confocal microscopy images of different wetting states (d-g). (a) Cassie state, (b) metastable state, (c) Wenzel state, (d) Cassie state, (e) critical pinning state, (f) metastable state, (g) Wenzel state. [71]

An alternative method to confocal microscopy is reflection interference contrast microscopy [34]. It can provide high lateral and out-of-plane resolutions which enable the investigation of the contact line zone on transparent solids also, this method is suitable for dynamic measurements [72].

In Figure I.28, a water droplet is deposited on a microstructured surface made up of hydrophobic PDMS (PolyDiMethylSiloxane) pillars and it is left to evaporate at ambient temperature. Since the PDMS surface is transparent, light will be reflected when it comes to contact with the bottom surface of the pillars and the liquid meniscus (Figure I.28.a) enabling the images construction of the liquid interface as the droplet impale into the pillars. During the liquid evaporation, the droplet volume decrease triggering a change in the droplet radius. This process continues while the penetration of the liquid into the pillars increases with time. When the penetration depth of the liquid is equal to the height of the pillars, the transition from Cassie-Baxter to Wenzel state is completed (Figure I.28.b).

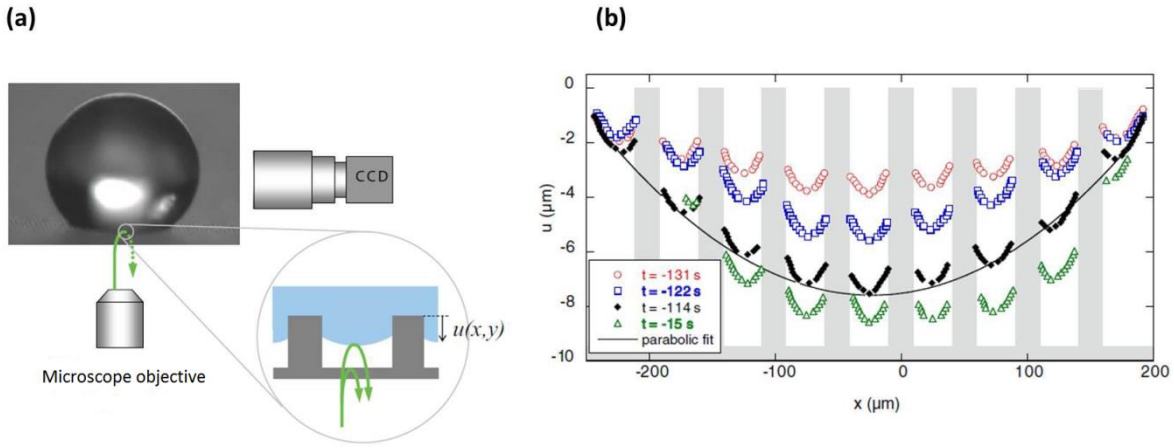


Figure I.28 Method of characterization of wetting by interference microscopy: Schematic of the principle of method (a) and evolution of the penetration profile of the liquid (water) in the network at different times (time t = 0 s corresponds to the Wenzel state) for PDMS micro-pillars 10 µm in diameter, 10 µm height and 50 µm spaced (b) [34]

### *I.D.2.c. Non-optical methods of following dynamic wetting*

Atomic force microscopy (AFM) is another tool used to visualize the dynamic wetting with high resolution in the atomic scale limit. The principle of AFM is the use of an extremely sharp tip connected to a cantilever which forms a spring, as the tip performs raster scan a textured surface, the cantilever bends and this bending is detected using a laser and a photodiode (Figure I.29). This bending is used as an indicative of the tip-surface interaction force. The AFM can be used to study the liquid penetration in the surface textures and also to create 3D images of the studied surface. AFM has been used as a real-time visualization tool to study the Cassie-Baxter wetting states on silicon nanopillars (~220 nm height and ~90 nm spacing) and superhydrophobic cicada wing (~200 nm height and ~170 nm spacing) with an accuracy in the nanometer range [73] .

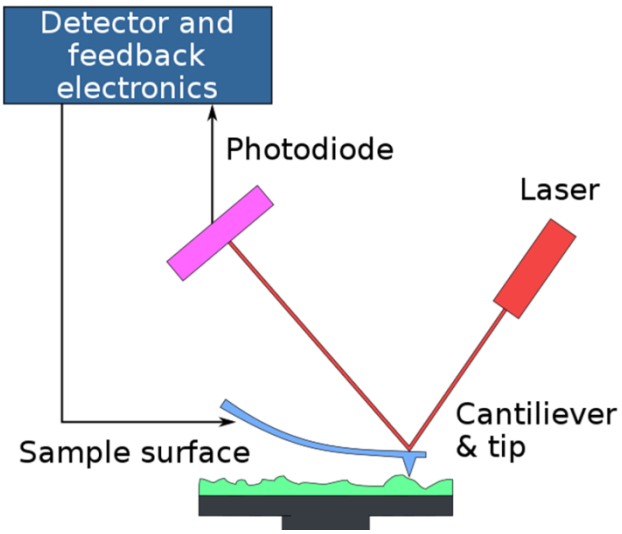


Figure I.29 Principle of AFM scanning

Electrochemical Impedance Spectroscopy (EIS) is a method that uses measurements of impedance of the system composed of the metallic structured surface, the air in the structures and the liquid deposited on the sample over a range of frequencies ($10^{-4}$ to $10^{6}$ Hz) [74] to give a real-time monitoring of the wetting phenomenon of a material. The wetting behavior of textured and porous surfaces could be studied as shown in Figure I.30. When the electrolyte solution penetrates into the surface textures, the air gap along with the liquid-solid separation distance decreases, as a result the impedance of the system decreases due to the replacement of the air volume inside surface structures by the liquid volume. The ability of EIS in monitoring wetting have been demonstrated by following the liquid penetration depth on superhydrophobic polymethylene surfaces [75], [76]. However, the EIS have several disadvantages such as being sensitive to surrounding environment and requiring bulky experimental setups [77].

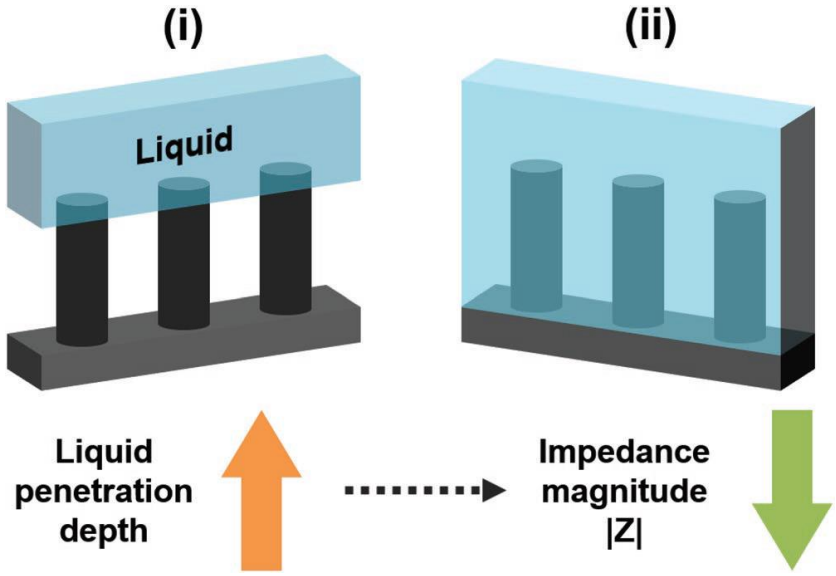


Figure I.30 Schematic of the electrochemical impedance spectroscopy (EIS) technique to monitor surface wetting and liquid penetration distance through variations in the impedance magnitude [19]

Another method has been developed for the kinetic monitoring of the liquid penetration inside nanostructures called ATR-FTIR (Attenuated Total Reflectance-FTIR) [78]. The principle of the method is demonstrated in Figure I.31. An infrared beam is sent through the sample (ATR crystal) and it is totally reflected on the sample inner surface, this lead to an evanescent wave being generated which penetrates the structured sample. The analysis of the output reflected signal makes it possible to conclude on the wetting state and the penetration length of the evanescent wave in the network (around one hundred nanometers) determines the height over which the information concerning the state wetting will be obtained.

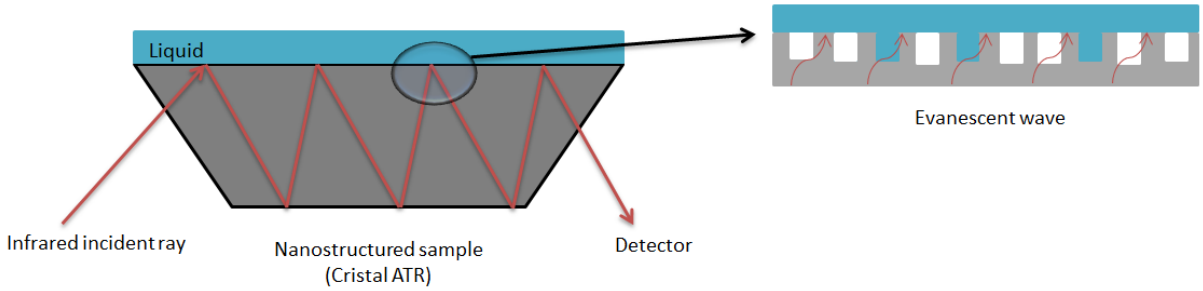


Figure I.31 Schematic of the ATR-FTIR method for wetting characterization

The ATR-FTIR can be used for real time monitoring of the wetting states and transitions on nanostructured surfaces. It is thus possible to detect over time the composite wetting states and the percentage of liquid penetration in the surface textures. Careful analysis of the wetting transition criterion is essential to avoid errors of wetting dynamics.
Another advantage of the ATIR-FTIR is the ability to use on opaque surfaces as it allows the passage of the infrared light.

Many acoustic methods have also been developed for the characterization of the wetting of microstructured surfaces and non-transparent surfaces. The Quartz Crystal Microbalance (QCM) utilizes the piezoelectric effect for generating acoustic shear waves [79]. Since shear waves tend to decay in liquids (depending on the liquid density and viscosity), as the liquid is deposited on the QCM electrode, the resonant frequency shifts and real-time information about the wetting state can be obtained [80]. While the QCM provides information about the wetting state on the whole dimension of the microbalance, it is impossible to conclude on the local wetting state.

An acoustic method based on using ultra-high acoustic reflectance is developed by Virgilio *et al*. [81] for the local characterization of the wetting states and the wetting transitions. The first works concerning the wetting of micro-pillars were carried out within the framework of the thesis of N. Saad in 2012 [82] at IEMN laboratory.

The ultra-high acoustic reflectance method consists of using piezoelectric transducers which generate high frequency acoustic waves (in order of some GHz's). The high frequency is necessary in order to separate the reflected echoes off micro / nanometric surface textures. These waves can travel through the volume of the textured surface reflecting of the bottom and top surfaces of the textures. In case of liquid presence inside the textures, the acoustic energy is absorbed by the liquid which in turn induces a decrease in the amplitude of the reflected echo and changing the value of the reflection coefficient. This indicates the presence of the liquid inside the textures. In order to characterize the wetting over large areas of the surface, multiple transducer arrays can be used enabling the characterization of the wetting at micro and nanometric scales.

In Figure I.32, the wetting state transition is demonstrated for hydrophobic treated silicon DTI trenches (4 µm in height) as function of the changing the liquid surface tension (% ethanol).

One can also see based on the acoustic reflection coefficient value for both the experimental and simulated values, if a state of total wetting is achieved or not.

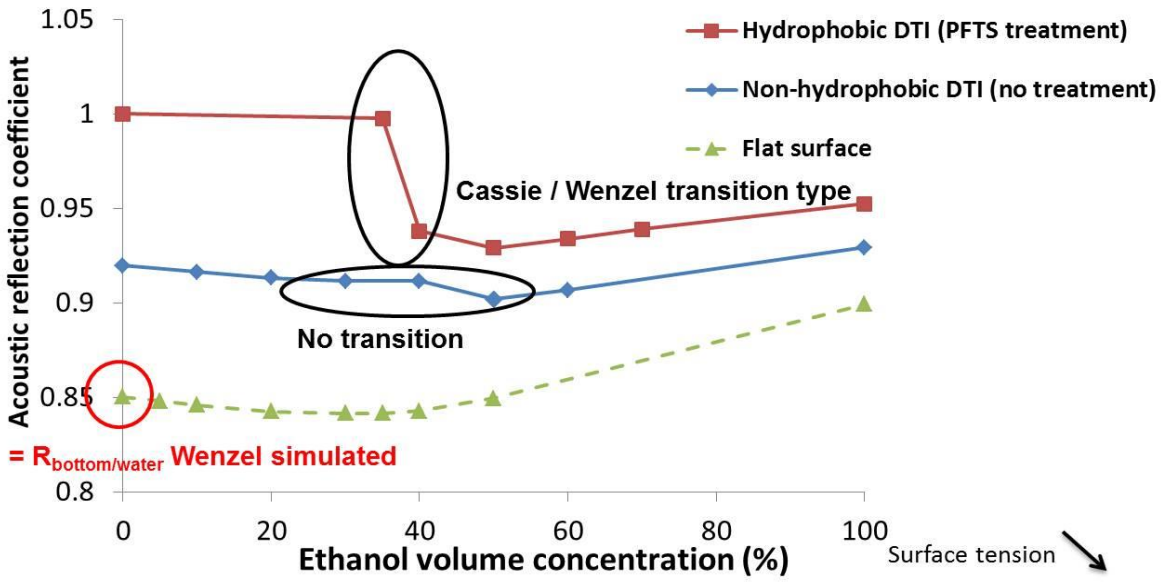


Figure I.32 Acoustic reflection coefficient measurement showing wetting transition for silicon DTI trenches (4 µm in height) in function of ethanol concentration [83]

This method was already used successfully to characterize the liquid droplet wetting on STMicroelectronics structured surfaces. We will explore this method in detail throughout the rest of this thesis and see how it could be adapted to the study of the wetting of DTI structures of different micrometric height as well as to the detection of wetting kinetics in a sense of a transition from droplet measurement to liquid flow (within a micro-channel) measurement. This transition will enable us to approach the industrial cleaning process used at STMicroelectronics. The following part is then dedicated to the flow of liquid in micro-channels.

## I.E. Wetting in micro-channels

### I.E.1. No-slip boundary condition

Let's consider a fluid moving inside an open channel and bounded by a wall (Figure I.33).

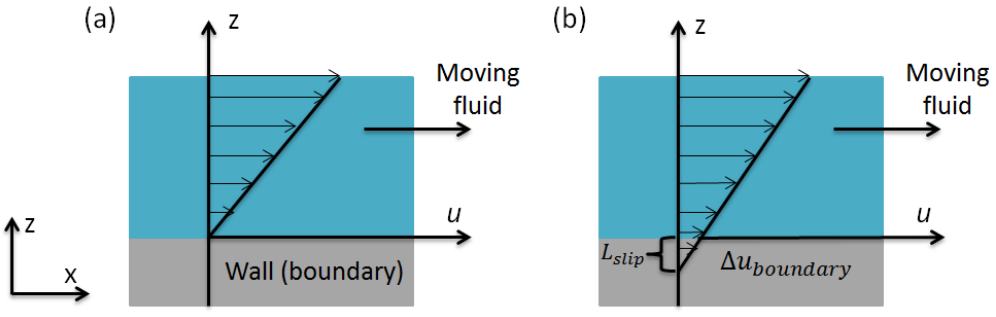


Figure I.33 Schematic of no-slip (a) and slip (b) boundary conditions

The no-slip boundary condition assumes that the velocity of the fluid layer at the boundary is zero. That is to say there is no relative movement between the fluid layer and the boundary. The slip boundary (for example in the cases of surface grooves presence) condition on the other hand assumes that the relative movement between the fluid layer and the boundary causes the fluid to have certain velocity up to a distance called slip length "$L_{slip}$" inside the boundary wall (Figure I.33.b). The difference between the velocity of the last layer of the fluid field and the boundary velocity can be given as:

$$\Delta u_{boundary} = \frac{\partial u_x}{\partial z}\Big|_{boundary} L_{slip} .$$

The slip length is dependent on the fluid solid interaction and can be determined experimentally.

### I.E.2. Flow bounded by superhydrophobic surface

The hydrodynamic flow inside a micro-channel bounded by superhydrophobic surface has been extensively discussed in literature for various applications including fluid manipulation, cells and proteins in lab-on-chip also for the fabrication of hydrophobic surfaces. Many studies of liquid flow in micro-channels over structured surfaces exist in literature, mostly concerning drag reduction.

Chen *et al*. modeled the effect of micro grooves on reducing the flow friction inside a micro-channel and it was found that micro-channel bounded with eccentric micro grooves (Figure I.34) induced less friction than aligning micro grooves, meaning the flow inside micro-channel with eccentric grooves requires less pump power [84]. A similar study on the effect of air filled trenches on reducing friction inside micro-channel was also done [85]. Also, another modeling was done to see the effect of transversely aligned grooves on changing the velocity profile, centerline profile and hydrodynamic length inside the plane channel [86] and it was found that the fully developed flow region (flow region where we have the maximum velocity reached) can be delayed due to the addition of the grooves as well as the velocity profile near the channel walls can change drastically (Figure I.35). As we can observe in Figure I.35, compared to smooth surface, the addition of transverse grooves delay the fully developed region until $x$ = 0.002 m and the more spaced the grooves are $L$ = 0.25 $\left(L = \frac{\Delta}{2H}\right)$ in Figure I.34), the higher the slip velocity.

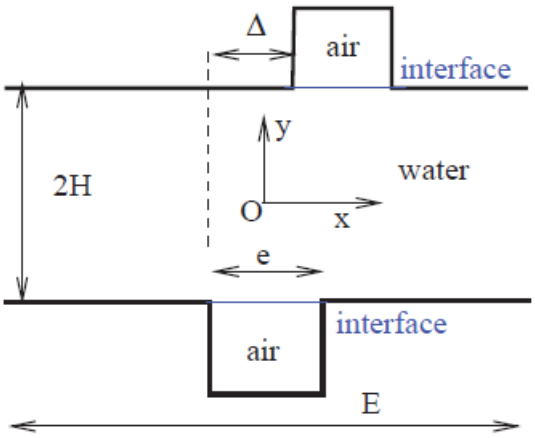


Figure I.34 Schematic cross-section of flow in micro-channel bounded by eccentric micro grooves [84]

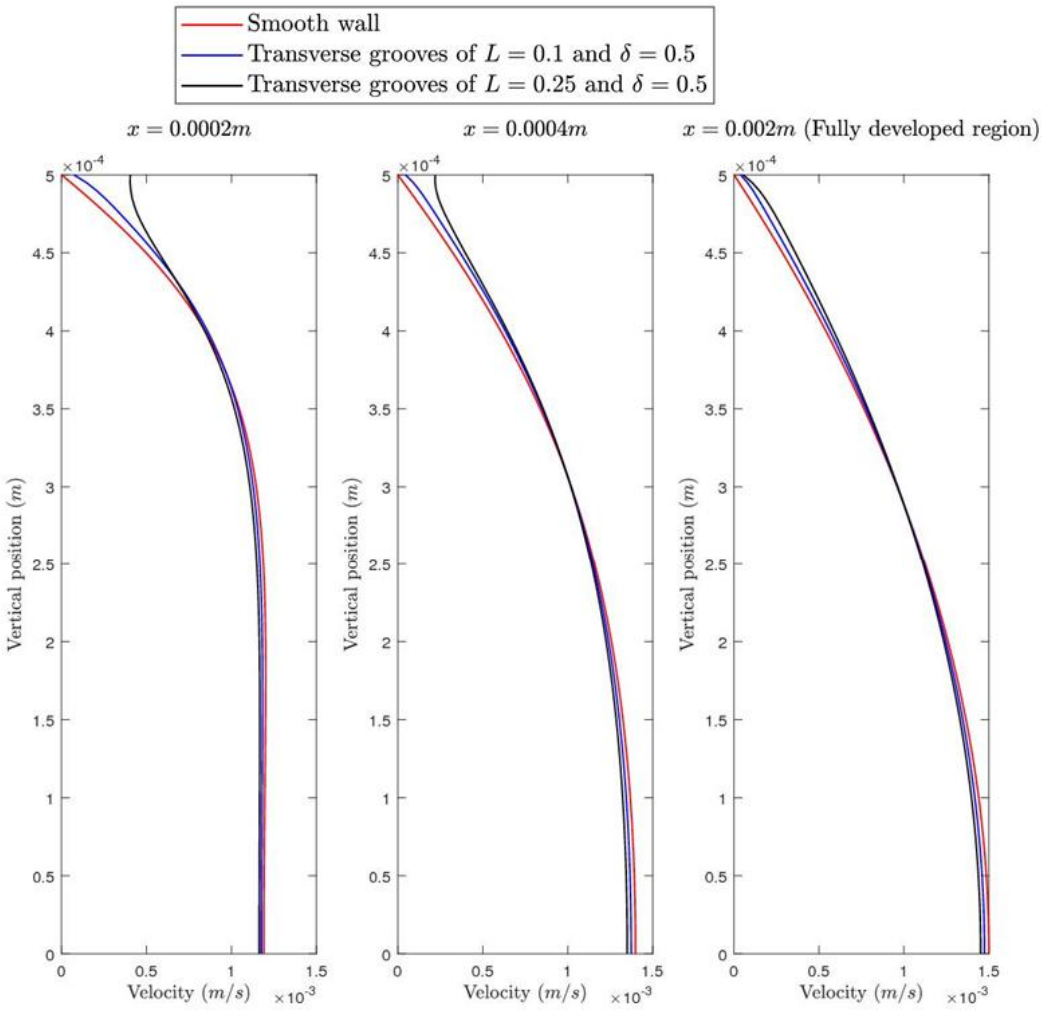


Figure I.35 Velocity profile at various axial locations for flow scenarios having smooth wall and superhydrophobic transverse grooves with different periodic spacing ($L$ = 0.1 and $L$ = 0.25) [86]

Another study done by Lee *et al.* [87] discusses the effect of slip length of micro / nanostructured submerged superhydrophobic (SHPo) surfaces in creating drag reduction for

flow systems. The drag reduction is achieved due the slippage created when a plastron (gas layer) is present between the surface features (Figure I.36). The study was restricted to laminar flows and it was found that plastron can be lost from the surface by various mechanisms including gas dissolution and meniscus deformation of the liquid interface. The loss of plastron means that the surface lost its drag slip length thus, its drag reduction characteristic. It was found that surfaces with larger slip length (large air fraction or large pitch) are more susceptible to lose their plastron through wetting transition leading to the replacement of the gas by liquid.

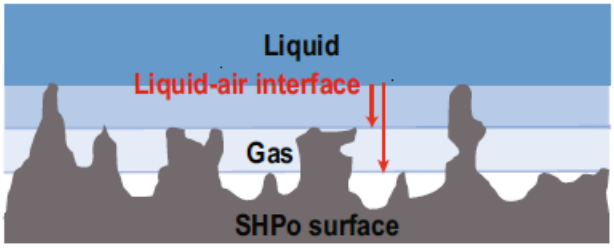


Figure I.36 Schematic of the plastron (gas layer) present between the surface features on submerged superhydrophobic (SHPo) surface [87]

While the above studies has an objective of preventing the wetting transition and conserving the plastron layer for drag reduction, in our study, the objective is to investigate if STMicroelectronics micro / nanostructures can be completely wetted (to be cleaned), hence, the liquid penetration into surface features and the replacement of the trapped gas pockets by the liquid.

### I.E.3. Wetting characterization: Transition from droplet to liquid flow

To this point we considered the wetting characterization of a liquid droplet on a solid surface which we consider as static wetting characterization. The droplet measurement and wetting characterization of several STMicroelectronics structures has already been studied at IEMN [10]. We saw in part I.B.2.d that modification of the liquid pressure or trapped air pressure can cause a transition to the Wenzel state of complete wetting. In order to approach the industrial cleaning process namely single wafer process which creates a moving fluid film on the silicon wafer (Figure I.37.a), we proposed the idea of making a micro-channel in which we recreate the fluid film used in the industrial process (Figure I.37.c). Pressure and liquid speed can be controlled inside this micro-channel thus, enabling wetting characterization under different hydrodynamic conditions. This micro-channel system will also give us the ability to control the drying phenomena of the structured silicon interface inside the micro-channel through the controlled injection of air stream to evaporate the injected liquid.

In chapter III, based on the fluid film thickness (Figure I.37.b), the micro-channel design and dimensioning will be introduced. Also, the pressure and fluid speed inside the micro-channel will be calculated.

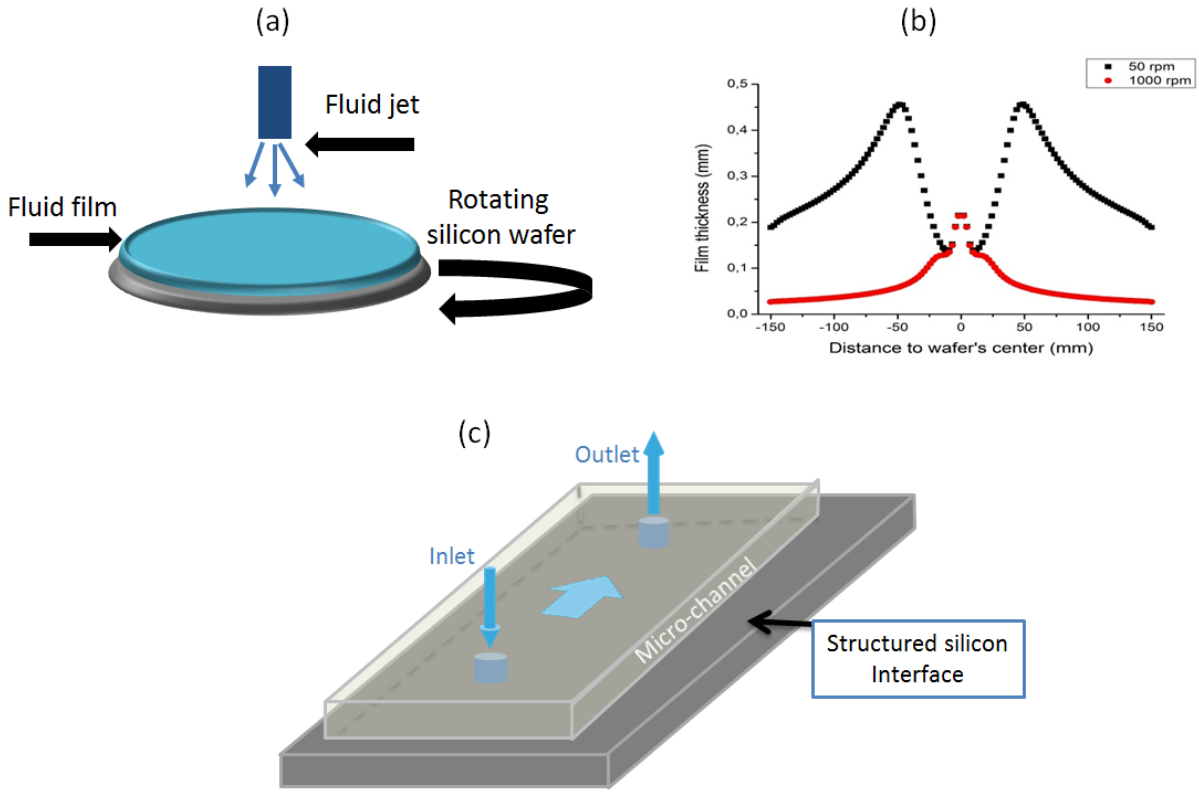


Figure I.37 Schematic of the industrial cleaning process (a) Simulation of the fluid film thickness "h" as function of distance to wafer's center using SC1 (etching solution) as liquid and for different rotational speeds [88] (b) Schematic of the proposed micro-channel system to recreate the industrial fluid film

### I.E.4. Flow in micro-channels bounded by textured surface: Poiseuille flow

Let's consider a micro-channel of length $l$ and height $h$ bounded by a solid surface and other textured surface with height of textures given as $e_0$ (Figure I.38). The flow in the micro-channel can be assumed to be a Poiseuille flow with a pressure gradient along the $x$ direction.

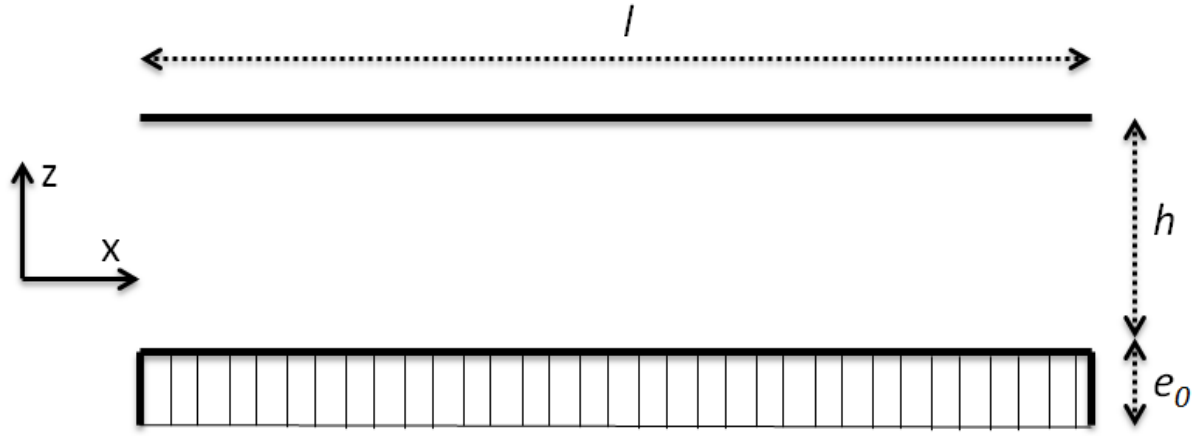


Figure I.38 Schematic of micro-channel bounded by a textured solid surface

Let's now consider the flow of a Newtonian, viscous and incompressible fluid (for example water) inside the micro-channel. The fluid motion is then described by the Navier-Stokes equations which take into account the balance of forces acting at any given region of the Newtonian fluid. Since our flow is confined inside a micro-channel, the Navier-Stokes equations can be simplified using the lubrication theory to obtain thin film equations. The condition to apply the lubrication theory being the studied geometry has one dimension being significantly smaller than the other dimension. In our case, we have the micro-channel height *h* much smaller than the length *l*. Therefore, the simplified governing equation for the velocity *u* in the *x* direction is given as:

$$\frac{\partial p}{\partial x} = \eta \frac{\partial^2 u}{\partial z^2} \qquad \text{Eq I-26}$$

where, $\eta$ the dynamic viscosity of the fluid and *p* the pressure. If we integrate Eq I-26 twice with respect to *z* and taking into account the no-slip boundary conditions at $z = 0$ and $z = h$, we get:

$$u = \frac{1}{2\eta}\frac{\partial p}{\partial x}(z^2 - hz)\,. \qquad \text{Eq I-27}$$

The vertical velocity component, *w* can be obtained by substituting Eq I-27 into the incompressibility condition:

$$\frac{\partial u}{\partial x} + \frac{\partial w}{\partial z} = 0\,.$$

Taking into account the no penetration condition at $z = h$, we have:

$$w = -\frac{1}{2\eta}\frac{\partial^2 p}{\partial x^2}\left(\frac{z^3}{3} - \frac{hz^2}{2} + \frac{h^3}{6}\right). \qquad \text{Eq I-28}$$

At the surface of the textures, the average downward velocity is given as:

$$w = -\frac{h^3}{12\eta}\frac{\partial^2 p}{\partial x^2}\,. \qquad \text{Eq I-29}$$

A mathematical model was adopted by Borg *et al*. [89] to describe an experimental setup of a micro-channel bounded by a superhydrophobic surface consisting of cylindrical pillars. This model showed the possibility of air pockets to be trapped between the pillars as the liquid (water) front advances.

In our case we have a closed micro-channel bound on one side by a micro-textured surface. As we saw from the equations above, the liquid penetration in the surface features is highly related to the different flow conditions (fluid speed, pressure gradient). Therefore, it will be interesting to see the wetting response of STMicroelectonics structures using a micro-channel under different hydrodynamic conditions.

## I.F. Conclusion:

During this chapter, the study of the physical phenomena governing the interaction between a liquid and a solid surface was introduced in the case of smooth surfaces then in that of heterogeneous surfaces with the study of Wenzel, Cassie, hemi-wicking and composites wetting states. Secondly, the problem of wetting in the microelectronics industry, arising from the problem of surface contamination, was presented more particularly for DTI silicon structures which will be studied in this thesis. Next, the presentation of different methods of wetting characterization at the macroscopic and microscopic scale made it possible to see, with varying precision depending on the method, the wetting states of a micro /nanostructured surface. The high frequency acoustic reflectance method has shown in the past to be well suited for determining the impale state of a liquid in network of micro-pillars and nano-pillars.

Finally, some concepts of flow in micro-channels bounded by a textured surface were introduced which were close to the microfluidic system that we will use to approach the industrial cleaning conditions used at STMicroelctronics. In the following chapter, the bases of the theory of the phenomena of acoustic wave propagation will be introduced in the first part before being able to detail the operating principle of the method in chapter III. In second part the Finite Difference Time Domain (FDTD) physical model will be presented to interpret the value of the reflection coefficient when its measurement does not allow a direct conclusion on the wetting state.

# II. Principles of Ultrasound Waves and Acoustic Modeling

In the previous chapter we briefly introduced at the end of wetting characterization methods the acoustic technique and we mentioned that we will adopt the high frequency acoustic method developed at IEMN by Virgilio *et al*. [10]. In the first part of this chapter we will present the basic principles of the physics behind the acoustics more specifically the ultrasonic waves in order to understand the principle and challenges of the reflectometry method that will be presented in Chapter III. We will investigate the propagation of an acoustic wave in a fluid to introduce the notion of acoustic wave. Then the propagation will be studied in a solid and finally we will present the central tool used in the reflectometry method: the piezoelectric transducer. In the second part, we will first look at the different types of models already developed in the literature, find out which aspects they may or may not suit our situations and then introduce our developed FDTD model [10] which will be used in the exploitation of experimental results in chapter IV.

## II.A. Principle of ultrasound waves

### II.A.1. Waves propagation in an infinite medium

#### *II.A.1.a. Propagation in a fluid: one-dimensional model*

Let's consider a vibrating membrane in a fluid as shown in Figure II.1. We will take the fluid as continuous, isotropic, homogenous and perfectly compressible which means the celerity is finite. No frictional forces will affect the system since the effect of viscosity is neglected. Throughout the chapter, the vector fields will be denoted as $\vec{K}$ and their components $K_{i,i=1,2,3}$ in the orthonormal system ($x_1$, $x_2$, $x_3$). The indices will be omitted in one dimensional situation.

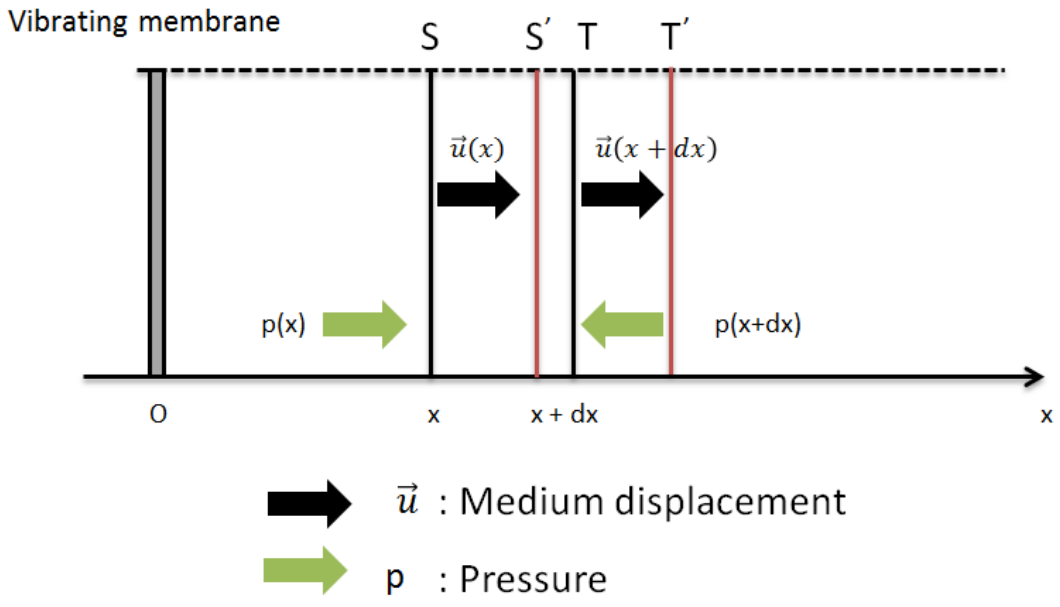


Figure II.1 Schematic diagram of disturbance propagation in a fluid medium

The vibrating membrane at O will undergo deformation which will propagate in the $\vec{x}$ direction. This deformation is characterized by three principle values: the fluid displacement $\vec{u}$, the velocity $\vec{v}$ which is related to the displacement $\vec{v} = \frac{\partial \vec{u}}{\partial t}$ and the pressure $p$ which is dependent on the displacement and time.

We will consider in the fluid a section ST of width *dx* and area $A_0$. When the disturbance reaches this section it will undergo deformation and attains a new position S'T'. The fluid section at point S is displaced by *u(x)* and at point T by *u(x+dx)*, then the forces acting at points S' and T' respectively as follows:

$$F_{S'} = A_0 p(x+u,t) \;\; and \;\; F_{T'} = -A_0 p(x+u+dx+du,t) = -A_0 \left[ p(x+u,t) + \frac{\partial p}{\partial x}(dx+du) \right].$$

Applying Newton's second law at the section ST of mass $dm = A_0 dx \rho_0$, with $\rho_0$ being the density of the fluid, we get:

$$A_0 dx \rho_0 \frac{DV_M}{Dt} = F_{S'} + F_{T'} \qquad \text{Eq II-1}$$

with $V_M$ being the velocity at which the section ST is displaced and it's valued as $V_M = v + V_m \frac{\partial u}{\partial x}$, then we have $\frac{DV_M}{Dt} = \frac{\partial v}{\partial t} + V_M \frac{\partial v}{\partial x}$ ($\frac{DV_M}{Dt}$ is called the total derivative of the velocity $V_M$ [90]).

If we consider $\frac{\partial u}{\partial x} \ll 1$ (case of small deformations), this approximation is called the linear acoustics approximation and defines the framework for all possible calculations thereafter. In nonlinear acoustics, this approximation is no longer valid.

Eq II-1 becomes:

$$\rho_0 \frac{\partial^2 u}{\partial t^2} = -\frac{\partial p}{\partial x} \qquad \text{Eq II-2}$$

where, $p = P_0 + \delta p$, with $P_0$ being the equilibrium pressure and $\delta p$ the added acoustic pressure. We note that the coefficient of fluid compressibility $\chi$ is given as:

$\chi = -\frac{1}{dV}\frac{\delta(dV)}{\delta p}$ with $\delta(dV)$ being the volume variation of the section ST of volume *dV*.

We have:

$$\delta p = -\frac{1}{\chi}\frac{\partial u}{\partial x} \qquad \text{Eq II-3}$$

Implementing the latter expression in Eq II-2, we get:

$$\frac{\partial^2 u}{\partial x^2} - \frac{1}{{c_0}^2}\frac{\partial^2 u}{\partial t^2} = 0 \;\; with \;\; c_0 = \frac{1}{\sqrt{\rho_0 \chi}}.$$

This equation is called the wave equation or D'Alembert's equation with $c_0$ being the rate of propagation of acoustic deformation in the fluid. This is the velocity of sound and is equal to 343 $m.s^{-1}$ and 1480 $m.s^{-1}$ in air and water at 20 ° C respectively.

The general solution of the equation can be represented as the sum of two functions *B* and *C*:

$u = B(x-ct) + C(x+ct)$.

*B* and *C* represent respectively the deformation propagation in the direction of increasing and decreasing *x*. The function B or C remains constant as long as the argument $x-ct$ or $x+ct$ remains constant regardless of the respective values of *x* and *t*. In the case of propagation faced by D'Alembert equations, the signal emitted at $x = 0$ and $t = 0$ is the same one found at $x = x_0$ and $t = x_0/c$.

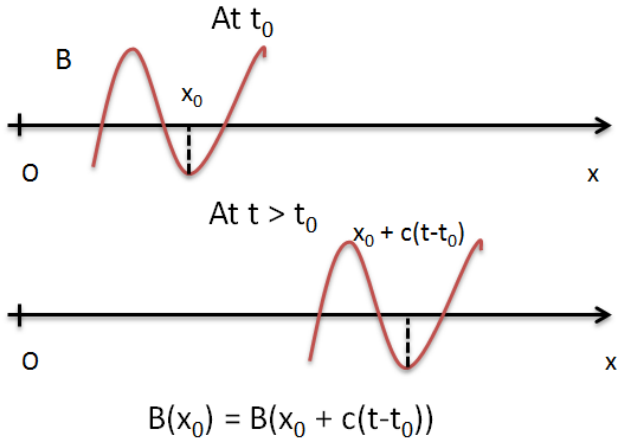


Figure II.2 Schematic of wave propagation in the x direction

Longitudinal and transverse waves are considered two types of bulk acoustic waves. They propagate in a solid medium following its volume length with the difference between them being the direction of propagation with respect direction of vibration. The transverse waves can only propagate in solids while the longitudinal waves can propagate in solids and fluids. In the case where the particles constituting the medium oscillate along the direction of the propagating wave, it's called longitudinal and in the case of transverse wave, when the particles oscillate perpendicularly to the direction of the propagating wave, it's called transverse (Figure II.3). It is for that the vector notation is necessary to represent the direction of vibration. The motion of the longitudinal waves causes pressure variation in the medium leading to compressions and rarefactions areas. The motion of the transverse waves constitutes multiple crests (peaks) and troughs.

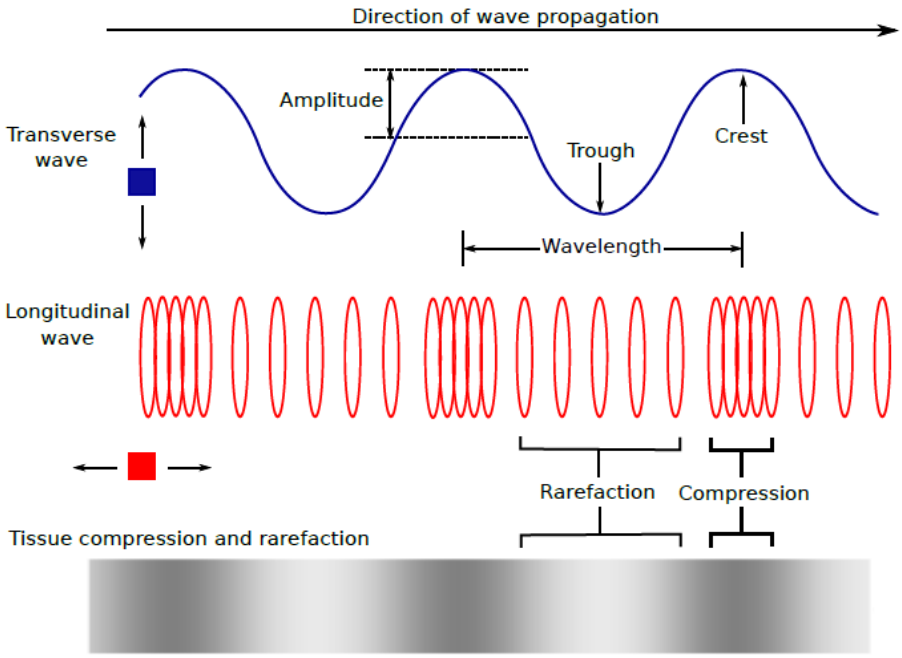


Figure II.3 Illustration of longitudinal and transverse waves [91].

There are different solutions but, we will limit our study to harmonic plane waves which can be written as: $Ae^{j(\omega t-\vec{k}.\vec{x})}$

where *A* is the amplitude of the wave, *j* is the imaginary complex number ($j^2$ = -1),

$\omega = 2\pi f = \frac{2\pi}{T}$ is the angular frequency (*f* being the wave's frequency and *T* is the wave's period), $\vec{x}$ is the position vector, $\vec{k}$ the vector wave number valued as $k = \frac{\omega}{c_0} = \frac{2\pi}{\lambda}$. $\lambda$ is the wavelength and it is related to the frequency by $\lambda = \frac{c_0}{f}$. The expression $(\omega t - \vec{k}.\vec{x})$ show the existence of infinite planes of normal vector $\vec{k}$. This shows that the vibration is the same for all points contained in this plane. This is why it is called plane wave.

A simplified model describing the notion of wave propagation was introduced through the study of deformation propagation in a fluid medium. We will now focus on the phenomena of propagation in a solid.

### *II.A.1.b. Propagation in a non-piezoelectric solid*

#### *II.A.1.b.1. Stress and strain tensors*

Now we will introduce the propagation of waves inside a solid, we will proceed in the same manner as the case of a fluid and apply Newton's second law for a solid volume element (similar to Eq II-1) subjected to deformation and determine the constituting laws that govern the deformation.

First we will introduce two tensors:

1- The strain tensor which is defined in the Cartesian space ($x_1$, $x_2$, $x_3$) as:

$$S_{ij} = \frac{1}{2}\left(\frac{\partial u_i}{\partial x_j} + \frac{\partial u_j}{\partial x_i}\right) \quad \text{Eq II-4}$$

where, $u_i$ is the component of displacement at axis $x_i$ of a point in space M($x_1$, $x_2$, $x_3$) and it's related to the velocity by $v_i = \frac{\partial u_i}{\partial t}$. Note that this tensor is symmetric ($S_{ij}$ = $S_{ji}$).

2- The stress tensor $\sigma_{ij}$ which is defined as the i$^{th}$ component of the force per unit area acting on a surface perpendicularly to j$^{th}$ axis. $\sigma_{ii}$ are called normal stresses while $\sigma_{ij}$ ($i \neq j$) are called shear stresses. This tensor is also symmetrical.

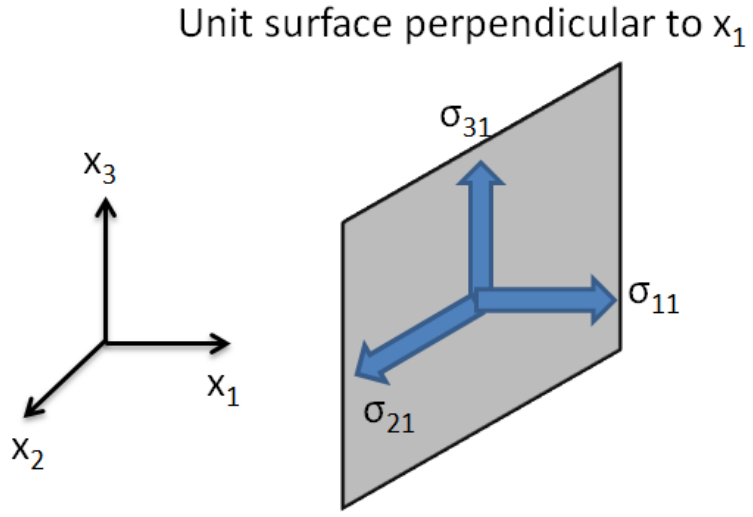


Figure II.4 Schematic of stress tensor components acting on a unit surface

Taking an element of surface with orientation $\vec{l}$ (not perpendicular to any of the Cartesian axes), then the component of the force acting on the unit surface on axis I is given as: $T_i(\vec{l}) = \sum_k \sigma_{ik} l_k$. This force is called the mechanical tension.

The shear and strain tensors are related to each other by Hooke's law as:

$$\sigma_{ij} = c_{ijkl} S_{kl} \quad \text{Eq II-5}$$

with $c_{ijkl}$ being the stiffness tensor.

To simplify the above summation we will adopt Einstein notation which states that when an index variable appears twice in a single term, it corresponds to the summation of all the values that this index can take. Therefore we will take the sum over all the values of k and l, we get:

$$\sigma_{12} = c_{1211}S_{11} + c_{1212}S_{12} + c_{1213}S_{13} + c_{1221}S_{21} + c_{1222}S_{22} + c_{1223}S_{23} + c_{1231}S_{31} + c_{1232}S_{32} + c_{1233}S_{33}\ .$$

Eq II-5 is further simplified using the expression of the strain tensor given in Eq II-4 also, taking into account the symmetric property of the tensors, we have:

$c_{ijkl} = c_{jilk}$ and $c_{ijkl} = c_{ijlk}$.

Then, Hooke's law becomes:

$$\sigma_{ij} = c_{ijkl} \frac{\partial u_l}{\partial x_k} \qquad \text{Eq II-6}$$

with the number of elastic constants being reduced from 81 to 36 (symmetry of tensors).

We will replace the indices (i,j) by a single value k using the following convention:

(11)↔1, (22)↔2, (33)↔3, (23)=(32)↔4, (31)=(13)↔5 and (12)=(21)↔6

The tensor of elastic constants then becomes:

$$c_{ij} = \begin{pmatrix} c_{11} & c_{12} & c_{13} & c_{14} & c_{15} & c_{16} \\ c_{21} & c_{22} & c_{23} & c_{24} & c_{25} & c_{26} \\ c_{31} & c_{32} & c_{33} & c_{34} & c_{35} & c_{36} \\ c_{41} & c_{42} & c_{43} & c_{44} & c_{45} & c_{46} \\ c_{51} & c_{52} & c_{53} & c_{54} & c_{55} & c_{56} \\ c_{61} & c_{62} & c_{63} & c_{64} & c_{65} & c_{66} \end{pmatrix}.$$

The values of the elastic constants depend on the characteristic of the solid material under study.

In our study, only the materials of the cubic system (platinum, silicon) and isotropic materials (silica, polymer) are considered here in more detail. Zinc oxide which belongs to the hexagonal system will be treated separately in the study of piezoelectric transducers. The tensors of elastic constants are written respectively for cubic systems and isotropic materials, $c_{ij}^{cubic}$ and $c_{ij}^{iso}$:

$$c_{ij}^{cubic} = \begin{pmatrix} c_{11} & c_{12} & c_{12} & 0 & 0 & 0 \\ c_{12} & c_{11} & c_{12} & 0 & 0 & 0 \\ c_{12} & c_{12} & c_{11} & 0 & 0 & 0 \\ 0 & 0 & 0 & c_{44} & 0 & 0 \\ 0 & 0 & 0 & 0 & c_{44} & 0 \\ 0 & 0 & 0 & 0 & 0 & c_{44} \end{pmatrix} \quad \text{(3 variables: } c_{11}, c_{12} \text{ and } c_{44}\text{)}$$

$$c_{ij}^{iso} = \begin{pmatrix} c_{11} & c_{12} & c_{12} & 0 & 0 & 0 \\ c_{12} & c_{11} & c_{12} & 0 & 0 & 0 \\ c_{12} & c_{12} & c_{11} & 0 & 0 & 0 \\ 0 & 0 & 0 & \frac{c_{11}-c_{12}}{2} & 0 & 0 \\ 0 & 0 & 0 & 0 & \frac{c_{11}-c_{12}}{2} & 0 \\ 0 & 0 & 0 & 0 & 0 & \frac{c_{11}-c_{12}}{2} \end{pmatrix}$$ (2 variables: $c_{11}$ *and* $c_{12}$ ).

In case of non-viscous fluid (absence of shear stresses), $c_{ij}^{iso}$ could be simplified by taking $c_{11}$=$c_{12}$.

In case of viscous fluid, a new parameter called the viscosity tensor "$\eta_{ijkl}$" is introduced. This new parameter is a fluid property and it's related to the internal friction of a moving fluid leading to energy dissipation. Thus, the displacement in a plane parallel to the viscous fluid induces a shear stress that varies linearly with the gradient of the tangential velocity.

To take into account the mechanical energy absorption by the viscous fluid, the generalized Hooke's law is written as:

$$\sigma_{ij} = c_{ijkl}\frac{\partial u_l}{\partial x_k} + \eta_{ijkl}\frac{\partial v_l}{\partial x_k}\,. \qquad \text{Eq II-7}$$

For the case of water, $\eta_{ijkl}$ takes the form of $c_{ij}^{cubic}$ with $\eta_{44}$ being the dynamic viscosity, $\eta_{12}$ the volume viscosity and $\eta_{11} = 2\,\eta_{44} + \eta_{12}$

In the case of solid material, the generalized Hooke's law doesn't apply since the absorption of energy is considered negligible.

After establishing a relation between the forces acting on a material and its deformations (Hooke's law), we move on to study the dynamic behavior of the material when it is passed by a wave in applying the Newton's second law.

***II.A.1.b.2. Plane waves in solid***

Newton's second law gives:

$$\rho\frac{\partial^2 u_i}{\partial t^2} = \frac{\partial \sigma_{ij}}{\partial x_j} \qquad \text{Eq II-8}$$

where $\rho$ is the density of the solid.

The above equation is the generalized form of the equation presented in the case of fluid (Eq II-2). Adding Hooke's law (Eq II-6) we get:

$$\rho\frac{\partial^2 u_i}{\partial t^2} - c_{ijkl}\frac{\partial^2 u_l}{\partial x_j \partial x_k} = 0\,. \qquad \text{Eq II-9}$$

Applying a solution in the form of plane wave $u_i = A_i F(t - \frac{\vec{n}.\vec{x}}{V})$ with, F($y$) = exp[j$wy$] $\vec{n}(n_i, n_j, n_k)$ the unit normal to the planes of the wave, $\vec{x}$ the displacement vector, $A_i$ the polarization and $V$ the wave phase velocity, we get:

$$\rho V^2 A_i = c_{ijkl} n_j n_k A_l \, . \qquad \text{Eq II-10}$$

This is the Christoffel equation linking the material properties to wave velocity. The solution of this equation allows predicting the sound velocities in a material starting from knowledge of its elastic properties.

The solution of the Christoffel equation gives rise to three plane waves with different orthogonal polarization ($\overrightarrow{A_{QL}}, \overrightarrow{A_{QT1}}, \overrightarrow{A_{AT2}}$) and different velocities ($V_{QL}$, $V_{QT1}$, $V_{QT2}$) which can propagate in the same direction $\vec{n}$ (Figure II.5).

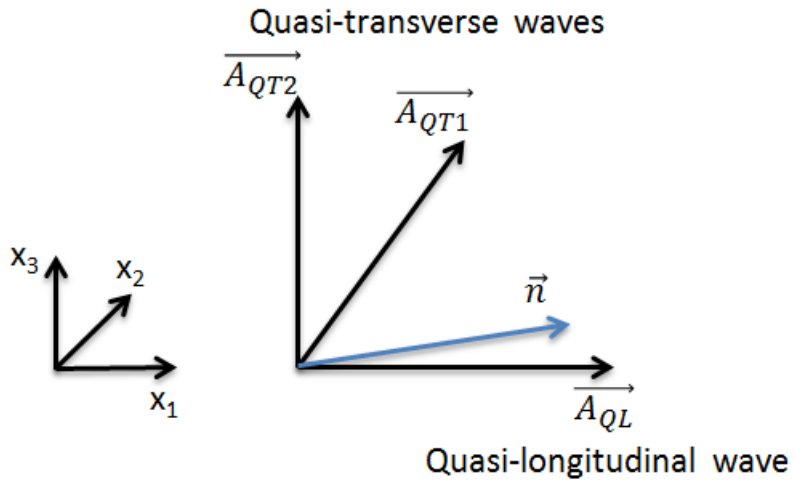


Figure II.5 Schematic of wave propagation in anisotropic solid

The vector polarization $\overrightarrow{A_{QL}}$ which is the closest to the direction of propagation ($\vec{n}$) is called quasi-longitudinal. The other polarizations $\overrightarrow{A_{QT1}}$ and $\overrightarrow{A_{QT2}}$ are called quasi-transverse. We are interested in the solutions for the isotropic and cubic systems. The other crystallographic systems solution are treated in [90], [92].

For the isotropic systems, solving the Christoffel equation yields two waves. The first one is purely longitudinal (polarization parallel to $\vec{n}$), the second one is purely transverse (polarization perpendicular to $\vec{n}$) and with two velocities respectively $V_L$ and $V_T$ :

$$V_L = \sqrt{\frac{c_{11}}{\rho}} \; ; \; V_T = \sqrt{\frac{c_{11} - c_{12}}{2\rho}} \, .$$

The velocities are independent of the propagation direction.

In the case of cubic systems, different waves of different polarization and velocities can be obtained depending on the propagation direction. A slowness curve is a plot that represents the inverse of the velocity, in seconds per meter of measured wave. The plotting of the slowness curve in a specific crystallographic plane allows the plot of the different polarization and velocities related to each direction of that plane. Figure II.6 shows the surface plane of the silicon (cubic system) the (001) plane. In this plane the propagation direction is given by an angle $\varphi$ which is the angle between the vector $\frac{\vec{n}}{V}$ and the axis [100]. We are interested in two values of the velocity particularly at points A and B. In the [100] direction, the longitudinal velocity (point A) and the transverse velocity (point B) are valued respectively: $c_{Si}$ = 8433 m.s$^{-1}$ and $c_{Si}^{trans}$= 5843 m.s$^{-1}$.

The vector $\overrightarrow{P_e}$ gives the direction of acoustic energy propagation. It is called a Poynting vector and by calculating the flux of this vector through a surface, we get the amount of energy that has passed through that surface for one second. The components of $\overrightarrow{P_e}$ are written as:

$$(P_e)_i = -\sigma_{ij}\frac{\partial u_j}{\partial t} = -c_{ijkl}\frac{\partial u_l}{\partial x_k}\frac{\partial u_j}{\partial t}. \qquad \text{Eq II-11}$$

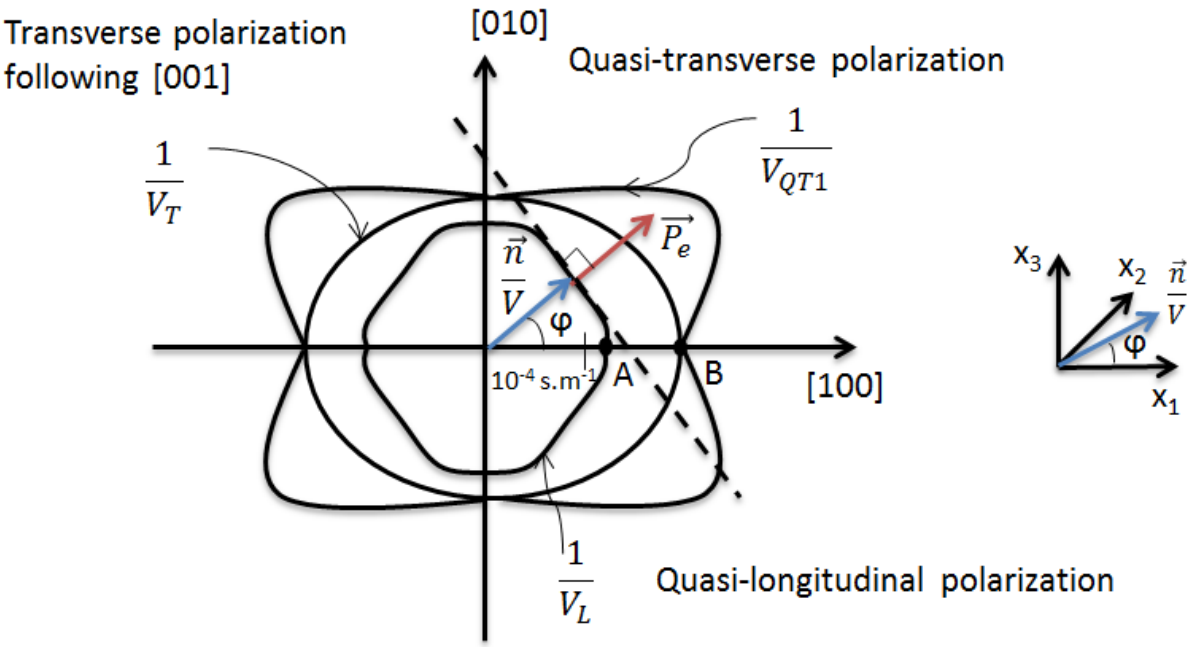


Figure II.6 Slowness surface of silicon in the (001) plane

### *II.A.1.c. Wave propagation in a piezoelectric solid*

A piezoelectric solid is defined as a solid that produces electrical signal under mechanical vibration (direct effect) and reciprocally vibrate under the action of electric field (indirect effect). An electromechanical coupling therefore exists between the electrical variables in the piezoelectric solid (electrical induction $\vec{D}$ and electric field $\vec{E}$) and the mechanical variables (stress $\sigma_{ij}$ and strain $S_{ij}$):

$$D_i = \varepsilon_{ij}E_j + e_{ijk}S_{jk} \quad and \quad \sigma_{jk} = c_{jklm}S_{lm} - e_{ijk}E_i$$

where, $\varepsilon_{ij}$ is the dielectric permittivity and $e_{ijk}$ is the tensor of piezoelectric constants.

In comparison with the non-piezoelectric solid, this coupling will cause all the equations found through applying Newton's second law to be modified along with the wave velocities propagating in the solid. The complete study of the propagation is not important for what follows. For a detailed study the reader can look at [90]. Dielectric and piezoelectric constants will be reintroduced in part II.A.4 of this chapter when studying piezoelectric transducers.

***II.A.1.d. Acoustic impedance***

The acoustic impedance is a physical property of a medium defined as how much resistance an acoustic wave will encounter when it's traversing the medium. In the case of a fluid, the acoustic impedance $Z_f$ of a progressive plane wave is:

$Z_f = \frac{\delta p}{v}$ where, $\delta p$ the acoustic pressure and *v* the particular velocity.

The acoustic impedance depends on the velocity of the wave in the fluid $c_0$ and the fluid density at rest $\rho_0$:

$Z_f = \rho_0 c_0$ .

In the case of solid medium, multiple impedances exist. Since several polarizations of the wave are possible, the acoustic impedance is then defined for each polarization i by $Z^i = \rho V_i$ where, $\rho$ the density of the solid at rest and $V_i$ the wave velocity of polarization i.

In a particular case where we have a plane wave propagating in an infinite medium which is homogenous and isotropic, the impedance is then called the characteristic impedance and it is the same at all points.

Here, it is the impedance related to the longitudinal wave that will be used. This impedance will be noted below simply as Z:

$Z = \rho c$ ; where, *c* the velocity of longitudinal wave in the solid.

The acoustic impedance is a real quantity for progressive plane waves. However, for standing plane waves (static waves confined between the boundaries of the medium), the impedance is given as a complex number equal to the real impedance presented previously added to the acoustic reactance of the medium in which the wave is propagating:

$Z = \rho c + ix$

with, *x* being the acoustic reactance of the medium.

We will see in parts II.A.3 and II.A.4 of this chapter that this notion of impedance is useful for the calculation of the reflection and transmission coefficients of a wave at an interface between two mediums and also for the study of piezoelectric transducers.

### II.A.2. Acoustic Attenuation

When an acoustic wave propagates through a medium, it loses some of its energy, this phenomenon is known as acoustic attenuation. The loss in the medium can be mainly divided into three categories [93]: Viscous loses, heat conduction loses [94] and internal molecular process losses. The viscous losses are mainly due shear deformation, compression or expansion of parts constituting the medium. Losses due to heat conduction are due to transfer of thermal energy from high temperature condensation to low temperature rarefactions. Finally, the internal molecular processes losses are due to the conversion of kinetic energy of the molecules into stored potential energy, rotational and vibrational energies and energies of association and dissociation in the case of wave propagating in ionic solution. In the case of a viscous fluid medium, the acoustic absorption is proportional to the square of the frequency, meaning the higher the frequency, the higher the attenuation will be.

### II.A.3. Waves propagation in a limited medium

Now we will study how a traveling wave behaves when it encounters an interface between two mediums of different densities and elasticities. When an incident wave propagates in one medium and reaches the interface with another medium, it will undergo reflection in the first medium and transmission (or refraction) in the second medium. We saw previously that three waves with polarizations perpendicular to each other and at distinct velocities could propagate in a solid. Thus, three reflected waves and three transmitted waves can form from a single incident wave. We will see in this part how it is possible to determine the directions of propagation, the polarizations and the amplitudes of the reflected and transmitted waves.

In what follows, harmonic plane waves will be considered and the displacement is written:

$u_i = {}^{o}u_i e^{j(\omega t - \vec{k}.\vec{x})}$ where, ${}^{o}u_i$ the amplitude component on axis i.

#### *II.A.3.a. Polarization and direction of reflected and transmitted waves*

Let's consider two mediums (non-piezoelectric) which are linked by an interface plane supposed perfect. This plane equation is written as: $\vec{l}.\vec{x} = 0$ where $\vec{l}$ is the unit normal to the plane.

At the plane level, the displacements $u_i$ and the mechanical tensions $T_i$ are continuous. We have:

$$\begin{cases} u_i^I + \sum_R u_i^R = \sum_T u_i^T \\ T_i^I + \sum_R T_i^R = \sum_T T_i^T \end{cases} \quad \text{Eq II-12}$$

where the exponents I, R and T correspond respectively to the incident, reflected and transmitted waves.

These continuity conditions require that at each instant we have:

1. $\omega^I = \omega^R = \omega^T$ for all points located in the two mediums
2. $\overrightarrow{k^I}.\vec{x} = \overrightarrow{k^R}.\vec{x} = \overrightarrow{k^T}.\vec{x}$ for all points located in the plane of equation $\vec{l}.\vec{x} = 0$

Also, the vectors $\overrightarrow{k^R} - \overrightarrow{k^I}$ and $\overrightarrow{k^T} - \overrightarrow{k^I}$ are perpendicular to the interface plane. Geometrically, this means that the vectors of the reflected and refracted waves are included in the plane of incidence defined by the normal to the interface and the vector of the incident wave. Also, their projections on the interface are equal to that of the vector of the incident wave. Let's take $\theta^I$, $\theta^R$ and $\theta^T$ as the angles of incidence, reflection and transmission respectively, then the previous statement is expressed mathematically as:

$$k^R \sin(\theta^R) = k^T \sin(\theta^T) = k^I \sin(\theta^I)\,. \qquad \text{Eq II-13}$$

This is the Snell-Descartes law and is demonstrated in Figure II.7 for which $\vec{l}.\vec{x} = 0$, $x_2 = 0$.

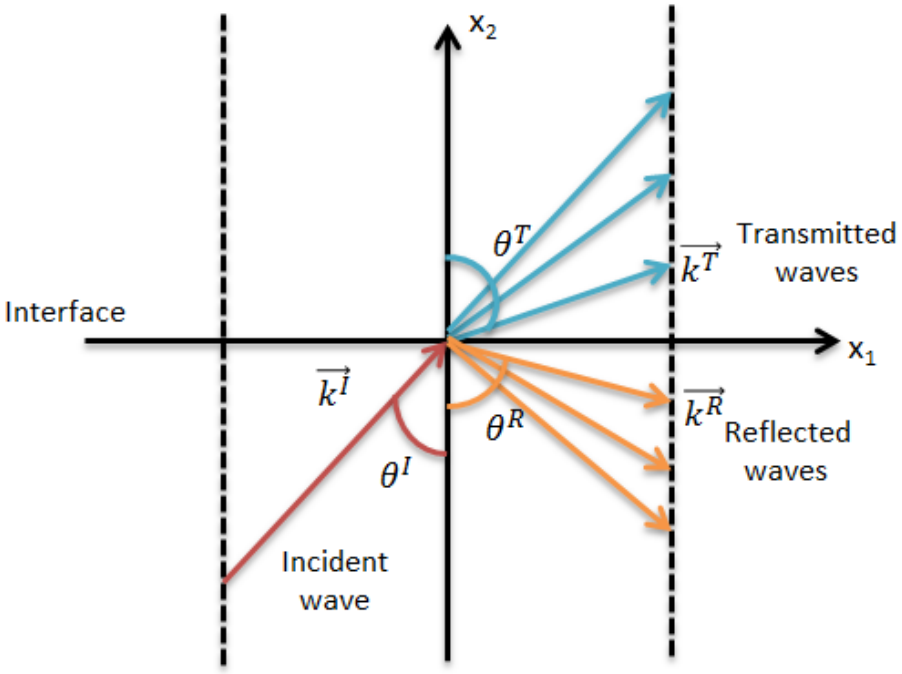


Figure II.7 Illustration of Snell-Descartes law

Eq II-13 makes it possible, by using the norm of the wave vector, to determine the polarizations of the reflected and transmitted waves and also their velocities. Also, with the slowness curves presented in Figure II.6 it is possible to geometrically obtain these parameters by plotting the slowness curves of the two mediums considered. In the example presented in Figure II.8, a quasi-transverse incident wave of velocity $V_2$ is considered. The projection of the vector of the incident wave on the [100] axis must be equal to the projection on the same axis of the vectors of the reflected and transmitted waves. We then obtain two transmitted waves one longitudinal and the other is transverse of respective velocities $V_L$ and $V_T$.

For the reflection, only the quasi-transverse wave of velocity $V_2$ exists. Taking into account the angle of incidence $\theta_c$, the quasi-longitudinal wave cannot exist to satisfy the condition of equality of the projections of the wave vectors, we then speak of a critical angle. This is the

angle of incidence beyond which the reflected quasi-longitudinal wave will no longer exist. The transverse wave of velocity $V_3$ cannot exist either, since it is polarized perpendicularly to the plane of incidence and the incident wave has no component following this direction.

Thus, it's possible starting with an incident wave of specific polarization to obtain the direction of propagation and the velocities of the reflected and transmitted waves at the interface level between two materials whatever the incident angle is. Therefore, to satisfy the continuity equation (Eq II-12), the conditions on the wave amplitudes of the reflected and transmitted waves also apply. The study of these conditions will introduce the notion of coefficient of reflection and transmission of a wave.

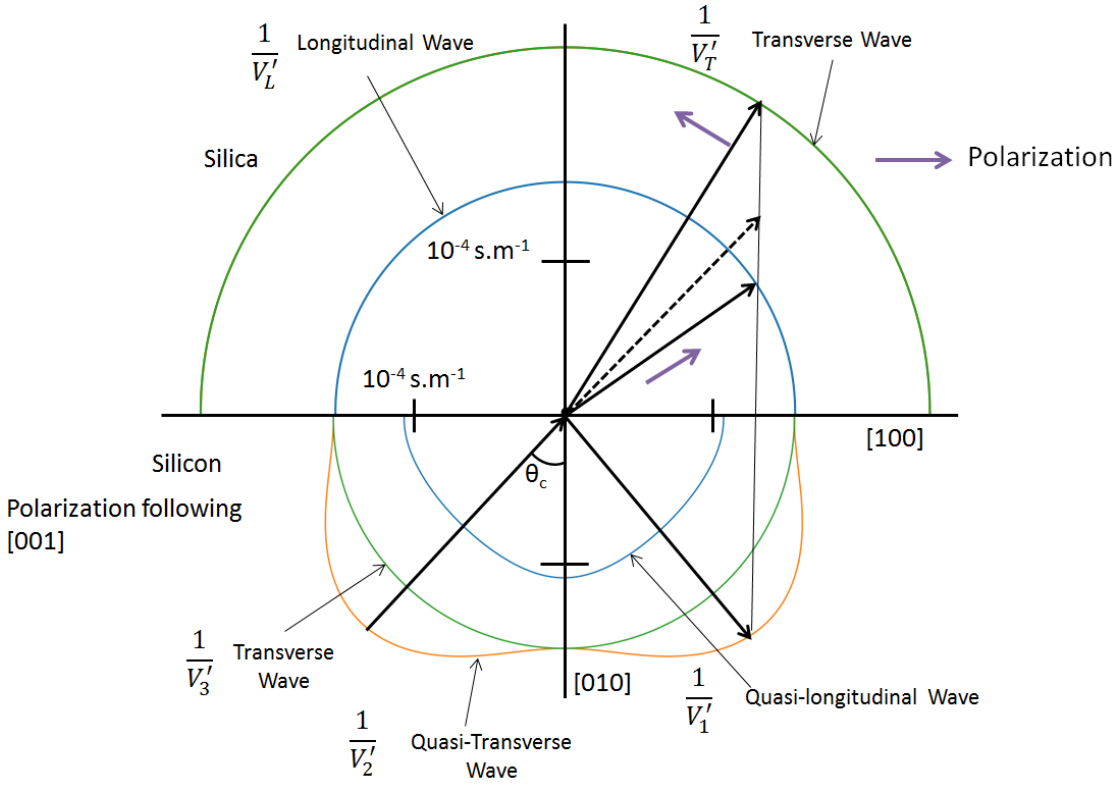


Figure II.8 Slowness curve of silicon/silica with quasi-transverse incident wave

### *II.A.3.b. Amplitude of the reflected and transmitted waves*

Developing the system given in Eq II-12 gives for the displacements amplitude as defined in II.A.3 $\left(u_i = {}^{o}u_i e^{j(\omega t - \vec{k}.\vec{x})}\right)$:

$$ {}^{o}u_i^I + \sum_R {}^{o}u_i^R = \sum_T {}^{o}u_i^T \, . \qquad \text{Eq II-14}$$

Remembering the mechanical tension is given as $T_i = T_{ij} l_j$ and Hooke's law:

$$T_{ij} = c_{ijkl} \frac{\partial u_k}{\partial x_l} = -j c_{ijkl} k_l {}^{o}u_k e^{j(\omega t - \vec{k}.\vec{x})} \, .$$

It becomes:

$$c_{ijkl}l_j\left(k_l^I{}^{\mathrm{O}}u_k^I+\sum_R k_l^R{}^{\mathrm{O}}u_k^R\right)=c'_{ijkl}l_j\sum_T k_l^T{}^{\mathrm{O}}u_k^T \qquad \text{Eq II-15}$$

with $c'_{ijkl}$ being the tensor of elastic constants of the medium where the wave is transmitted.

In our study of wetting using acoustic waves behavior we will focus in detail on particular cases encountered:

- Normal incidence for two isotropic solids, isotropic solid / void, isotropic solid / fluid for longitudinal and transverse waves
- Oblique incidence for isotropic solid/ void and isotropic solid / fluid for longitudinal waves

***II.A.3.b.1. Normal incidence***

Let's consider the propagation of a longitudinal or transverse wave with a normal incidence on the interface (zero angle of incidence) between two isotropic solids. A reflected wave and a transmitted wave of the same polarization as the incident wave appear at the interface (Figure II.9).

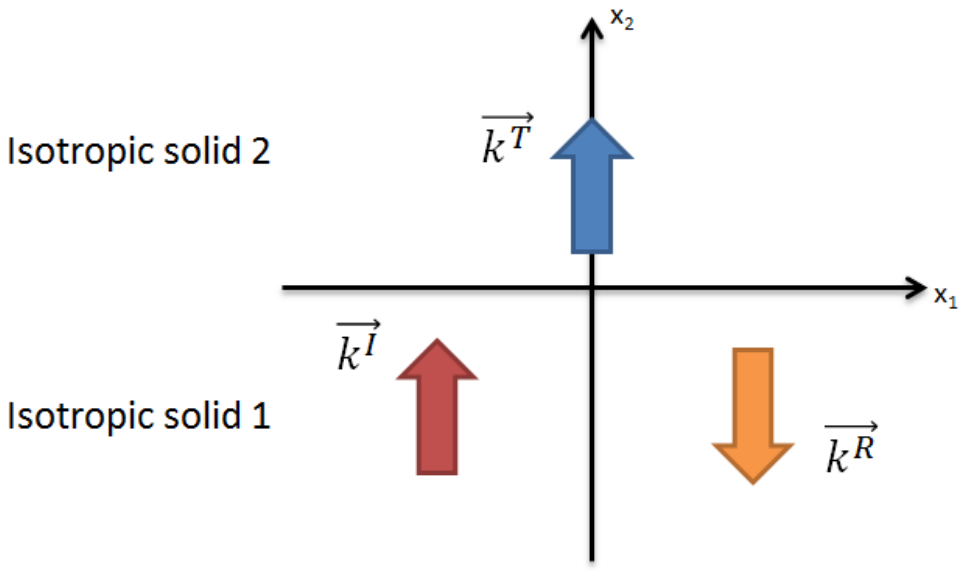


Figure II.9 Schematic showing reflection and transmission of a longitudinal (or transverse) wave on the interface between two isotropic solids

Applying the continuity conditions (Eq II-14 and Eq II-15) gives:

$${}^{\mathrm{O}}u^I+{}^{\mathrm{O}}u^R={}^{\mathrm{O}}u^T$$

and

$c_{11}(k^I{}^{\mathrm{O}}u^I+k^R{}^{\mathrm{O}}u^R)=c'_{11}k^T{}^{\mathrm{O}}u^T$ for longitudinal incident wave

$\frac{c_{11}-c_{12}}{2}(k^I{}^{\mathrm{O}}u^I+k^R{}^{\mathrm{O}}u^R)=\frac{c'_{11}-c'_{12}}{2}k^T{}^{\mathrm{O}}u^T$ for transverse incident wave.

We define the reflection and transmission coefficients as function of amplitudes respectively:

$$r = \frac{{}^{o}u^{R}}{{}^{o}u^{I}} \;\; and \;\; t = \frac{{}^{o}u^{T}}{{}^{o}u^{I}}.$$

We note that:

$$\begin{cases} k^{I}c_{11} = \omega Z_1 \;\; and \;\; k^{T}c'_{11} = \omega Z_2 \;\; for\ longitudinal\ wave \\ k^{I}\dfrac{c_{11} - c_{12}}{2} = \omega Z_1 \;\; and \;\; k^{T}\dfrac{c'_{11} - c'_{12}}{2} = \omega Z_2 \;\; for\ transverse\ wave \end{cases}$$

where, $Z_1$ and $Z_2$ are the acoustic impedances relative to longitudinal and transverse waves, we then get for the displacement coefficients of reflection and transmission:

$$r_{12} = \frac{Z_1 - Z_2}{Z_1 + Z_2} \qquad \text{Eq II-16}$$

$$t_{12} = \frac{2Z_1}{Z_1 + Z_2}. \qquad \text{Eq II-17}$$

The cases where the transmission medium is void or fluid are special cases of the previous formulas.

For the case of void (vacuum), there is no transmitted wave; only the condition of continuity of mechanical tensions must be validated (taking $c'_{ijkl} = 0$), we then have:

$r = 1$ and $t = 0$.

In case of non-viscous fluid, the transverse wave doesn't exist in the fluid:

- For longitudinal wave incidence, Eq II-16 and Eq II-17 are still valid
- For transverse wave incidence, $r = 1$ and $t = 0$.

### *II.A.3.b.2. Oblique incidence*

Now we will do a detailed study of the reflection and transmission of a longitudinal wave on the interface of an isotropic solid and vacuum or fluid with a non-zero incident angle (Figure II.10).

In the case of vacuum, considering Snell-Descartes law, the incident wave gives rise to two reflected waves. The first one is a longitudinal wave of wave vector $k^{RI} = k^{I}$ and reflection angle equal to the incidence angle ($\theta^{I}$) and amplitude ${}^{o}u_{L}$. The second reflected wave is transverse of vertical amplitude ${}^{o}u_{t}$, wave vector $k^{Rt}$ and reflection angle $\theta^{Rt}$ where $\sin(\theta^{Rt}) = \frac{k^{I}}{k^{Rt}}\sin(\theta^{I})$. The acoustic waves cannot propagate in vacuum. In applying the continuity conditions and Snell-Descartes law we can have two reflection coefficients, one for

the reflected longitudinal wave $r_{LL}$ and the other for the transverse reflected wave $r_{LT}$ (also called conversion factor into transverse wave). The two coefficients are written as:

$$r_{LL} = \frac{{}^{o}u_L}{{}^{o}u^I} = \frac{\kappa^2 \sin(2\theta^I)\sin(2\theta^{Rt}) - \cos^2(2\theta^{Rt})}{\kappa^2 \sin(2\theta^I)\sin(2\theta^{Rt}) + \cos^2(2\theta^{Rt})} \qquad \text{Eq II-18}$$

$$r_{LT} = \frac{{}^{o}u_t}{{}^{o}u^I} = \frac{2\kappa \sin(2\theta^I)\cos(2\theta^{Rt})}{\kappa^2 \sin(2\theta^I)\sin(2\theta^T) + \cos^2(2\theta^T)}$$

with $\kappa = \frac{V_T}{V_L}$.

In the case of a fluid, we have identical polarization forming in reflection but, we have a transmitted longitudinal wave with angle of refraction $\theta^T$ where $\sin(\theta^T) = \frac{k^I}{k^T}\sin(\theta^I)$. The two reflection coefficients have then to be modified as:

$$r_{LL} = \frac{{}^{o}u_L}{{}^{o}u^I} = \frac{\kappa^2 \sin(2\theta^I)\sin(2\theta^{Rt}) - \cos^2(2\theta^{Rt}) + \frac{Z_f \cos(\theta^I)}{Z \cos(\theta^T)}}{\kappa^2 \sin(2\theta^I)\sin(2\theta^{Rt}) + \cos^2(2\theta^{Rt}) + \frac{Z_f \cos(\theta^I)}{Z \cos(\theta^T)}} \qquad \text{Eq II-19}$$

$$r_{LT} = \frac{{}^{o}u_t}{{}^{o}u^I} = \frac{2\kappa \sin(2\theta^I)\cos(2\theta^{Rt})}{\kappa^2 \sin(2\theta^I)\sin(2\theta^T) + \cos^2(2\theta^T) + \frac{Z_f \cos(\theta^I)}{Z \cos(\theta^T)}}.$$

In the case where we have interface between two anisotropic solids, the calculation of the reflection coefficients is much more complex because we can have three reflected waves and three waves transmitted in the media. The exact calculation is not analytically possible and it is therefore necessary to use numerical methods to obtain the values of the coefficients.

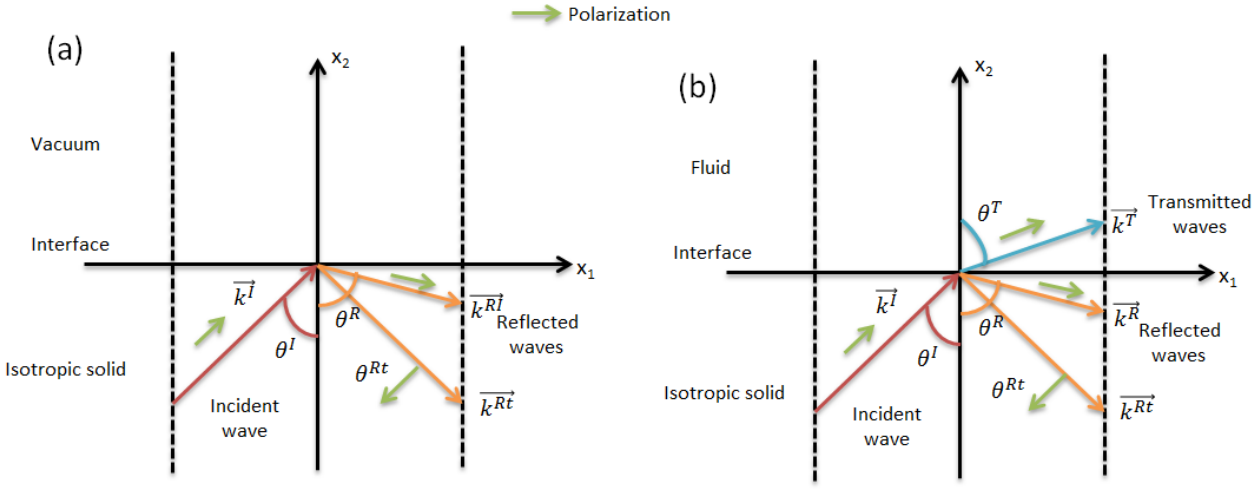


Figure II.10 Schematic of reflection and transmission of an incident longitudinal wave on the interface of isotropic solid and vacuum (a) and isotropic solid and fluid (b)

### *II.A.3.c. Guided waves*

Throughout this chapter we discussed the waves propagating in an infinite volume. However, when the medium is limited by two parallel flat surfaces for example, the acoustic waves will propagate between these two planes by being reflected alternately on each surface. The propagation is then limited by the two planes and it occurs by following the geometry of the medium thus, the wave is defined as guided. There are many types of guided waves. We can just briefly present two main types of waves that are generally used in acoustics.

#### *II.A.3.c.1. Rayleigh wave*

The Rayleigh wave (Figure II.11) was discovered in 1885 by Lord Rayleigh and corresponds to the propagation of a wave guided by a free surface of a semi-infinite crystal. We mention the surface wave because unlike bulk (volume) waves (longitudinal and transverse waves) the wave propagates parallel to the surface of the medium. Rayleigh wave include both longitudinal and transverse motions forming an elliptical polarization motion. The amplitude of the Rayleigh wave motion decreases exponentially as the distance from the surface increases. At a depth of about one wavelength, the amplitude of the displacements vanishes.

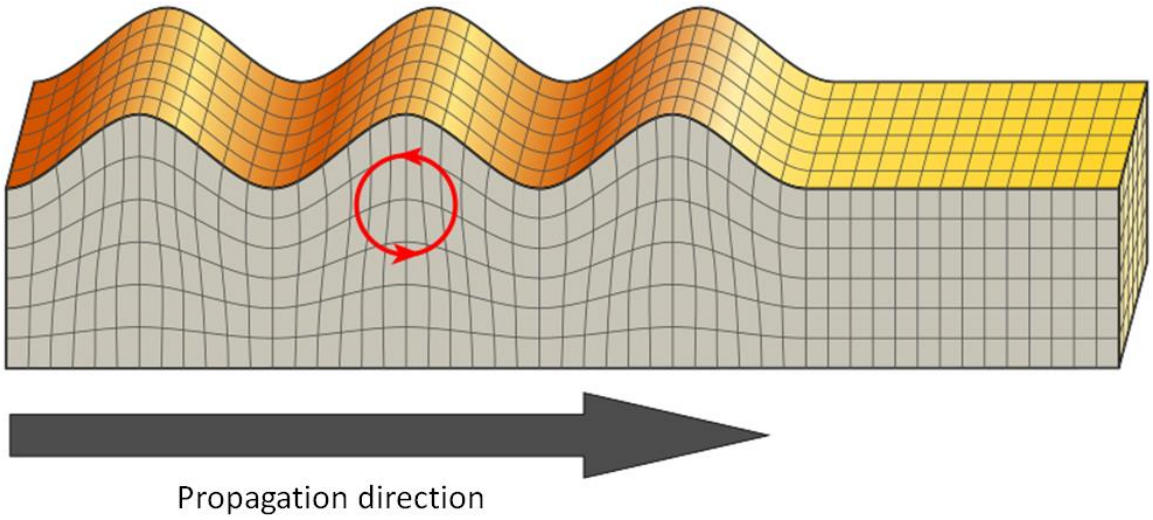


Figure II.11 Schematic of Rayleigh wave propagation

The Rayleigh wave is one type of surface waves. Depending on the configuration of medium, the surface wave can be defined:

- Stoneley wave exists when the wave propagates along the separation surface between two different mediums such as solid-solid or solid-fluid interfaces.
- Scholte wave exists if one of the two solid mediums is replaced by a liquid.

#### *II.A.3.c.2. Lamb wave*

Lamb waves are specific kind of surface acoustic waves that propagate in two dimensional planes forming a plate whose thickness is comparable to the wavelength. This kind of wave was first introduced in 1917 by the English mathematician Horace Lamb. In case of an isotropic material and if the plate is surrounded by vacuum, we have Lamb waves. For a plate

immersed in a fluid, we will then have generalized Lamb waves. The deformations of the plate are direct result of the coupling between longitudinal and transverse (vertical) displacements.

Two main types of Lamb wave modes can exist. The first where two faces of the plate vibrating symmetrically (symmetrical modes) whereas in the second mode, the two faces vibrate in parallel (anti-symmetric modes). The different modes are shown in Figure II.12.

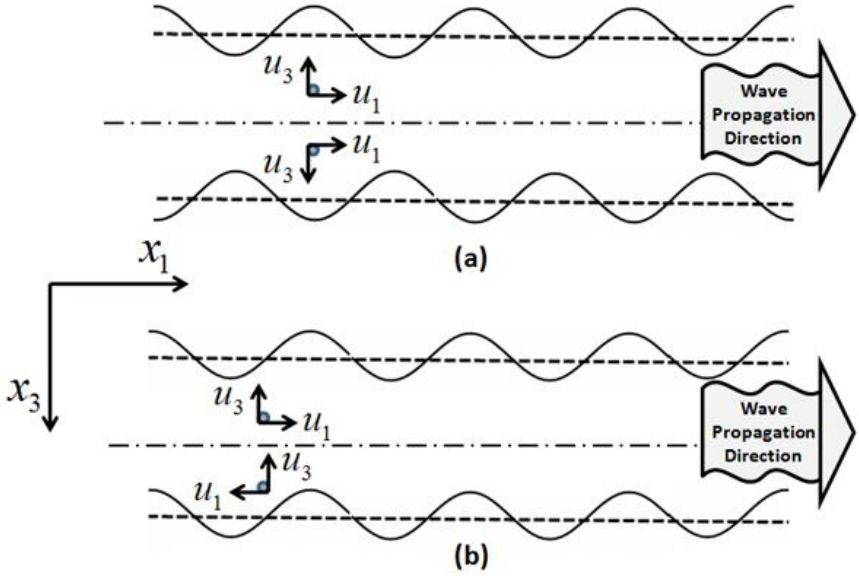


Figure II.12 (a) Symmetric and (b) anti-symmetric mode of lamb wave [95].

There exist other guided waves that can propagate in plate-like structures such as horizontal transverse waves. If the plate is directly connected to a substrate such as elastic solid (having higher wave velocity), we then have Love waves.

### *II.A.3.d. Concept of reduced impedance*

To introduce the notion of reduced impedance we will consider the case of longitudinal wave propagation with a normal incidence to the surface. The shear stress is negligible and the stress is written simply $\tau$ and it is opposite to the acoustic pressure $(\tau = -\delta p)$. The acoustic impedance of the medium is then written $Z = \frac{-\tau}{v}$.

In Figure II.13 we consider three semi-infinite media with acoustic impedances $Z_1$, $Z_2$ and $Z_3$ and with medium 2 being an intermediate medium between the other two. Thus, using Eq II-16 and Eq II-17 we can calculate the reflection and transmission coefficients. Therefore, we can return to a simpler case where it's possible to associate impedance $Z_{3,2}^{red}$ which is equivalent to the two impedances $Z_1$ and $Z_2$ of the two mediums (Figure II.13). This equivalent impedance is called reduced impedance and it's defined as the impedance of an infinite medium by taking the values of the stress field and the velocities at the input and output of the intermediate layer $(\tau_e, v_e)$ and $(\tau_s, v_s)$ respectively.

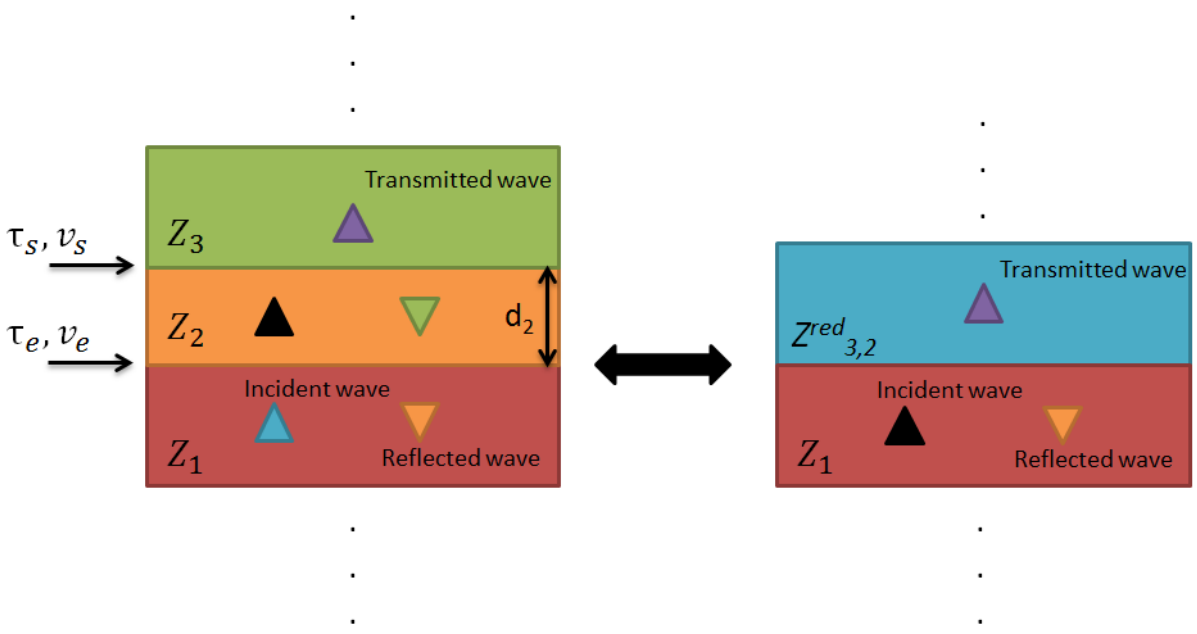


Figure II.13 Schematic illustration of reduced impedance

Writing the fields values at the $Z_2$ / $Z_3$ interface, we obtain:

$$\begin{pmatrix}\tau_e\\ v_e\end{pmatrix} = \begin{pmatrix}\cos(\theta_2) & -jZ_2\sin(\theta_2)\\ \dfrac{-j\sin(\theta_2)}{Z_2} & \cos(\theta_2)\end{pmatrix}\begin{pmatrix}\tau_s\\ v_s\end{pmatrix} \quad with \;\; \theta_2 = k_2 d_2$$

$k_2$ and $d_2$ are respectively the wave vector and the thickness of layer 2.

We also have $Z_3 = \frac{-\tau_s}{v_s}$.

The reduced impedance of layers 2 and 3 is defined as:

$$Z^{red}_{3,2} = \frac{-\tau_e}{v_e} = Z_2\frac{1 + r_{23}e^{-2j\theta_2}}{1 - r_{23}e^{-2j\theta_2}} \qquad \text{Eq II-20}$$

where $r_{23} = \frac{Z_2 - Z_3}{Z_2 + Z_3}$.

We can then introduce the corresponding reflection coefficient:

$$r^{red}_{1,3} = \frac{Z_1 - Z^{red}_{3,2}}{Z_1 + Z^{red}_{3,2}}. \qquad \text{Eq II-21}$$

If we have more layers of different materials stacked next to each other, we can apply the same method consecutively by taking two neighboring layers and finding their reduced impedance each time (Figure II.14).

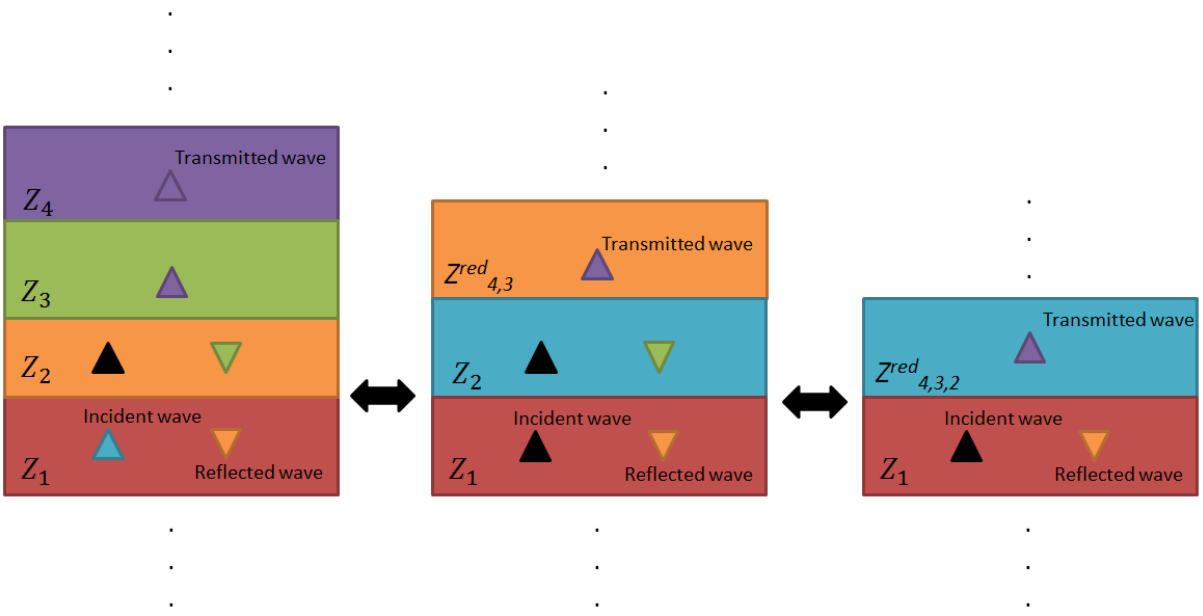


Figure II.14 Schematic for calculating the reduced impedance for 4 stacked layers

This method will very useful for estimating the theoretical electrical impedance of a piezoelectric transducer composed of different media (electrodes) in which the wave can propagate as we will see in chapter III when we introduce our piezoelectric transducers.

### II.A.4. Piezoelectric transducer

#### *II.A.4.a. Choosing the acoustic wave*

The use of the acoustic waves in characterizing the wetting state is a form of Non-Destructive Testing (NDT). Therefore, the choice of the acoustic wave will be made on a criteria that it will not modify the testing environment and samples. The modifications undergone by the wave during its propagation (phase, velocity, amplitude: reflection, transmission, absorption) which are exploited to characterize the medium without degrading it is the main objective. Depending on the intended application, the type of acoustic wave, the frequency and the power level must be carefully chosen. We can cite a few examples of application:

- Guided Love waves of frequencies range in the hundreds of megahertz allow the detection of liquid properties [96], [97], [98], detection of bio-organisms in liquid media [99] and evaporation kinetics [100].

- Guided Lamb waves but with a frequency of around ten kilohertz can be used to detect defects (found in centimeters) in the walls of steel pipes [101] and damage detection in composite materials [102].

- Lamb waves used at a frequency of the order of megahertz for the detection of millimeter-sized defects in millimeter-thick steel plates [103], [104], [105] and aluminum thin plates [106], [107].

- Scanning Acoustic Microscopy (SAM) uses volume waves of frequencies ranging from 100 MHz to 2 GHz to study the internal microstructure of non-transparent materials. It allows the detection of defects inside battery cells [108] and assessing the quality of metal thermo-compression bonds [109]. Also, through the generation of surface acoustic waves (Rayleigh waves), SAM can be used to measure mechanical properties of a medium [110].

From the examples mentioned above, one can see that different types of acoustic waves and their typical frequency from one application to another. The smaller the objects to characterize the more it will be necessary to use high frequencies. Indeed, the higher the frequency, the shorter the wavelength in the medium and the more sensitive the acoustic wave will be to changes in the mechanical properties (density and elasticity) of the smallest objects.

In our case, we need to characterize silicon structures at micro/nanometric scale. Thus, several challenges need to be considered:

- Detection of liquid penetration inside the structures.

- Usage of ultra-high frequency for the wave to be able to detect micro/nanotexturation.

Therefore, it makes sense to choose a volume wave with a frequency of the order of gigahertz using a piezoelectric transducer of few microns in thickness. The size of the piezoelectric transducer will be in order of few hundred microns in diameter because of constraints related to the experimental bench and the transducer electrical adaptation as we will see in Chapter III. The longitudinal wave is chosen because, as will be seen in chapter III, it is possible to use in order to determine the presence or absence of liquid in the surface textures through the calculation of the reflection coefficients at the level of the structured interface. The transverse wave had shown interesting simulation results for the study of drying of STMicroelectronics silicon structures in the previous thesis done at IEMN [10], but as we will see in Chapter III, it will be difficult to use and exploit.

Next we will choose what type of transducer will be used to produce the longitudinal wave of a few gigahertzes and how to mathematically describe its electrical impedance.

### *II.A.4.b. Choice of the piezoelectric transducer*

The piezoelectric transducer is an important element in the generation of the ultra-high frequency acoustic waves and allows the analysis of their reflective signals. The piezoelectric character (generally made of crystals and certain ceramic materials) is very useful since both direct and indirect effects are necessary. The transducer at one point serves as a receiver and it produces electricity under the action of a mechanical stress (direct effect) and at other point as a transmitter because it emits an acoustic wave under the effect of an electric field (indirect effect).

There are several types of piezoelectric materials used for the piezoelectric transducers. The materials are used are evidently always anisotropic. Depending on the desired vibrational frequency, the type of the transducer generating longitudinal wave will vary.

Some of the most used piezoelectric materials are: The quartz, lithium niobate (LiNbO3), zinc oxide (ZnO), aluminum nitride (AlN) and PZT (Lead Zirconate Titanate) ceramics. In the frequency range of below 25 MHz, the piezoelectric transducer will often be a ceramic plate of thickness of the order of a hundred microns. Most often, the acoustic impedance of the transducer is too different from that of the propagation medium thus, it is necessary to adapt the impedance by inserting intermediate layers between the transducer and the propagation medium in order to make efficient conversion of electrical energy into acoustic energy on transmission and vice versa on reception as well as to ensure good mechanical coupling for a good transmission of the mechanical displacement. The use of composite transducers allows the reduction of the number of impedance-matching layers. The transducer is then composed of piezoelectric ceramic elements stacked in cascade or sandwiched next to each other and often separated by metallic elements (Figure II.15). In cascade piezoelectric ultrasonic transducer, the electrical parallel and the mechanical series can multiply the ultrasonic power and ultrasonic intensity respectively [111].

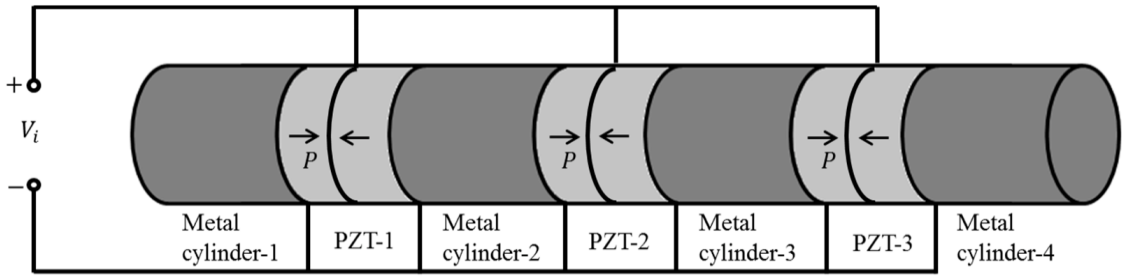


Figure II.15 Schematic of cascade piezoelectric ultrasonic transducer [111]

Also, smart intelligent structures for piezoelectric ceramic are being largely used as they are highly efficient [112]. Two examples of this structures are the “cymbal” and “moonie” piezoelectric resonators (Figure II.16) consisting of piezoelectric ceramic sheet sandwiched between two metal end caps.

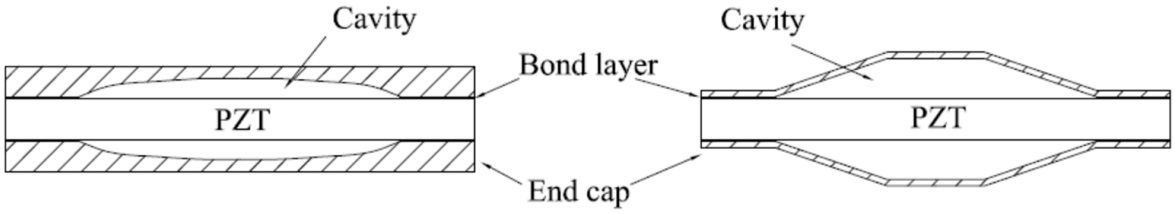


Figure II.16 Schematic of the moonie (left) and cymbal (right) piezoelectric resonators [112]

For higher frequencies in the order of hundreds of megahertz, scanning acoustic microscope (SAM) can be used to characterize the surface of a material [113]. It consists of transducer emitting ultrasonic waves, mechanical scanner and a processor to analyze the images. The transducer is made up of a magnet and a radiofrequency coil. The transducer crystals are often made up of lithium niobate, quartz or Zinc Oxide (ZnO). A water coupling medium is used between the studied material and the transducer to ensure effective transmission of the acoustic waves.

Finally, for frequencies in the order of gigahertz, we will be depositing the piezoelectric material in the form of a thin film by magnetron sputtering on a metallized substrate (the metal constitutes one of the transducer's electrodes) in order to obtain thicknesses from micron to hundred nanometers. The so-called external rear electrode will then be deposited over the piezoelectric material layer. ZnO is a piezoelectric crystal which will be used for making this type of transducer since it fits our application. The transducer geometry, the different materials used and the fabrication processes will be presented in detail in chapter III.

### *II.A.4.c. Electrical impedance of the piezoelectric transducer*

The electrical impedance $Z_t$ of a transducer is defined as the ratio of the voltage across the terminals of the transducer to the circulating current *I*. The theoretical calculation of the electrical impedance will be important in dimensioning the different parts of the transducer.

The transducer will be fabricated on the surface of a silicon wafer (substrate). It consists of a layer of ZnO between two layers of platinum electrodes. We can see the geometry of the transducer with the different acoustic impedances in Figure II.17. It is modeled as a ZnO layer between two semi-infinite media, by using the reduced impedance at the front of the transducer $Z_{fr}^{red}$ and at the back $Z_{ba}^{red}$.

The voltages, electrical current and different mechanical forces produced are all directly related to each other. The electrical impedance can be obtained in writing the different coupling relations. It is given as $Z_t$ [90]:

$$Z_t = \frac{1}{jC_0 2\pi\omega} + \frac{{K_{ZnO}}^2}{C_0 2\pi f}\frac{Z_{ZnO}}{\theta_{ZnO}}\frac{2Z_{ZnO}(\cos(\theta_{ZnO})-1) + j(Z_{fr}^{red}+Z_{ba}^{red})\sin(\theta_{ZnO})}{Z_{ZnO}(Z_{fr}^{red}+Z_{ba}^{red})\cos(\theta_{ZnO}) + j({Z_{ZnO}}^2 + Z_{fr}^{red}Z_{ba}^{red})\sin(\theta_{ZnO})} \qquad \text{Eq II-22}$$

where *f* is the functional frequency, $C_0$ static capacity of the transducer, $K_{ZnO}$ electromechanical coupling coefficient of ZnO, $Z_{ZnO}$ acoustic impedance of ZnO and $\theta_{ZnO} = k_{ZnO}d_{ZnO}$ ($k_{ZnO}$ being the wave vector inside ZnO and $d_{ZnO}$ the thickness of the ZnO layer).

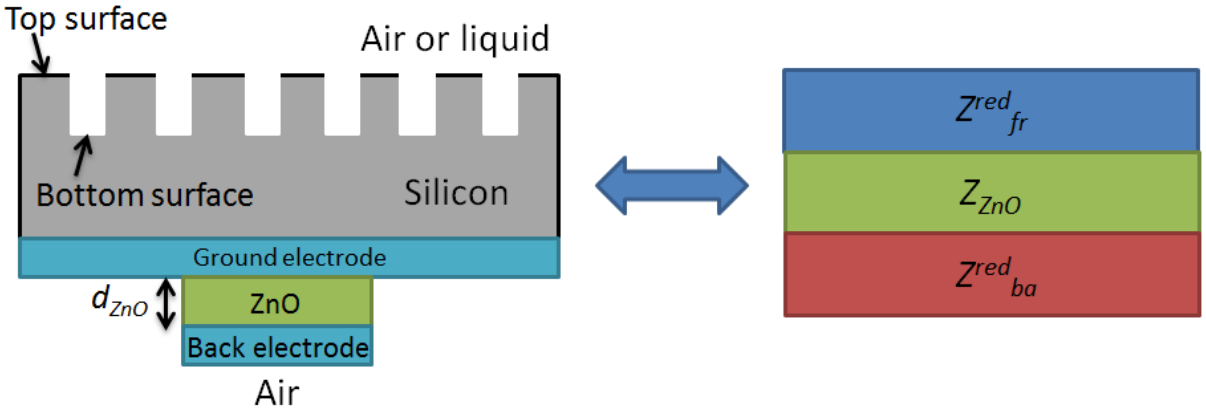


Figure II.17 Schematic of layers reduction for a real transducer setup

The static capacity and the electromechanical coefficient can be expressed in terms of constants introduced in II.A.1.c taken for ZnO:

$$C_0 = \frac{\varepsilon_{33} S_{ZnO}}{d_{ZnO}}$$ Eq II-23

$$K_{ZnO}{}^2 = \frac{e_{333}{}^2}{\varepsilon_{33}{}^2 c_{33} + e_{333}{}^2}.$$

To study the electro-acoustic behavior of the transducer, we consider semi-infinite silicon (to prevent acoustic reflections). The impedance of the transducer is then purely electrical ($Z_t^{el}$), we can then model the transducer as being composed of a resistance $\mathrm{Re}(Z_t^{el})(\omega)$ in series with a reactance $X_A(\omega)$ and a capacitor (Figure II.18). The resistive part represents the dissipation of energy in the form of acoustic radiation (it is not related to electrical losses by Joule effect which are not taken into account in this modeling). Thus, it's the real part of the transducer impedance which characterizes the acoustic response.

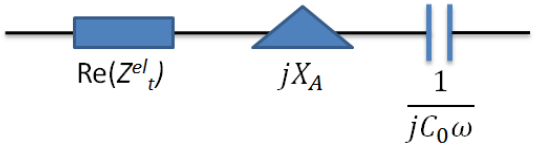


Figure II.18 Piezoelectric transducer representation as an electrical circuit

The average value of the mechanical power transported by the emitted acoustic waves $\langle P_t \rangle$ is:

$$\langle P_t \rangle = \frac{1}{2} Re\left(Z_t^{el}\right) |I|^2.$$ Eq II-24

## II.B. Simulation: acoustic wave / structured surface interaction

The objective behind the simulation in the thesis work is to understand how the acoustic wave will interact with the micro / nanostructured interface between silicon and air depending on the relationship between the wavelength and the characteristic dimensions of the structures (trenches) on one side. On the other side the simulation will give us the values of the reflection coefficients with presence of the liquids inside the nanometric trenches in order to compare with the experimental values and better understand the DTI wetting state.

We note that the simulation here links wetting state through acoustic response but is not intended to predict the dynamics of the fluids within the texturing. The liquid flow inside the micro-channel and on top of the interface will not be considered. Two different cases are then considered: the acoustic wavelength is greater or smaller than the thickness of the structured interface between silicon and air. In the first case, only one reflection will take place on the structured interface. In the second case, multiple reflections and different propagation modes can appear in the structures. In addition, the effect on the reflection coefficient of the two layers ($Si_3N_4$ + $SiO_2$) on top surface of the DTI wafer will be studied.

### II.B.1. Finite difference model (FDTD model)

#### *II.B.1.a. Interest in the method*

The FDTD developed in a previous thesis By Virgilio *et al*. [10] at IEMN has been chosen in the case where the wavelength is smaller or comparable to the height of the texturing (For detailed information about the choice of the FDTD model, the reader is invited to consult the previous work done [10]). Propagative modes can appear in the structures and their separation in time is possible however, for wavelengths very close to the height of the texturing, this separation is not optimal and the echoes partially mix. It is then difficult to identify the reflection on the bottom surface of the structures that enable us to calculate the most useful reflection coefficient to conclude on the wetting state. Figure II.19 shows the echo diagram (amplitude of the reflected signal received from the transducer, see III.A) of the DTI cross trenches 4 µm deep for a transducer center frequency of 3 GHz which corresponds to a wavelength in silicon of 2.8 µm. By comparing this echo diagram with that on a smooth surface, we see that the reflection on the bottom of the trenches (see III.A.3) is poorly defined in time and ranges from 180 ns to 184 ns. This is due to the fact that the wavelength is comparable to the height of textures. In this case, we are unable to get information about the reflection coefficient on the bottom of the structures and thus, give information about the wetting state.

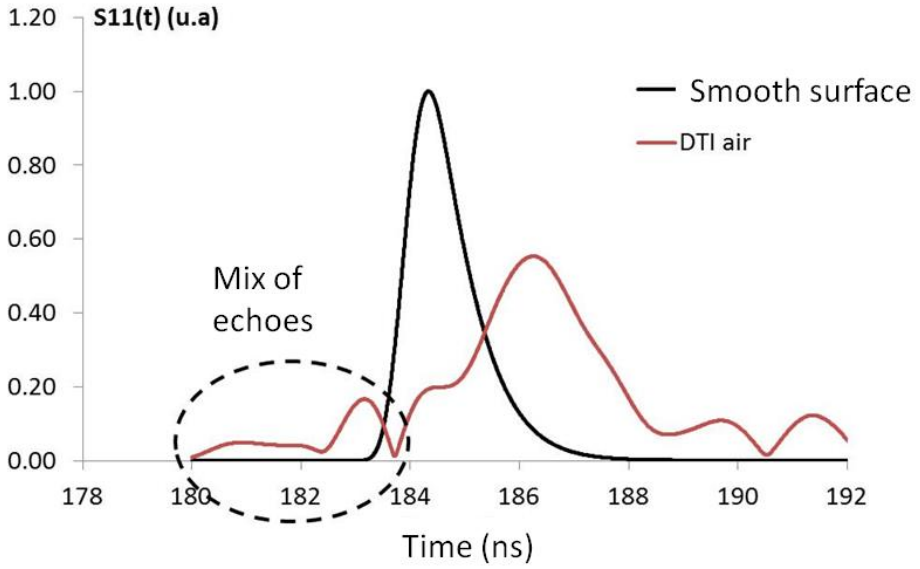


Figure II.19 Experimental echo diagram of DTI exposed to air for transducers of 3 GHz central frequency in the frequency band [0.5 GHz; 5 GHz] [10]

The FDTD model is able to predict the order of magnitude of the center frequency of the transducer necessary to separate the echoes and identify over time the reflection on the bottom of the structures. The accuracy of the model also is sufficient to be able to calculate the reflection coefficients on the bottom of the structures according to the state of wetting (Cassie or Wenzel). In addition, when the experimental value of the reflection coefficient on the bottom surface of the structures (trenches) is intermediate between 0.86 (Wenzel state) and 1

(Cassie state), the FDTD model could be useful in predicting the state of wetting in the bottom of the trenches (Figure II.20).

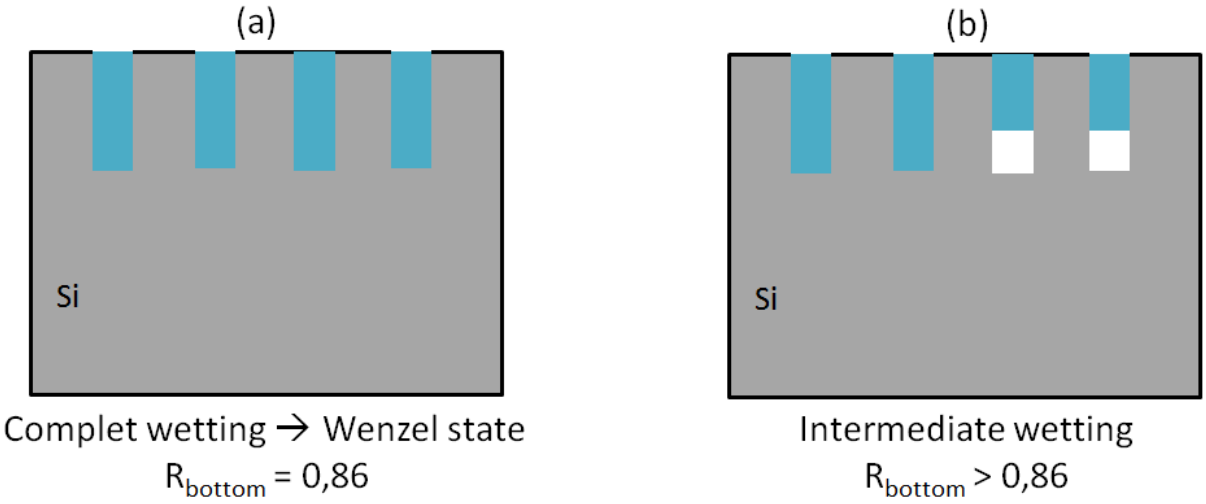


Figure II.20 Schematic of complete wetting (a) and intermediate wetting inside DTI (b)

To solve a partial differential problem, different approaches are possible. All of the existing methods can be classified into two large families. The first consists in looking for approximate solutions of the exact equations governing the problem. For example, the so-called finite element type solution approximation methods are used. The second is to approximate the equations of the problem and look for exact solutions. We talk about equation approximation methods. The FDTD model belongs to this family. The choice of method then turned to the second type for its simplicity of implementation and lower calculation times.

### *II.B.1.b. Principle of the method*

The principle of FDTD is explained as follows: The magnitude fields describing the problem (displacement, velocity, stresses) are discretized and placed on a grid of which each point of space is located by its coordinates (i, j) and separated from the other points by a distance $\Delta x_1$ in $x_1$ direction and $\Delta x_2$ in $x_2$ direction. Each point in space is associated with the values of the components of the different fields according to the Virieux method [114] (Figure II.21). The equations of the problem will then be discretized through the discretization of the partial derivatives. The Virieux method deals with geometries in 2D dimension.

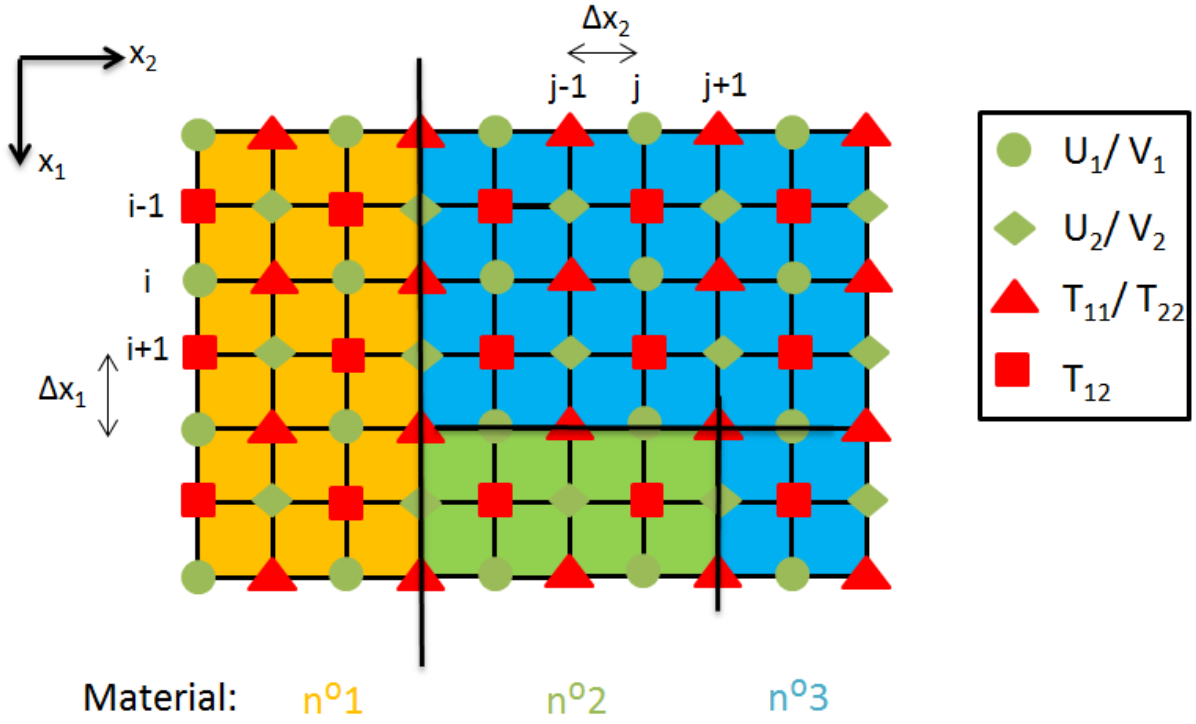


Figure II.21 Discretization scheme of the problem in 2D

The displacement field $u(x_1, x_2)$ is calculated by the Taylor expansion in $x_1 \pm \Delta x_1$ at instant t:

$$u(x_1 + \Delta x_1, x_2) = u(x_1, x_2) + \Delta x_1 \frac{\partial u(x_1, x_2)}{\partial x_1} + \frac{\Delta x_1{}^2}{2!} \frac{\partial^2 u(x_1, x_2)}{\partial x_1{}^2} + \frac{\Delta x_1{}^3}{3!} \frac{\partial^3 u(x_1, x_2)}{\partial x_1{}^3} + \cdots$$

and

$$u(x_1 - \Delta x_1, x_2) = u(x_1, x_2) - \Delta x_1 \frac{\partial u(x_1, x_2)}{\partial x_1} + \frac{\Delta x_1{}^2}{2!} \frac{\partial^2 u(x_1, x_2)}{\partial x_1{}^2} - \frac{\Delta x_1{}^3}{3!} \frac{\partial^3 u(x_1, x_2)}{\partial x_1{}^3} + \cdots$$

At order 1 we have:

$$u(x_1 + \Delta x_1, x_2) = u(x_1, x_2) + \Delta x_1 \frac{\partial u(x_1, x_2)}{\partial x_1} + O(\Delta x_1{}^2) \qquad \text{Eq II-25}$$

and

$$u(x_1 - \Delta x_1, x_2) = u(x_1, x_2) - \Delta x_1 \frac{\partial u(x_1, x_2)}{\partial x_1} + O\left(\Delta x_1{}^2\right). \qquad \text{Eq II-26}$$

By doing the difference between Eq II-25 and Eq II-26:

$$u(x_1 + \Delta x_1, x_2) - u(x_1 - \Delta x_1, x_2) = 2\Delta x_1 \frac{\partial u(x_1, x_2)}{\partial x_1} + O\left(\Delta x_1{}^2\right).$$

The partial derivative of the displacement file is then written as:

$$\frac{\partial u(x_1, x_2)}{\partial x_1} = \frac{u(x_1 + \Delta x_1, x_2) - u(x_1 - \Delta x_1, x_2)}{2\Delta x_1}. \quad \text{Eq II-27}$$

This formula is called that of the centered difference. The value of the field at $x_1$ does not need to be known for the calculation of the derivative of the field. There are also two other formulations called respectively forward and backward difference:

$$\frac{\partial u(x_1, x_2)}{\partial x_1} = \frac{u(x_1 + \Delta x_1, x_2) - u(x_1, x_2)}{\Delta x_1} \quad \text{Eq II-28}$$

and

$$\frac{\partial u(x_1, x_2)}{\partial x_1} = \frac{u(x_1, x_2) - u(x_1 - \Delta x_1, x_2)}{\Delta x_1}. \quad \text{Eq II-29}$$

Note that the partial derivative has been transformed into a simple finite difference. These formulas will be valid for all the partial derivatives of the various components of the fields whatever the direction of derivation and also compared to the time variable. Solving the different equations of the problem is then simplified and only subtractions and multiplications are used to conduct the study.

In what follows, we will use this method in order to discretize the propagation equations introduced in II.A of this chapter and then to calculate at each moment and at each position in space the value of the different fields.

### *II.B.1.c. Geometrical structures studied*

A 2D model has been chosen for the simulation in order to evade excessive memory usage and calculation time. For instance, considering the DTI network (Figure II.22), if we were to simulate this geometry in 3D we have to take the 2.47 x 2.81 $\mu m^2$ repeated pattern. Knowing this geometry has a silicon dioxide ($SiO_2$) layer of thickness equal to 7.5 nm thus, taking the space step $\Delta x$ = 7.5 nm/2 = 3.75nm as the bare minimum for stability, gives mesh size of 659 (2470 nm/3.75 nm) x 749 (2810 nm/3.75 nm). Taking the frequency as 4 GHz ($\lambda = 8433\ m.s^{-1} / 4x10^3 = 2.11\ \mu m$). As for the third dimension we will take it 11 µm (5 µm of silicon + 4 µm trench depth + 2 µm layer of liquid of air). This gives a total mesh size of 659 x 749 x 2933 (11000 nm/3.75 nm) in 3D.
Also, in 3D we have 12 unknowns to solve for: the stress matrix ($T_{11}$, $T_{12}$, $T_{13}$, $T_{22}$, $T_{23}$, and $T_{33}$) and three velocity components ($V_1$, $V_2$, $V_3$) and three space displacements ($U_1$, $U_2$, $U_3$). Compared to 2D simulation in which we have to solve for 7 unknowns ($T_{11}$, $T_{12}$, $T_{22}$, $V_1$, $V_2$, $U_1$ and $U_2$), transitioning to 3D simulation has about double the factor of calculation. Therefore, in terms of simulation time, the 3D simulation time could take: 749 (mesh size) multiplied by 2 (double unknowns) multiplied by simulation time in 2D thus, 1498 multiplied by 2D simulation time. This large time factor leads us to favor the 2D simulation.

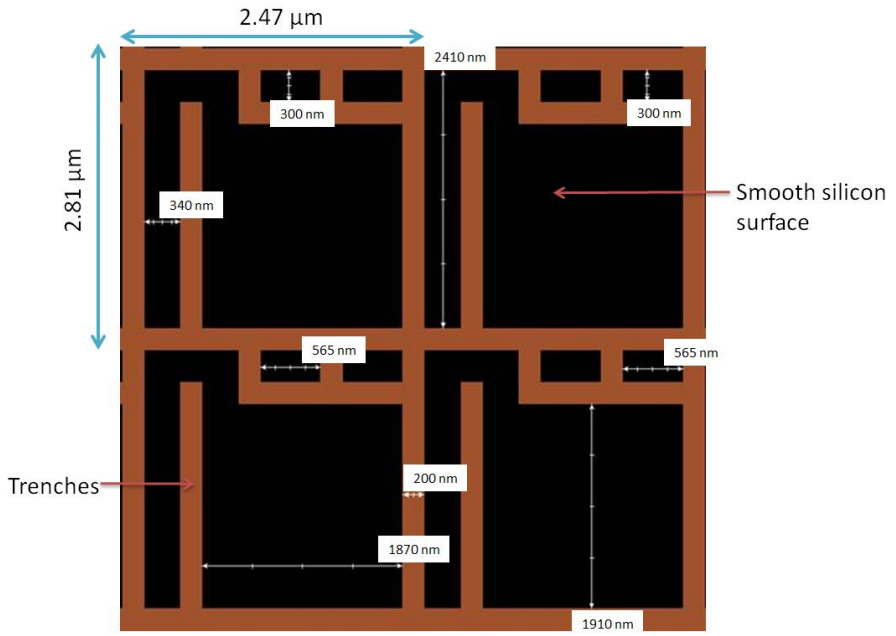


Figure II.22 Top view SEM image of the DTI network

In Figure II.23 we can see a representation of the studied geometry of the structures. This is a two-dimensional model and the third dimension of space is considered infinite. This is the situation of parallel trenches etched in silicon, of length considered infinite (i.e. infinite periodic repetition of the trenches), of width $a_b$, spaced from each other by $a_h$ and depth $e_r$. Depending on the wetting condition (Cassie or Wenzel), the trenches will be filled with air or water. The exact geometry of the DTI is given in III.E.

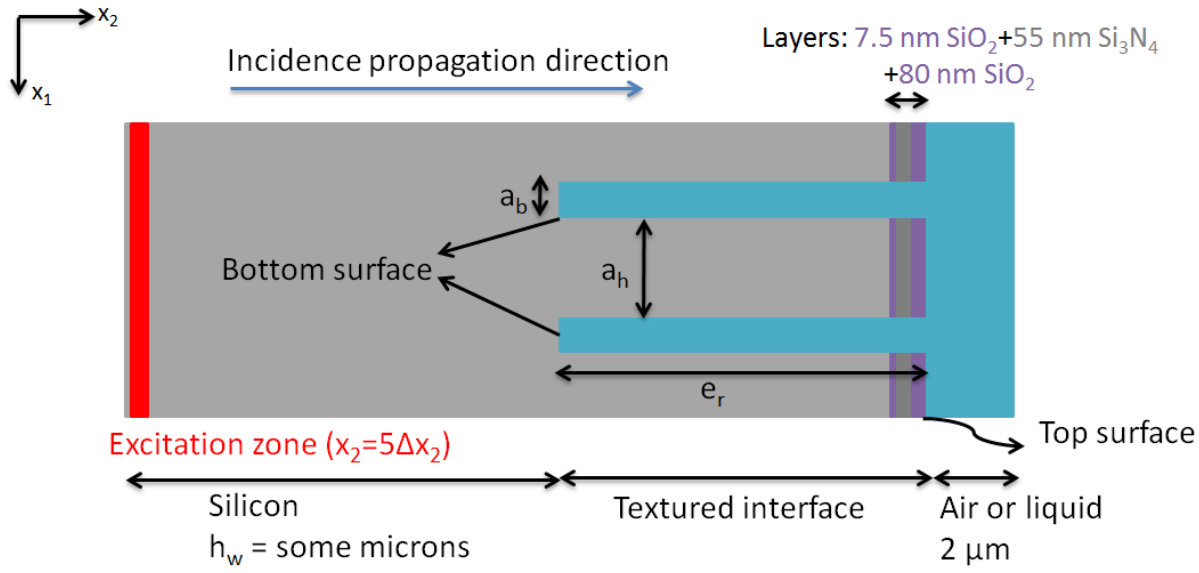


Figure II.23 Schematic of the studied geometry

The mechanical constants of the different materials constituting the geometry are:

- Silicon: $c_{11}$ = 16.56.$10^{10}$ $N.m^{-2}$, $c_{12}$ = 6.39.$10^{10}$ $N.m^{-2}$, $c_{44}$ = 7.95.$10^{10}$ $N.m^{-2}$ and $\rho$ = 2329 $kg.m^{-3}$ [90], all viscoelastic constants are taken to be zero

- Water: $c_{11}$ = 2.22.10$^{9}$ $N.m^{-2}$, $\rho$ = 1000 $kg.m^{-3}$, $\eta_{12}$ = 2.23.10$^{-4}$ $Pa.s$, $\eta_{44}$ = 1.0.10$^{-3}$ $Pa.s$, $\eta_{11}$ = 2.22.10$^{-3}$ $Pa.s$ [115]

- Silicon dioxide $SiO_2$: $c_{11}$ = 7.85.10$^{10}$ $N.m^{-2}$, $c_{12}$ = 1.61.10$^{10}$ $N.m^{-2}$, $c_{44}$ = 3.12.10$^{10}$ $N.m^{-2}$ and $\rho$ = 2203 $kg.m^{-3}$, longitudinal velocity $c_{SiO2}$ = 5800 m.s$^{-1}$ [116],all viscoelastic constants are taken to be zero

- Silicon nitride $Si_3N_4$: $c_{11}$ = 54.22.10$^{10}$ $N.m^{-2}$, $c_{12}$ = 19.34.10$^{10}$ $N.m^{-2}$, $c_{44}$ = 33.82.10$^{10}$ $N.m^{-2}$ and $\rho$ = 3930 $kg.m^{-3}$, longitudinal velocity $c_{Si3N4}$ = 12912 m.s$^{-1}$ [117], all viscoelastic constants are taken to be zero

- Air: taking into account the great discontinuity of mechanical properties with the other materials and their low values, all the constants will be taken zero except $\rho$ = 1 $kg.m^{-3}$

The initial excitation occurs at $x_2 = 5\Delta x_2$ with a direction of propagation of the wave along the $x_2$ axis. We notice that we are shifting slightly from the edge of the domain so as not to interfere with the boundary condition explained later. In order to avoid a too large number of points in space which would lengthen the computation time unnecessarily, the thickness of the silicon wafer to the left of the interface is taken only as some microns (In reality it's 785 µm) and the fluid covering the interface 2 µm. The $\Delta x_1$ and $\Delta x_2$ space steps are chosen in order to have a sufficient number of points per wavelength, generally about 100 points. In order to mesh the shape of the structure correctly space steps can differ in the two directions, according with the greatest common divisor of sub-structures.
In all cases, space steps are adjusted so that sub-structures contain a minimum of 3 points. As the mesh is conformal, in case of very thin layers, the thinner layer imposes the discretization of all the structure.
For Figure II.23, we have, $\Delta x_1 \approx \Delta x_2 = \frac{7.5\ nm}{2} = 3.75\ nm$ .
In order to ensure a stability of the calculation algorithm, the determination of the time step $\Delta t$ must verify the stability condition of Courant-Friedrich-Levy [118]:

$$\Delta t \leq \frac{1}{c_{max}\sqrt{\frac{1}{{\Delta x_1}^2} + \frac{1}{{\Delta x_2}^2}}}$$

where, $c_{max}$ is the maximum phase velocity of the different materials in the structure. In our situation, we will have $c_{max} = c_{Si3N4}$ = 12912 $m.s^{-1}$.

### *II.B.1.d. Discretized propagation equations*

In this part, only the calculation scheme is considered. The various instants will be noted by exposing components of the fields considered and the position of the space will be identified by the indices (i, j) (Figure II.21). The values of the initial conditions and of the boundary conditions will be specified subsequently.

The calculation of the different fields is based on a recurrence scheme in the time domain. The even and odd instants separated by $\Delta t$ are considered.

At the odd instant $t = (2n+1)\Delta t$ , the displacement fields ($u_1$, $u_2$ ) and velocity fields ($v_1$, $v_2$) are calculated from the previous instants, we have:

$$\begin{cases} u_1^{2n+1}(i,j) = u_1^{2n-1}(i,j) + 2\Delta t v_1^{2n}(i,j) \\ u_2^{2n+1}(i+1,j+1) = u_2^{2n-1}(i+1,j+1) + 2\Delta t v_2^{2n}(i+1,j+1)\,. \end{cases} \quad \text{Eq II-30}$$

Note that the indices of $u_2$ are different in space compared to those of $u_1$ because the grids of the two components are spatially shifted (Figure II.21).

$$\begin{cases} v_1^{2n+1}(i,j) = v_1^{2n}(i,j) + \Delta t \dfrac{\partial v_1^{2n}}{\partial t}(i,j) \\ v_2^{2n+1}(i+1,j+1) = v_2^{2n}(i+1,j+1) + \Delta t \dfrac{\partial v_2^{2n}}{\partial t}(i+1,j+1)\,. \end{cases} \quad \text{Eq II-31}$$

These two systems of equations are simply calculated using the partial derivative discretization formulas (centered and forward schemes). To calculate the velocity and displacement at the next instant, we use Newton's law and generalized Hooke's law introduced in II.A (Eq II-8 and Eq II-7).

The application of Newton's law gives:

$$\begin{cases} \dfrac{\partial v_1^{2n+1}}{\partial t}(i,j) = \dfrac{1}{\rho(i,j)}\left[\dfrac{\partial \sigma_{11}^{2n+1}}{\partial x_1}(i,j+1) + \dfrac{\partial \sigma_{12}^{2n+1}}{\partial x_2}(i+1,j)\right] \\ \dfrac{\partial v_2^{2n+1}}{\partial t}(i+1,j+1) = \dfrac{1}{\rho(i+1,j+1)}\left[\dfrac{\partial \sigma_{12}^{2n+1}}{\partial x_1}(i+1,j+2) + \dfrac{\partial \sigma_{22}^{2n+1}}{\partial x_2}(i+2,j+1)\right]. \end{cases}$$

The stresses are calculated with Hooke's law:

$$\begin{cases} \sigma_{11}^{2n+1}(i,j) = c_{11}\dfrac{\partial u_1^{2n+1}}{\partial x_1}(i,j-1) + c_{12}\dfrac{\partial u_2^{2n+1}}{\partial x_2}(i-1,j) + \eta_{11}\dfrac{\partial v_1^{2n+1}}{\partial x_1}(i,j-1) + \eta_{12}\dfrac{\partial v_2^{2n+1}}{\partial x_2}(i-1,j) \\ \sigma_{22}^{2n+1}(i,j) = c_{12}\dfrac{\partial u_1^{2n+1}}{\partial x_1}(i,j-1) + c_{11}\dfrac{\partial u_2^{2n+1}}{\partial x_2}(i-1,j) + \eta_{12}\dfrac{\partial v_1^{2n+1}}{\partial x_1}(i,j-1) + \eta_{11}\dfrac{\partial v_2^{2n+1}}{\partial x_2}(i-1,j) \\ \sigma_{12}^{2n+1}(i,j) = c_{44}\left[\dfrac{\partial u_1^{2n+1}}{\partial x_2}(i-1,j) + \dfrac{\partial u_2^{2n+1}}{\partial x_1}(i,j-1)\right] + \eta_{44}\left[\dfrac{\partial v_1^{2n+1}}{\partial x_2}(i-1,j) + \dfrac{\partial v_2^{2n+1}}{\partial x_1}(i,j-1)\right]. \end{cases}$$

With all the elastic constants $c_{kl}$ and of viscosity $\eta_{kl}$ taken in (i, j).

Finally, the partial derivatives of the displacement and velocity fields included in the stresses equation system are simply calculated by the centered discretization scheme (Eq II-27). We can now calculate at the following even instant:

$$\begin{cases} v_1^{2n+2}(i,j) = v_1^{2n}(i,j) + 2\Delta t \dfrac{\partial v_1^{2n+1}}{\partial t}(i,j) \\ v_2^{2n+2}(i+1,j+1) = v_2^{2n}(i+1,j+1) + 2\Delta t \dfrac{\partial v_2^{2n+1}}{\partial t}(i+1,j+1) \end{cases}.$$

At the following odd instant $t = (2n+3)\Delta t$ , we can calculate again the fields of displacement and velocity with the equations Eq II-25 and Eq II-26 and repeat the rest of the calculation like before. The recurrence algorithm can be summed up in Figure II.24.

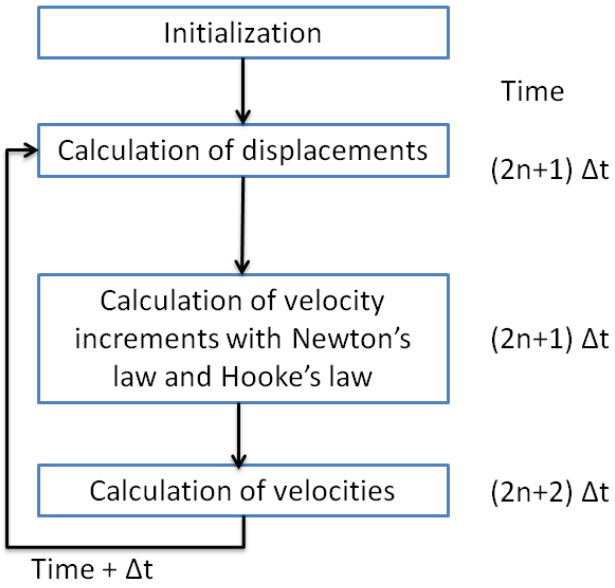


Figure II.24 Schematic of the computation recurrence of the fields of displacements, velocities and stresses

In order to avoid excessive discontinuities of mechanical constants between the different materials, the density $\rho$ is taken:

$$\rho(i,j) = \sqrt[4]{\rho(i+1,j)\rho(i-1,j)\rho(i,j+1)\rho(i,j-1)}\,.$$

This formula is also applied to all elastic and viscosity constants.

### *II.B.1.e. Boundary conditions*

In this paragraph we will introduce the conditions at the edges of the domain specifically at $x_1 = 0$ , $x_1 = 2(a_h + a_b)$ , $x_2 = 0$ and $x_2 = h_w + e_r$ .

For the direction $x_1$ the field is periodic. All the values of the fields are then taken equal in $x_1 = 0$ and $x_1 = 2(a_h + a_b)$.

For the direction $x_2$, it is necessary to avoid the reflections on the edges of the field taking into account the discontinuity of the mechanical constants of materials. To do this, we use the absorption conditions of the displacement and velocity fields. According to [119], the field of displacement and velocity at $x_2 = 0$ and $x_2 = h_w + e_r$ are equal at each odd instant:

$$\begin{cases} u_2^{2n+1} = u_2^{2n-1} + 2\Delta t v_2^{2n} + \dfrac{C\Delta t - \Delta x_2}{C\Delta t + \Delta x_2} 2\Delta t v_2^{2n} \\ v_1^{2n+1} = v_2^{2n} + \Delta t \dfrac{\partial v_2^{2n}}{\partial t} + \dfrac{C\Delta t - \Delta x_2}{C\Delta t + \Delta x_2} \Delta t \dfrac{\partial v_2^{2n}}{\partial t} \end{cases}.$$

And at each even instant, we will have for the velocity:

$$v_2^{2n+2} = v_2^{2n} + 2\Delta t \frac{\partial v_2^{2n+1}}{\partial t} + \frac{C\Delta t - \Delta x_2}{C\Delta t + \Delta x_2} 2\Delta t \frac{\partial v_2^{2n+1}}{\partial t}$$

with C the phase velocity in the material at the edges of the domains ($x_2 = 0$ and $x_2 = h_w + e_r$).

### *II.B.1.f. Excitation conditions*

Here we will determine the initial conditions of excitation on the edge of the field in $x_2 = 5\Delta x_2$.

At $t = 0$, all the fields are zero, we are at equilibrium. Then at time $t = \Delta t$ , an excitation is created on the boundary wall at $x_2 = 5\Delta x_2$. The excitation condition is only for $v_2$ because the study is done for a longitudinal excitation of the transducer, which corresponds to the real excitation. Note that the transverse wave study is also possible by performing the excitation with $v_1$.

In order to visualize the velocity field in the structure, it was preferable to choose an excitation of the finest possible width in time. Therefore, we choose an excitation which is close as possible to a Dirac pulse type excitation by reducing the width of the apodization window over time. We have:

$$v_2^t = \sin(2\pi f_0 t) H(2t) \quad for\ t \leq \frac{2}{f_0}.$$

The apodization window chosen is a Blackman window H (t) (for numerical stability) and is equal to:

$$H(t) = 0.42 - 0.5\cos(2\pi f_0\, t) + 0.08\cos(4\pi f_0\, t)\,.$$

### *II.B.1.g. Validation of the model on a smooth surface*

To verify the coherence of the model with the experimental measurements, we first study the reflection of the acoustic wave on a smooth silicon surface without the presence of the $SiO_2$ and $Si_3N_4$ layers, and then we will introduce these layers in the modeled geometry and see the variation of the reflection coefficient.

### *II.B.1.g.1. Calculation of the Silicon / water reflection coefficient*

In this part we are going to verify the value of the reflection coefficient of silicon/water on a smooth silicon wafer without the silicon dioxide and silicon nitride layers. For the calculation, we used a Dirac impulse on a silicon / air interface then silicon / water. For each case, the $v_2$ longitudinal velocity field echo diagram is recorded. In order to obtain the echo diagrams, the $v_2$ velocity field is averaged and recorded at each instant in $x_2 = 10\Delta x_2$ then we take the modulus of this value. The parameter obtained is then identified with $S_{11}(t)$ (see III.A) measured with the network analyzer. The echo diagrams are shown in Figure II.25. The total thickness of the silicon is taken as 5 µm. The separation time between the emission and the reception of the wave is $\Delta T$ = 1.21 ns. Using the velocity of longitudinal wave in silicon $c_{Si}$ (8433 m.s$^{-1}$), we can calculate the theoretical thickness of the silicon which is equal to $\frac{\Delta T c_{Si}}{2} = 5.1\,\mu m$. Thus, we find a value very close to the value entered in the modeled geometry.

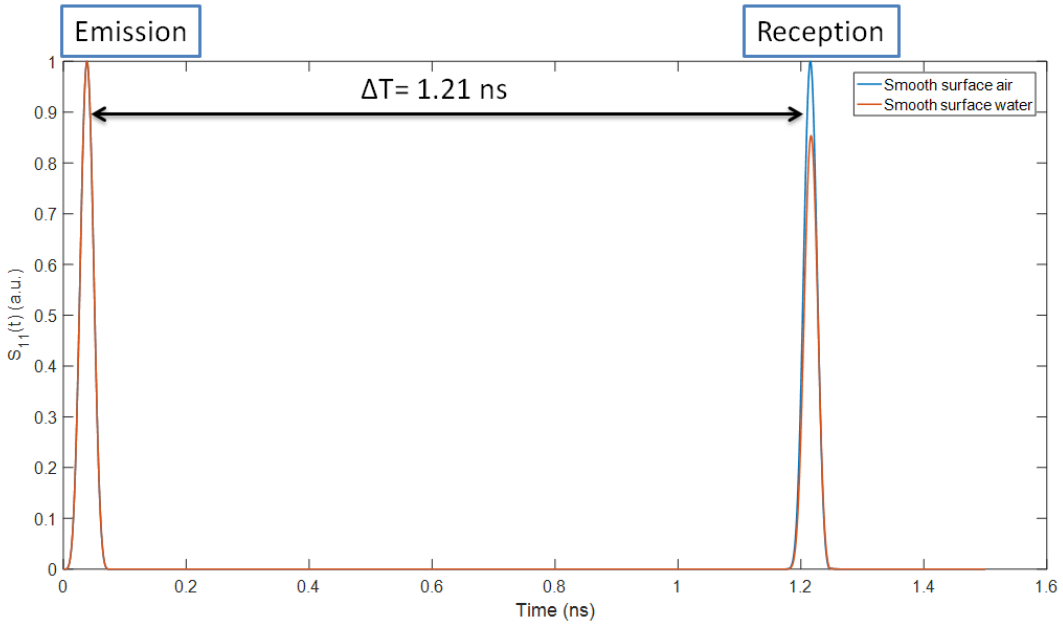


Figure II.25 Echoes diagrams on a smooth silicon interface covered with air and water

The value of the simulated reflection coefficient $r_{Si/water}^{FDTD}$ (see III.A.3 for reflection coefficient equation) is equal to the amplitude of the echo on a smooth surface exposed to water (no need to normalize in air in this case because the amplitude of the echo at air is 1). We find a value of 0.85 which is very close to the theoretical value of 0.86.

### *II.B.1.g.2. Calculation of the Si +$Si_3N_4$+ $SiO_2$ / water reflection coefficient*

Now we will see the effect on the reflection coefficient of the silicon nitride and silicon dioxide layers found on the DTI wafers. We will model a smooth surface as in the previous section. We take the thickness of the silicon as 5 µm and we add to the modeled geometry there layer which are 7.5 nm $SiO_2$, 55 nm $Si_3N_4$ and 80 nm $SiO_2$. The echoes diagram is

shown in Figure II.26. We can observe multiple echoes appearing mainly $A_{11}$, $A_{12}$. To understand these echoes we must look at the velocity field $v_2$ using images of the simulated acoustic interactions recorded at different instants (Figure II.27).

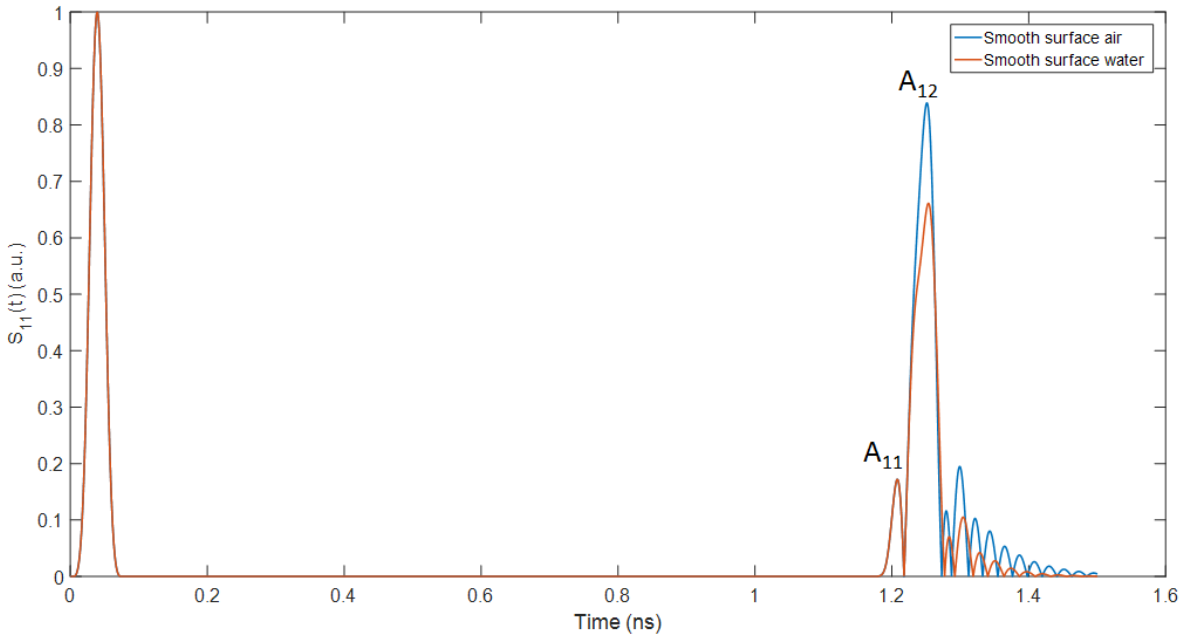


Figure II.26 Echoes diagram on a smooth silicon interface with the addition of $SiO_2$ and $Si_3N_4$ layers

In Figure II.27, the incident wave reaches the interface of the layers at instant 0.61 ns which correspond to the time for the longitudinal wave to traverse the silicon thickness ($d = tc_{Si}$ =0.61(8433 m/s) ~ 5.1 µm). At instant 0.64 ns, a reflected wave ($A_{11}$) is formed due to the passage of the wave in the layers ($SiO_2$ and $Si_3N_4$) interface and the transmitted wave reaches the air. Then, at instant 0.65 ns we can observe another reflected wave $A_{12}$ forming and traversing the layered interface. The $A_{11}$ reflected is received by the source at instant 1.21 ns and we can observe multiple reflected waves in cascade behind $A_{12}$ which are apparent in the echoes diagram (Figure II.26). Finally the $A_{12}$ reflected wave is received at instant 1.25 ns.

Between the instants 1.3 ns and 1.4 ns (i.e. in 0.1 ns) we could see 6 different echoes. Thus, each echo takes about 16.7 ps. If we calculate the round trip times in the layers (the two $SiO_2$ layers + the $Si_3N_4$ layer) we get:

$$t_{(SiO_2)_1} = \frac{2(e_{SiO_2})_1}{c_{SiO_2}} = 2.6\,ps;\quad t_{Si_3N_4} = \frac{2e_{Si_3N_4}}{c_{Si_3N_4}} = 8.5\,ps;\quad t_{(SiO_2)_2} = \frac{2(e_{SiO_2})_2}{c_{SiO_2}} = 27.6\,ps$$

where, $(e_{SiO_2})_1$, $e_{Si_3N_4}$ and $(e_{SiO_2})_2$ correspond to the thickness of the first silicon dioxide layer, silicon nitride layer and second silicon oxide layer respectively.

The 6 echoes visible on the curve which appear in a time span of 16.7 ps correspond to arrangements between the different round trips in the layers, written mathematically as:

$$16.7 = mt_{(SiO_2)_1} + nt_{Si_3N_4} + pt_{(SiO_2)_2}$$

where *m*, *n* and *p* are whole natural numbers.

A possible solution is m = 3, n = 1 and p = 0.

The value of the simulated reflection coefficient $r_{Si+layers/water}^{FDTD}$ is equal to the amplitude of the $A_{12}$ echo on a surface exposed to water divided by the same echo on a surface exposed to air. We find a value of 0.79 which is different from the experimental value we measured (0.83). This difference could be related to different thickness of the $SiO_2$ layer which can vary by a margin of 20 nm. In Table II-1 we performed two more simulations taking in each case 60 nm and 70 nm as the thickness of the $SiO_2$ outer layer while conserving all the other parameters.

We can see that for a 60 nm thickness of silicon dioxide we have a very close value of the simulated reflection coefficient to the experimental one (0.83). We can't confirm that this thickness is the precise one since we don't know the acoustic characteristics of the other layers and their precise thickness. However, this 60 nm thickness will be adopted from now on to perform the simulation since it gives result close to the experimental measurement.

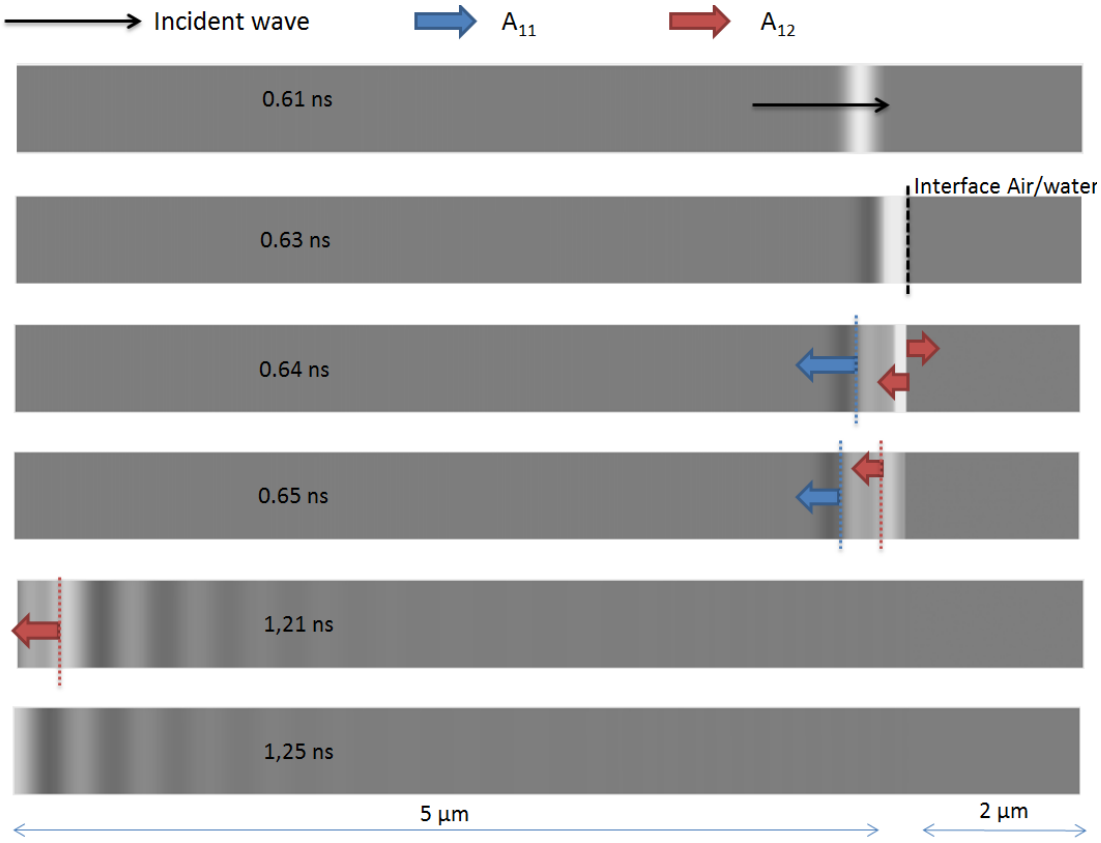


Figure II.27 Visualization of the $v_2$ longitudinal velocity field on a smooth interface with $SiO_2$ and $Si_3N_4$ layers exposed to air

Table II-1 Simulated reflection coefficient on a smooth surface with different thickness of $SiO_2$ layer

| Thickness of $SiO_2$ | 60 | 70 | 80 |
|---|---|---|---|
| $r_{Si+layers/water}^{FDTD}$ | 0.82 | 0.79 | 0.79 |

### *II.B.1.h. General results of the model*

#### *II.B.1.h.1. Separation of echoes on a micro-structured interface*

In this part we will use the FDTD model to simulate a structured interface with a thickness of 4 µm in order to separate the echoes between the bottom and the top of this interface (Figure II.23) to be able to measure the reflection coefficient on the bottom of the interface and thus determine the wetting state. The 4 µm thickness corresponds to the smallest micrometric thickness of the real DTI wafer studied. We have seen that at 3 GHz a good separation was not possible for the case of DTI trenches (Figure II.19). Therefore, we simulate with a Dirac signal (half period of a sinus 4 GHz frequency) the reflection of the acoustic wave on a micro-structured interface of thickness $e_r$ = 4 µm. The pattern width parameters are $a_b$ = 200 nm and $a_h$ = 340 nm and the unstructured silicon thickness $h_w$ = 5 µm. The echo diagram obtained is compared with that on a smooth surface in the air for identical thickness parameters (Figure II.28).

The reflection on the smooth surface appears at the same time as the second echo $A_{top}$ (top surface in Figure II.23) on the structured surface (2.2 ns). Thus, $A_{top}$ corresponds to the reflection of the wave on the top of the structured interface. At instant 1.2 ns, the $A_{bottom}$ (bottom surface in Figure II.23) echo appears which corresponds to the reflection on the bottom of the interface. Another echo $A_1$ appears at 2.5 ns. It will not be useful for determining the wetting state because the echo on the bottom of the interface has been separated. However, it can be identified by visualizing the sound field in the structure, as it will be seen in the next part.

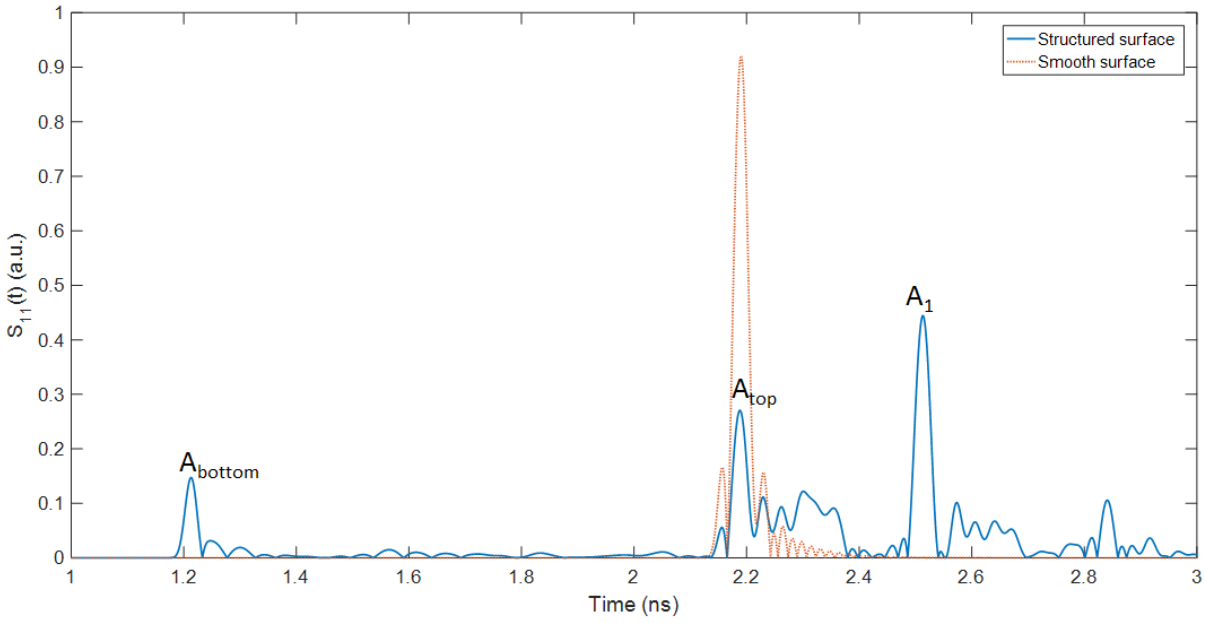


Figure II.28 echo diagrams of a micro-structured interface and on a smooth surface exposed to air

### *II.B.1.h.2. Visualization of the acoustic field on a micro-structured interface*

To visualize the field in the structure and better understand the interaction of the acoustic wave with the structured interface, again we observe the velocity field of $v_2$ at different instants (Figure II.29).

At instant 0.63 ns the incident wave reaches the bottom surface (that is on the left) of the trenches. Part of the wave is then radiated from the bottom of the trenches (0.65 ns) towards the source. These two radiated waves then recombine at instant 0.67 ns to recreate a longitudinal wave propagating towards the transducer ($A_{botom}$). The other part of the wave that is not radiated then propagates inside the interior walls of the trenches ($A_{top}$). This wave will then reflect at the top of the interface (1.13 ns) and then return to the transducer after exiting the interface at 1.590 ns. This wave has a velocity identical to a purely longitudinal wave in the structure. By considering the time $\Delta T$ between the entrance and the exit of the wave at 0.63 ns and 1.59 ns respectively, we can recalculate the thickness of the structured interface which is equal to:

$$\frac{\Delta T c_{Si}}{2} \approx 4.1\ \mu m\ .$$

This value (4.1 µm) is very close to 4 µm. The small difference could be related to the passage of the wave through the different layers ($SiO_2$ and $Si_3N_4$) found on top of the structured interface which have different longitudinal wave velocity than that for silicon (II.B.1.c).

The third echo $A_1$ does not appear immediately as the incident wave enters the structure. At instants 0.65 ns to 0.69 ns, this echo is not visible. However, at 0.67 ns, energy is radiated at 45 ° from the surface of the trench walls downstream from $A_{top}$. At 0.69 ns, the radiation reaches the wall opposite to that of emission and is re-emitted forward to form a new longitudinal-type wave at 1.13 ns. Once the wave has been formed, the distance in space between the two echoes $A_{top}$ and $A_1$ remains constant over time (instants 1.13 ns to 2 ns), which means that the velocity of the wave is that of the longitudinal wave. Regarding the amplitude of the wave, we see that it increases over time (at 2 ns the amplitude is greater than at 1.59 ns) and that of $A_{top}$ decreases over time (the amplitude at 1.59 ns is much lower than at 0.65 ns). Thus, $A_{top}$ loses energy by radiating energy backwards which is picked up by $A_1$. The other echoes appearing after $A_1$ in time are formed by the same phenomenon of back radiation. We can see that $A_1$ will also radiate energy backwards (visible at 2 ns). Different successive echoes are then formed in a cascade by this radiation of energy from the surface of the walls.

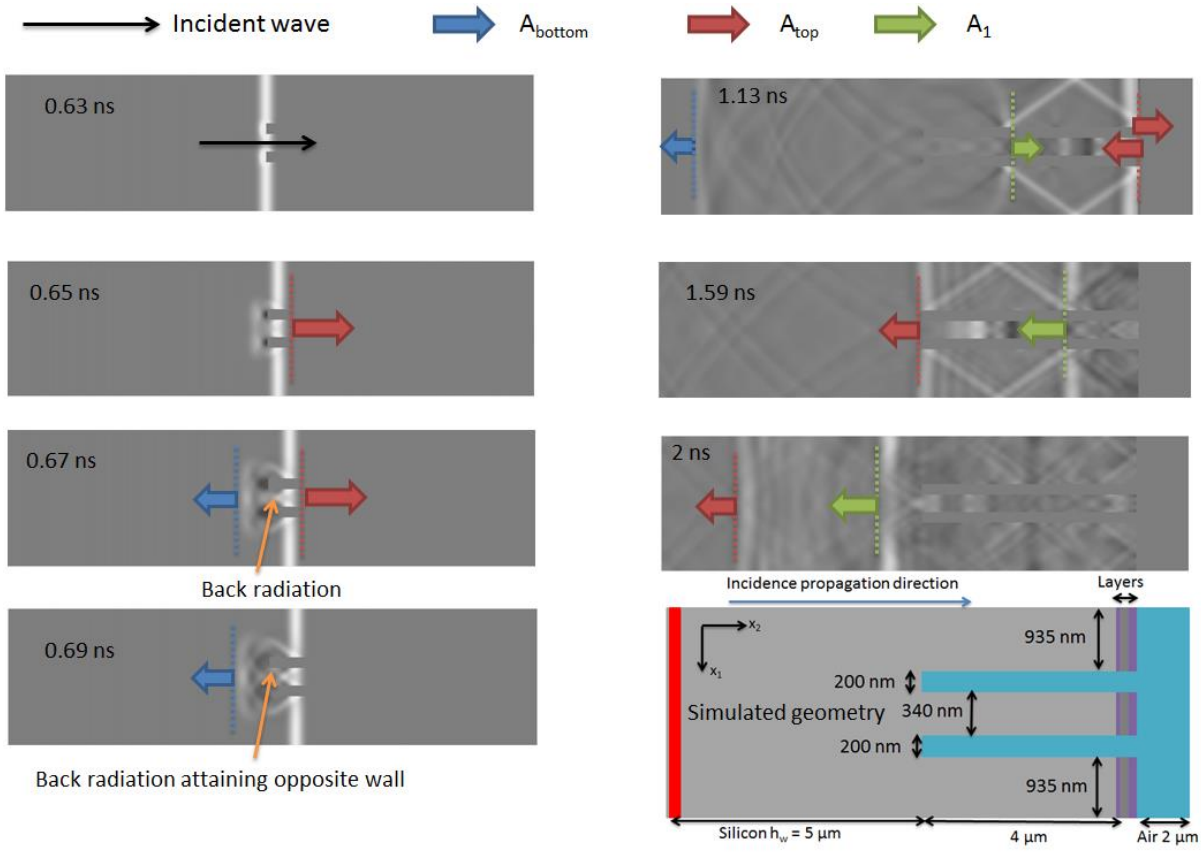


Figure II.29 Visualization of the $v_2$ longitudinal velocity field on a micro-structured interface (simulated geometry) exposed to air for a Dirac-type pulse

In chapter IV, we will see the difficulty encountered with the FDTD model in the calculation of the reflection coefficients (top and bottom of trenches) of the real DTI geometry.

## II.C. Conclusion

In this chapter, we introduced the fundamental principles necessary for understanding acoustic waves including: propagation equations, wave polarization and velocity, acoustic impedance, reflection and transmission coefficients. We also saw that for the characterization of the wetting of a micro / nanotextured surfaces, the choice of the acoustic wave turned to a longitudinal volume wave with a frequency of the order of gigahertz produced by a zinc oxide piezoelectric transducer. We also saw that none of the models identified in the literature could be directly applied for the study of wetting with the high frequency acoustic reflection method. We then introduced a model using a finite difference numerical approach (FDTD) to observe the wave propagation within the texturing when the wavelength is smaller or of the same order of magnitude as the thickness of the texturing. We used this model to see the effect of the silicon dioxide and silicon nitride layers on the reflection coefficients. Also, we saw the separation of echoes which will allow the calculation of the reflection coefficients on the bottom and the top of the structured interface. This model will be applied for the study of the wetting of DTI. In the following chapter, the method of high frequency acoustic

reflectometry as well as various experimental devices implemented to carry out the study of the wetting of textured surfaces will be presented. Also, we will introduce the concept and fabrication steps for the PolydiMethylSiloxane (PDMS) microchannels used for creating liquid flow on the silicon textured surface.

**Chapter III. Method of high frequency acoustic reflectometry and experimental setup 94**

# III. Method of High Frequency Acoustic Reflectometry and Experimental Setup

We have introduced in Chapter I the importance of wetting characterization for silicon micro/nanostructures and how it impacts the quality of the electronic products in the semiconductor industry. Also, we mentioned the importance of uniform drying of the structured silicon wafer in conserving the proper form of the micro/nanostructures. For STMicroelectronics the interest lies in the study of the cleaning (wetting state) and drying behavior of the Deep Trench Isolation (DTI) silicon structure. Therefore, the high frequency acoustic reflectometry method was then used to be able to conclude on the behavior of liquids in these critical structures.

After establishing the basics of acoustic wave propagation in the previous chapter, the reflectometry method (developed previously by Virgilio *et al.* [10]) will be studied in more detail. In this chapter, we will present the general principle of the method as well as the experimental bench and setup for the characterization of the wetting. We will also detail the way of designing piezoelectric transducers from their size to the manufacturing process used. In addition, we will present the micro-channels design and fabrication undergone during this thesis in order to establish a flow of the liquid. The aim is, to be as closely as possible to the conditions of "single wafer" cleaning process used at STMicroelectronics and to characterize the wetting and drying processes under these conditions. Thus, the design and dimensioning of the micro-channel will be presented as well as the PDMS based techniques used to fabricate and bond this micro-channel to DTI sample wafer. Finally, the liquids used for wetting characterization will be presented.

## III.A. General principle of the method

The objective is to study the wetting of the textured face (front face) of a DTI silicon wafer provided by STMicrolectronics at the micrometric or nanometric scale. This texturing is made up of trenches of 200 nm width, 4 μm – 7 μm depth. On the back side of the wafer, a zinc oxide piezoelectric transducer, deposited by cathodic sputtering at the IEMN, sends an acoustic wave of central frequency in the gigahertz range. This wave will reflect off the textured interface between the silicon and the upper medium (liquid or air) and returns to the transducer. The electrical response of the transducer (containing the acoustic reflected information) is then determined by measuring the electrical reflection coefficient of the latter using a network analyzer Figure III.1.

Wetting state characterization (Cassie-Baxter, Wenzel and intermediate states) will be done using different liquids. The electrical response of the transducer in presence of a liquid will be different to that in the case where there is no liquid (air). Acquiring the two responses (liquid / air) makes it possible to calculate the acoustic reflection coefficient and conclude about the wetting state.

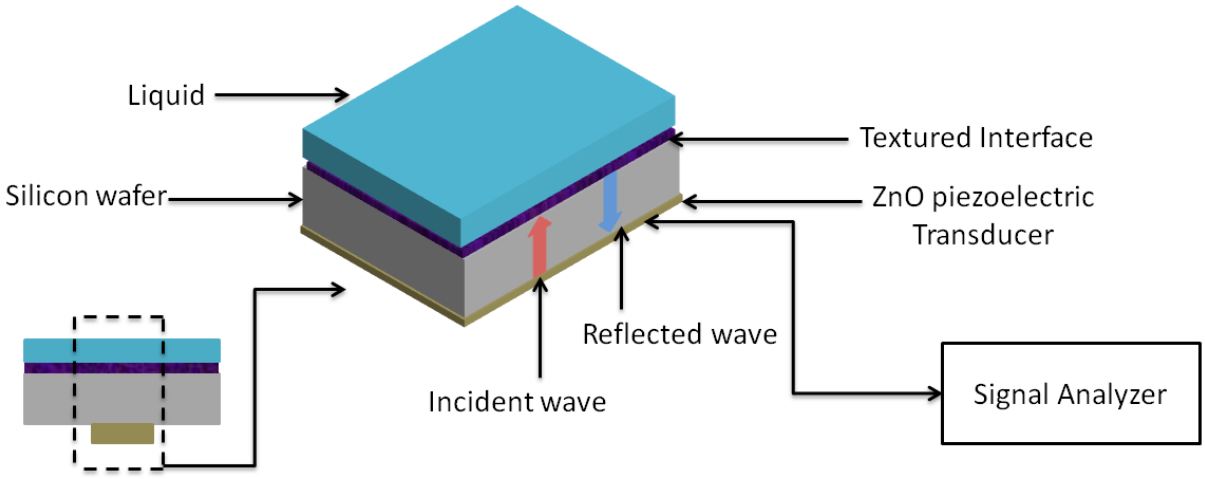


Figure III.1 Schematic showing principle of high frequency acoustic reflectometry

The network analyzer makes it possible to extract the parameter S also called the scattering coefficient or distribution coefficient. This parameter is widely used in electronics and it represents the transfer function between the input and output signals of a multipole. For a quadrupole, the linear system is given mathematically as:

$$\begin{cases} U_1 = S_{11}V_1 + S_{12}V_2 \\ U_2 = S_{21}V_1 + S_{22}V_2 \end{cases}$$

with ($U_1$ , $V_1$) and ($U_2$ , $V_2$) are respectively the (input, output) signals at each gate (Figure III.2).

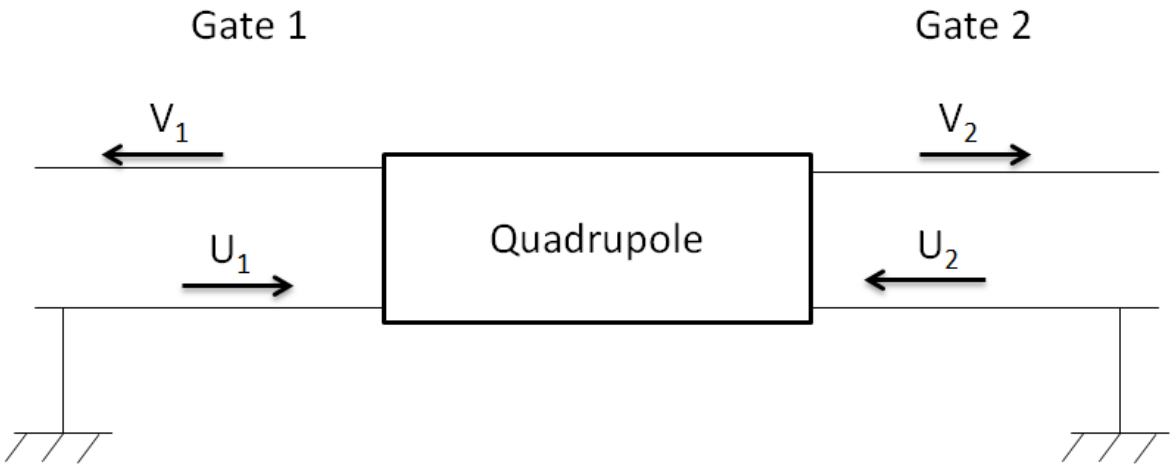


Figure III.2 Schematic of a quadrupole

For our case, one signal is emitted at the input (incident wave) and one signal is received at the output (reflected wave). Thus, the parameter that will be used is $S_{11}$, and it equal to the ratio of the incident and reflected signals at the input, it written as:

$$S_{11} = \frac{V_1}{U_1}.$$

This parameter is directly related to the transducer electrical impedance ($Z_t$) by:

$$S_{11} = \frac{Z_t - Z_0}{Z_t + Z_0}$$

where, $Z_0$ is the characteristic impedance of the transmission wire and it is equal to 50Ω.

The measurement of the parameter $S_{11}$ is done as a function of the frequency. Also, $S_{11}$ can be represented as a function of time by doing an inverse Fourier transformation. Therefore, two representations are possible to study the acoustic wave reflection. Both approaches will be used to interpret the wetting results. The representation as a function of time $S_{11}(t)$ (called echo diagram) will be preferred because it makes it possible to directly observe the transmission, reception and separation times between the different echoes and the calculation of the different reflection coefficients at each interface (bottom and top of textures). When the reflection coefficients strongly depend on the frequency of the incident wave, the analysis of the frequency signal $S_{11}(f)$ will be used.

**III.A.1. Signal treatment**

The received acoustic signal can be analyzed using Fourier transform. Let's consider an emitted acoustic signal g(t), the function G(t) = $\mathcal{F}$[g(t)] is the Fourier transform of g with $\mathcal{F}$ being the Fourier transform operator and is equal to:

$$G(f) = \int_{-\infty}^{+\infty} g(t) e^{-j2\pi ft} dt \, .$$

To find the acoustic signal in the time domain, it is sufficient to use the inverse Fourier transformation $\mathcal{F}^{-1}$ on a spectral (in the frequency domain) signal:

$$\mathcal{F}^{-1}[G(f)] = \int_{-\infty}^{+\infty} G(f) e^{j2\pi ft} df \, .$$

Starting from the measurement of the parameter $S_{11}(f)$, it is possible to calculate the signal in the time domain using inverse Fourier transformation of this parameter to obtain the echo diagram:

$$S_{11}(t) = \int_{-\infty}^{+\infty} S_{11}(f) e^{j2\pi ft} df.$$

The signal analyzer can perform this operation numerically. Figure III.3 shows an example on a silicon/water interface.

The $S_{11}(f)$ on Figure III.3.a shows oscillations around a central frequency of 1.9 GHz. The oscillations are very rapid so that we can see its periodicity and we are only able to observe one form (one color) on the graph.

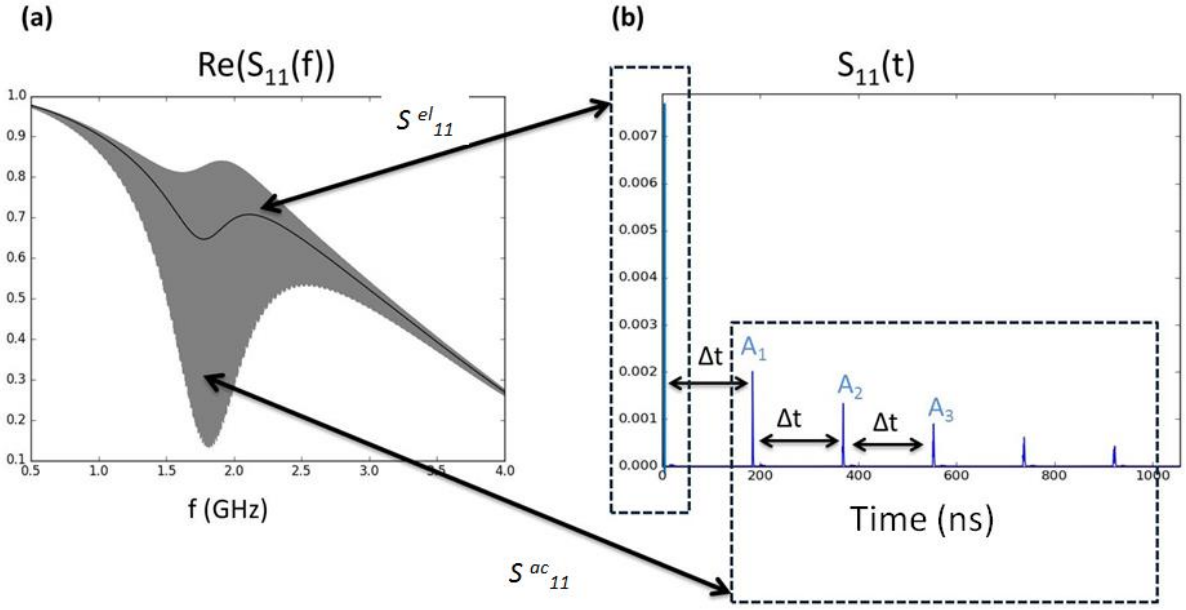


Figure III.3 Measured real part of the parameter $S_{11}$(f) of a circular ZnO transducer of thickness 1 µm with platinum electrodes of thickness 100 nm (a) and corresponding echo diagram $S_{11}$ (t) on silicon wafer of thickness 775 µm covered with water (b) [10]

At the level of the transducer, phenomena of superposition of the incident and reflected waves take place with a phase shift that varies according to the frequency. Thus, the amplitude of the total vibration measured by the transducer (amplitude of the sum of the incident and reflected wave) is greater for two waves (incident and reflected) in phase and lower for two waves in opposite phase. This phenomenon is often characterized by the standing wave ratio SWR (ratio of maximum and minimum values of total vibration). The frequency spacing of these rapid oscillations is $\Delta f = \frac{c_{Si}}{2e_w}$ with $c_{Si}$ the propagation velocity in silicon and $e_w$ the thickness of the silicon wafer. The mean value of $S_{11}(f)$ corresponds to the intrinsic response of the transducer without taking into account the acoustic reflections in the sample wafer corresponding to purely electrical response $S_{11}^{el}(f)$. The fast oscillations, which correspond to the different reflections of the acoustic wave in the sample, correspond to purely acoustic response $S_{11}^{ac}(f)$.

On Figure III.3.b we can see the inverse Fourier transform of the signal $S_{11}(f)$, also called echo diagram. This diagram represents the different reflections that take place at the silicon/water interface as function of time. The first echo with very small time delay ($S_{11}^{el}(t)$) corresponds to the reflection of the electric wave on the transducer. This reflection occurs since the transducer is not electrically adapted to the transmission cable and the delay then corresponds to that of an electromagnetic wave in the portion of cable between the calibration plane and the transducer. The other different echoes shown correspond to the round trips of the wave in the silicon wafer ($S_{11}^{ac}(t)$). The time separating two consecutive echoes $\Delta t$ corresponds to the propagation time taken by the wave to travel twice the thickness of the wafer $e_w$. Using this time and the wave propagation velocity inside the silicon $c_{Si}$, we can find experimentally the thickness of the wafer $e_w$ as:

$$e_w = \frac{1}{2} c_{Si} \Delta t \, .$$

Generally, we can write the parameter $S_{11}$ as:

$$S_{11}(f) = S_{11}^{el}(f) + KS_{11}^{ac}(f) \Leftrightarrow S_{11}(t) = \mathcal{F}^{-1}[S_{11}^{el}(f)] + \mathcal{F}^{-1}[KS_{11}^{ac}(f)]$$

with $K$ the electro-acousto-electrical conversion coefficient [120].

### III.A.2. Smooth interface

In the case where the interface is smooth with no textures, we have:

$$S_{11}(f) = S_{11}^{el}(f) + Kr_{smooth} e^{\frac{-j2\pi f.2e_w}{c_{Si}}} + K \sum_{n=2}^{+\infty} r_0^{n-1} r_{smooth}^{n} e^{\frac{-j2\pi f.2ne_w}{c_{Si}}}$$

where, $r_{smooth}$ is the reflection coefficient between the smooth silicon wafer and the medium (air or liquid) located above the front face of the wafer and $r_0$ is the reflection coefficient between the silicon wafer and the transducer which corresponds to the fraction of acoustic energy not converted into an electrical signal by the transducer (Figure III.4).

In the case where $r_{smooth}$ is independent of the frequency, we have:

$$S_{11}(t) = \mathcal{F}^{-1}[S_{11}^{el}(f)] + r_{smooth}\mathcal{F}^{-1}\left[Ke^{\frac{-j2\pi f.2e_w}{c_{Si}}}\right] + \mathcal{F}^{-1}\left[K\sum_{n=2}^{+\infty} r_0^{n-1} r_{smooth}^{n} e^{\frac{-j2\pi f.2ne_w}{c_{Si}}}\right].$$

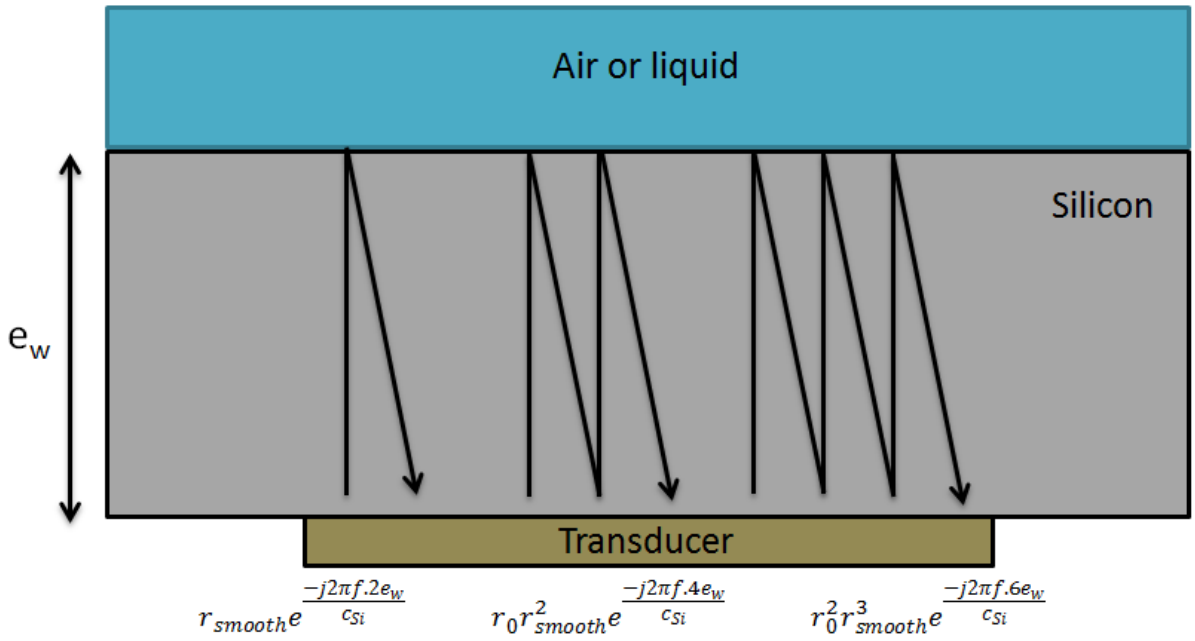


Figure III.4 Schematic of different reflections inside a silicon wafer in the case of smooth interface

Using the echo diagram we can find the value of the reflection coefficients. The useful signal that will be used for this purpose is the signal that only did one round trip inside the wafer. This signal has amplitude $A_1$ and it's given as:

$$A_1 = |r_{smooth}| \left| \mathcal{F}^{-1} \left[ K e^{\frac{-j2\pi f.2e_w}{c_{Si}}} \right] \right| .$$

The value of $K$ is unknown, thus, the direct calculation of $r_{smooth}$ in the case of liquid presence on the front face of the wafer using the above expression is not possible. An indirect method to calculate $r_{smooth}$ consists of normalizing the amplitude obtained in the presence of liquid with the equivalent amplitude obtained when the wafer is exposed to air. We have:

$$\frac{A_1^{liquid}}{A_1^{air}} = \left| \frac{r_{smooth}^{liquid}}{r_{smooth}^{air}} \right| = \left| \frac{r_{Si/liquid}}{r_{Si/air}} \right| = r_{Si/liquid} \quad (r_{Si/air} = 1) .$$

### III.A.3. Textured interface

In the case of textured interface, multiple reflections and transmission can occur at the level of the interface making the situation more complex. In Figure III.5 we can see that multiple echoes can occur with time $t = \frac{2e_w}{c_{si}}$, each echo noted $A_{1n}$ corresponds to particular reflection in the texture. The first echo $A_{11}$ on the bottom of the textures gives information about the reflection coefficient at this level and hence, the state of wetting at the bottom level of the textures. The other echoes $A_{1n,n>1}$ correspond to reflections on the top of the interface for distinct propagation modes n with propagation velocities $v_n$ and reflection coefficients $r_n$. The values of these reflection coefficients give information if the liquid is present at the vertical of the transducer. Without taking into account the electrical part of the signal and the different round trip echoes inside the wafer, the parameter $S_{11}(f)$ is written as:

$$S_{11}(f) = K r_{bottom} e^{\frac{-j2\pi f.2h_w}{c_{Si}}} + K e^{\frac{-j2\pi f.2h_w}{c_{Si}}} \sum_{n=2}^{+\infty} r_n e^{\frac{-j2\pi f.2e_r}{v_n}}$$

where, $e_r$ is the depth of the textured interface and $h_w = e_w - e_r$ .

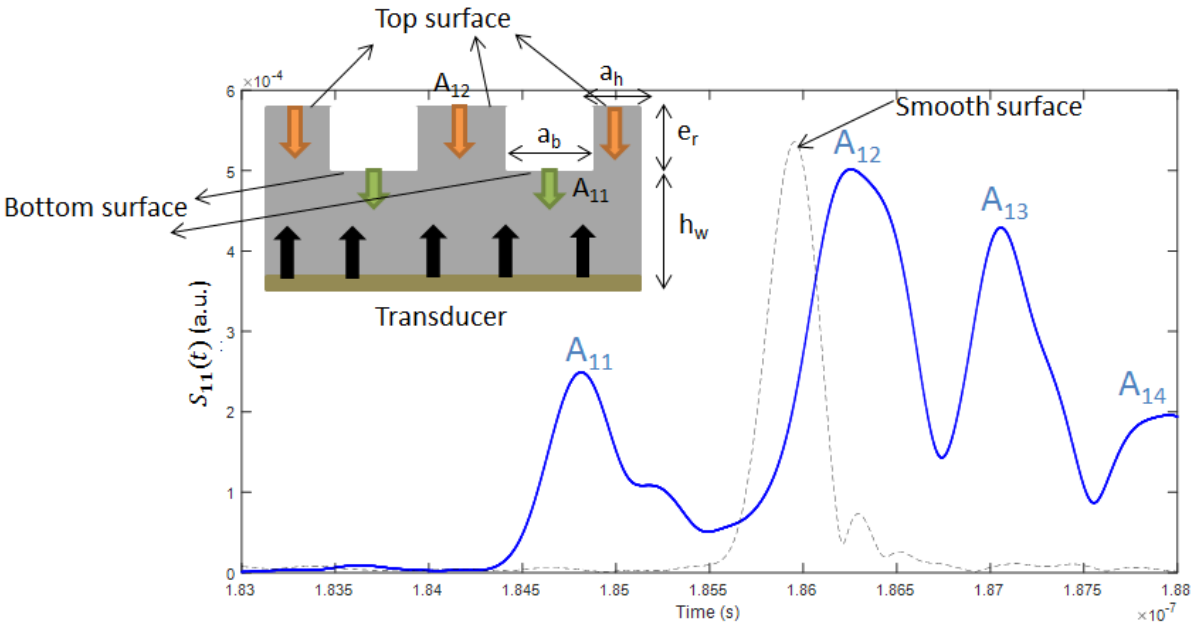


Figure III.5 Echo diagram example in the wafer exposed to air with an interface consisting of 200 nm ($a_b$) trenches and depth of 5 µm ($e_r$)

Depending on the value of the wavelength $\lambda_{Si}$ in silicon and the dimensions of the surface structures, several cases can take place:

- $\lambda_{Si} \ll e_r, a_h, a_b$ ($a_h$ and $a_b$ are shown on Figure III.5), then the propagation in the structure is considered in free wave (guided mode doesn't exists). We have: $S_{11}(t) = r_{bottom}\mathcal{F}^{-1}\left[Ke^{\frac{-j2\pi f.2h_w}{c_{Si}}}\right] + r_1\mathcal{F}^{-1}\left[Ke^{\frac{-j2\pi f.2e_w}{c_{Si}}}\right]$.

  In the presence of liquid, the reflection coefficients on the top and bottom surfaces (bottom surface corresponds to $A_{11}$ echo reflection surface and top surface corresponds to $A_{12}$ echo reflection surface (Figure III.5)) are given as:

  - In the Wenzel state (Figure I.8.a):

$$|r_{bottom}| = \frac{A_{11}^{liquid}}{A_{11}^{air}} = r_{Si/liquid} \quad and \quad |r_{top}| = |r_1| = \frac{A_{12}^{liquid}}{A_{12}^{air}} = r_{Si/liquid}\,.$$

  - In the Cassie-Baxter state (Figure I.8.b):

$$|r_{bottom}| = \frac{A_{11}^{air}}{A_{11}^{air}} = 1 \quad and \quad |r_{top}| = |r_1| = \frac{A_{12}^{liquid}}{A_{12}^{air}} = r_{Si/liquid}\,.$$

  For the water as the liquid, we have: $r_{bottom} = r_{top} = 0.86$ [121] in the Wenzel state and $r_{bottom} = 1$; $r_{top} = 0.86$ in the Cassie-Baxter state.

- $\lambda_{Si} \gg e_r, a_h, a_b$ ; The wave phase shift between the input and output is negligible. Hence, different propagation modes get mixed and a single echo is obtained. The reflection coefficient for this unique echo $A_{11}$ is written in presence of a liquid as [10]:

    - In the Wenzel state:

$$|r_{mix}| = \frac{A_{11}^{liquid}}{A_{11}^{air}} = r_{Si/liquid} \,. \qquad \text{Eq III-1}$$

    - In the Cassie-Baxter state:

$$|r_{mix}| = \frac{A_{11}^{liquid}}{A_{11}^{air}} = \varepsilon_b r_{Si/air} + \varepsilon_h r_{Si/liquid} = \varepsilon_b + \varepsilon_h r_{Si/liquid} \,. \qquad \text{Eq III-2}$$

    Where, $\varepsilon_b$ and $\varepsilon_h$ are respectively the surface area fractions of the bottom and top surfaces ($\varepsilon_h = 1 - \varepsilon_b$).

- $\lambda_{Si} \sim e_r, a_h, a_b$ ; For the intermediary cases it is difficult to predict in advance the values of the reflection coefficients on the bottom and top of the structure. FDTD simulation (discussed in chapter IV) will be used to predict the value of the different reflection coefficients.

Since $\lambda_{Si}$ and $f$ are inversely proportional, the objective is to try to use very high frequency to approach the case where $\lambda_{Si} \ll e_r, a_h, a_b$ in order to predict the state of wetting on the bottom surface of the structures easily.

## III.B. Dimensioning and performance of the transducers

The elements constituting the piezoelectric transducer are shown in Figure III.6. Before we introduce the techniques used to fabricate the transducers, the dimensions of the different layers: Platinum ground electrode, zinc oxide layer and platinum back electrode, must be determined.

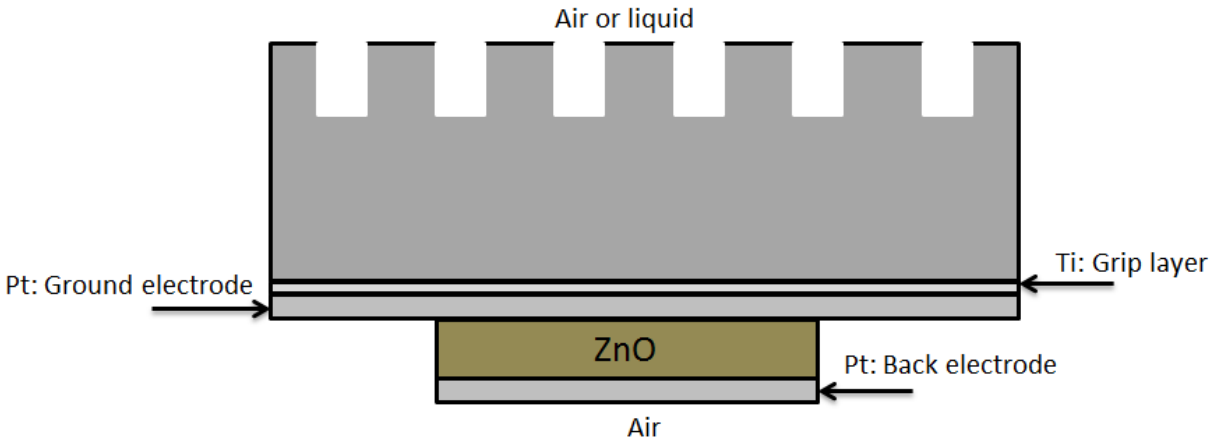


Figure III.6 Schematic of different layers constituting the piezoelectric transducer

### III.B.1. Dimensioning of the transducers

The ZnO layer, ground electrode and the back electrode are the constituting elements of the transducer and which control its resonance frequency. The objective is to theoretically obtain the optimal values of these three parameters to have resonance at a desired frequency with a signal at maximum amplitude reception. We consider the acoustic emission in semi-infinite silicon. Only the purely electrical part of the transducer impedance is thus calculated $Z_t^{el}$. Also, we remind that the elastic power supplied to the line is directly proportional to Re($Z_t^{el}$) (Eq II-24).

Christophe Virgilio performed a study for the transducer dimensioning for the high frequency acoustic characterization in his thesis at IEMN [10]. Since we adopted the same method of characterization, we list the important ideas of his findings:

- The thickness of the platinum back electrode should be as small as possible to have high resonant frequency

- The smaller the thickness of the ground electrode and the ZnO the higher the resonant frequency and the smaller the amplitude of Re($Z_t^{el}$)

- The calculation of the thickness of the ZnO and the platinum ground electrode is performed on the basis to get $\left|S_{11}^{el}(f)\right|$ attain a minimum value

- To evade the problem of electrical continuity, the thickness of the platinum should not be smaller than 50 nm.

A summary of the thickness of different layers as function of the resonant frequency is presented in Table III-1.

Table III-1 Simulation results for the optimum material thickness values as a function of the desired resonant frequency for a 100 µm diameter transducer [17]

| Frequency (GHz) | 2 | 3 | 5 |
|---|---|---|---|
| Thickness of back electrode (nm) | 50 | 50 | 50 |
| Thickness of ground electrode between the Si and ZnO (nm) | 50 | 50 | 50 |
| Thickness of ZnO (nm) | 1160 | 670 | 310 |

Another thing to note, that beyond 6 GHz, it will be difficult to increase the frequency further. To maintain a value of impedance equal to 50 Ω at resonance, the diameter becomes too small to be able to make the electric contact with the measuring tips. Consequently a high mismatch in impedance is created (Table III-2).

Table III-2 Variations of the transducer diameter as a function of the resonant frequency for a real part of 50 Ω [10]

| Frequency (GHz) | 1 | 3 | 6 | 8 |
|---|---|---|---|---|
| Diameter of the transducer (µm) | 160 | 50 | 24 | 16 |

### III.B.2. Diffraction impact

The transducer being of finite dimensions emits a wave that has finite spatial extension. A plane wave which has infinite spatial extension doesn't exist in reality. Thus, the transducer emits a wave with certain angular spectrum (Figure III.7) then, the wave is diffracted. The energy emitted by the transducer is concentrated in the central lobe which is forming at the peak an angle $\alpha$ called the beam divergence angle, written as:

$\alpha \approx \frac{\lambda_{si}}{r_t}$ if $r_t >> \lambda_{Si}$ with $r_t$ the radius of the transducer.

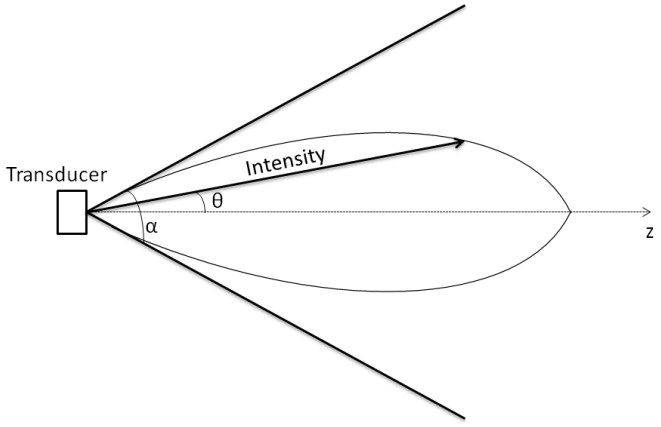


Figure III.7 Schematic diagram of the transducer radiation

We can see that $\alpha$ and $r_t$ are inversely proportional hence, the larger the radius of the transducer compared to the wavelength, the lesser the wave diffracts.

All the measurements with the presence of liquid on the wafer interface will be normalized with respect to the case of presence of air. Since, the transducer will diffract in the same way. Therefore, the energy lost in the presence of liquid due to diffraction is the same energy lost in the presence of air, and with the normalization, the diffraction will not have an impact on the measurement. For Si/liquid interface, we saw that the reflection coefficient will depend on the angle of incidence thus, the diffraction (Eq II-19). The normalization will not remove this effect which will always be present on the value of the reflection coefficient.

In the thesis done at IEMN [10], it had been shown through simulation the effect of diffraction on the value of the reflection coefficient for a transducer of diameter equal to 100 µm, here we will mention the results of that simulation. The impact of diffraction will be the highest in the case of using very small transducer with small frequency value. For a transducer of 100 µm and frequency of 500 MHz, the effects of diffraction are negligible at first order.

In order obtain the best compromise between measurement zone width, and transducer not too mismatched electrically, the diameter of 100 µm was chosen to carry out all the measurements for resonant frequencies ranging from 2 GHz to 5 GHz on bands contained within [0.5 GHz; 8 GHz].

Table III-3 shows the different dimensions of the transducers.

Table III-3 Dimensions of the transducers

| Diameter | Thickness | |
|---|---|---|
| | Electrodes (Pt) | ZnO layer |
| 100 µm | 50 nm | Depending on the desired resonant frequency: from hundreds of nanometers to some microns |

## III.C. Transverse wave generation

The high frequency acoustic characterization method was developed based on the use of piezoelectric transducers which generates longitudinal waves but, it has been shown through simulation method (which will be presented in Chapter IV) in [10] that the use of transverse waves can give more information about the wetting state inside the silicon surface textures. The simulation (simulation method presented in Chapter II) proved that through the use of the transverse waves it is possible to know the percentage of liquid inside the interface structures hence, to know if these structures are dry or how much liquid is present along their length (Figure III.8). The transverse wave makes it possible to obtain this information since its direction of propagation is perpendicular to its direction of oscillation. Thus, it interacts with

the vertical walls of the surface textures creating reflections, unlike the longitudinal wave which reflects on the top and bottom surface of the textures. The transducers that were developed in the previous work at IEMN [10], were able to generate longitudinal and transverse waves but, the signal of the transverse waves was very low and unusable.

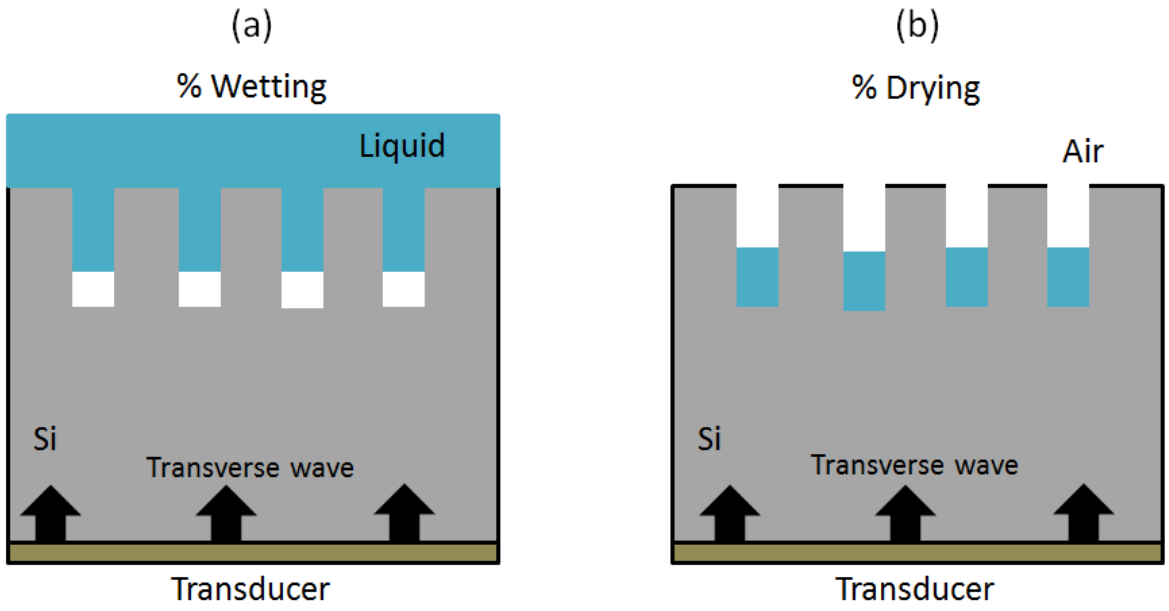


Figure III.8 Schematic of the use of transverse waves on structured interface for the study of wetting (a) and drying (b)

Here we will present a modification to the transducers fabrication process particularly the deposition of the ZnO piezoelectric layer, increasing the transverse signal generated by the transducers. First we will represent the old technique of magnetron sputtering of ZnO thin film then we will introduce the modification to this technique in order to generate higher signal of transverse waves.

### III.C.1. R.F. magnetron sputtering of ZnO

The ZnO thin film is deposited by a technique called Radio Frequency (R.F.) magnetron sputtering which is shown in Figure III.9. In a chamber under vacuum ($10^{-2}$ pa), an R.F. electric field is applied between the anode (silicon wafer on which the ZnO film will be deposited) and the cathode (ZnO material) in the presence of argon gas (inert gas). This technique is fast for depositing thin layer of a material on the surface of the wafer. The application of the electric field will ionize the gas and produce cold plasma made up of ions, electrons, photons and neutral atoms. The high-energy $Ar^+$ ions are attracted by the cathode and erodes away its surface, ejecting on impact by transfer of momentum the atoms of the material to be deposited (ZnO) on the wafer as well as secondary electrons. The atoms ejected in the direction of the substrate then condense on the wafer and the secondary electrons will transfer their kinetic energy to the neutral gas atoms allowing their ionization (the plasma is then self-sustained). The use of R.F. and non-direct current voltage is necessary for oxides materials since they require high voltages to ignite and maintain plasma.

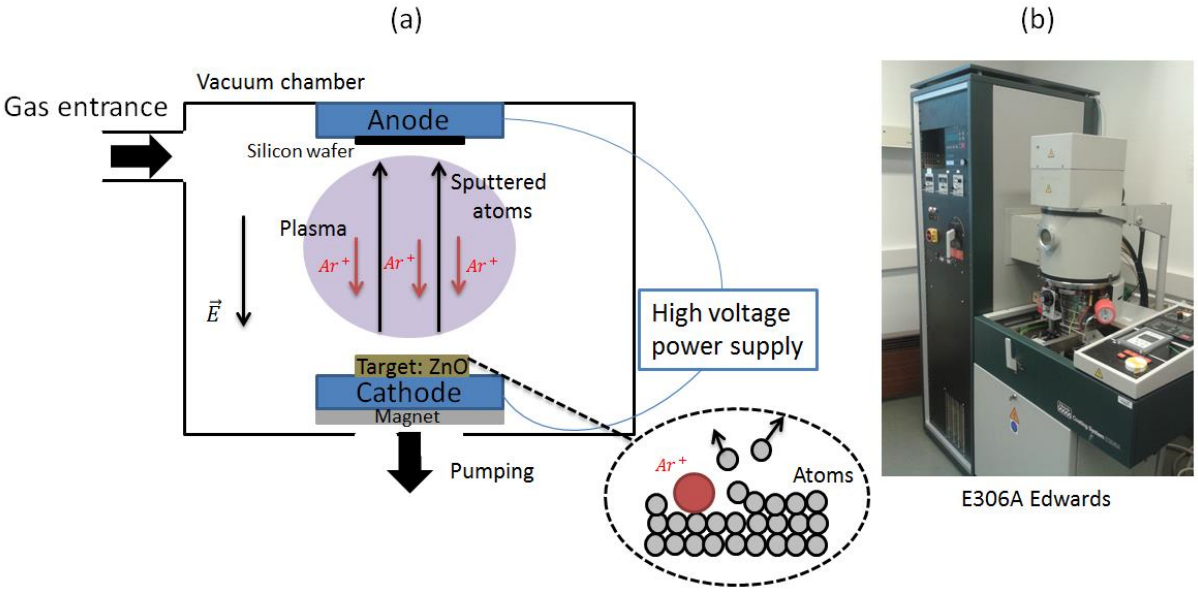


Figure III.9 Schematic of magnetron sputtering (a) and photograph of the sputtering equipment (b)

The magnets located at the cathode create a magnetic field perpendicular to the electric field and act as an electron trap that reshape their trajectory into a cycloidal path which greatly increase the probability of ionizing the sputtering gas. Also, confining the electrons can help prevent damage caused by direct impact of these electrons with the substrate or the film to be deposited. The electrons are then located at the surface level of the target (ZnO) and the amount of ionized argon atoms is therefore greater. The argon gas is used since it doesn't reacts with the other process gases and it produces higher deposition rate of the material due to the high molecular weight of argon atom.
The thickness of the deposits can range from hundreds of nanometers to several microns. Note that the thickness of the deposit will be slightly less at the edges than in the center of the sample. This inhomogeneity then causes variations in the resonant frequency of the transducer depending on its position on the sample. At the edges, the resonant frequency is greater (the amplitude of this variation will be more marked for thinner deposited films). In addition, the alignment of the ZnO crystallites is not perfectly in line with the thickness of the wafer which induces the transverse waves. Thus, during the electrical excitation of the transducer, there will mainly be a longitudinal wave emitted but also, to a lesser extent, the emission of a transverse wave will be observed.

Table III-4 shows the parameters used to deposit the ZnO film on the silicon wafers. The duration of the process depends on the thickness desired (resonant frequency).

Table III-4 Used parameters to perform magnetron sputtering

| Power | Pressure | Flow rate ratio $Ar/O_2$ | Deposition speed |
|---|---|---|---|
| 120 W | 0.02 mbar | 8 | 13 nm/min |

### III.C.2. Process adjustment: Deposition of ZnO inclined c-axis

To modify and favor transverse wave generation of the transducers, the crystallite orientation of the ZnO thin film has to be changed. One way of achieving that is the use of a blind [122] inside the vacuum chamber just above the wafer to obtain oblique incidence of the sputtered atoms in order to influence the growth of the ZnO thin film. We fixed a smooth 3 inches silicon wafer of 400 µm thickness in the vacuum chamber and then we added a rectangular blind made up of aluminum near the wafer's center (Figure III.10). The height of the blind was 30 mm and its thickness is 1 mm.

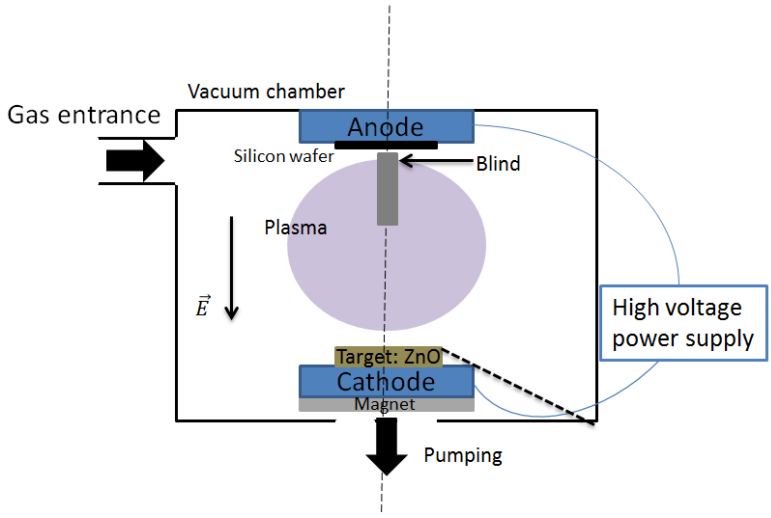


Figure III.10 Modification of the magnetron sputtering chamber with the addition of a blind between the substrate (silicon wafer) and the target

In Figure III.11 the cross-section SEM image of the deposited ZnO film is shown. We can observe that the inclination of the crystallite orientation is approximately 14.5° to the normal of the surface thus, favoring the excitation both the transverse and the longitudinal waves. Note that however, the inclined crystallite orientation is strongly dependent on the distance from the blind. The c-axis inclination will be higher in areas close to the blind or close to the wafer's edges.

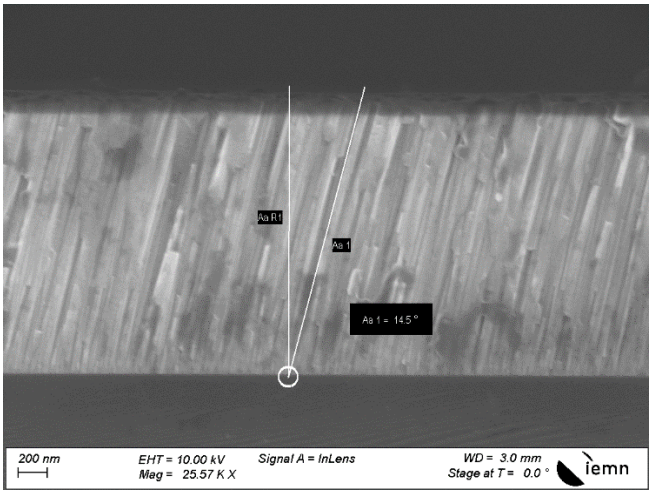


Figure III.11 Cross-section SEM image of the ZnO film with 14.5° inclined c-axis [123]

Figure III.12 shows the parameter $S_{11}(f)$ (resonance diagram) of two transducers taken on two different smooth silicon wafers, the difference is that on one of the wafers the ZnO is deposited by the addition of a blind. Figure III.12.a shows $S_{11}(f)$ parameter on transducer made without the addition of the blind, the position of the transducer is taken at the edge of the silicon wafer where the crystal orientation of the ZnO is not perfectly vertical so that we can see the generation of the transverse waves, we can see by observing this figure that most of the signal generated is related to the longitudinal waves (resonating at central frequency of 0.9 GHz) while small signal is belonging to the transverse waves. In Figure III.12.b we can see the transducer $S_{11}(f)$ parameter with the addition of a blind, we can observe clearly the two distinguished signals, one belonging to the transverse waves (resonating at central frequency of 0.8 GHz) and the other signal related to the longitudinal waves (central frequency at 1.4 GHz). By comparing signals from the two transduces It is clear that the addition of the blind create larger signal produced by the transverse waves.

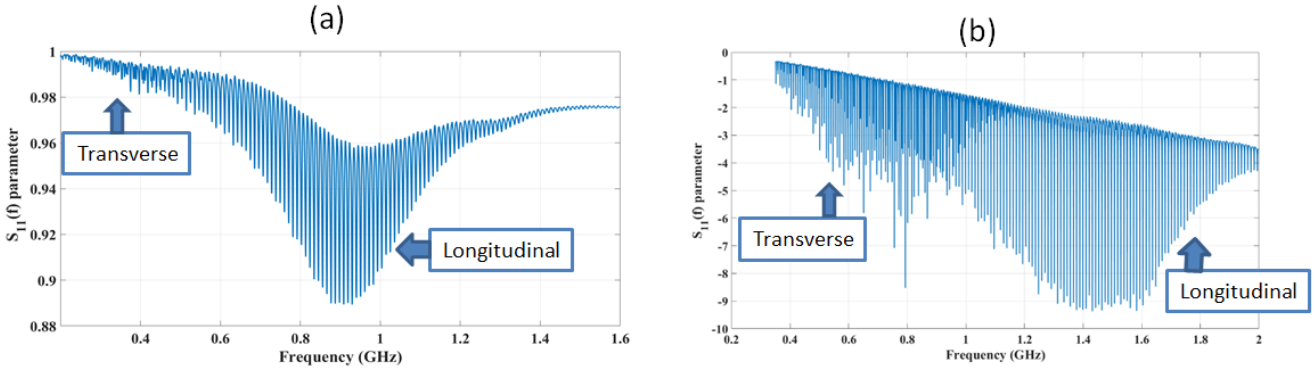


Figure III.12 Parameter $S_{11}(f)$ for a transducer (a) without a blind and (b) with the addition of a blind [123]

Figure III.13.a and Figure III.13.b represent respectively the echo diagrams of Figure III.12.a and Figure III.12.b. The echo diagram of the transducer without blind (Figure III.13.a) obtained using inverse Fourier transform over f = [0.2-1.6 GHz], shows multiple echoes with time, we are mainly interested in two the "LL" at t = 95 ns and "SS" at t=137 ns (L is the symbol for longitudinal wave and S for the transverse wave) which correspond respectively to longitudinal wave incidence and reflection and transverse wave incidence and reflection along the wafer's thickness. The longitudinal echo comes first in time since the velocity of longitudinal wave in silicon (8433 $m.s^{-1}$) is higher than the transverse wave velocity in silicon (5843 $m.s^{-1}$). We notice that the echo "LL" appears two more times at 2t = 2(95 ns) = 190 ns and at 3t = 3(95 ns) = 285 ns due to multiple reflections inside the wafer. On the other hand the multiple reflections of "SS" echo can't be seen since they have very small amplitudes. Taking the ratio amplitude ($S_{11}(t)$) of "LL" at t = 95 ns over "SS" at t = 137 ns, we get a value of 18.

Figure III.13.b is found using inverse Fourier transform over f = [0.35-2 GHz], shows the echo diagram of the transducer with the addition of a blind. Again the "LL" echo appears three times at t = 95 ns, 190 ns and 285 ns. Here we can notice the "SS" echo appears for a second time at t = 274 ns due to second reflection inside the wafer (2(137 ns)). Also, on this echo diagram we can notice a new echo "LS" at t = 232 ns which corresponds to incident

longitudinal wave propagating in the wafer and a reflected transversal wave. This “LS” echo is due to second reflection in the wafer since it’s located between the second “LL” and “SS” echoes. However, the first “LS” echo is very small in amplitude to be seen between the first two “LL” and “SS” echoes. Taking the ratio amplitude ($S_{11}(t)$) of “LL” at t = 95 ns over “SS” at t = 137 ns, we get a value of 2.

Comparing the two echo diagram, we conclude that with the addition of the blind we managed to increase significantly the amplitude of the transverse wave with respect to the longitudinal ones.

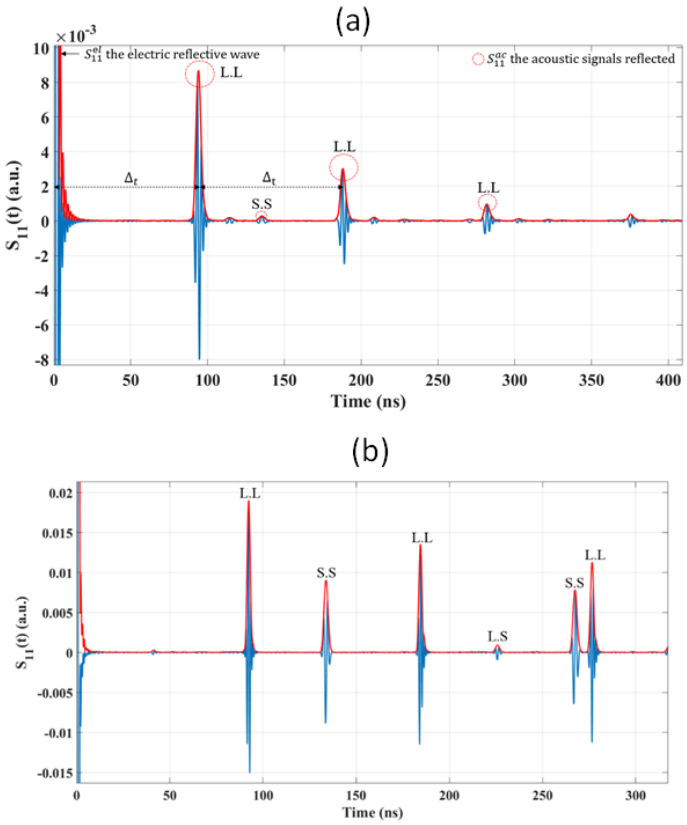


Figure III.13 Echo diagram $S_{11}(t)$ of a (a) transducer without blind over f=[0.2-1.6GHz] and (b) transducer with the addition of a blind over f=[0.35-2GHz] [123]

It is important to note that the amplitude ($S_{11}(t)$) of the reflected wave will depend on the range of chosen operating frequencies, the lower frequencies favor increase in amplitude of the reflected transverse waves and higher frequencies favoring the increase in amplitude of the reflected longitudinal waves.

In conclusion, the addition of the blind to the ZnO magnetron sputtering improves the piezoelectric transducer response in generating the transverse wave signal which was observed by amplitude increase with respect to the longitudinal waves. In what follows, we will explore the response of the transverse waves on STMicroelectronics DTI wafers.

### III.C.3. Transverse wave response: DTI wafer

The objective here is to see the transverse wave response on a textured interface. Therefore, we used a STMicroelectronics DTI wafer sample (with trench depth of 4 µm) and we deposited the ZnO film using a blind.

The medium above the DTI wafer is air and the thickness of the wafer is $d$ = 785 ± 5 µm. In Figure III.14 we can see the echoes diagram of the transverse waves. We can observe that the amplitude is very small compared to what we obtained on a smooth surface. This can be related to the diffusion of the acoustic energy inside the silicon structures (trenches network). In addition, we can observe before the echo $A_{11}$ some noise or mix of echoes which appear also between $A_{11}$ and $A_{12}$. This mix of echoes could be explained by the echo $A_{12}$ being composed of several echoes (at least two) that appear at different time delay which are very close in order to have this mix of echoes. The noises which appear before $A_{11}$ is the results of multiple reflections of the waves (longitudinal and guided wave) which are faster hence, come before in time.

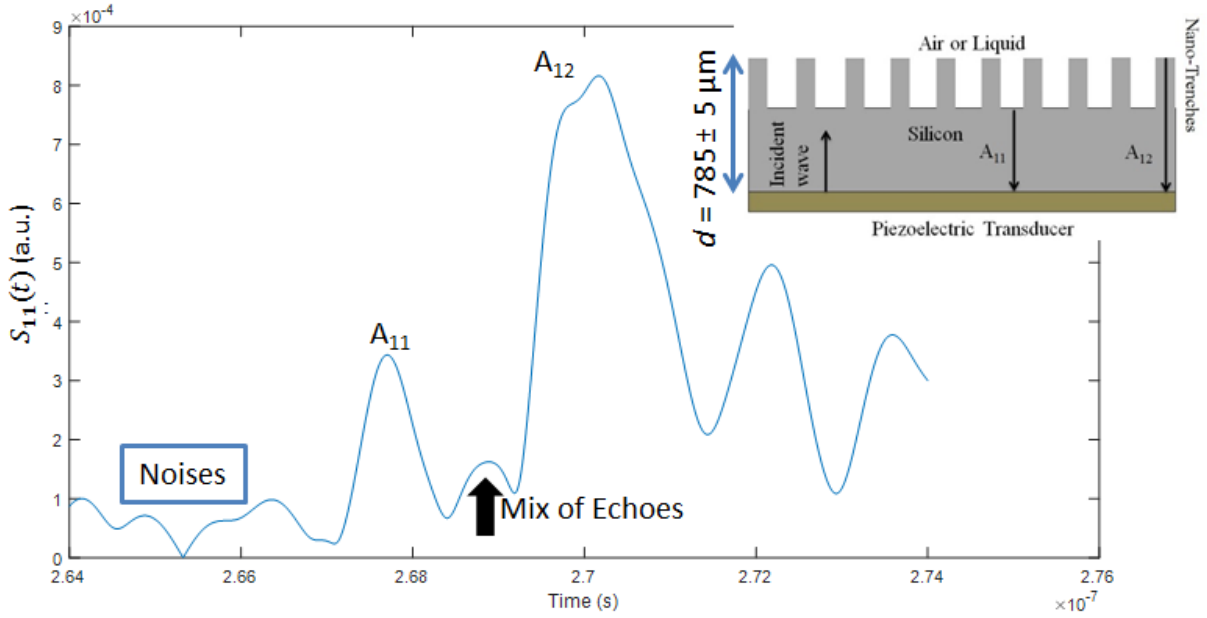


Figure III.14 Echoes diagram of a DTI (4 µm) silicon wafer with air as the medium above

Figure III.15 shows the echoes diagram on a DTI 7 µm etch depth wafer. The thickness of the wafer is $d$ = 785 ± 5 µm. Let's take $V_L$ = 8433 m.s$^{-1}$ and $V_T$ = 5843 m.s$^{-1}$ the longitudinal and transverse velocities respectively in silicon. The reflected signal is measured on two positions on the wafer's surface, at a smooth surface and at the DTI matrix. The "LL" echo at $t_{LL} = 186.1\ ns$ $\left(\sim t_{LL} = \frac{2d}{V_L}\right)$ corresponds to incident and reflected longitudinal wave on a smooth surface (red plot). At the same position, we can see the echoes corresponding to the DTI matrix (blue plot) with the amplitude significantly decreased (compared to smooth surface) due to scattering. The "TT" echo at $t_{TT} = 268.7\ ns$ $\left(\sim t_{TT} = \frac{2d}{V_T}\right)$ corresponds to incident and reflected transverse wave on a smooth surface (yellow plot). At the same position of the

"TT" echo, the reflected signal of the DTI matrix can be seen (blue plot) with the amplitude slightly decreased (compared to smooth surface). Also, an echo "LT" at at $t_{LT} = 227.4\,ns$ $\left(\sim t_{TT} = \frac{d}{V_L} + \frac{d}{V_T}\right)$ corresponds to incident longitudinal (or incident transverse) wave and reflected transverse (or reflected longitudinal) wave on the DTI matrix (blue plot). Considering the DTI matrix, we can find several echoes showing between "LT" and "TT" echoes and seem to be mixed with the "TT" echo. This may indicate reflections due to guided waves. These reflected signals between "LT" and "TT" echoes are what we call noise that makes analyzing the "TT" signal difficult.

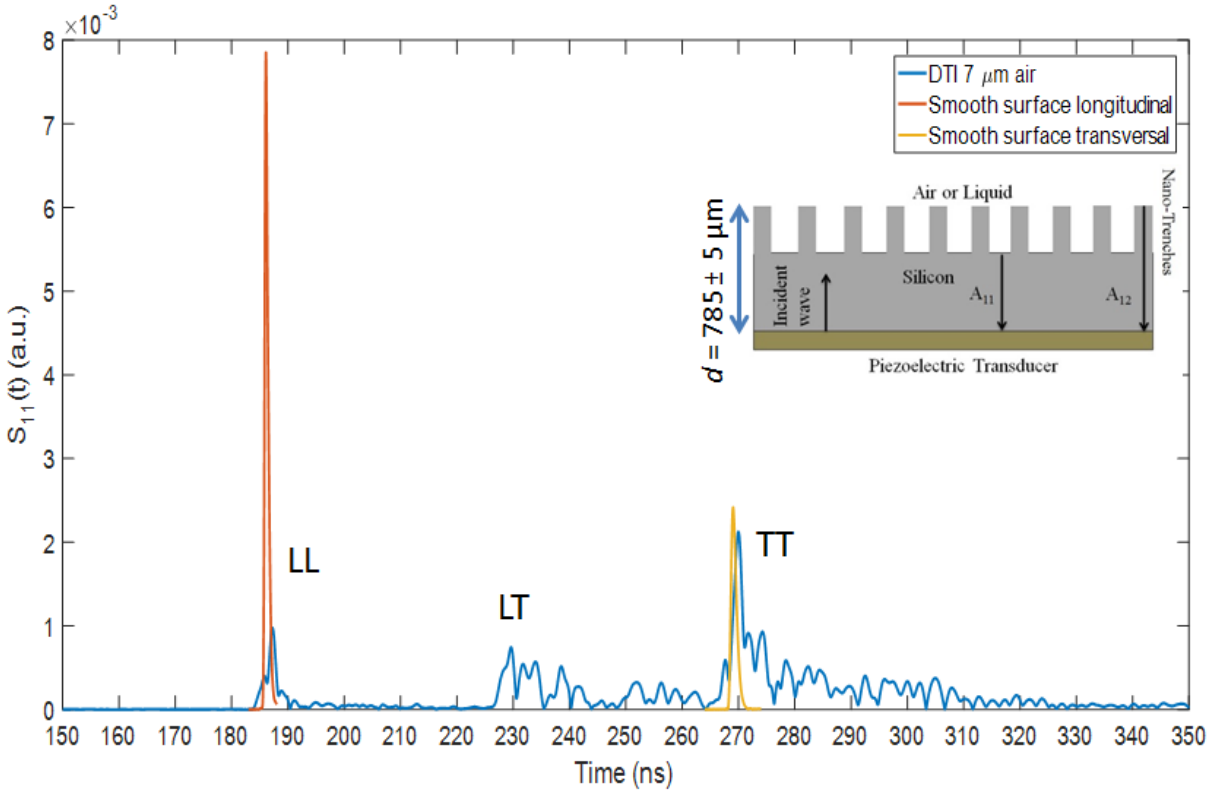


Figure III.15 Echoes diagram of the different reflected signals on DTI (7 µm) wafer exposed to air

In Figure III.16 we can see the echoes diagram the for DTI wafer of 7 µm trench depth between [264 - 276] ns. We can see the same mix of echoes that appeared on the 4 µm DTI wafer but these noises have higher amplitude. We noticed that with the increase of trenches depth the echoes mix and noises got higher making it difficult to analyze the echoes diagram.

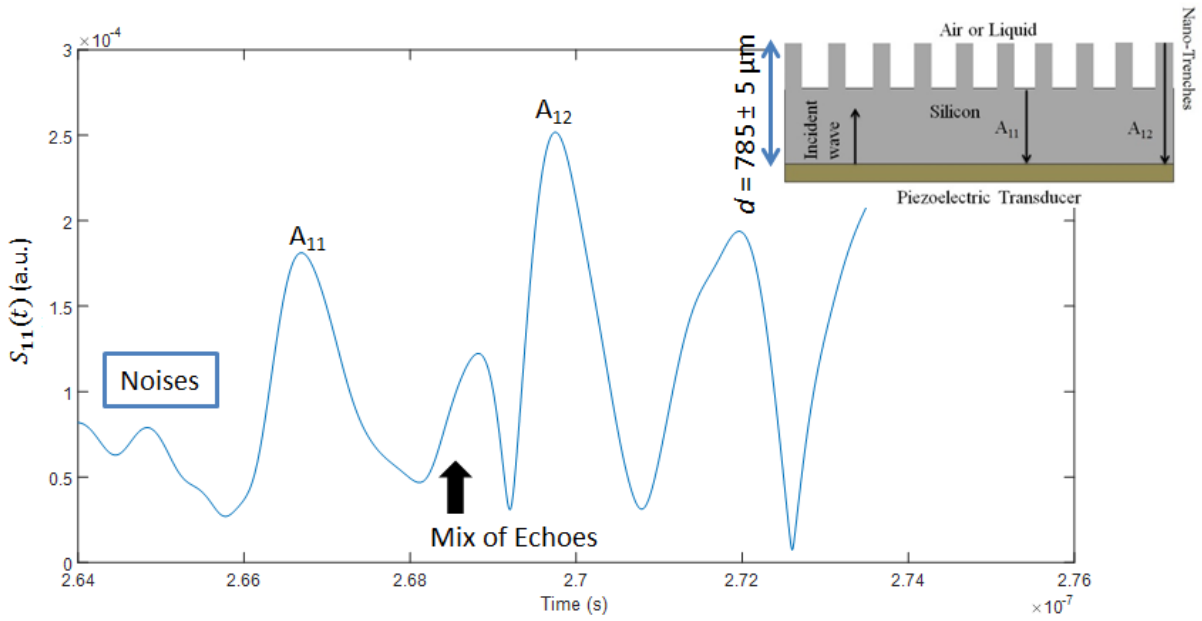


Figure III.16 Echoes diagram of a DTI (7 µm) silicon wafer with air as the medium above structured interface

In conclusion, the echoes diagram of the transverse wave on a structured interface (DTI) is difficult to analyze and extract information about the wetting state due to two reasons:

- Low amplitude compared to the longitudinal waves which leads problems with precision of measurements
- Noises and mix of echoes due to guided waves which make information extraction difficult

Due to these reasons, the focus was shifted to the longitudinal waves and the ZnO film will be deposited without the addition of the blind to get the maximum amplitude of the longitudinal mode.

## III.D. Steps of transducers fabrication

In Figure III.17 we can see the different steps used in the transducers fabrication which include:

1. Deposition by the process of thermal evaporation of bonding layer 10 nm of titanium (Ti) and 50 nm layer of platinum (Pt) ground electrode on the DTI wafer

2. Photolithography process which define the shape and size of the transducers

3. Deposition by R.F. magnetron sputtering the piezoelectric zinc oxide (ZnO) film

4. Deposition by the process of thermal evaporation the platinum (Pt) back electrode

5. Removal of the resist left on the wafer by the “lift-off” process

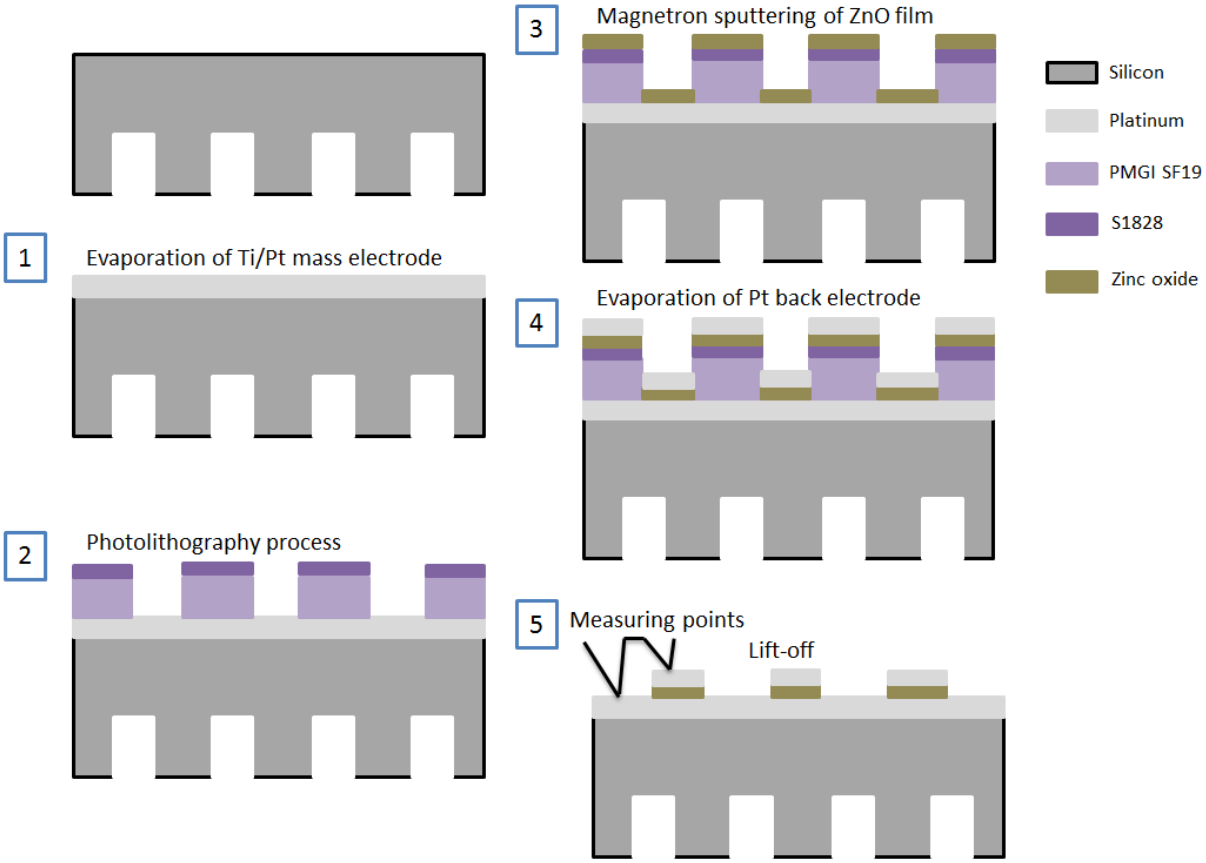


Figure III.17 Schematic of different steps included in the fabrication of the transducers

### III.D.1. Vacuum evaporation

It is a method based on physical vapor deposition (PVD). The material (in our case titanium of platinum) is placed on a crucible which is heated under vacuum ($10^{-3}$ to $10^{-4}$ pa) until it reaches the boiling point of the material. This causes the material to evaporate. The vapor is condensed on the substrate (silicon wafer in our case) which is placed vertically above the crucible to form a thin metallic layer (Figure III.18). The process is highly used to obtain metal layer of thickness ranging from some nanometers to a hundred of nanometers.

The crucible is heated by a resistor via Joule's effect. A high intensity current passes through a filament which in turn heats up the crucible. The disadvantage is the use of high powers for the highest temperatures. If the boiling point is too high to be reached by this process, an electron gun can be used. The amount of energy deployed is about 15 keV, i.e. a temperature of 174 MK. Evaporation is carried out on a MEM 550S bench (Plassys).

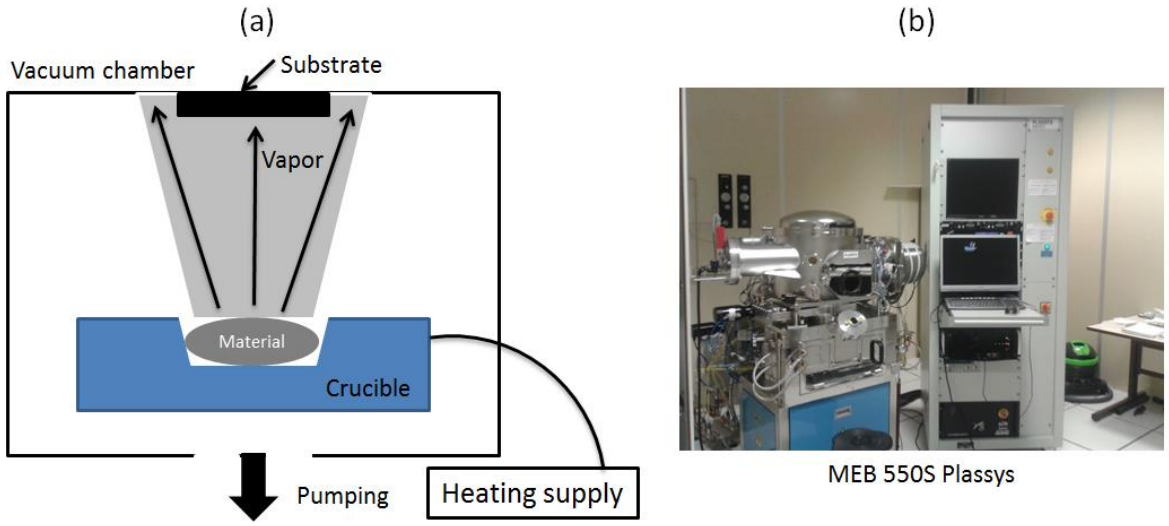


Figure III.18 Schematic of the principle of thermal evaporation (a) and picture of the evaporation bench (b)

### III.D.2. Photolithography

Photolithography known also as optical lithography is a set of processes to pattern an image from a photomask onto a medium which contains photosensitive resist. In our case, the photomask contains the shape and sizes of the transducers to be patterned on the back side of the sample (silicon wafer). These patterns are transferred to a photosensitive resist, previously deposited on the sample by spin coating, which is then exposed to UV radiation and then dissolved in a solvent (developer or stripper).

There are two forms of photosensitive resists: positive resists where the exposed areas will be revealed during development process and negative resists where the non-exposed areas will be. In our situation, a positive resist will be employed.

The photolithography process (Figure III.19) starts with the deposition of 10 nm of titanium layer and 50 nm of platinum successively by thermal evaporation process then a deposition of thick 8 µm layer of PMGI SF19 resist (Microchem Corporation) which comes in the form of viscous liquid and then dispensed by spin coating (RC8 Karl Süss) on the back of the wafer before a layer of 1.5µm of S1828 (Shipley Corporation) which is in the form of soluble liquid is added also via the spin coater process. After that, the resist is exposed to UV light using a photomask and an aligner (MA6/BA6 Süss Microtec). The next step consists of using commercial developer MF 319 (Microposit) to remove the UV exposed resist and obtain the pattern of the transducers in the resist layer.

After established the transducers patterns on the wafer, a ZnO film is deposited using R.F. magnetron sputtering process (III.C.1) then 50 nm of platinum (back electrode) is deposited on the back of the wafer using thermal evaporation process. The last step called “lift-off” is carried out to remove the remaining resist on the wafer. The sample is placed in a stripper solution called SVC-14 (Kayaku advanced materials Inc.) at 70 $^{O}$C with the action of magnetic agitator for about 3 hours. Then the wafer is cleaned with acetone bath for 5 min. The sample is then rinsed with IPA and then dried under $N_2$.

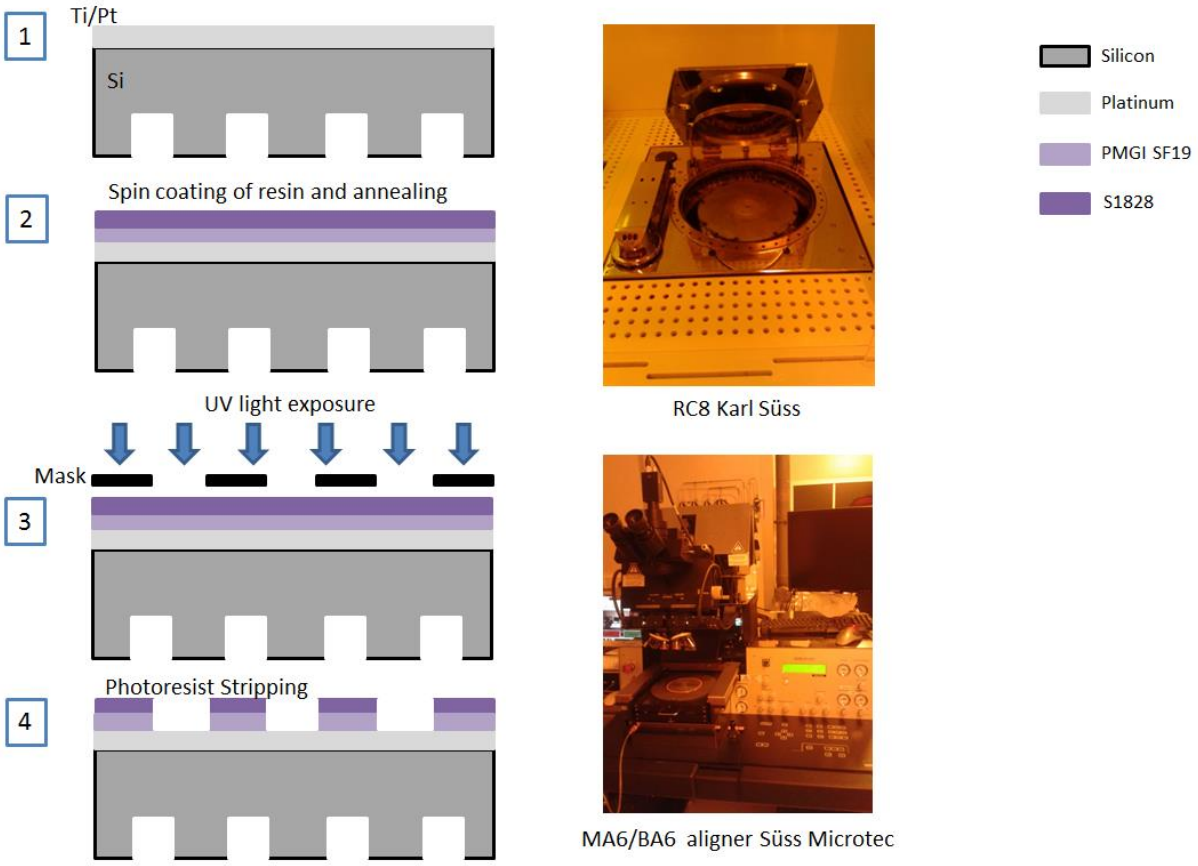


Figure III.19 Schematic of the different steps included in photolithography

## III.E. DTI structures studied

The Deep Trench Isolation (DTI) structures are made up of etched trenches inside the silicon. There are crosses of 200 nm width and depth ranging from 4 µm up to 7 µm. In Figure III.20 we can see the configuration of the trenches inside a DTI matrix, where the etched trenches are given in brown color and the black color represents the top smooth surface of the wafer. Whatever the situation, a transducer will cover multiple patterns.

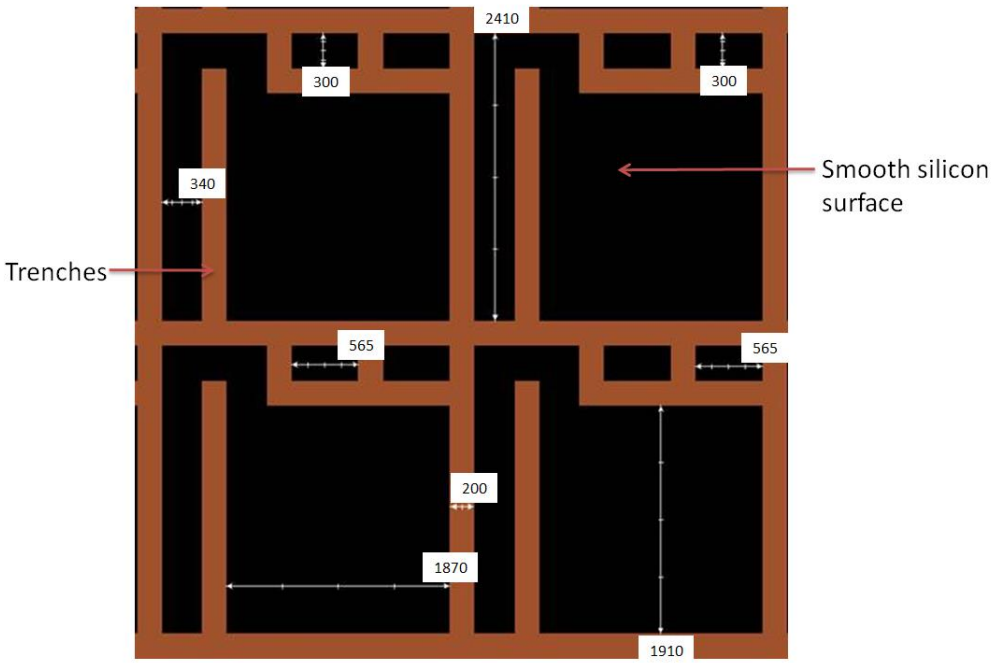


Figure III.20 Schematic of the etched trenches configuration in the DTI matrix with dimensions given in nanometers

On the DTI wafer we will choose one matrix to bond the PDMS micro-channel to it and characterize its wetting behavior. In Figure III.21 we can see two matrices chosen which have the same size (2.1 x 2.3 $mm^2$) and have also the same internal geometry of trenches (Figure III.20). These matrices have been chosen since they contain the largest concentration of bottom surface (trenches) with respect to top surface (about 20 to 25 % of bottom surface) which is important in receiving high amplitude of the reflected acoustic signal on the bottom surface.

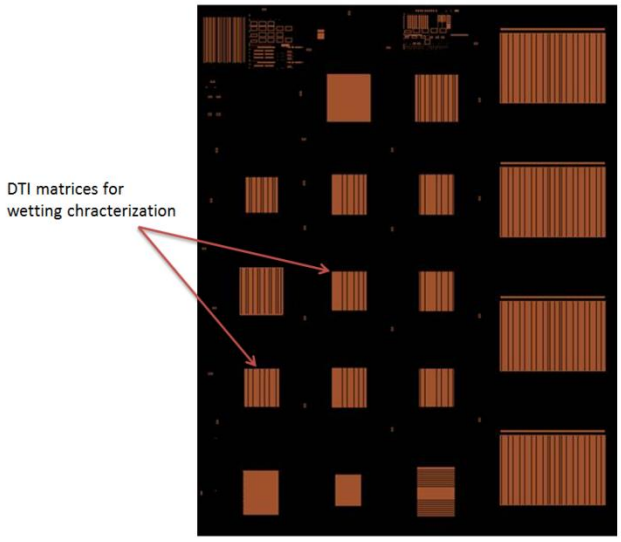


Figure III.21 Schematic of different sizes of matrices found on the DTI wafer

The wetting characterization will be done on four DTI wafers of different etch depth (4 µm, 5 µm, 6 µm and 7µm). It's important to note that on the silicon top surface of the wafer there are

three layers deposited, stacked as follows: 7.5 nm of silicon oxide ($SiO_2$), 55 nm of silicon nitride ($Si_3N_4$) and 80 nm ($\pm$20 nm depending on the wafer) of silicon dioxide ($SiO_2$). The presence of these two layers is uniquely on the top surface and not inside the etched trenches. These two layers can change the value of the reflection coefficient on the top surface of the wafer as we saw when we performed the simulation on a smooth silicon surface (II.B.1.g.2).

## III.F. Design and fabrication of micro-channels

To achieve the transition from static (droplet) to dynamic (fluid flow) wetting characterization and to approach the conditions of single wafer industrial cleaning process (Figure I.15.b), the idea of used a micro-channel was proposed. The objective is to approach the fluidic conditions used for wafers cleaning in STMicroelectronics and recreate these conditions in the micro-channel which will be placed on top of the structured interface (DTI silicon wafer) in order to characterize the wetting behavior (Figure III.22). Since we cannot make wafer rotation as done in the industrial cleaning process, to recreate the fluid flow, PolyDimethylSiloxane (PDMS) which is a transparent polymer is chosen to fabricate the micro-channel. This material is highly used in the domain of micro-fluidics [124],[125] and the techniques to prepare this polymer was already used at the IEMN. In addition, the PDMS is compatible with the different liquids that will be used through this thesis.

In what follows we will introduce the dimensioning of the PDMS micro-channel based on fluidic data coming from the industrial process. The different steps of fabricating this micro-channel will be presented.

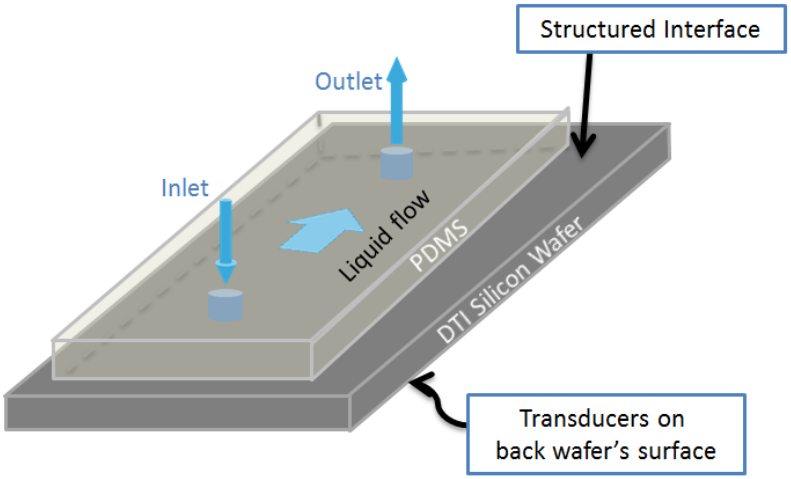


Figure III.22 Schematic of microfluidic system with PDMS micro-channel attached to a DTI silicon wafer with piezoelectric transducers

### III.F.1. Design of the PDMS micro-channel

In the single wafer cleaning process, the fluid jet coupled with the rotation of the wafer creates a fluid film of thickness "*h*" on top of the wafer (Figure III.23.a). The value of *h* is not

homogeneous and strongly depends on the position from the center of the wafer. To approach the same fluidic conditions, we will take our PDMS micro-channel height as *2h* to achieve the same fluid flow profile (Figure III.23.b), since it is a closed channel compared to the open jet system used in cleaning industrial wafers.

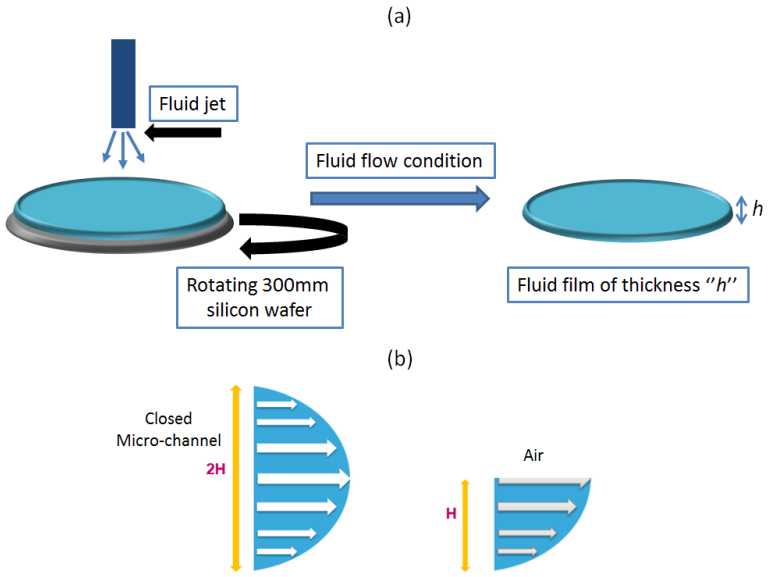


Figure III.23 Schematic of the fluid film created during the single wafer cleaning process (a) and schematic of the velocity profile in a closed micro-channel compared to the open industrial system exposed to air (b)

In Figure III.24 we can see the variation of *h* over the wafer's surface as a function of the radius and the rotational speed. For the SC1 solution used which has very close density and viscosity values as water, we can observe that *h* is the highest near the center because of the formation of a vortex below the surface of the liquid due to the passage of the liquid from a supercritical (high pressure jet) to subcritical state [126], then it starts to decrease gradually until it reaches the minimum at the wafer's edges.

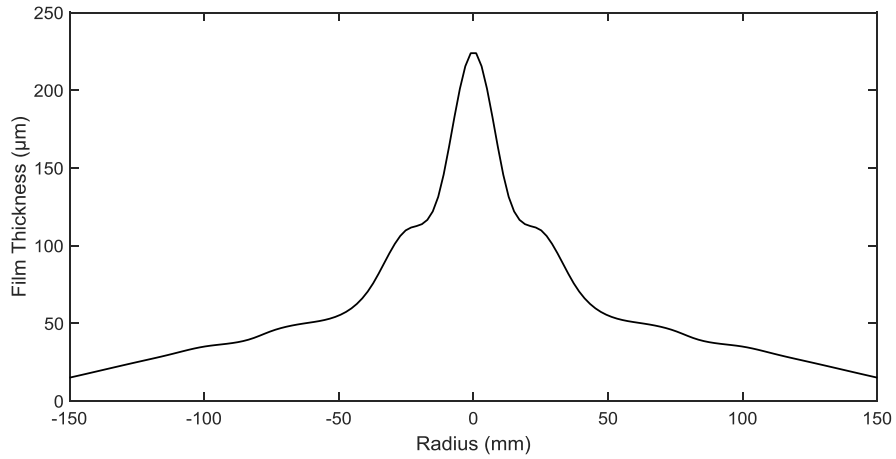


Figure III.24 Simulation of the fluid film thickness "h" as function of wafer's radius using SC1 (etching solution) as liquid and rotational speed of 1000 r.p.m. [88]

The liquid film thickness can be written as an empirical equation [127] as:

$$h = 0.782 \times Q^{0.33} \times \nu^{0.33} \times \omega^{-0.67} \times r^{-0.67}$$ Eq III-3

where, $Q$ is the flow rate [$m^3$/s], $\upsilon$ the kinematic viscosity [$m^2$/s], $\omega$ is the rotational speed [rd/s] and $r$ the radial distance from the wafer center [m].

Eq III-3 shows good agreement with the simulation results (Figure III.24) and will be used to calculate the liquid film thickness.

The radial speed of the liquid on the rotating wafer is written as [44]:

$$u_r = \frac{\omega^2 r h^2 \left[1 - \left(1 - \frac{z}{h}\right)^2\right]}{2\nu}$$ Eq III-4

where, $u_r$ the radial velocity of the fluid [m/s] and $z$ is the vertical distance from the surface of the wafer to the top of the fluid film height given as function of $h$ [m].

Here we will take the average of the radial speed so, we will integrate $u_r$ as function of $z$ from 0 to $h$ and then divide it by $h$, it will be reduced to:

$$u_r = \frac{\omega^2 r h^2}{3\nu}.$$ Eq III-5

This radial speed will be used as the liquid speed inside the PDMS micro-channel.

A 2D schematic of the micro-channel including its length and width is shown in Figure III.25. The length and width of the micro-channel have been choose respectively as 3.3 mm and 3.1 mm to cover a 2.3x2.1 $mm^2$ DTI matrix (trenches network) on the surface of the wafer. The process of fitting the micro-channel over the DTI matrix was tedious since the size of the matrix was very small and the micro-channel required careful placement in order to cover all the matrix area. Another challenge was to fit the piezoelectric transducers (100 μm in diameter) on the other face of the silicon wafer below the matrix that we will use for acoustic measurements.

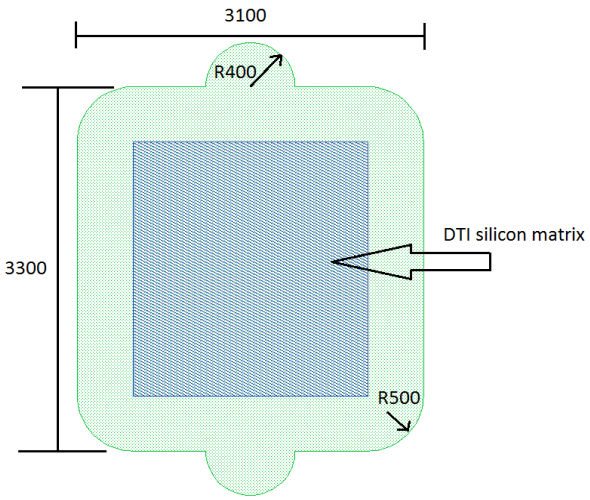


Figure III.25 2D Schematic of the micro-channel covering DTI matrix with dimensions given in micrometers

The pressure loss inside the micro-channel is calculated in order to ensure that the flow from inlet to outlet will not require high pressures due to multiple reasons that include pump specification, bonding of the PDMS to the silicon, microfluidic connections and ensuring that there is no PDMS deformation.
The characteristics of the liquid flow inside the micro-channel are given as:

$$D = \frac{2ab}{a+b}$$

$$R_e = \frac{Du_r}{\nu}$$

$$f = \frac{64}{R_e} \frac{1}{\frac{2}{3} + \frac{11}{24}\left(\frac{b}{a}\right)\left(2 - \frac{b}{a}\right)} \quad [128]$$

where, $D$ is the hydraulic diameter [m], $a$ and $b$ are the cross sectional dimensions of the micro-channel (width and thickness ($2h$) respectively) [m], $R_e$ the Reynolds number and $f$ friction coefficient.

We have then the pressure loss inside the micro-channel written as:

$$\Delta P = \rho f \frac{L}{D} \frac{{u_r}^2}{2} \qquad \text{Eq III-6}$$

with $\rho$ the density of the fluid [Kg.m$^{-3}$] and $L$ the length of the micro-channel [m].

The pressure loss for two micro-channels of approximately 40 µm and 80 µm in thickness (height) is shown in Table III-5. Both pressure losses calculated were low which shouldn't cause any issues related to the microfluidic system.

Table III-5 Hydrodynamic conditions for water at 20˚C and at industrial flow rate used at STMicroelectronics of 0.12 L/min. The corresponding pressure loss is shown for two micro-channels of ~80 µm and ~ 40 µm in thickness (2h).

| $2h$ [µm] | $Q$ [L/min] | $\nu$ [$m^2$/s] | $\omega$ [r.p.m] | $r$ [mm] | $h$ [µm] | $u_r$ [m/s] | $\Delta P$ [mbar] |
|---|---|---|---|---|---|---|---|
| 82.54 | 0.12 | 1.0e$^{-6}$ | 800 | 50 | 41.27 | 0.2 | **12.56** |
| 39.54 | 0.12 | 1.0e$^{-6}$ | 1000 | 120 | 19.77 | 0.17 | **42.34** |

### III.F.2. PMDS micro-channel fabrication

In order to fabricate the micro-channel we used PDMS which is an organic polymer that has the following chemical formula [$SiO(CH_3)$]n. The number *n* represents the siloxanes bonds and it generally affects the PDMS elasticity. For low *n* the PDMS is in the form of a viscous liquid, while for high *n* the PDMS is elastic solid.

In this work we used the commercial PDMS kit (Sylgard 184, Dow Coming) which is composed of the PDMS base and a curing agent solution. These two (PDMS base and curing agent) are to be weighed, mixed, degased and heat treated.

The different steps involved in fabricating the PDMS micro-channel are shown in Figure III.26.

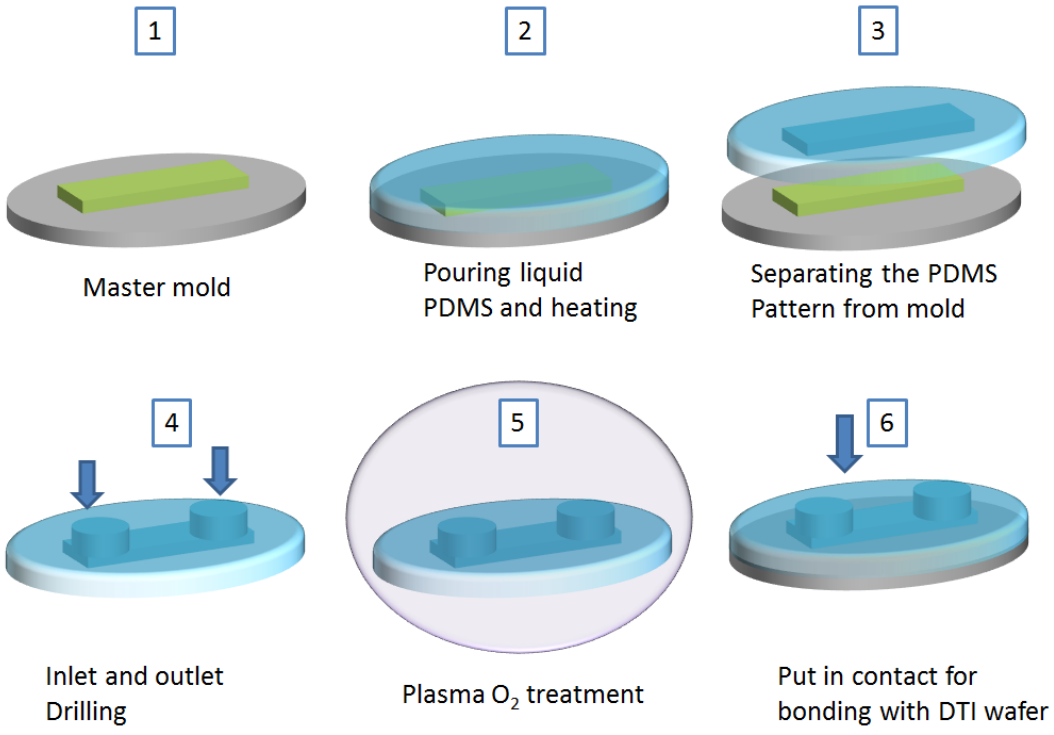


Figure III.26 Schematic of the different steps involved in making a PDMS micro-channel

The process starts with a master mold which defines the dimensions and thickness of the micro-channel. This mold is made on a 3 inch smooth silicon wafer with a process called laser lithography.

The laser lithography (Appendix A) process was used due to its rapid fabrication time compared to classical photolithography; instead of the fabrication of an optical mask, the design of a software based mask is needed.

The process starts with the deposition of a 2 µm layer of SU-8 2002 (Kayaku advanced materials Inc.) resist (which serves as a bonding layer between the silicon and the mold resist that will deposited later) on the smooth silicon wafer by spin coating, then annealing takes place to harden the resist.

Then another resist layer SU-8 2035 or SU-8 2075 (Kayaku advanced materials Inc.) is deposited by spin coating and annealing step is also taken to harden the resist. The choice of the resist and the thickness both depend on the desired thickness of the micro-channel, for the 40 µm micro-channel, SU-8 2035 was used and SU-8 2075 was taken for the 80 µm one.

After depositing the resist, the wafer is passed to the direct laser bench KLOE Dilase 650 (Figure III.27). A GDS file, created by CleWin layout editor, detailed the micro-channel pattern to be written. Through an optimization of the laser processing, the writing speed was fixed to 30 $mm.min^{-1}$, wave length of 375 nm and 100% laser power.
The power and the laser writing speed had to be adjusted multiple times to avoid cracks in the resist (See Appendix A.3).

The final step includes the heating of the wafer to make the patterned (by laser) resist soluble. Then the wafer is placed in a MicroChem's SU 8 developer solution where only the resist areas unexposed to laser are removed.

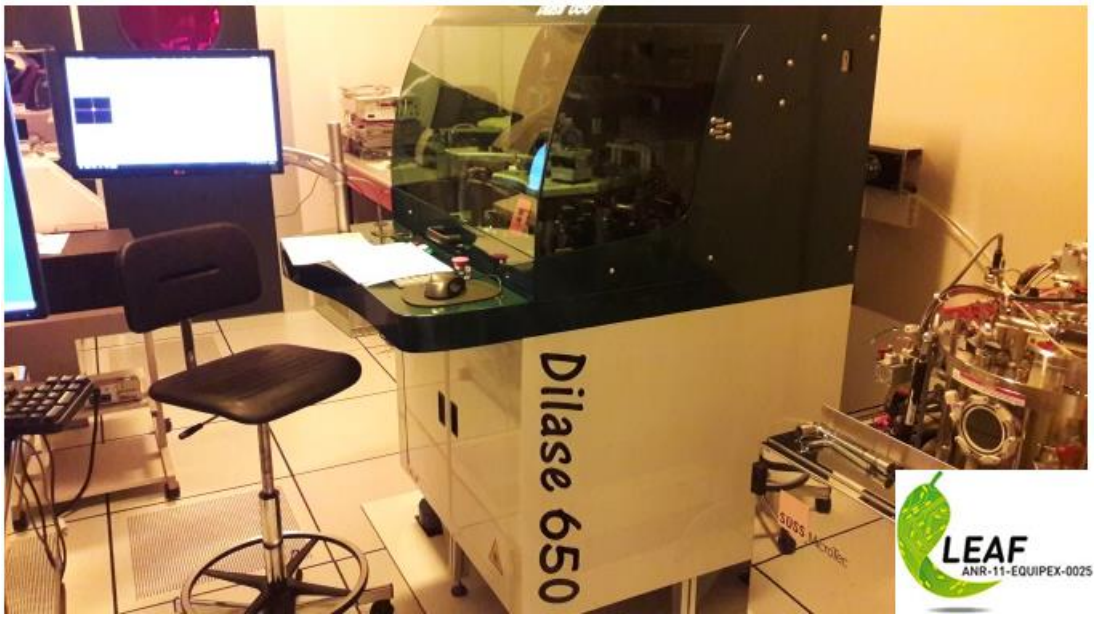


Figure III.27 Direct laser bench KLOE Dilase 650

After preparing the mold, the next step is preparing the PDMS mixture. First we add 30 g of the PDMS base into a cup then we add 1/10 of the amount PDMS curing agent into the same cup (3 g). Then the cup is putted into a planetary mixer (ARV310, Thinky USA, INC) (Figure III.28.a) for about 1 minute under a vacuum pressure of 30 KPa and a rotational speed of 2000

r.p.m. The purpose of this operation is that, both liquids (base and curing agent) will be properly mixed and that the air bubbles in the resulting solution will be also removed under vacuum.

The PDMS solution is then poured on the mold and put in an oven at 70 $^{O}$C for 3 hours to polymerize the PDMS. After the heating process, the PDMS which contain the micro-channel pattern is detached from the mold. Then the inlet and outlet of the micro-channel is drilled into the PDMS using a biopsy punch with diameter equal to 2 mm.

Next the surface of the PDMS micro-channel is treated with Electro-Technic Products (Chicago, IL) hand-held corona plasma discharger (Figure III.28.b) for 1 minute. A high voltage applied to the equipment electrode creates a plasma “corona” discharge in the small ambient atmosphere between the electrode and the treated surface. The treatment removes organic, hydrocarbon material by chemical reaction with reactive oxygen radicals and ablation by energetic oxygen ions. The result is silanol (SiOH) groups created on the surface (Figure III.29).

Then the PDMS micro-channel is immediately placed over the DTI silicon wafer at the specified position in order to cover the DTI matrix. Upon contact, a bridging bond Si-O-Si is created at the interface making an irreversible seal. Note that the surface of the DTI wafer was not exposed to the plasma $O_2$ since it can transform the surface to hydrophilic changing its wettability. The last step includes heating the DTI wafer in an oven at 70 $^{O}$C for 1 hour to strengthen the bond with PDMS micro-channel.

It is good to note that the fabrication process of a single DTI wafer with transducer and micro-channel can take up to one to two weeks to be ready for measurements. This is due to the number of required steps included in the fabrication processes. Another point is that some equipment are found at different locations (two different laboratories) requiring lot of displacement to prepare the sample.

(a) (b)

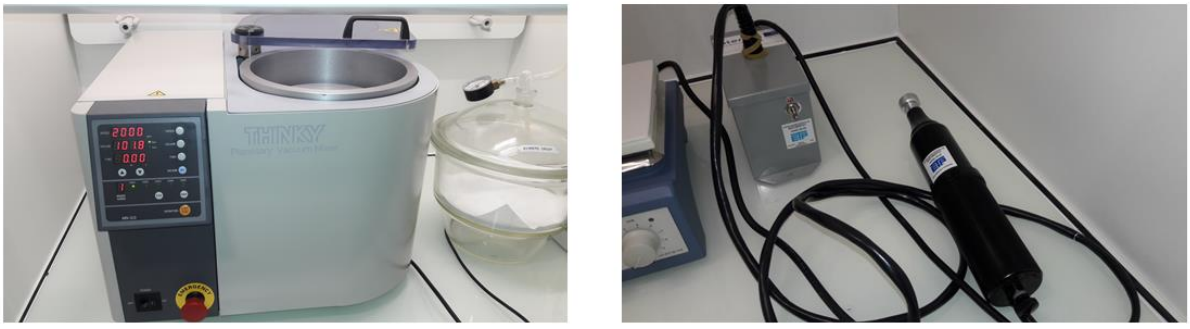


Figure III.28 Photograph of Thinky mixer used to prepare the PDMS (a) and plasma $O_2$ equipment used to bond the PDMS micro-channel to the DTI silicon sample (b)

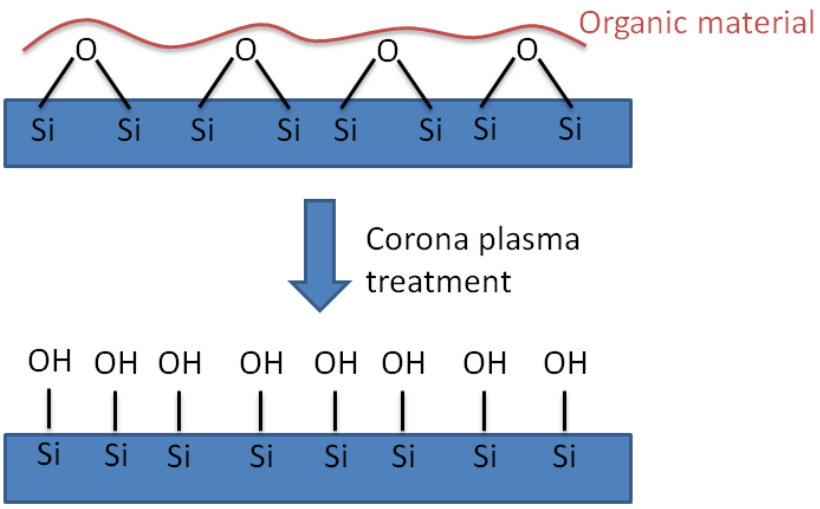


Figure III.29 Schematic of surface cleaning by plasma $O_2$

## III.G. Measurement Bench and protocols

In this section we are going to introduce the different equipment used for the wetting characterization of the DTI. The next part will deal with the protocols used for measurements over structured silicon interface in both time and frequency domains.

### III.G.1. Measurement bench

The acoustic measurements are done using a bench called "Backside prober" where the measurement points are placed on the back face of the wafer. The DTI wafer will be placed in a way that the structured interface where the PDMS micro-channel is bonded is visible during the measurements. This constraint results in an arrangement of the piezoelectric element (the transducers) under the visible face of the sample. The electrical contact on the transducer will be made using a measuring point (tip) placed under the sample. Its positioning is done using a camera also located under the sample which allows the micrometric displacements of the measurement point (Figure III.30). Also, the holder in which the DTI wafer is placed on has suction holes to prevent the movement of the wafer, since the contact between the tip and the transducer can be affected by the slightest movement of the wafer.

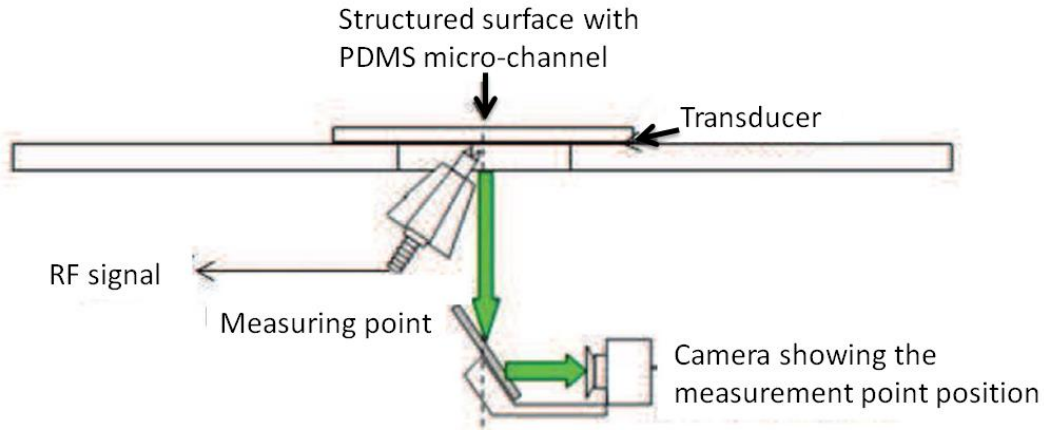


Figure III.30 Schematic of the setup used to position the measurement point [10]

The measurement is carried out using a "ROHDE & SCHWARTZ" type ZVA 8 network analyzer with a frequency band of up to 8 GHz. The microfluidic system MFCS-FLEX (from Fluigent company) controls the flow of liquid by varying the pressure from some mbar up to 1 bar. The liquid will be feed to the micro-channel at a pressure of 300 mbar through a series of microfluidic tubes then air will be sent at a pressure of 1 bar to dry the liquid from the micro-channel. Another fluidic pump called Agilia syringe pump (Fresenius Kabi AG) (Figure III.32) capable of injecting liquid into the micro-channel at flow rates varying from 100 $\mu l.h^{-1}$ up to 120 $ml.h^{-1}$, will be used to inject the liquid into the micro-channel at different flow rates as we will see in Chapter V. Figure III.31 shows the entire diagram of the measuring bench.

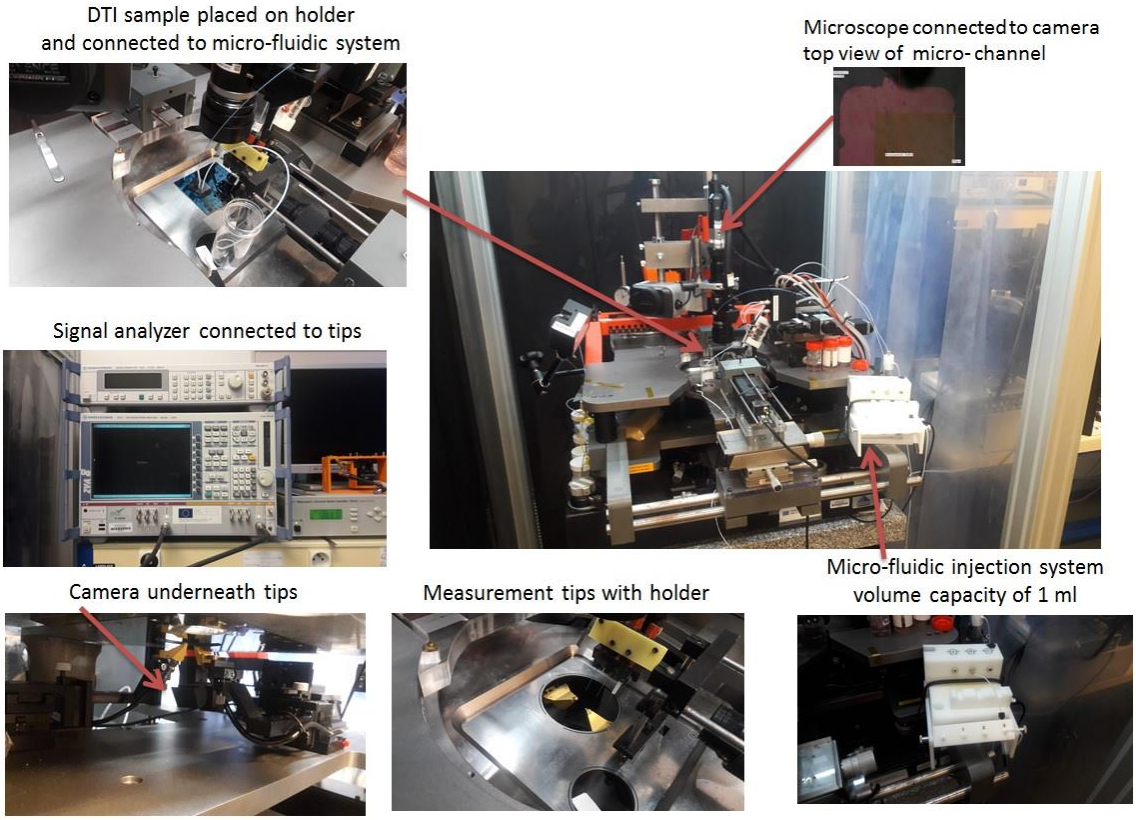


Figure III.31 Photo of the high-frequency acoustic reflectometry wetting characterization bench

Figure III.32 Syringe pump used to inject liquid at different flow rates

In order to obtain good repeatability of the measurement, an electrical calibration of the measurement system is necessary before carrying out a wetting measurement in order to avoid phase losses and rotations (linked to the cable lengths between the measurement tips and the network analyzer) which can be very large in the gigahertz range. Using a calibration substrate, the device records, for three different situations (short circuit, open circuit, circuit loaded on 50Ω) the value of the signal is measured over a frequency band of [500 MHz; 8 GHz]. This calibration file is then stored and called for each measurement.

For each measurement, the number of sweep points on the frequency band is 10000 (the greater the number of points, the longer the sweep will be) with an IF ("Intermediate Frequency") band of 10 kHz which sets the resolution bandwidth. Using the IF band we can determine the minimum frequency space between two signals visible on the screen. Thus, the narrower this band, the better the resolution, but the longer the scanning time will be. Each scan then lasts about twelve seconds.

### III.G.2. Measurement protocol for structured silicon (time measurement)

1. Connection of the micro-channel inlet tube to the microfluidic pump (Fluigent)

2. Placement of the sample maintained by a suction system at the sample holder. Loading the calibration file and adjusting the various parameters of the network analyzer (scan, IF band, frequency band, display)

3. Placing the outlet tube of the micro-channel in a small beaker

4. Loading a Matlab program which serves as an acquisition tool of data from the network analyzer to calculate the reflection coefficients on the top and bottom surface of the structures as function of time

5. Recording of $R_{bottom}$ and $R_{top}$ (reflection coefficients on the bottom and top surface of the DTI structures) when the micro-channel contain no liquid (air)

6. Injection of the liquid (used to characterize wetting) into the micro-channel at a pressure of 300 mbar

7. Recording of $R_{bottom}$ and $R_{top}$ on the same structured area with the presence of liquid

8. Injection of air in the micro-channel at a pressure of 1 bar to eliminate the presence of liquid (drying phase) and recording of $R_{bottom}$ and $R_{top}$ during the drying process

9. To take another measurement, start over at step 4

Note that before the injection of the liquid, we can check the stability of the reflection coefficients which are monitored in real time to ensure that the variation is to the thousandth. If the variation is larger the program is rebooted before the liquid injection.

With the Matlab program a plot showing the two reflection coefficients (bottom and top of structures) is obtained as function of time. The plot shows three phases of variation: The first phase before injection of liquid ($R_{bottom} = R_{top} = 1$), the second phase during liquid injection in the micro-channel ($R_{bottom}$ and $R_{top} < 1$) and the third phase is the drying phase where the $R_{bottom}$ and $R_{top}$ increase until reaching a value of 1.

When using water / alcohol mixtures, their variation in composition will have an impact on the value of the reflection coefficient over time (see III.H) even if a stable state of wetting is obtained. A recording phase of the reflection coefficient on a smooth surface as a function of the concentration is then necessary.

## III.H. Liquids used

In order to study the influence of the surface tension of the liquid on the wetting state, different water / alcohol mixtures were studied: water / ethanol and water / isopropanol (IPA). The range of surface tensions scanned for these two mixtures is quite similar (Figure III.33.a) although lower values can be reached for water / IPA mixtures. The acoustic behavior of the mixtures was also compared by measuring the reflection coefficient on a smooth silicon wafer between the silicon and the mixture (Figure III.33.b). The variations observed are due to variations in the acoustic impedance of the mixture Z as a function of its alcohol content. Once again we can see that the variations are small between the two mixtures. We have:

$$r_{Si/liquid} = \frac{Z_{Si} - Z_{mixture}}{Z_{Si} + Z_{mixture}} \quad with \;\; Z_{mixture} = \rho_{mixture} c_{mixture}$$

with $\rho_{mixture}$ and $c_{mixture}$ the density and speed of sound in the mixture which vary depending on the alcohol concentration of the mixture.

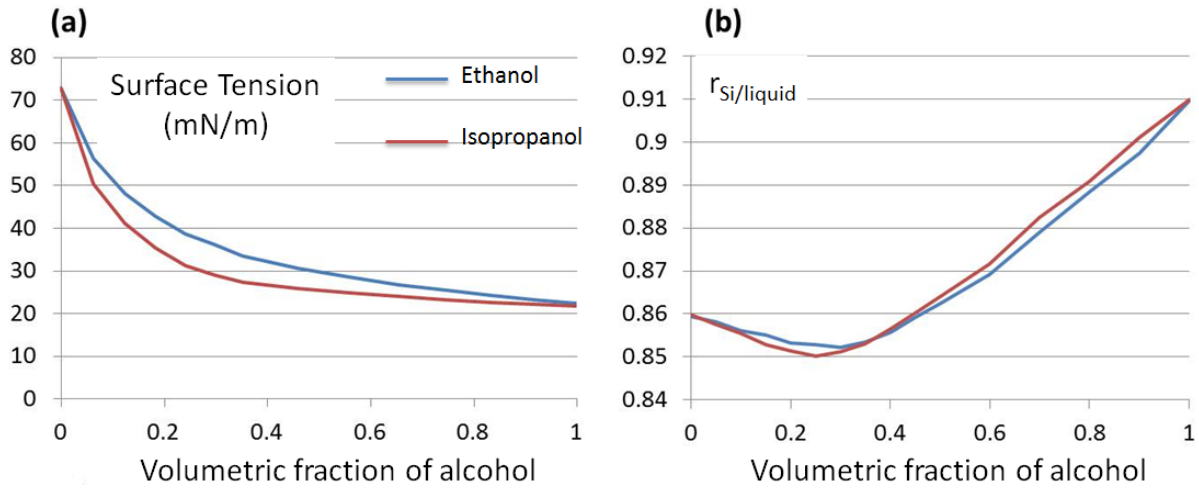


Figure III.33 Variations in the properties of water / ethanol and water / isopropanol mixtures: surface tension [10] (a) and reflection coefficient on a smooth interface between silicon and liquid as a function of the volume fraction of alcohol [10] (b)

For the measurement inside the micro-channel, the choice of the mixture (water/ethanol or water/isopropanol) has little importance. The reflection coefficient both mixtures for the same concentration is almost the same (Figure III.33.b). Nonetheless, the difference between ethanol and isopropanol is that the ethanol is more hygroscopic (capturing more humidity from atmosphere) than IPA, but the micro-channel will be closed so there is no concern about humidity interference. In addition, since IPA is slightly less volatile than ethanol, it will evaporate more slowly than ethanol when using water / alcohol mixtures. For that reason, the measurements on the DTI wafers will be carried using water/ethanol mixtures.

Another solution named SC1 will be used for the measurements. This solution is used in STMicroelectronics as a cleaning solution (presented in part I.C.1 of Chapter I) to remove particle contaminants from the wafers. In our measurements we will use a highly diluted version of the solution which contains: 80 parts $H_2O$, 1 part ammonia solution ($NH_4OH$ (30%)) and 2 parts hydrogen peroxide solution ($H_2O_2$ (30%)). The reason behind choosing a highly diluted solution is to avoid a highly basic medium which can damage the PDMS. Since the solution is highly diluted, the reflection coefficient on a smooth silicon wafer between the silicon and the solution will be the same as water ($r_{Si/SC1}$ = 0.86).

## III.I. Conclusion

In this chapter, the method used for measuring wetting by high frequency acoustic reflectometry was presented. The improvement of the transverse signal generation of the transducers by changing the ZnO crystallite orientation was also presented along with its response on DTI interface. The manufacturing methods of the transducers, the dimensions of the structured layers to be studied as well as the liquids and surface treatments used for the study of the wetting of STMicroelectronics structures were also presented. In addition we introduced the PDMS micro-channels, their dimensions and fabrication process as a method for dynamic wetting characterization. Two micro-channels of 40 µm and 80 µm were chosen

based on hydrodynamic calculations to ensure that the pressure loss was in the range of tens of millibars. In the following chapter, we will use the FDTD model to try and find the reflection coefficients on the DTI and discuss the difficulties encountered in the simulation. Also, we will introduce the experimental measurements of the reflection coefficients to the study of the different wetting states of STMicroelectronics DTI structures.

# IV. Wetting Characterization of STMicroelectronics DTI Structures

The high frequency acoustic reflectometry method and the measurement conditions used to determine the wetting state of STMicroelectronics DTI structures were explained in Chapter III. Chapter II presented the FDTD theoretical models necessary for the interpretation of the reflection coefficients when it was not possible to conclude on the state of wetting with the experimental measurements.

In this chapter, experimental measurements of the acoustic reflection coefficient on STMicroelectronics DTI wafers are presented using different liquids in order to characterize their wetting and drying behavior. We will also discuss about the fact that the FDTD theoretical model is applicable to the cases of real DTI structures and if it allows the interpretation of the measurements.

We used two different micro-channels thickness of 40 µm and 80 µm to recreate the same fluid film thickness at two different locations from the center of the actual industrial silicon wafer (300 mm in diameter) at radii 50 mm and 120 mm respectively (Table III-5).

We will present the wetting characterization of the DTI structures as follows:

- DTI (4 µm, 5 µm , 6 µm and 7 µm trenches depths) with 40 µm PDMS micro-channel thickness

- DTI (4 µm, 5 µm , 6 µm and 7 µm trenches depths) with 80 µm PDMS micro-channel thickness

## IV.A. 40 µm PDMS micro-channel: Static data acquisition

In this section we are going to introduce the experimental measurements of the acoustic reflection coefficients using different distilled water / ethanol mixtures on four different trenches depth DTI wafers (4 µm, 5 µm, 6 µm and 7 µm). The different liquids will be injected in the 40 µm PDMS micro-channel. Based on the values obtained for the reflection coefficients which will be calculated directly from the echoes diagram we're going to give conclusions about the wetting behavior. In addition we are going to try and use the FDTD model to simulate the wetting state of the real DTI geometry.

### IV.A.1. 40 µm PDMS micro-channel: Echo diagrams

First we represent the experimental echoes diagram of the depth DTI (4, 5, 6 and 7 µm etch depth) exposed to air (micro-channel empty). All the measurements were carried out with transducers with a diameter of 100 µm, with a central frequency between 3.5 GHz and 4 GHz on the band [1 GHz; 6 GHz]. The position of the transducers with respect to the micro-channel will vary (center and edges) since it was difficult to align them directly underneath

the DTI matrix. One example of edge alignment of the 100 µm transducer is shown in Figure IV.1.

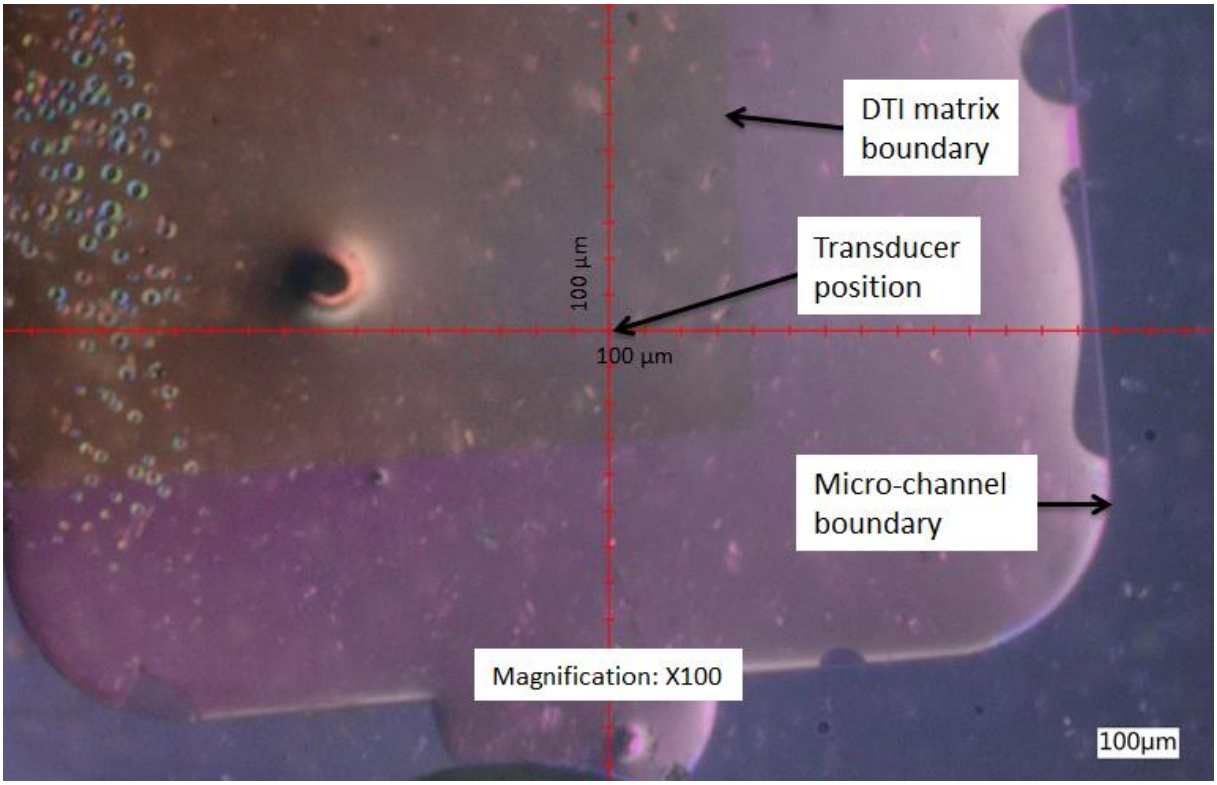


Figure IV.1 Photo of the transducer alignment under the micro-channel

The echo diagrams of the smooth surface and the DTI 4, 5, 6 and 7 µm are shown in Figure IV.2 through Figure IV.5 respectively.

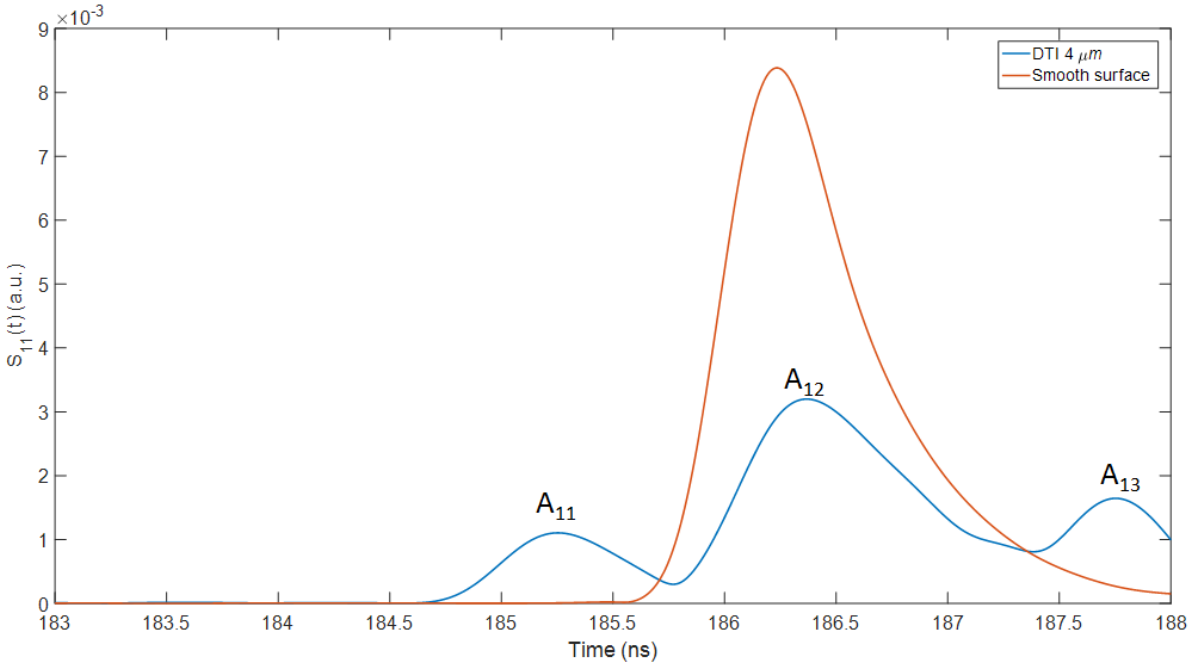


Figure IV.2 Experimental echoes diagram of 4 µm DTI exposed to air

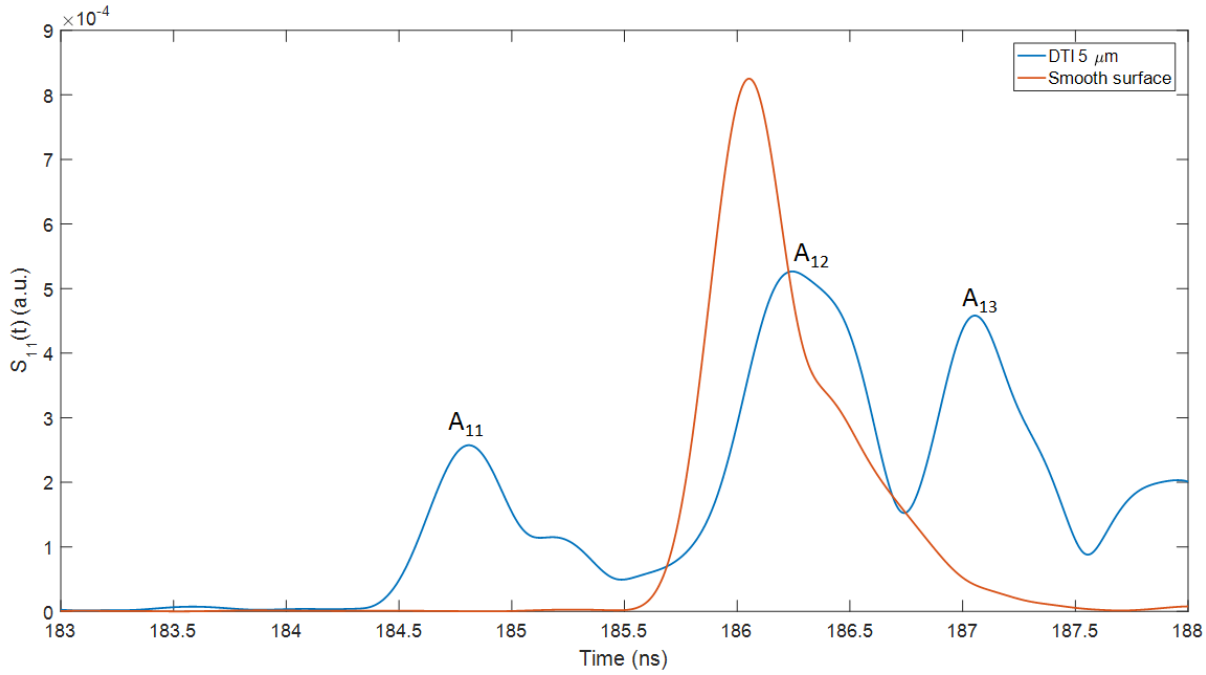


Figure IV.3 Experimental echoes diagram of 5 µm DTI exposed to air

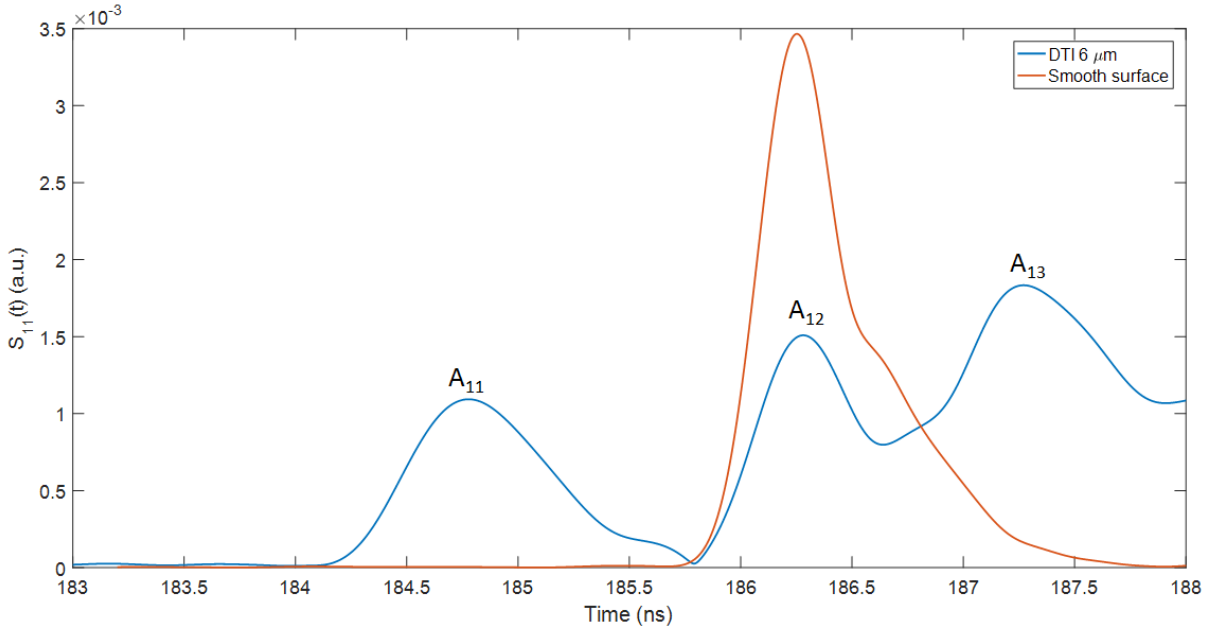


Figure IV.4 Experimental echoes diagram of 6 µm DTI exposed to air

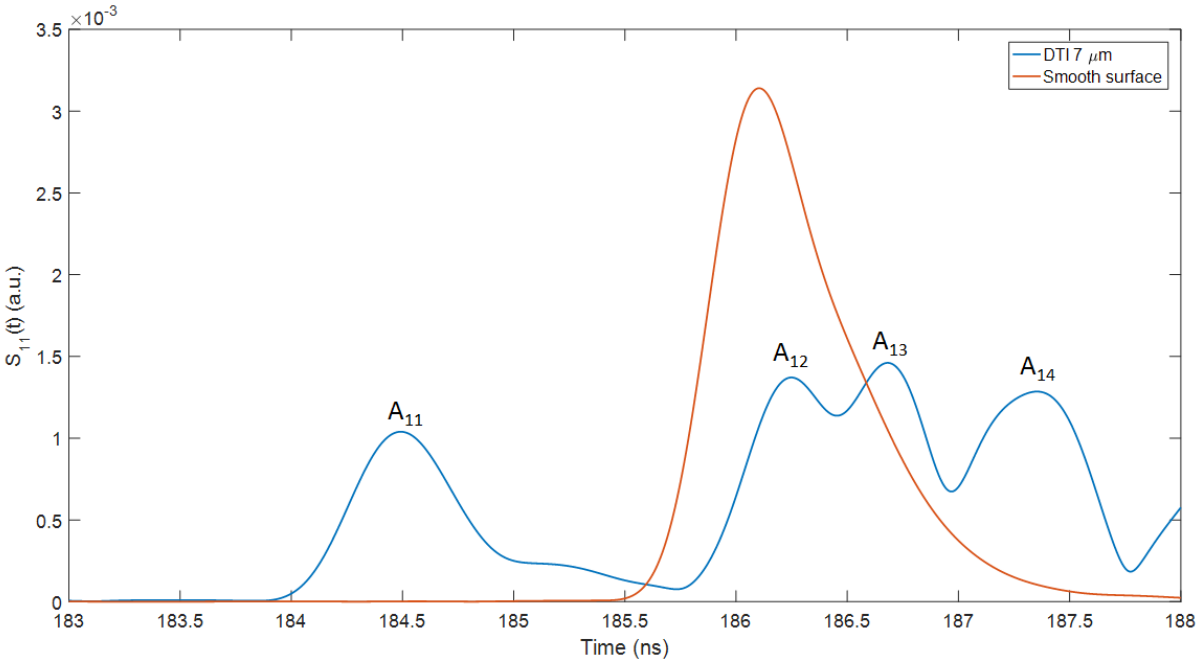


Figure IV.5 Experimental echoes diagram of 7 µm DTI exposed to air

**Discussion**

We can observe three different echoes on the DTI 4, 5 and 6 µm:

- The first echo $A_{11}$ which is the bottom surface echo,
- The second echo $A_{12}$ which seems to be mixed with the third echo $A_{13}$.

It can also be noted that there seems to be a case of mixed echoes between $A_{11}$ and $A_{12}$ which could correspond to the mode change of the longitudinal wave in the DTI network. In the case of DTI 7 µm (Figure IV.8), in addition to the three echoes that appear for the other DTI (4, 5 and 6 µm), we can observe the apparition of a new echo $A_{14}$ which is mixed with $A_{13}$. It could be related to a new mode which appears due to larger DTI depth (7 µm). We note that to understand these different echoes it's necessary to use an acoustic model for simulation the acoustic interactions with the DTI network.

The time difference between $A_{11}$ and the echo on the smooth surface is 1 ns (Figure IV.2), leading to an effective etch depth equal to $\frac{c_{Si}\Delta t}{2}$ = 4.2 µm ($c_{Si}$ is the longitudinal velocity of sound in silicon equal to 8433 m.s$^{-1}$). Similarly, we can find the time difference in other figures which correspond to 1.25 ns, 1.5 ns and 1.62 ns, leading to effective etch depths of 5.3 µm, 6.3 µm and 6.8 µm. Therefore, we can see that the etch depth of the DTI can vary from a wafer to the other due to the fact that during the dry etch process at STMicroelectronics.

### IV.A.2. Interpretation with the FDTD model

In order to simulate the DTI geometry using the 2D FDTD model, 6 different cross sections must be taken into account as shown in Figure IV.6. These sections were taken to be able to obtain all the cases possible for the variation of the acoustic reflection coefficient.

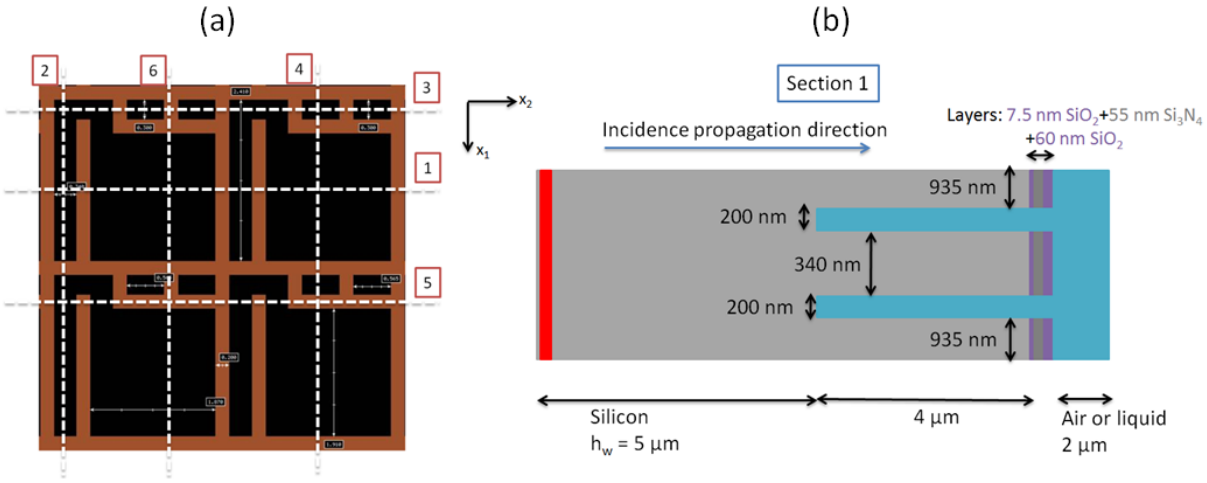


Figure IV.6 (a) Different sections taken in the real DTI network, and (b) example of section 1 representation in 2D

The FDTD impulse diagram of the simulated sections is shown in Figure IV.7, the direction perpendicular to the section is taken as infinite. We can observe in the impulse diagram that echo ($A_{11}$) of the bottom surface of all sections comes at the same instant. It is separated from the rest of the echoes, but with different amplitudes. Also, the sections 1 and 4 appear to give the same echoes response since the two geometries in 2D have approximately the same dimensions (Figure II.23). The other echoes ($A_{12}$ and $A_{13}$) for all sections are remarkably different with different positions in time and amplitudes. This difference in position time can be related to different propagation modes. Qualitatively, we can understand that for the real DTI network, the mixture of the different contributions of the different modes leads to complex echo diagrams. Thus, the construction of the experimental echoes diagram is only possible by the development of a 3D acoustic model.

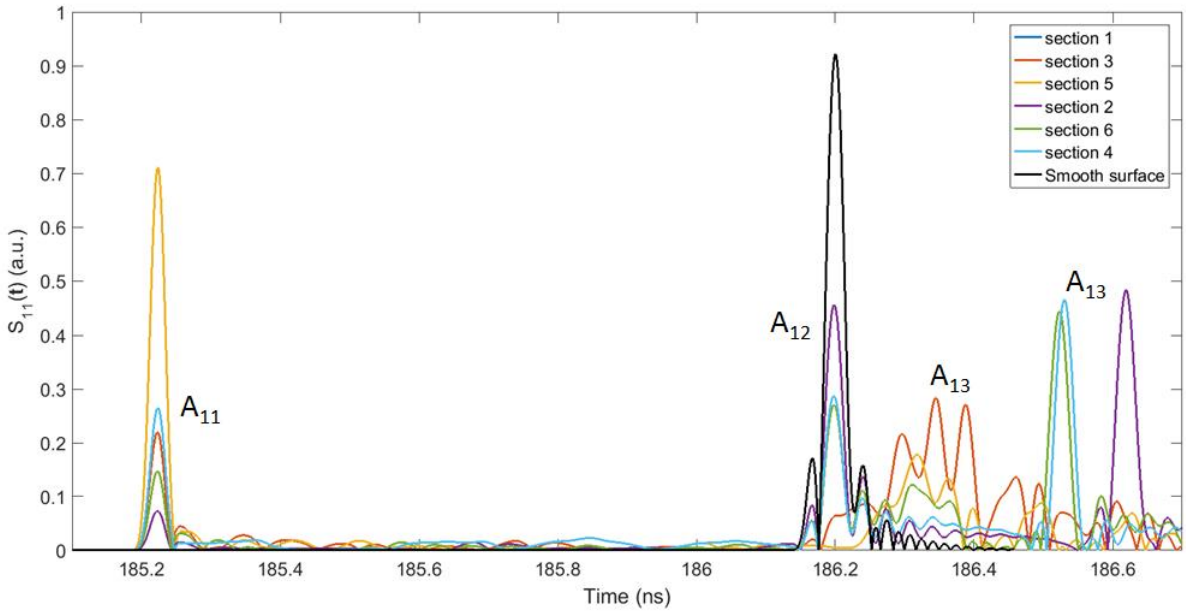


Figure IV.7 Simulated impulse response diagram of the different DTI sections exposed to air

Therefore, the use of the 2D FDTD model to understand the top surface echoes of the experimental echoes diagram is difficult due to the contribution of the different sections. Also, the calculation of the simulated reflection coefficient is not possible since it will be a mix of the different reflection coefficients of the simulated sections.

In what follows, for the obtained results of the different DTI samples, we will focus on the experimental reflection coefficients with different liquids on the bottom surface and based on the values obtained we will make conclusions on the wetting state. Nevertheless, the information from the top echo can be used for kinetic interpretation even though we cannot interpret the absolute value.

### IV.A.3. Determination of the wetting state

To determine the state of the wetting inside the trenches we will focus on the $A_{11}$ echoes. We recall the expressions of the reflection coefficients seen in chapter III:

$$|r_1| = \frac{A_{11}^{liquid}}{A_{11}^{air}} \; and \; |r_2| = \frac{A_{12}^{liquid}}{A_{12}^{air}}.$$

The measurements were done using mixtures of distilled water (DW) / ethanol injected inside the 40 µm deep micro-channel at room temperature. Between each liquid measurement the air is injected until the DTI network is completely dry and we retain the reflection coefficient with air ($r_1$ = 1). The reflection coefficients $r_1$ for the DTI 4, 5, 6 and 7 µm are shown in Figure IV.8.

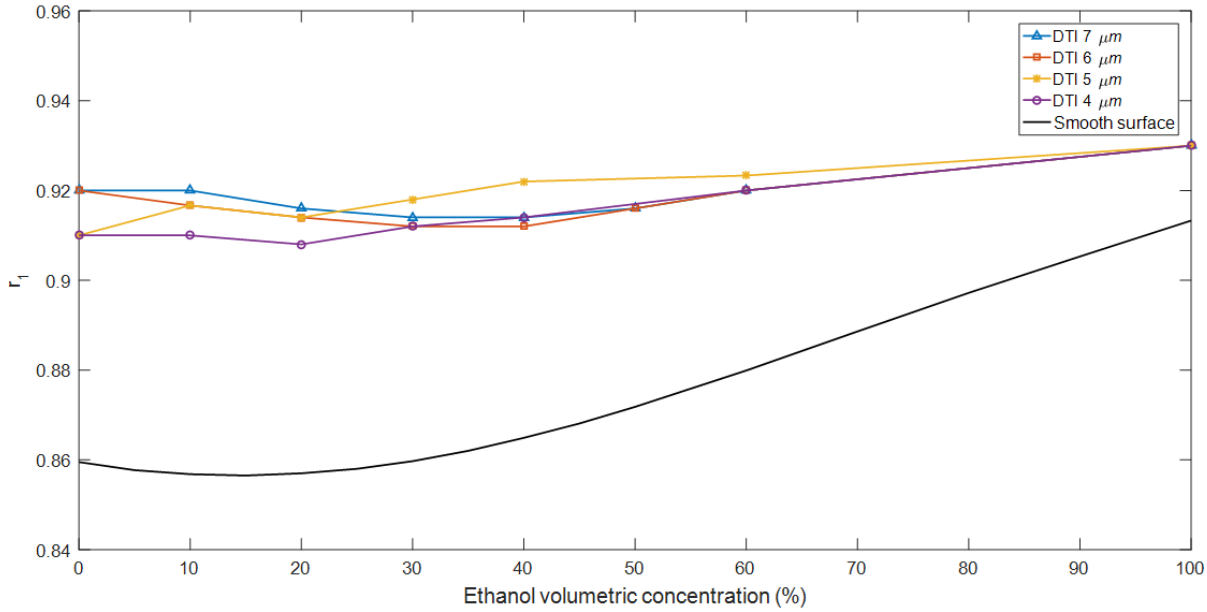


Figure IV.8 Variations of the reflection coefficient $r_1$ on the bottom of the DTI 4, 5, 6 and 7 µm for different distilled water / ethanol mixtures

**Discussion**

The precision of the measurements on the DTI samples is $\Delta r_1 = 0.005$ and it was obtained by calculating the standard deviation on 20 measurements points with DW injected inside the micro-channel. The DW was used since it is less likely to evaporate compared to mixtures containing ethanol.

We can observe from the obtained values for the DTI network that $r_1$ values are always superior to those obtained for silicon smooth surface. For example, in the case of water and pure ethanol for the DTI 4 µm we obtained values of 0.91 and 0.93 respectively which are significantly higher than the values obtained on smooth surface (0.86 and 0.91). These superior values indicate that wetting inside the trenches is not total and could be related to air being present in the network. Thus, the amount of reflected energy will be greater than that in a purely Wenzel state, implying an increase in the reflection coefficient and non-complete wetting inside the trenches.
Approximately the same wetting response is observed on the four DTI samples despite the aspect ratio difference of the trenches ranging from 20 for the 4 µm DTI up to 35 for the 7 µm DTI sample.

### IV.A.4. Wetted surface: DTI with 40 µm micro-channel

It was concluded from the comparison of the reflection coefficients ($r_1$) measured on the different DTI samples with the theoretical reflection coefficient obtained on a smooth surface ($r_{Si/liquid}$) that we have a state of partial wetting with the use of different water / ethanol mixtures. Two scenarios are possible in the case of partial wetting. The first one considers a uniform wetting on all the etched trenches but with trapped air pockets and a changing

meniscus depending on the contact angle (Figure IV.9.a and Figure IV.9.b). In fact, the DTI are etched using the Bosch process which uses octafluorobutane ($C_4F_8$) as the polymer deposition gas [129]. The $C_4F_8$ coating is reportedly hydrophobic and has very similar contact angles obtained on a smooth silicon surface coated with perfluorodecyltricholorosilane (PFTS) [130]. In the case of PFTS, we can find in literature that using this coating on a smooth silicon surface, we can obtain hydrophobic contact angles (> $90^{O}$) for surface tensions above 46 $mN.m^{-1}$ and hydrophilic for lower surface tensions [131]. Thus, depending on the ethanol concentration (changing surface tension), the local contact angles inside the DTI can change.

In the second scenario we have a composite wetting state where some trenches are completely filled with liquid and others are filled with air (Figure IV.9.c). In either case, it is possible to calculate the unit area fraction of wetted surface $S_w$ using the following relation:

$$r_1 = S_w r_{Si/liquid} + (1 - S_w) r_{Si/air} \,. \qquad \text{Eq IV-1}$$

Knowing that $r_{Si/air} = 1$ , we get:

$$S_w = \frac{1 - r_1}{1 - r_{Si/liquid}} \,.$$

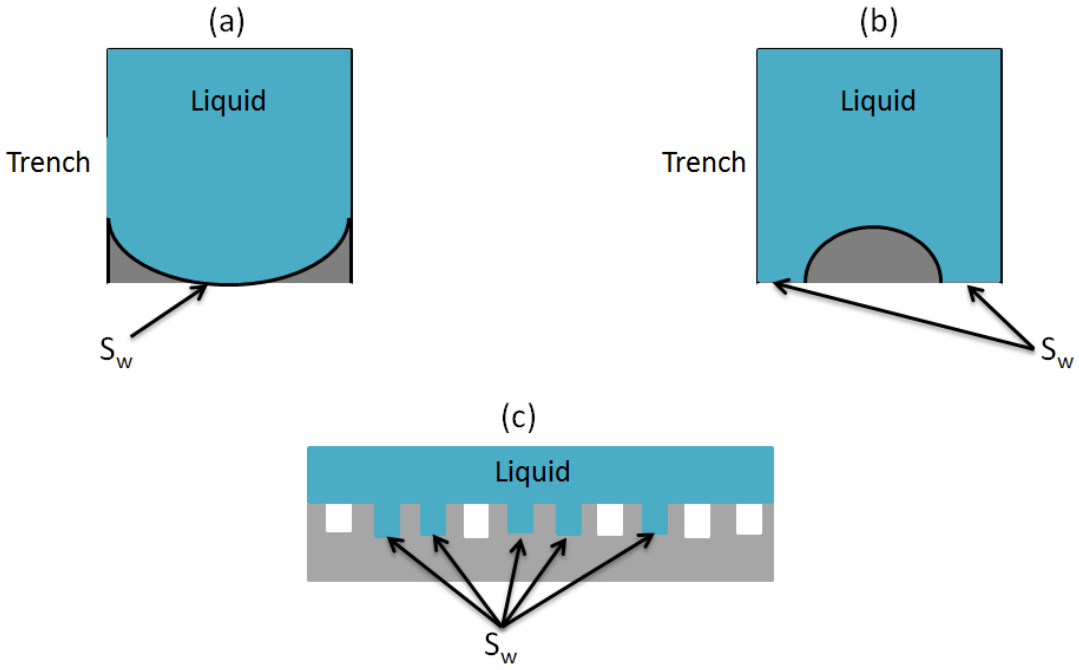


Figure IV.9 Schematic of possible cases behind partial wetting (a) for non-wettable hydrophobic trench surface with trapped air pockets, (b) wettable hydrophilic trench surface with trapped air pockets and (c) composite state with some trenches filled with liquids and others with air

Using the calculated reflection coefficients $r_1$ for the different ethanol / water mixtures, the percentage of wetted surface (% $S_w$) is plotted against the percentage of ethanol concentration by volume (% Eth) for the four DTI samples (Figure IV.10).

We can observe that the general trend on all the four DTI samples was an increase in the surface area as the ethanol concentration increases, starting from about 60 % wetted area for water up to 80 % wetted area for pure ethanol.

While $S_w$ can give general idea about partial wetting state, it was difficult to differentiate between the percentages of wetted surface of the different ethanol / water mixtures since the percentage error on $S_w$ was dependent on the ethanol concentration by the following equation:

$$Error = \frac{\Delta S_w}{S_w} = \frac{\Delta r_1}{1 - r_1}$$

where, $\Delta r_1$ found from multiple data measurements and taken as 0.005.

The percentage error ranged from 6 % for water up to 9 % for pure ethanol as we can observe using the error bars on Figure IV.10.

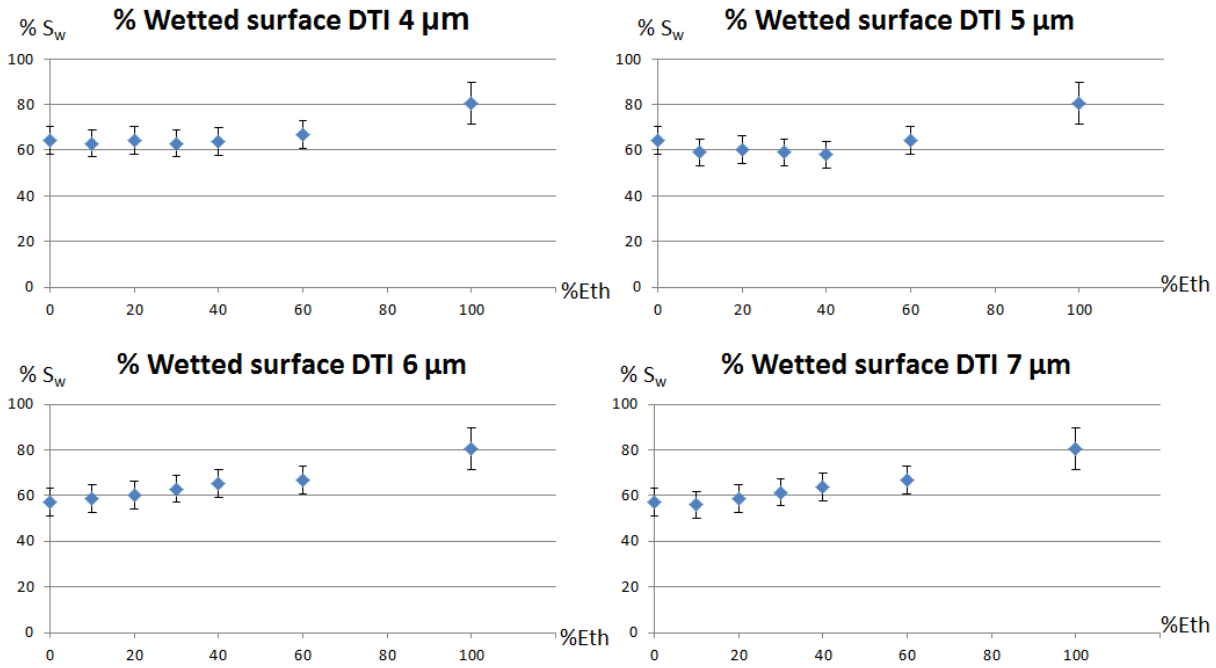


Figure IV.10 Percentage of wetted surface (% $S_w$) for different ethanol / water concentration on the DTI samples with 40 µm micro-channels

## IV.A.5. Conclusion

The wetting state inside the 200nm trenches (4.2, 5.3, 6.3 and 6.8 µm real depth) is not total which could be related to air being trapped inside the DTI network. Even in the case of pure ethanol which has a low surface tension of 22.31 $N.m^{-1}$, the reflection coefficient was higher than the one obtained with smooth surface. The partial wetting was estimated using the percentage of wetted surface, to be in the range of 60 % to 80% for water and pure ethanol respectively. The utilization of the FDTD 2D model wasn't effective in understanding the wetting state due to the complex geometry of the DTI network. Therefore, developing a 3D

acoustic model is necessary to conclude more precisely on the state of wetting. In the next part we will introduce a new technique used to follow the measurements with the 80 μm depth micro-channel which will give us more insight on the wetting and drying state.

## IV.B. 80 μm PDMS micro-channel: Automatic data acquisition

In this section we are going again to present the experimental measurements using different distilled water / ethanol mixtures on four different trenches depth DTI wafers (4 μm, 5 μm, 6 μm and 7 μm). A new technique for measuring the reflection coefficients in real-time using Matlab will be introduced. In addition, we are going to present measurements done using SC1 solution and see the wetting response. The different liquids will be injected in the 80 μm PDMS micro-channel.

### IV.B.1. Reflection coefficient in real-time

Until now we have calculated the reflection coefficient directly from the echoes diagram by taking the ratio of the bottom surface amplitudes of DTI when the PDMS micro-channel is filled with liquid and when it is filled with air. We also notice that the precision and stability of the reflection coefficient increases when we have higher amplitude of the reflected echoes. The amplitude on the DTI silicon interface was low (1-2 a.u.) because of the acoustic diffusion compared to the smooth silicon surface (15-20 a.u.). To make the measurements more stable, we used two measurement points, one on the DTI matrix and the other on a smooth surface then we normalized the reflected signals taken on the DTI surface by the amplitude of the signal taken on the smooth surface. Also, the new samples were made without the use of a blind (III.C.2). Not using the blind made longitudinal waves amplitude higher (III.C.3). Using these new samples with higher longitudinal wave amplitude, the measurements of the acoustic reflection coefficient became more stable and a precision of $\Delta r_1$ = 0.0025 was achieved.

To make the process of data acquisition more efficient (shorter calculation time of reflection coefficients), a MatLab program was created to calculate the acoustic reflection coefficient as function of time. This program takes the values of the echo's amplitudes directly from the signal analyzer and calculates the acoustic reflection coefficient on the bottom ($r_1$) and top ($r_2$) surface of the trenches.

An example of one measurement done on a DTI 6 μm with 80 μm height micro-channel is shown in Figure IV.11. The blue dots represent the variation of $r_1$ and the red dots represent the variation of $r_2$. The acquisition time between two consecutive values was about 12 seconds which is tremendous improvement compared to the pervious manual acquisition method that took from 1 – 2 minutes to calculate one data point of the reflection coefficient. There are three phases shown on the figure:

- Phase 1 represents the state where the micro-channel was empty and the DTI was exposed to air ($r_1 = r_2 = 1$),

- Phase 2 represents the transition phase where we inject liquid (here water) into the micro-channel ($r_1$ = 0.92),
- Finally, phase 3 represents another transition phase where we start injecting air into the micro-channel to dry it (here air injection starts at t =1100 sec) and the reflection coefficients get their original values ($r_1 = r_2 = 1$).

Here we notice that $r_2$ takes a value above 1, this can be related to the mix of echoes that takes place between the two echoes ($A_{12}$ and $A_{13}$ on Figure IV.4).

From this point forward, all the data acquisition figures for the reflection coefficients will be obtained using the new acquisition method (acquisition time is 12 seconds).

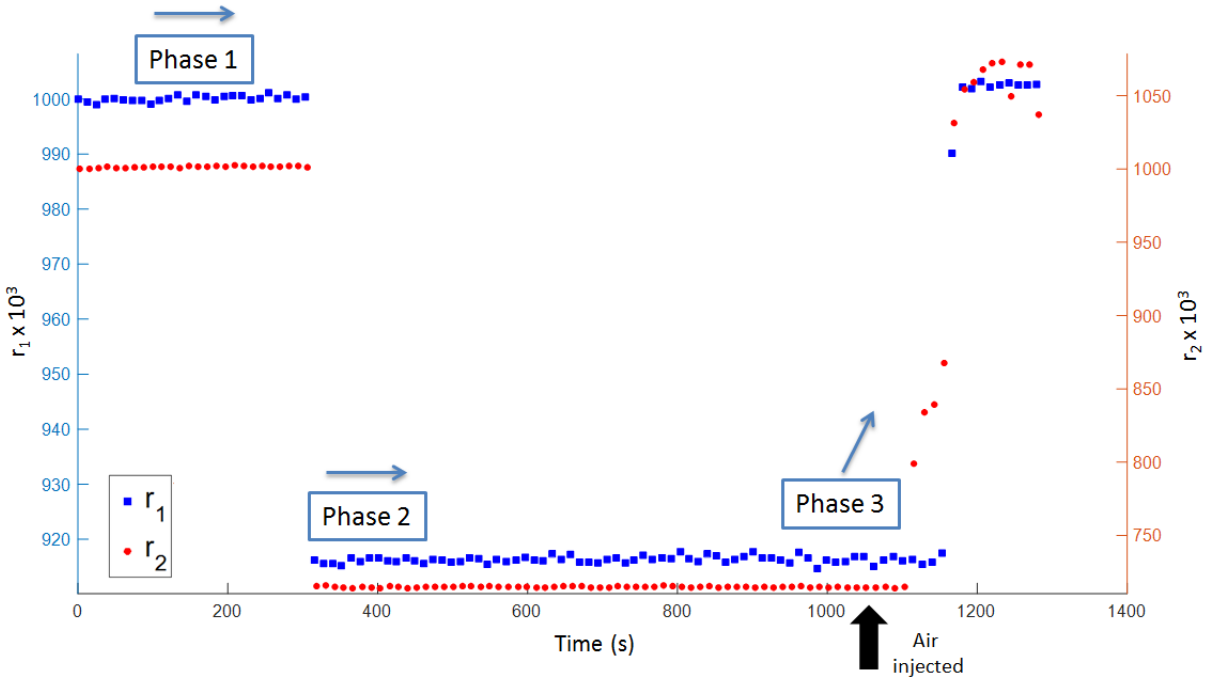


Figure IV.11 Variation of the acoustic reflection coefficients $r_1$ and $r_2$ with time for DTI 6 µm with 80 µ micro-channel injected with water: initial phase (phase 1), injection of liquid (phase 2) and injection of air for drying the liquid (phase 3)

As we will see later this method of acquisition will be useful in observing the variation of the wetting state during the transition phases.

### IV.B.2. Water / ethanol mixtures measurements

The measurements of the acoustic reflection coefficient $r_1$ using water/ethanol mixtures are shown in Figure IV.12. The precision of the measurements on the DTI samples is $\Delta r_1$ = 0.0025 and it was obtained by calculating the standard deviation on 20 measurements points with DW injected inside the micro-channel.

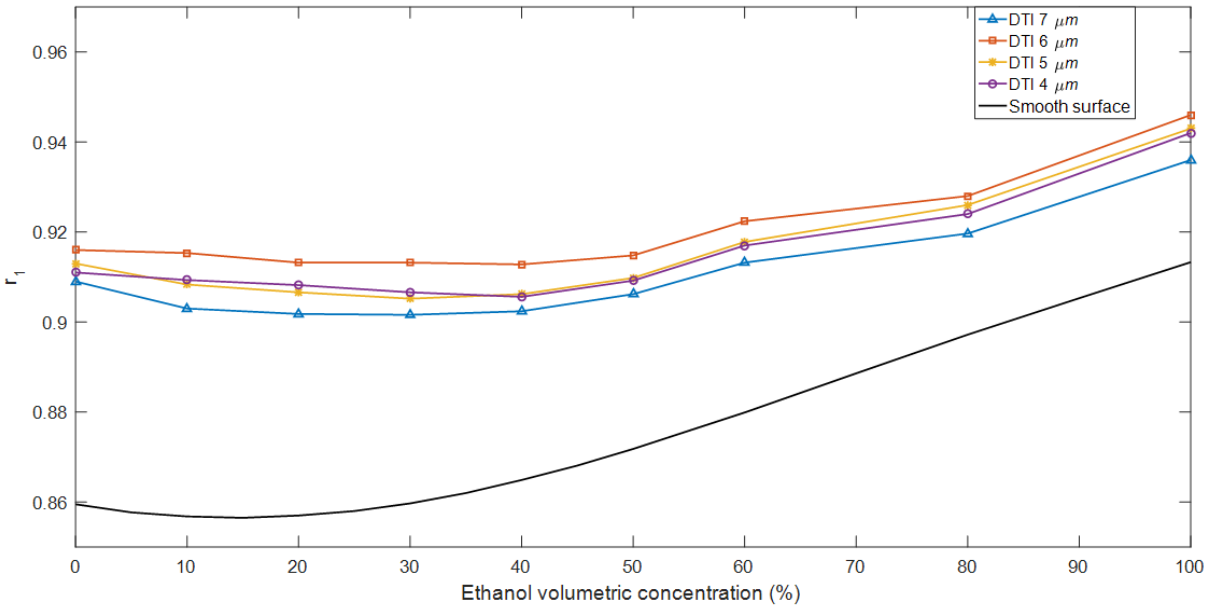


Figure IV.12 Variations of the reflection coefficient $r_1$ on the bottom of the DTI 4, 5, 6 and 7 µm for different distilled water / ethanol mixtures injected in the 80 µm micro-channel

Table IV-1 Variations of the reflection coefficient $r_1$ on the bottom of the DTI 7, 6, 5 and 4 µm for different distilled water and ethanol mixtures injected in the 40 and 80 µm micro-channel

| Sample | 40 µm micro-channel | | 80 µm micro-channel | |
|---|---|---|---|---|
| | Water | Pure ethanol | Water | Pure ethanol |
| DTI 4 | 0.91 | 0.93 | 0.91 | 0.94 |
| DTI 5 | 0.91 | 0.93 | 0.91 | 0.94 |
| DTI 6 | 0.92 | 0.93 | 0.92 | 0.94 |
| DTI 7 | 0.92 | 0.93 | 0.91 | 0.94 |

In observing the different curves for the DTI samples, we can notice a similar response to the measurements obtained with the 40 µm micro-channel. All the obtained values for $r_1$ are superior to the ones obtained on a smooth surface suggesting the same conclusion mentioned for the 40 µm micro-channel with partial wetting on the bottom of the trenches.

Table IV-1 contains the values of $r_1$ for water and ethanol used inside the two micro-channels (40 and 80 µm thickness) for different DTI samples. The variations of $r_1$ for the same trench depth between the two micro-channels are in the range of $\pm$ 0.01. This shows that the change of the liquid film thickness "2*h*" from 40 µm to 80 µm has little impact on the wetting state.

### IV.B.3. Wetted surface: DTI with 80 µm micro-channel

The percentage of wetted surface % $S_w$ (see IV.A.4) is calculated here again and plotted against the ethanol concentration (% Eth) for the DTI samples with 80 µm micro-channel (Figure IV.13).

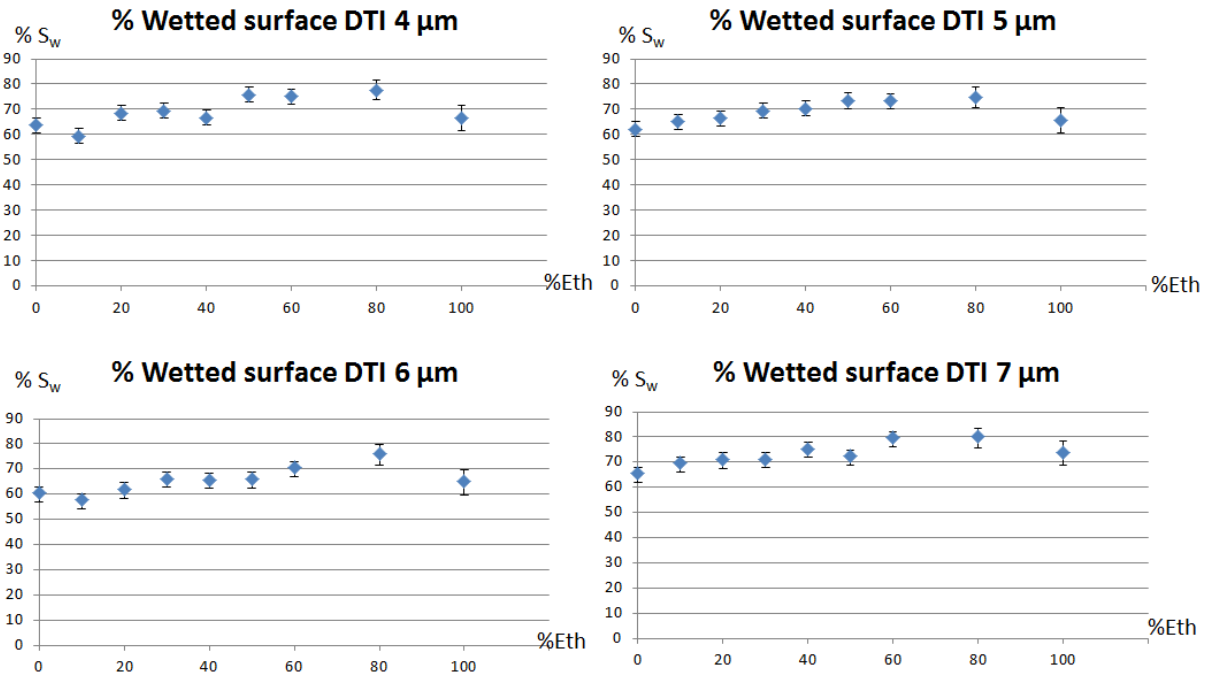


Figure IV.13 Percentage of wetted surface (% $S_w$) for different ethanol / water concentration on the DTI samples with 80 µm micro-channels

As in the case of 40 µm micro-channel, % $S_w$ ranged from 60 % for water up to 80 % with the increasing ethanol concentration. As was discussed in IV.B.1, the precision of the measurement on the reflection coefficient is improved with the introduction of the real-time measurements technique which in turn reduced the percentage error on $S_w$. The percentage error ranged from for 3% for water up to 5 % for pure ethanol as illustrated using the error bars. However, the percentage error was still too high to differentiate the wetted surface between the different ethanol concentrations.

The general trend of the plot for all the DTI samples was an increase in the wetted surface as the ethanol concentration increases in the mixture except for the points corresponding for 80 % ethanol and the pure (100%) ethanol for which we can observe a decrease that was surprising.
In general, if we consider the bibliography about solubility of nitrogen and oxygen which are the main constituents of air (21% oxygen and 78% nitrogen) in water or ethanol, we find that the solubility of both these gases is higher in ethanol than in water [132], [133], [134]. Thus, the diffusion of air in the pure ethanol should be higher than the 80% ethanol / water mixture. Thus, it means that we should expect a higher wetted surface for pure ethanol than for mixtures which contain water.

Therefore, up to now, a possible explanation would be that this decrease is due to the error rate on $S_w$ valued 4 % for 80% ethanol concentration and 5 % for pure ethanol. All errors here calculated for $\Delta r_1 = 0.0025$ (see part IV.A.4).

In order to get a precise measurement of the wetted surface, higher precision on the value of the reflection coefficient $r_1$ is needed that would require higher amplitude of the reflected acoustic signal. This higher amplitude was difficult to achieve due to the diffusion (energy

loss) of the acoustic waves in the DTI network. Nevertheless, it makes it possible to have a quantitative evaluation of the wetting state.

### IV.B.4. Flow rate effect

Another pump generating different flow rates ranging up to 120 ml.h$^{-1}$ compared to the previous measurements where a flow rate between 4 ml.h$^{-1}$ and 5 ml.h$^{-1}$ was used. The micro-channel inlet was connected to this pump by a microfluidic tube of internal diameter equal to 0.5 mm. The effect of changing the flow rate with time was studied using two different liquids which are distilled water and ethanol. The sample was chosen to be the DTI 4 µm with micro-channel of 80 µm thickness. The DTI 4 µm was chosen because it presents the lowest aspect ratio (20) which is the ratio of the trenches depth (4 µm) to the trenches width (200 nm). If any changing on the wetting state occurs it will be easier to observe on the lowest aspect ratio structures. Also, ethanol and water were chosen since they represent the two extremities of the surface tension (22.31 mN.m$^{-1}$ and 72.75 mN.m$^{-1}$ respectively).

#### *IV.B.4.a. Flow rate changing: Ethanol*

The measurements with ethanol on the DTI 4 µm are shown in Figure IV.14. At different time delays the flow rate was changed (Table IV-2). The syringe pump is first started with a flow rate = 10 ml.h$^{-1}$ and it will take some time for the liquid to reach the micro-channel inlet (fluidic tubes connected to inlet). At t = 280 sec ethanol reaches the micro-channel (shown by the transition of the reflection coefficients) with a flow rate of 10 ml.h$^{-1}$, $r_1$ decreases from 1 to a value of 0.94 which was previously obtained for the DTI 4 µm (Table IV-1). After this transition, $r_1$ stays stable throughout the flow rate changing from 10 ml.h$^{-1}$ up to 120 ml.h$^{-1}$. Calculating the fluid speed ($u$) at flow rate ($Q$) equal 120 ml.h$^{-1}$ taking 0.5 mm ($D$) as the internal diameter of the tube, we get:

$$u = \frac{Q}{\frac{\pi D^2}{4}} = 0.17\ m.s^{-1}\ .$$

We note that this fluid speed is very close to the one calculated in Table III-5 and used at STMicroelectronics cleaning system for 80 µm height micro-channel (0.2 m.s$^{-1}$). The use of flow rate above 120 ml.h$^{-1}$ was not possible due to the pump characteristics (beyond the maximum flow rate).

These results show that there is no wetting transition occurring with the flow rate change.

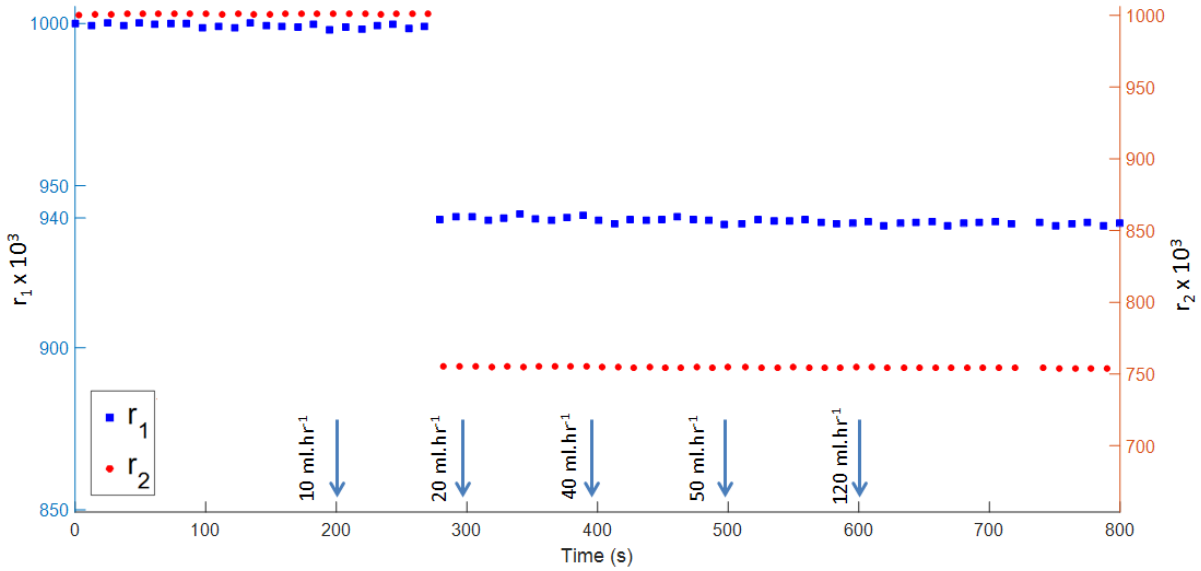


Figure IV.14 Variation of the acoustic reflection coefficients $r_1$ and $r_2$ with time for DTI 4 µm with 80 µ micro-channel using different flow rate of pure ethanol

Table IV-2 Flow rate changing of ethanol at different time delays

| Time (s) | Flow rate (ml.h$^{-1}$) |
|---|---|
| 200 | 10 |
| 300 | 20 |
| 400 | 40 |
| 500 | 50 |
| 600 | 120 |

### *IV.B.4.b. Flow rate changing: Water*

The same measurement with distilled water on the DTI 4 µm is shown in Figure IV.15. At different time delays the flow rate was changed (Table IV-3). At t = 350 sec water reaches the micro-channel with a flow rate of 10 ml.h$^{-1}$, $r_1$ decreases from 1 to a value of 0.92 which was slightly higher than 0.91 obtained for the DTI 4 µm (Table IV-1). After this transition, $r_1$ stays stable throughout the flow rate changing from 10 ml.h$^{-1}$ up to 120 ml.h$^{-1}$. Here again the same response is obtained with water: there is no wetting transition occurring with the flow rate changing.

The two flow rates (liquid speeds inside the micro-channel) measurements with water and ethanol show that changing it from 10 ml.h$^{-1}$ to 120 ml.h$^{-1}$ has no effect on the wetting transition inside the trenches.

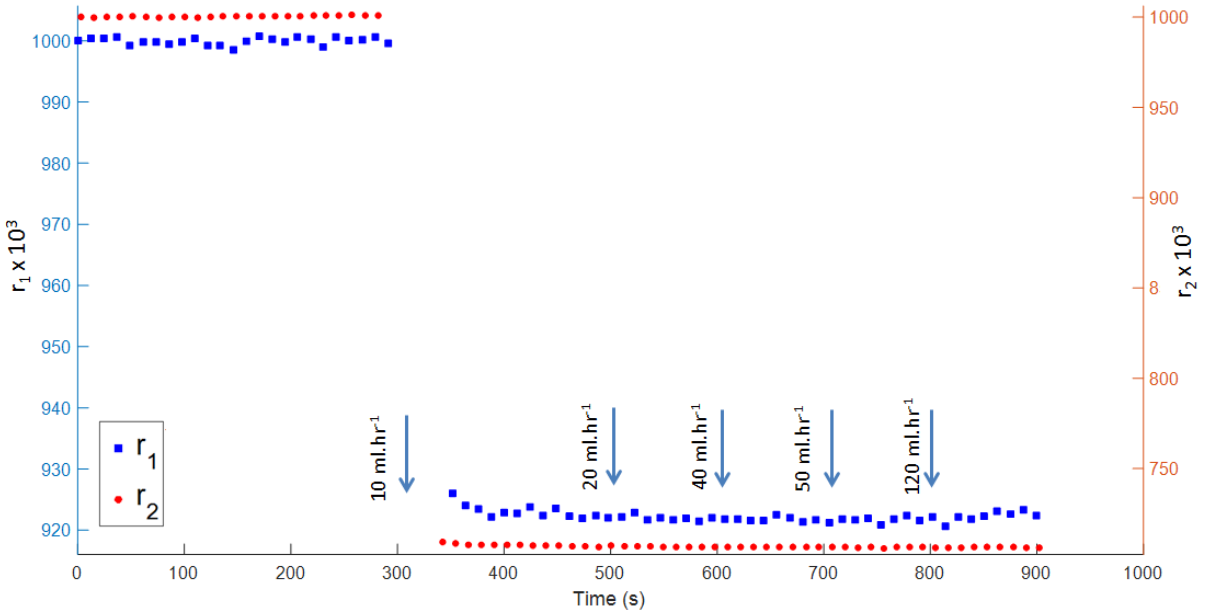


Figure IV.15 Variation of the acoustic reflection coefficients $r_1$ and $r_2$ with time for DTI 4 µm with 80 µ micro-channel using different flow rate of distilled water

Table IV-3 Flow rate changing of water at different time delays

| Time (s) | Flow rate (ml.h$^{-1}$) |
|---|---|
| 300 | 10 |
| 500 | 20 |
| 600 | 40 |
| 700 | 50 |
| 800 | 120 |

### IV.B.5. Standard Cleaning 1 (SC1) measurements

Until now for all the different mixtures of water / ethanol, a partial and non-complete wetting was observed. The idea behind using the SC1 solution (see part III.H of Chapter III for its description) is to eliminate any organic material from the DTI that could prevent the complete wetting. The SC1 solution used in our measurements was highly diluted solution and not the same used at industry due to the fact that higher concentration of ammonia (about 2 %) can cause damage by acting as a catalyst for an hydrolysis reaction to our PDMS micro-channel.

The measurement of the acoustic reflection coefficients ($r_1$ and $r_2$) are plotted with time for DTI 6 µm sample with 80 µm micro-channel are shown in Figure IV.16. The measurements correspond to four phases:

- Phase 1 is the initial phase where the micro-channel is empty,
- In phase 2, the micro-channel is injected with liquid,
- Phase 3 corresponds to wetting transition after injection of air to dry the micro-channel,
- Phase 4 corresponds to the complete drying of the micro-channel and the return to the initial phase (phase 1).

In observing Figure IV.16, at phase 1 we have the micro-channel empty ($r_1$ = $r_2$ = 1), at t = 212 sec we can see the impact of liquid filling the micro-channel. The values of the bottom and top reflection coefficients fall instantly to reach phase 2 ($r_1$ = 0.92 and $r_2$ = 0.75). The values of the reflection coefficients obtained here are similar to the ones obtained with water (Figure IV.11). This result was expected since the SC1 is highly diluted ($r_{Si/SC1}$ = 0.86). At t = 1000 sec, air is injected in the micro-channel to dry it. The liquid inside the micro-channel starts to be pushed to the micro-channel outlet. At t = 1123 sec a transition from phase 2 to phase 3 takes place, the $r_2$ increases gradually and $r_1$ decreases to reach a value of 0.87 at t = 1220 sec which is close to the theoretical value on a smooth surface for complete wetting ($r_{Si\,/\,SC1}$ = 0.86). Finally, a transition to phase 4 takes place where the micro-channel is completely dry and the reflection coefficients regain their original value close to 1. Here again $r_2$ takes a value above 1, this can be related to the mix of echoes on the top surface or acoustic mode changes due to wetting state evolution of the DTI.

A remarkable transition from phase 2 to phase 3 occurred in the case of DTI 6 µm (Figure IV.16) where we saw that $r_1$ reached a value of 0.87 which is very close to the value obtained for complete wetting ($r_{Si\,/\,water}$ = 0.86) indicating quasi-complete wetting behavior on the bottom surface of the DTI.

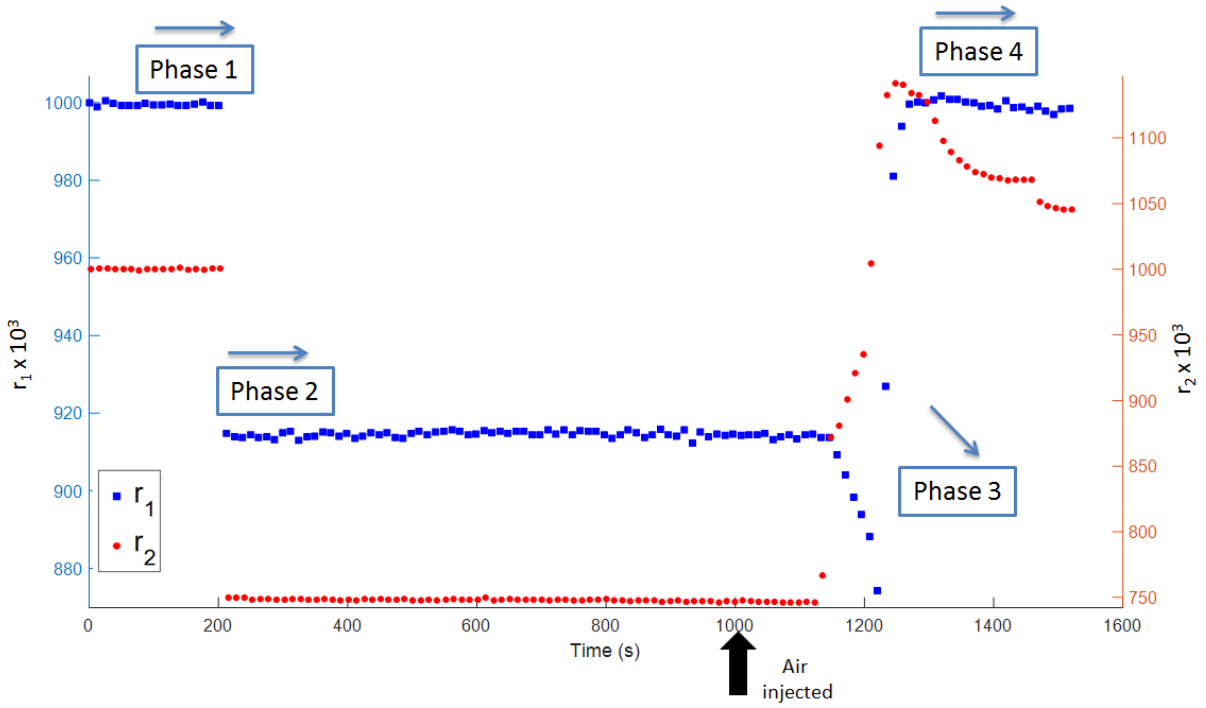


Figure IV.16 Variation of the acoustic reflection coefficients $r_1$ and $r_2$ with time for DTI 6 µm with 80 µ micro-channel injected with SC1 solution: initial phase (phase 1), injection of liquid (phase 2), wetting transition (phase 3) and complete drying (phase 4)

The transition from phase 2 to phase 3 was accompanied by the observation (using the microscope positioned above the micro-channel) of bubbles exiting the DTI network (Figure IV.17.b). This confirms the theory we proposed about trapped air pockets inside the trenches which inhibited the total wetting. The origin of these bubbles is correlated to the observation of bubbles when the SC1 was injected in the micro-channel (Figure IV.17.a) and inside the

beaker of the prepared SC1 solution. Indeed they are due to the presence of oxygen ($O_2$) generated due to the decomposition of hydrogen peroxide:

$$2H_2O_2 \rightarrow 2H_2O + O_2 .$$

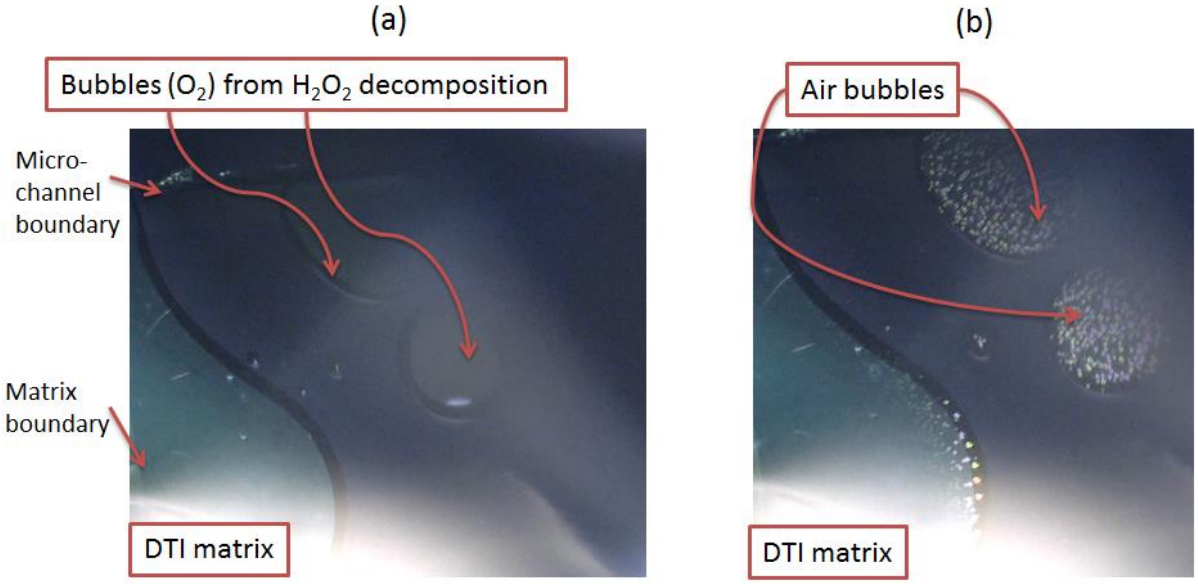


Figure IV.17 Observed bubbles during the injection of the SC1 solution in the micro-channel (a) and air bubbles exiting the DTI network during the drying phase (b)

A similar transition was observed on the DTI 4 µm sample (Figure IV.18). Here again $r_1$ equal to 0.91 at phase 2 similar to the value obtained for water (Table IV-1). The injection of air into the micro-channel starts at t = 250 sec, after about 70 sec (t = 320 sec) the liquid is no longer observed on the top surface of the DTI ($r_2$ increases) and a transition takes place from phase 2 to phase 3 where $r_1$ decreases to a minimum of 0.89 at t = 536 sec. This transition shows that the percentage of wetted bottom surface has increased. Nonetheless, it is still lower than the one obtained for smooth surface ($r_1 = 0.89 > r_{Si\,/\,water} = 0.86$) and we still have partial wetting state. Another transition takes place from phase 3 to phase 4 where $r_1$ increases to 0.91 and stays constant until t = 721 sec in which the final transition to phase 5 takes place where $r_1$ will continue to increase until reaching the value of 1. Here the final value of 1 for $r_1$ is not shown due to the large time span taken to reach this value (about an hour). This could be related to injected air pressure was lower than 1 bar due to some pressure leakage in fluidic connections during the drying phase.

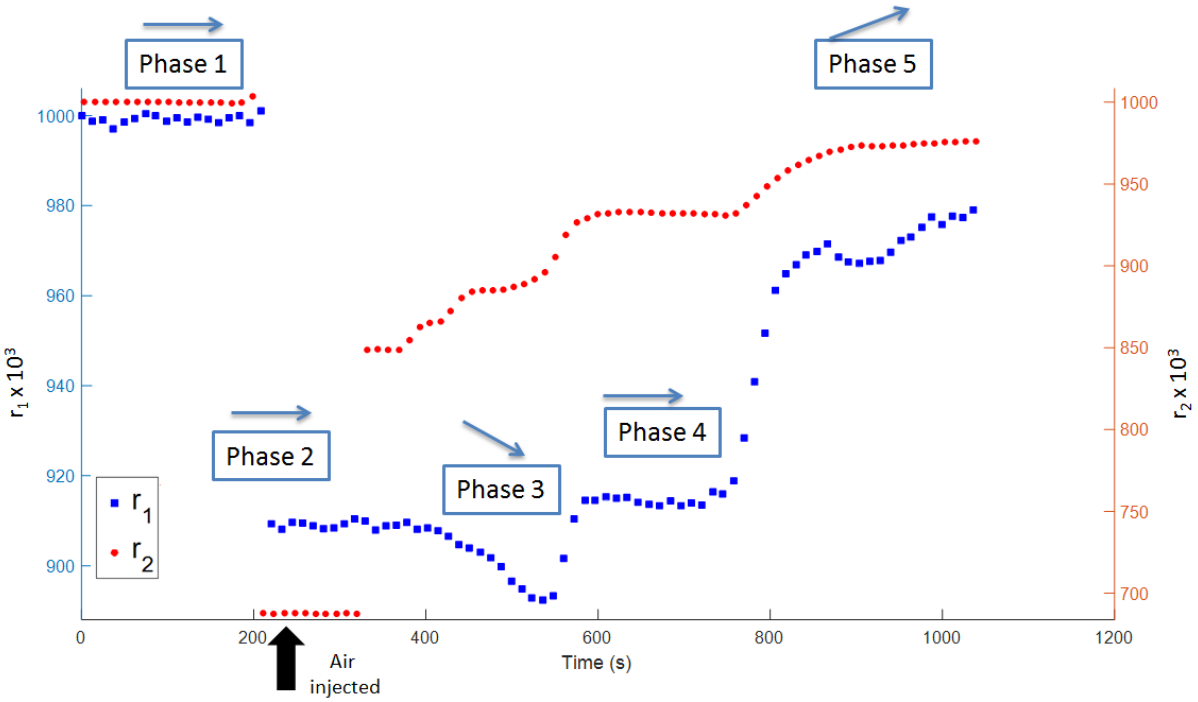


Figure IV.18 Variation of the acoustic reflection coefficients $r_1$ and $r_2$ with time for DTI 4 µm with 80 µ micro-channel injected with SC1 solution: initial phase (phase 1), injection of liquid (phase 2), first wetting transition (phase 3), second wetting transition (phase 4) and complete drying (phase 5)

It is important to note that the transition from phase 2 to phase 3 was not always systematic. It was dependent whether the trapped air is able to exit the DTI network or not. The same measurement with SC1 solution was also performed on the DTI 5 µm and 7 µm samples, but the transition wasn't observed: it gave the same response as that with water like the one obtained for DTI 6 µm (Figure IV.11). Even for the DTI 4 µm and 6 µm the transition wasn't always observed.

In this part, the wetting behavior was studied using real diluted industrial solution (SC1) on the different DTI samples. During the drying phase, appearance of bubbles showed that they were trapped in the DTI network. From the observation of the bubbles at the injection of the SC1 into the micro-channel, it seems that there is some link between the wetting transition and the bubbles formed from the decomposition of $H_2O_2$. Therefore, in the next part we focus on the measurements using hydrogen peroxide solution at 30% concentration (Ready to use and available at the laboratory) with a new DTI 6 µm sample. Also, we will test a new DTI 5 µm sample with the hydrogen peroxide solution (30%) to see if we obtain the wetting transition.

### IV.B.6. $H_2O_2$ (30%) measurements

Following the remarkable wetting transition we obtained with the SC1 solution on the DTI 6 µm, two new samples of DTI 5 µm and 6 µm with 80 µm micro-channel have been fabricated.

The hydrogen peroxide solution at 30% concentration will be used as the liquid to perform the measurements.

Figure IV.19 shows the acoustic reflection coefficients ($r_1$ and $r_2$) values for the DTI 5 µm sample. Liquid is injected into the micro-channel at t = 123 sec where a transition from phase 1 to phase 2 takes place, $r_1$ and $r_2$ decrease to 0.9 and 0.7 respectively. The value taken by $r_1$ here is slightly lower than the value obtained with water for the DTI 5 µm sample (Table IV-1). At t = 300 sec, air is injected into the micro-channel to dry it. Finally a transition from phase 2 to phase 3 takes place shortly after air injection, at t = 362 sec ($r_1 = r_2 = 1$).
As we can observe, the wetting transition is again not observed on the new sample of DTI 5 µm with the $H_2O_2$ (30%) solution. The transitions show a similar pattern obtained with water with the difference being that $r_1 = 0.90$ instead of 0.91.

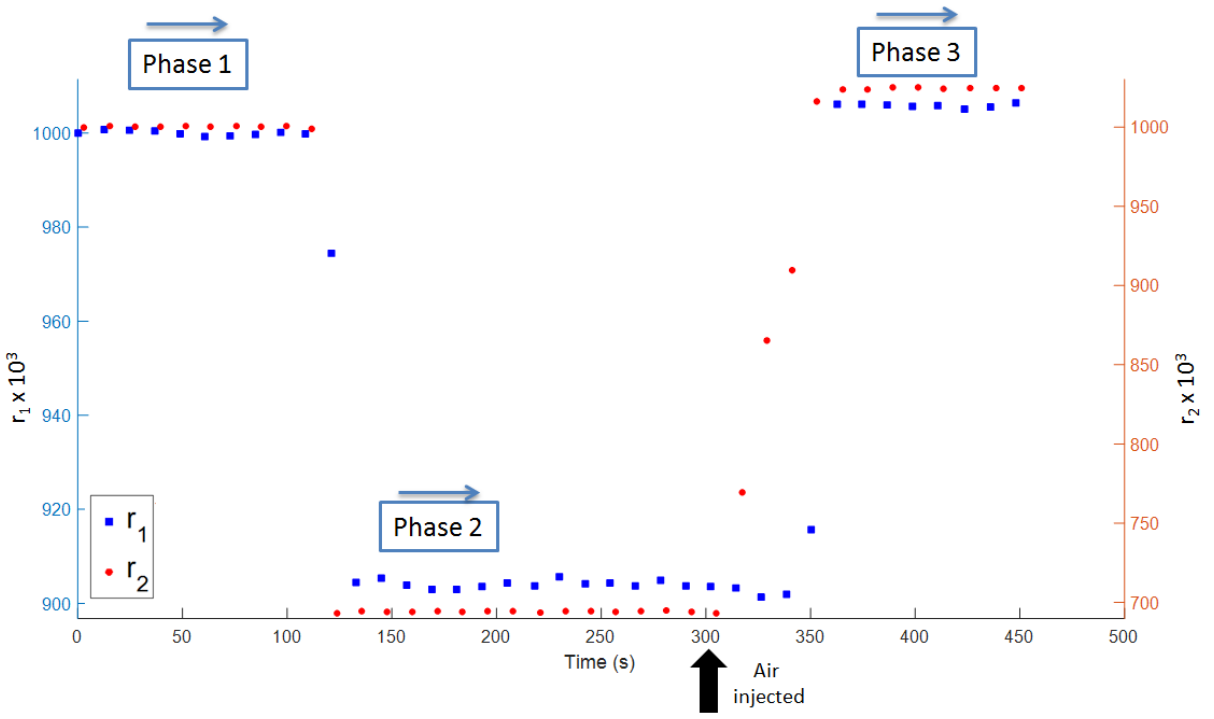


Figure IV.19 Variation of the acoustic reflection coefficients $r_1$ and $r_2$ with time for DTI 5 µm with 80 µ micro-channel injected with $H_2O_2$ (30%) solution: initial phase (phase 1), injection of liquid (phase 2) and complete drying (phase 3)

The measurement with the $H_2O_2$ (30%) solution was also carried out on a new DTI 6 µm sample (Figure IV.20). In phase 2 $r_1$ takes the value of 0.90 slightly lower than the value obtained with SC1 solution since here the $H_2O_2$ is more concentrated (30% of total volume). However the acoustic reflection coefficient on smooth surface for the $H_2O_2$ (30%) gives the same value obtained for water ($r_{Si\ /\ water} = r_{Si\ /\ H2O2\ (30\%)} = 0.86$). Air is injected at t = 300 sec. At t = 455 sec, a transition can be observed from phase 2 to phase 3 where $r_2$ increases to 0.60 and $r_1$ starts decreasing slowly to reach 0.88 at t = 646 sec indicating a wetting transition on the bottom of the trenches. Yet, no air bubbles could be observed by the camera on top of the micro-channel. Finally, a transition from phase 3 to phase 4 instantly takes place where $r_1$ and $r_2$ take the value of 1 (micro-channel is completely dry).

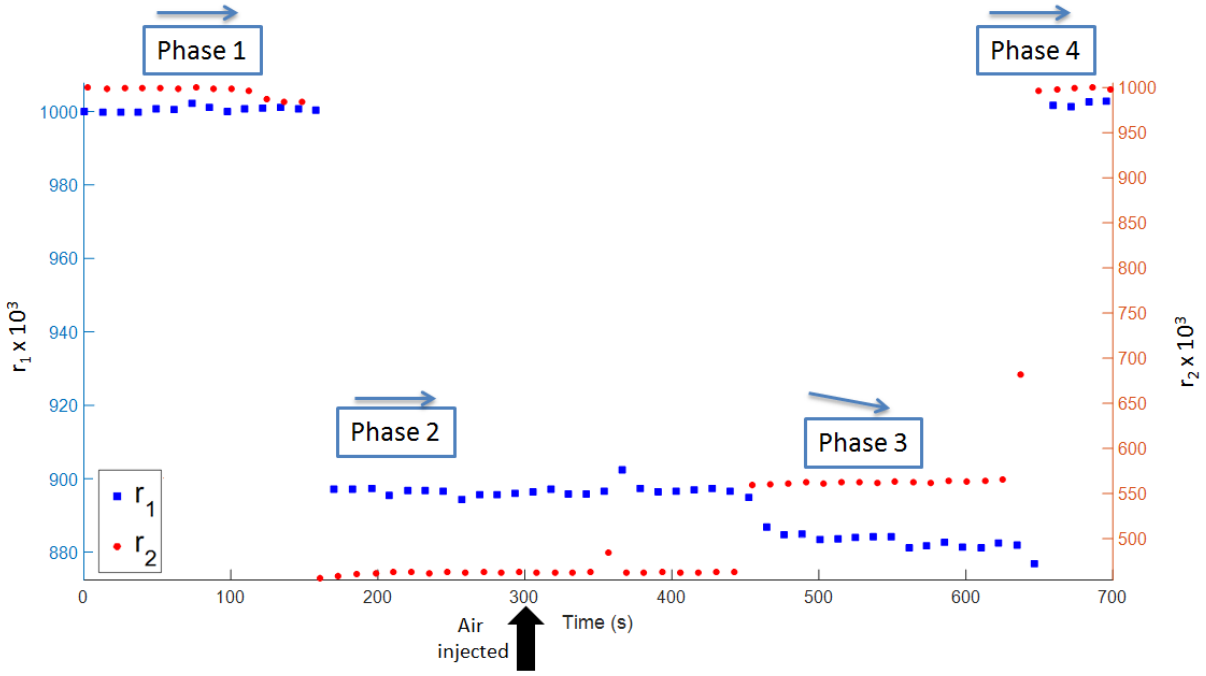


Figure IV.20 Variation of the acoustic reflection coefficients $r_1$ and $r_2$ with time for DTI 6 µm with 80 µ micro-channel injected with H2O2 (30%) solution: initial phase (phase 1), injection of liquid (phase 2), wetting transition (phase 3) and complete drying (phase 4)

As we saw, even if the wetting transition appeared multiple times on the DTI 6 µm, this observation wasn't systematic. Also, we formulated a hypothesis in part IV.B.5 that the wetting transition is directly linked with the observation of $O_2$ bubbles in the injected solution. However, as we can see in Figure IV.21, a wetting transition to total wetting state for pure ethanol ($r_1$ = 0.91 = $r_{th/ethanol}$) on the DTI 4 µm, with 80 µm micro-channel, could be observed during the drying phase (phase 3) without the appearance and influence of the $O_2$ bubbles. This wetting transition observation with ethanol confirms that this transition is directly related to the pressure changes inside the micro-channel when we inject air at 1 bar (liquid is injected at 300 mbar).

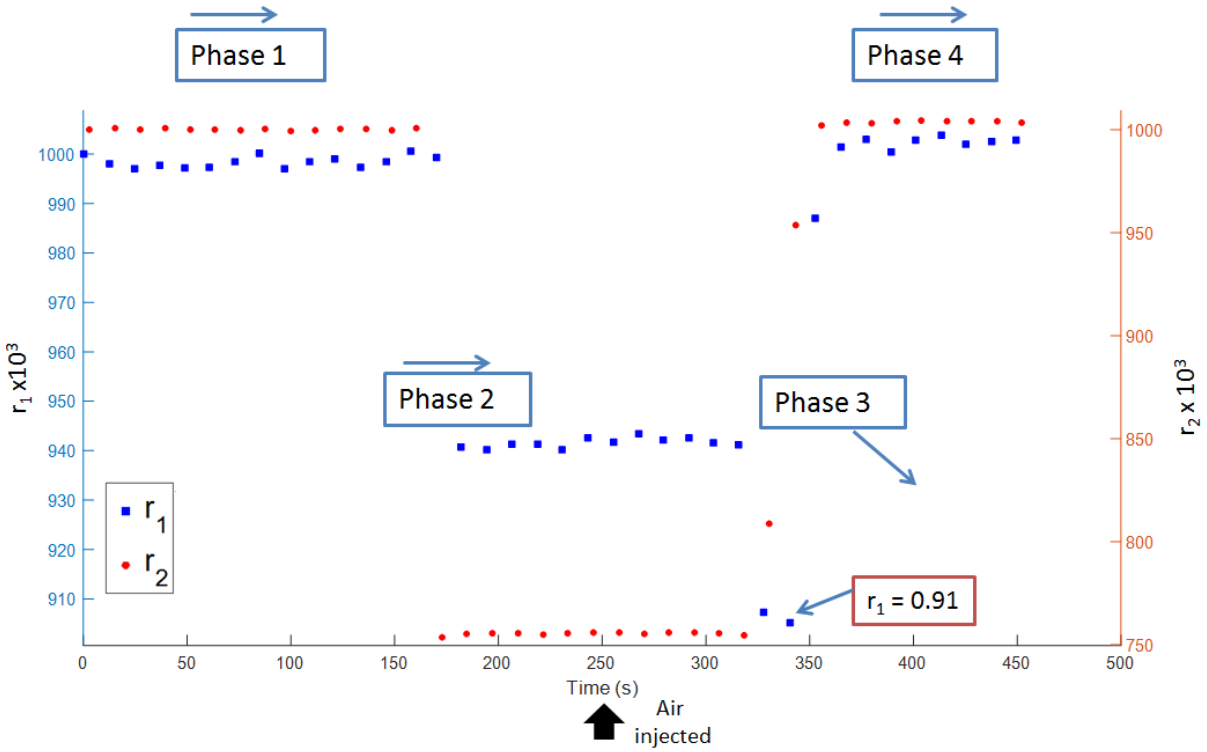


Figure IV.21 Variation of the acoustic reflection coefficients $r_1$ and $r_2$ with time for DTI 4 µm with 80 µ micro-channel injected with pure ethanol: initial phase (phase 1), injection of liquid (phase 2), wetting transition to complete wetting (phase 3) and complete drying (phase 4)

To understand the pressure change effect one explanation could be formulated. The pressure is balanced between the liquid on one side (Laplace pressure), which is acting downward on the liquid air meniscus and the pressure generated from the trapped air pockets on the bottom of the trenches on the other side which is acting upwards on the liquid air meniscus (Figure IV.22). When air is injected into the micro-channel at a pressure of 1 bar, the pressure of the suspended liquid increases and pushes further on the air pockets. It reduces their volume leading to a diffusion of these pockets into the liquid and the increase in the wetted bottom surface area of the trenches (air pockets replaced by the liquid). This diffusion of the air pockets into the liquid could also explain the phenomenon observed in Figure IV.17.b showing tiny air bubbles exiting from the DTI network.

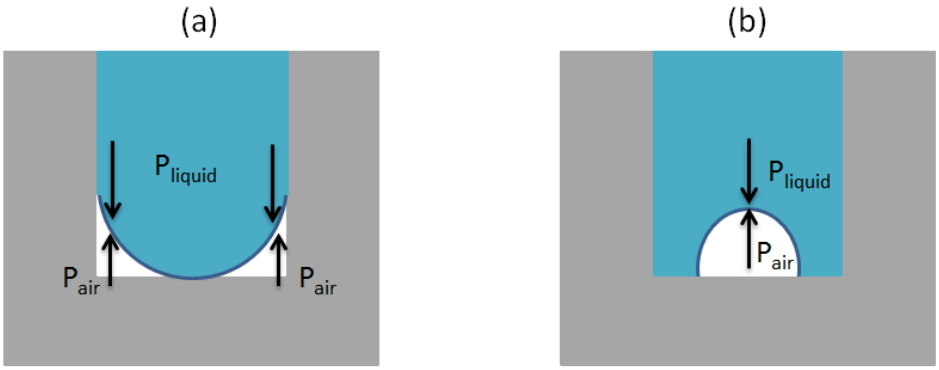


Figure IV.22 Pressure equilibrium between trapped air pockets and suspended liquid inside the DTI for (a) hydrophobic surface and (b) hydrophilic surface

In the next part we're going to see the effect of changing the flow rate or liquid speed inside the micro-channel on the wetting state.

## IV.C. Drying and pattern collapse

As discussed in part I.C.4.b of chapter I, the drying process is an important process in the semiconductor industry since it can lead to defects known as pattern collapse.

During the course of our measurements we noticed that on the majority of samples, some wetting state modifications occurred particularly with the measurements carried out with water: using the same samples which showed partial wetting behavior with water before, after some time delay when we repeat the same measurements, they tend to show little or no wetting at all.

The measurement with water is repeated over the DTI 7 µm sample with 80 µm micro-channel (Figure IV.23). The water reaches the micro-channel at t = 124 sec, where we can see immediately a transition on the $r_2$ from 1 to 0.79 indicating the presence of water on the top surface of the DTI. However, $r_1$ stays stable throughout this transition, within the precision of the measurement ($\pm 0.001$). It confirms that the water didn't reach the bottom surface of the trenches. Air is injected at t = 231 sec to dry the micro-channel after which we can see immediate transition of $r_2$ from 0.79 back to 1. Throughout the different transitions, $r_1$ stayed stable indicating that no wetting occurred on the bottom surface of the trenches. Contrary to the partial wetting where we obtained a value of 0.91 for $r_1$ (Table IV-1), the same sample shows now that it has undergoes a modification of the DTI matrix which makes it impossible the penetration of water to the bottom surface of the trenches.

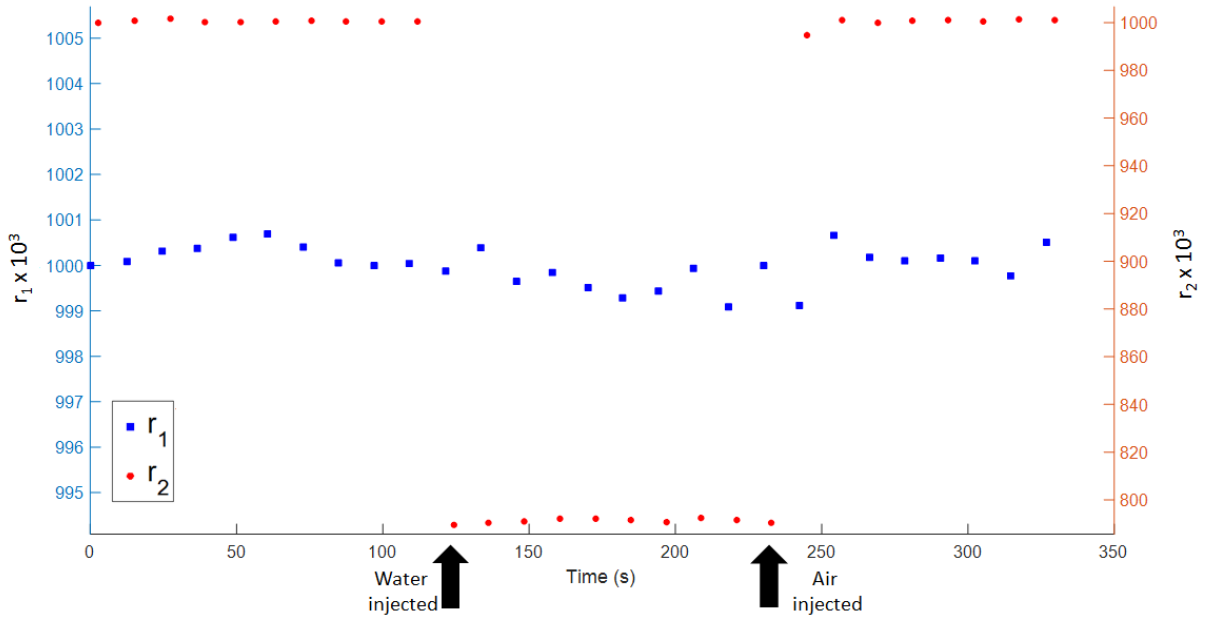


Figure IV.23 Variation of the acoustic reflection coefficients $r_1$ and $r_2$ with time for DTI 7 µm with 80 µ micro-channel injected with water and showing signs of pattern collapse

Another measurement is carried out on the same DTI 7 µm sample, but now with ethanol as the liquid (Figure IV.24). At t = 85 sec ethanol reaches the micro-channel where we can see instantaneous transition for $r_1$ from 1 to 0.94 which is the value obtained in a previous measurement for the same sample (Table IV-1). After this transition, $r_1$ stays stable throughout the liquid flow giving the same response as obtained in previous measurements. At t = 222 sec, air is injected into the micro-channel to dry and at t = 250 sec, $r_1$ takes the original value of 1. This shows that the wetting response of sample didn't change with ethanol.

The different response of wetting between ethanol and water for the sample showing pattern collapse could be explained by the form of trenches deformation (Figure IV.25). When the two trenches next each other deform, the space between them become very small. The water is no longer able to penetrate into them due to high surface tension (72.75 $mN.m^{-1}$) while ethanol was still able to penetrate due to much lower surface tension (22.31 $mN.m^{-1}$).

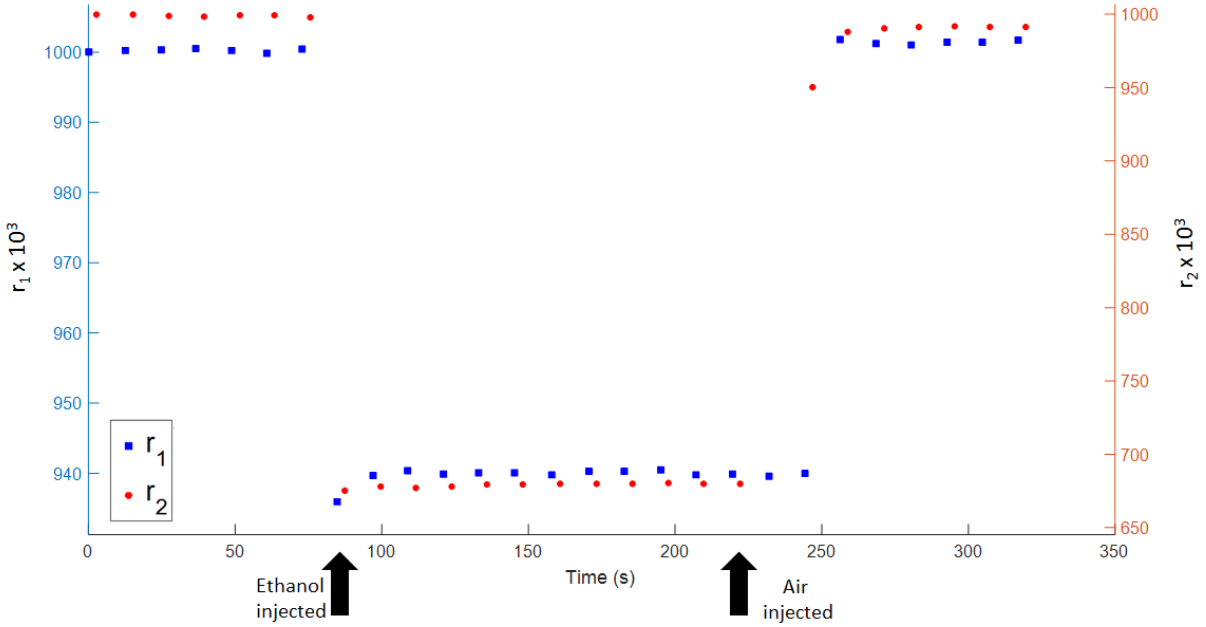


Figure IV.24 Variation of the acoustic reflection coefficients $r_1$ and $r_2$ with time for DTI 7 µm with 80 µ micro-channel injected with ethanol and showing signs of pattern collapse

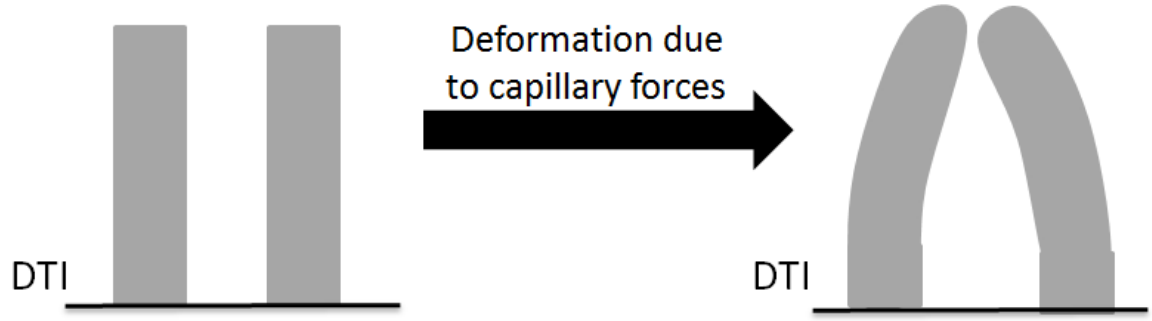


Figure IV.25 Schematic of DTI structures deformation due to capillary forces resulting from the drying process

A similar response is also obtained with the DTI 4 µm with 80 µm micro-channel (Figure IV.26). At t = 86 sec, water enters the micro-channel where we can see instant transition of $r_2$ while $r_1$ decreases slowly with time to reach a value of 0.98 which is higher than the one obtained before (0.91). At t = 330 sec, air is injected into the micro-channel. At about t = 470 sec $r_1$ and $r_2$ start to increase slowly to reach a value of 1 at t = 546 sec. Similar observation of pattern collapse was also seen on the DTI 5 µm and 6 µm. The small transition of $r_1$ indicate that the deformation of the DTI network is not total and some trenches could be intact.

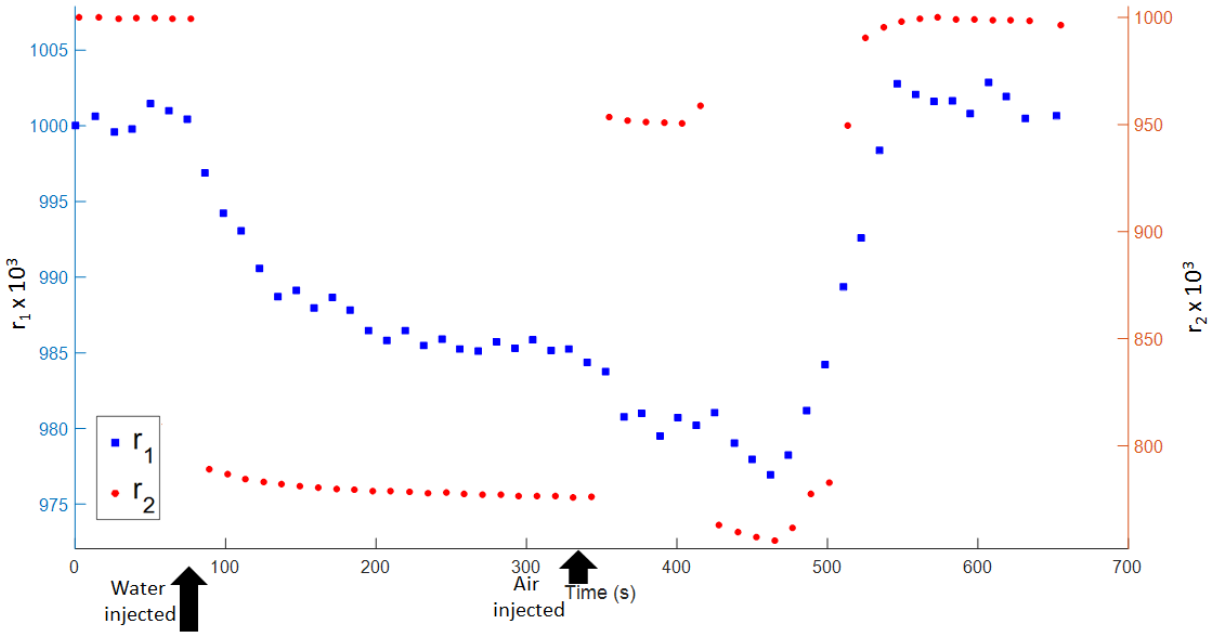


Figure IV.26 Variation of the acoustic reflection coefficients $r_1$ and $r_2$ with time for DTI 4 µm with 80 µ micro-channel injected with water and showing signs of pattern collapse

The worst response of the pattern collapse was observed on the DTI 7 µm sample where there is no wetting measured on the bottom surface of the trenches. This could be related to the aspect ratio of the trenches (ratio of trench's depth to width), the higher the aspect ratio the more susceptible the trenches to pattern collapse.

Another reason which can lead to pattern collapse is the drying method used (Figure IV.27). Yeh *et al*. published results dealing with experiments done to dry line structures [135]. They use four different methods of drying: evaporation in stagnant room air, drying in vacuum oven, drying by flowing nitrogen stream and drying by spin drier at 4500 r.p.m. for 3 minutes. Their results showed that the sample dried in the stagnant room air took the longest time to dry and the samples dried by flowing nitrogen stream and the spin dried very quickly.

Also the samples which were dried by spin drying and the flowing nitrogen stream exhibited superior resistance to pattern collapse. Since air is composed mostly of nitrogen and oxygen, in our case, the drying using air flow can take higher time than using nitrogen flow. This means that our samples are susceptible to pattern collapse which we observed by the seemingly no wetting response with water on the four different DTI samples (4, 5, 6 and 7 μm).

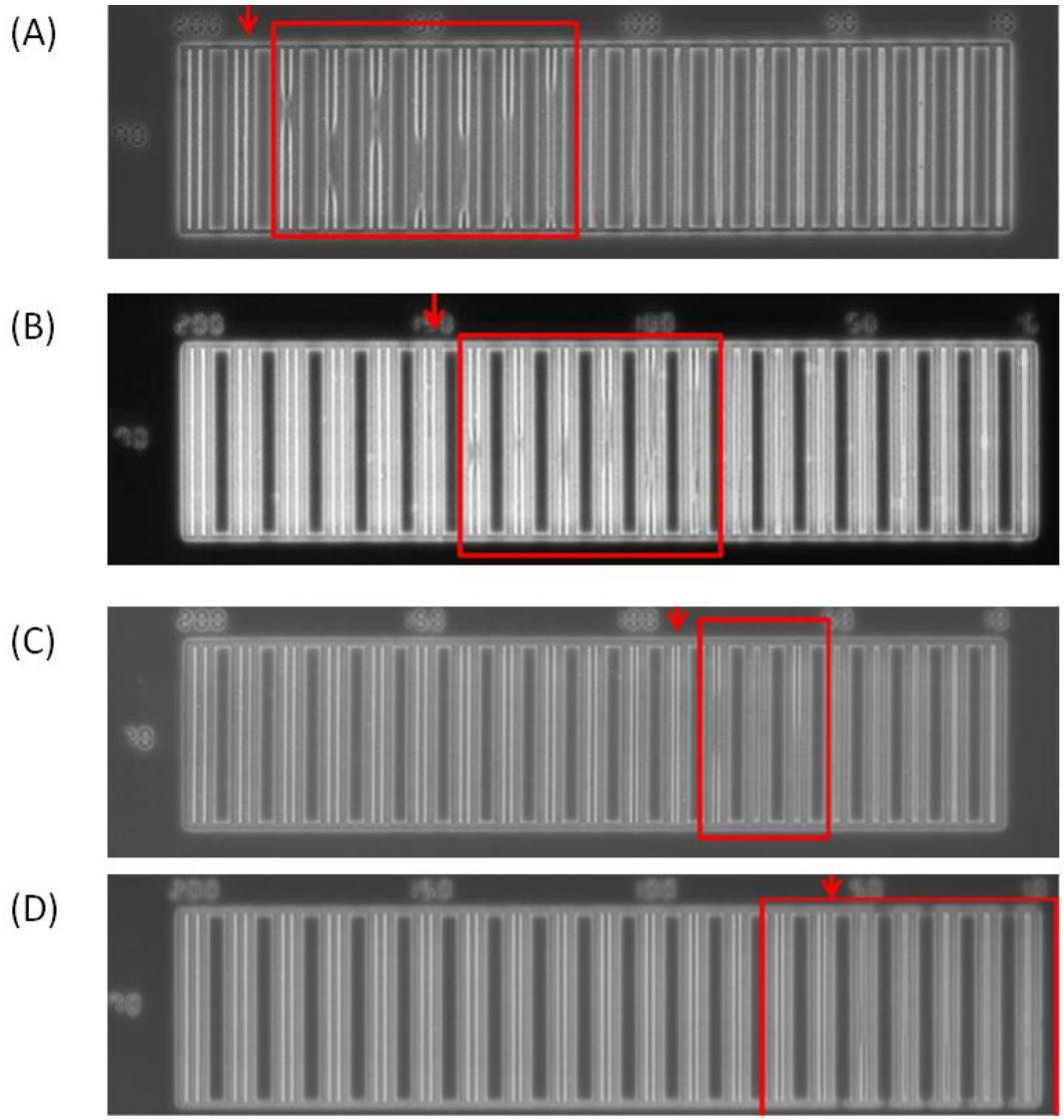


Figure IV.27 SEM images for different drying methods. Nominal 70 nm wide line pairs dried (A) in stagnant room air, (B) in a vacuum room oven, (C) under flowing dry nitrogen gas, and (D) by spin drying at 4500 r.p.m. for 3 mins [135].

To observe the pattern collapse more closely, SEM images of the four DTI samples (4, 5, 6 and 7 µm etch depth) have been taken (Figure IV.28). We can see that the pattern collapse is clearly seen on the DTI 6 µm and 7 µm (Figure IV.28.c and Figure IV.28.d respectively), and it is linked to the small rectangular pillars represented by the red arrows while the larger pillars represented by the blue arrows are intact. These pillars have dimensions of (300 x 565 $nm^2$) and the larger pillars have dimensions of (1.8 x 1.9 $\mu m^2$) so, we get an aspect ratio (ratio of the pillar height to its lateral dimension) of 20 and 23 for the small pillar of DTI 6 µm and 7 µm respectively while the aspect ratio for the larger pillars is 3 and 4 for DTI 6 µm and 7 µm respectively.

As we discussed in part I.C.4.b of chapter I, the larger the aspect ratio the more susceptible the structures to pattern collapse since they will experience larger capillary forces which explain the fact that the smaller pillars with larger aspect ratio (20 and 23) undergo deformation. The DTI 4 µm and 5 µm (Figure IV.28.a and Figure IV.28.b respectively) matrices seem unaffected by the pattern collapse as we can observe the DTI motif is intact. The aspect ratio of the small pillars of DTI 4 µm and 5 µm is 13 and 17 respectively, meaning that the limit of the aspect ratio before observing the pattern collapse is between 20 (DTI 6 µm) and 17 (DTI 5 µm).

The pattern collapse could be observed up closely by the bending of the small rectangular pillars (Figure IV.29). We can observe the smaller pillars bended and attached to the larger ones due to the formation of silicon dioxide ($SiO_2$) solid bridges. These bridges form with time and to break this kind of bond hydrofluoric (HF) cleaning is used at industry.

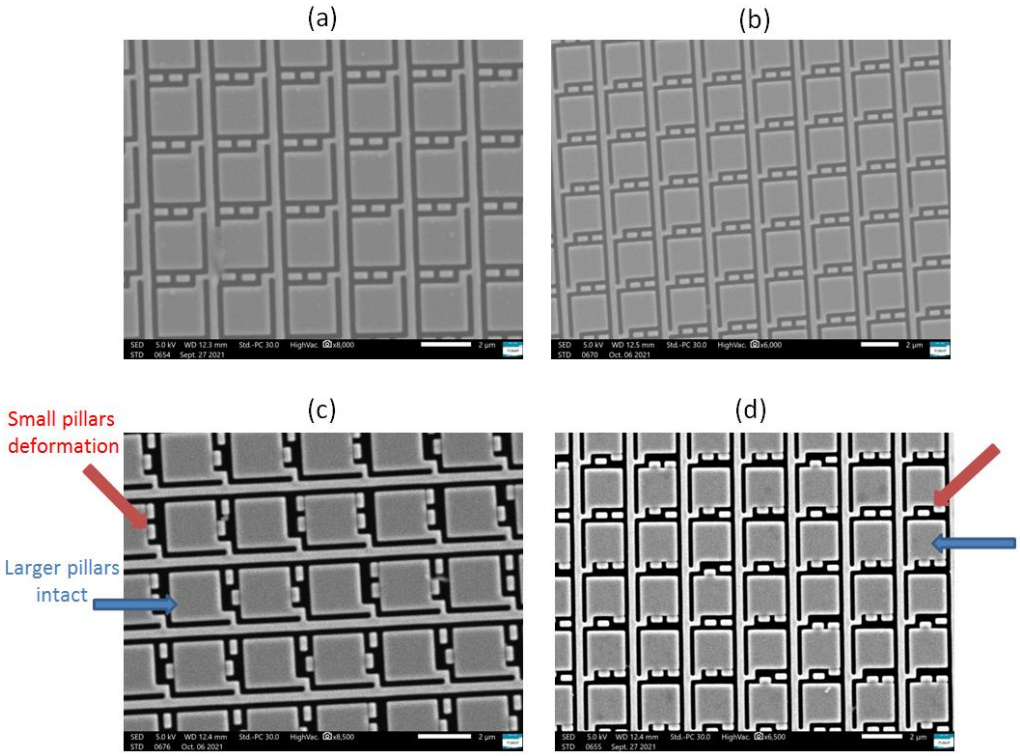


Figure IV.28 SEM images of the DTI matrix showing the etched trenches (black color) and the silicon pillars (grey color) for (a) 4 µm, (b) 5 µm, (c) 6 µm and (d) 7 µm etch depth (Special thanks to Karim Dogheche, Engineer IEMN)

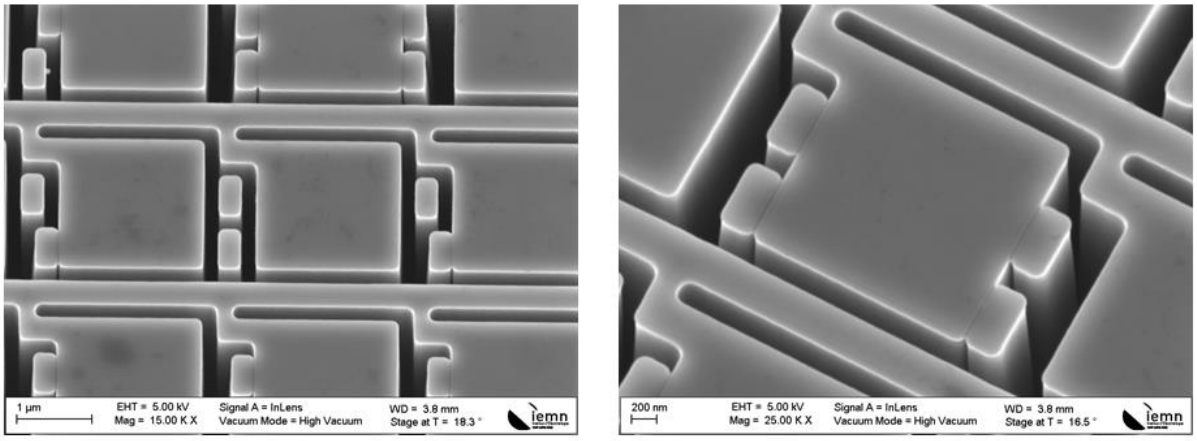


Figure IV.29 SEM images of the DTI 7 µm matrix showing the deformation and bonding of the small pillars to the larger pillars (Special thanks Paul Moustiez, Phd IEMN)

The SEM images provided evidence of the pattern collapse on the DTI 6 µm and 7 µm. However, it doesn't explain the changing of the wetting behavior with water ($r_1$ = 1) on all the samples since the DTI 4 µm and 5 µm seem to be not deformed. Furthermore, even on the DTI 6 µm and 7 µm, the larger pillars are intact which should induce some partial wetting. In fact the partial wetting response is obtained again on the DTI 4 µm and 7 µm with 80 µm micro-channel when we use a 15 % ethanol / water mixture with surface tension of about 46 $mN.m^{-1}$ (Figure III.33.a) as we can see on Figure IV.30. We can observe that the transition from phase 1 to phase 2 (partial wetting) is slow with the appearance of multiple measure point on the $r_1$ curve and again we can see the total wetting transition from phase 2 to 3 ($r_1$ = 0.86) during the drying of the micro-channel. A similar response was observed with the DTI 7 µm with 80 µm micro-channel.

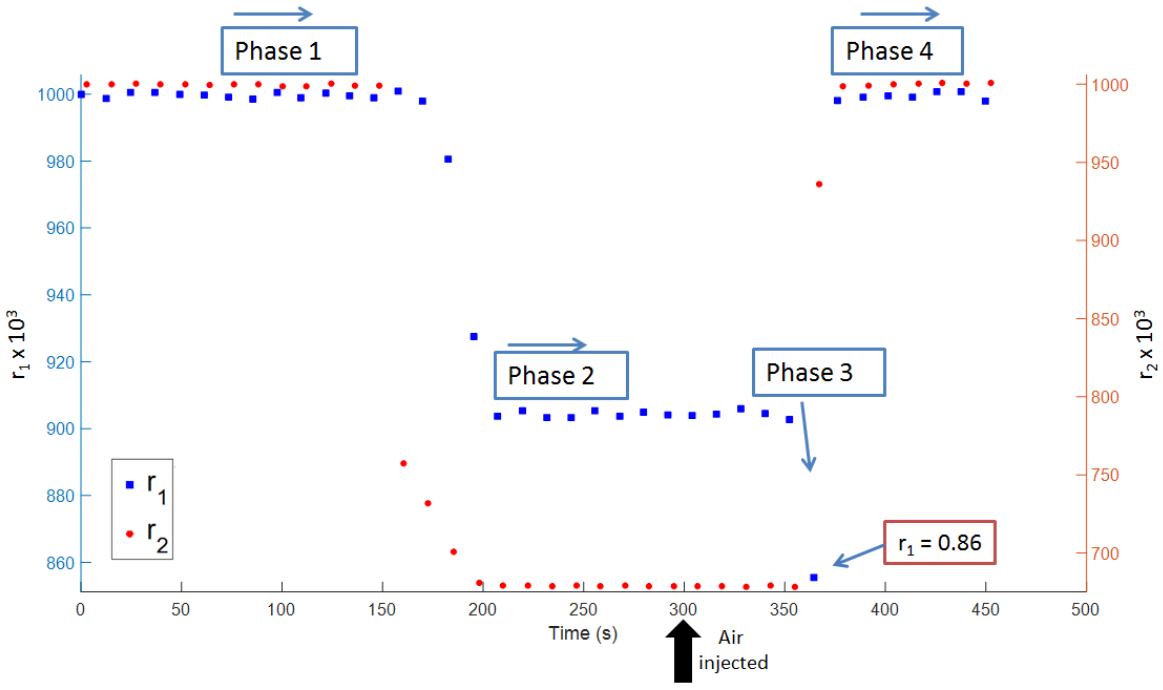


Figure IV.30 Variation of the acoustic reflection coefficients $r_1$ and $r_2$ with time for DTI 4 µm with 80 µ micro-channel showing changing wetting behavior injected with 15 % ethanol / water mixture

This wetting changing behavior indicates that the surface of the DTI has undergone modification inhibiting the partial wetting with water and even with 10 % ethanol / water mixture, presenting surface tension equal to 72.6 $mN.m^{-1}$ and 52 $mN.m^{-1}$ respectively. If we plot the acoustic reflection coefficient on the bottom surface of the trenches $r_1$ on the DTI 4 µm with 80 µm micro-channel after the wetting changing behavior, we will obtain the form given in Figure IV.31. It seems that for high surface tensions between water and 15 % ethanol / water mixture, the value of $r_1$ changed from 0.91 to 0.98 indicating little wetting of the bottom surface and for the rest of the ethanol concentrations, the response stayed the same.

A similar observation was reported by Virgilio *et al*. [83] for the DTI which was subjected to hydrophobic PerFluorooctylTrichloroSilane (PFTS) surface treatment (Figure I.32). It was reported that with PFTS treatment, the reflection coefficient drops from 0.98 to 0.92 for ethanol concentrations between 20% and 50% corresponding to surface tensions between 42.9 $mN.m^{-1}$ and 30 $mN.m^{-1}$. This indicates that our DTI surfaces characteristic had changed to being slightly hydrophobic after repeated measurements of injected liquids and drying. It is important to note that these changes were observed after some time delay on all the used DTI samples (4 , 5 , 6 and 7 µm) with both the 40 µm and 80 µm micro-channels.

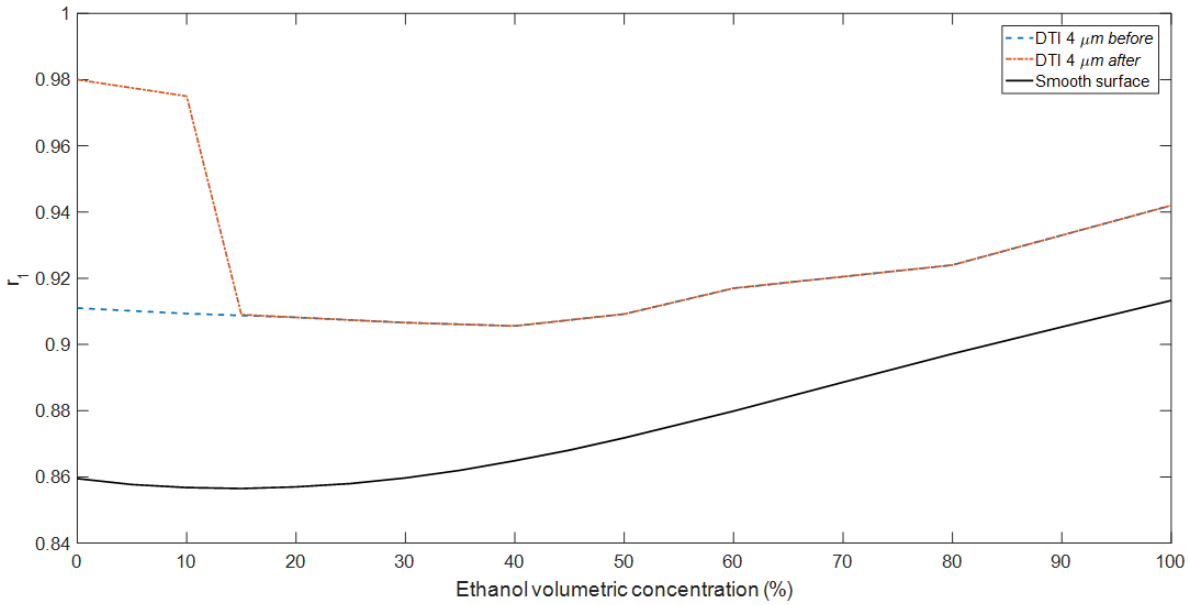


Figure IV.31 Variations of the reflection coefficient $r_1$ on the bottom of the DTI 4 µm before and after wetting changing behavior for different distilled water / ethanol mixtures injected in the 80 µm micro-channel

The modification of the surface characteristic of the DTI after several measurements could be related to the appearance of watermarks [136], [137]. The mechanism of watermarks generation is given in Figure IV.32. The process starts with the diffusion of the oxygen from the ambient air to the water and then to the silicon surface (I). An oxidation reaction takes place at the silicon surface, generating silica $SiO_2$ (II). The generated silica undergoes a hydration reaction and gets dissolved into water as molecules (III and IV). Some of the hydrated silica may ionize producing protons ($H^+$) and silicate ions (V). Finally, the silica ions diffuse into the water accelerating the dissolution of the silica (VI).

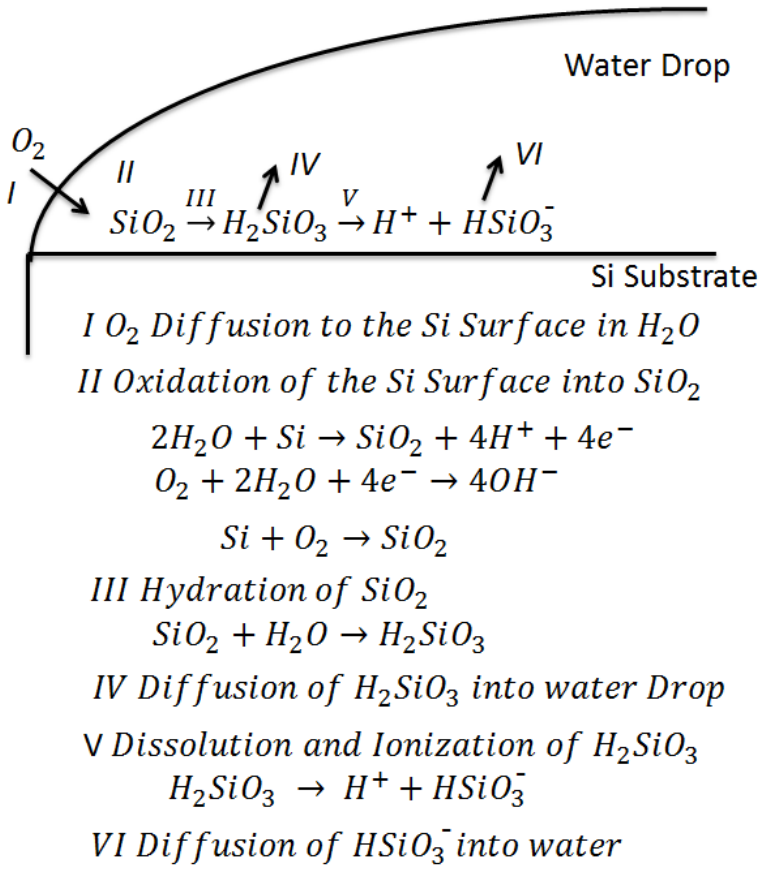


Figure IV.32 Mechanism of watermarks generation. Reproduced from [138]

The result of this reaction is the increase in the concentration of hydrated oxide with time. At the end, when the water completely evaporates, an oxide film is left on the surface of the silicon.

An experiment has been done to see the effect of oxygen in atmosphere in generating watermarks on the surface of the DTI wafer: a DI water drop is deposited on the surface and left to evaporate in the atmosphere (Figure IV.33). Microscopic image of the DTI surface is taken before the water drop deposition (Figure IV.33.a) where we can see the surface is properly clean. After the evaporation of the first water drop, several small water marks appear on the surface (Figure IV.33.b). These watermarks increase in number after the evaporation of the second water drop (Figure IV.33.c) giving evidence that several water marks will be present on the surface of the DTI wafer after the injection of different liquids used and the drying using atmospheric air in the PDMS micro-channel.

In semiconductor industry, to remove watermarks, a diluted hydrofluoric acid (HF) solution is used. However, since the PDMS can degrade under acidic environment [139], we couldn't use this option to remove the formed oxide films.

The formed silica films (watermarks) are considered as surface defects. However, it doesn't explain the changing hydrophobic response of the DTI samples, with water, after several use of the surface for measurements since the silica is considered as hydrophilic. Therefore, the hydrophobic response is related to other surface phenomenon.

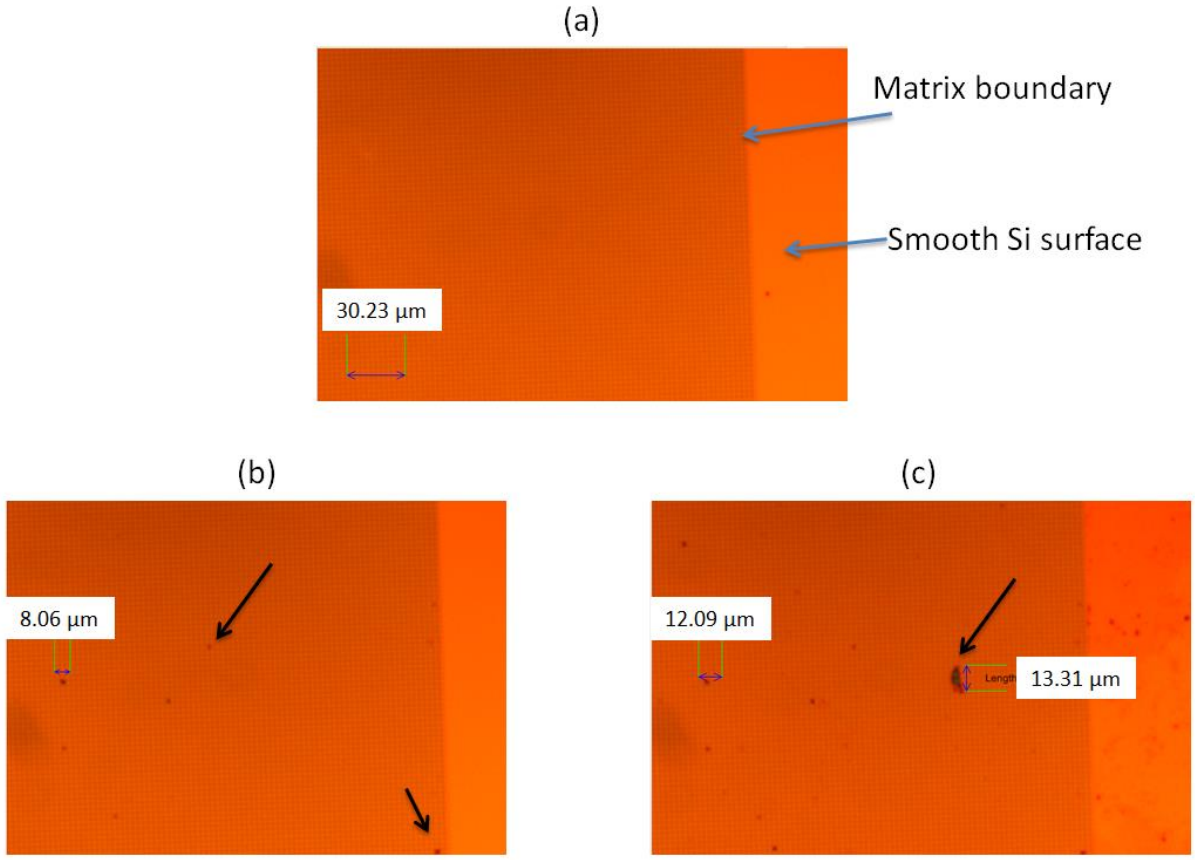


Figure IV.33 Microscopic images of DTI surface showing watermarks after evaporation of water drop (black arrows) (a) Before deposition of water drop, (b) After evaporation of first water drop and (c) After evaporation of second water drop.

Indeed, in literature we found one phenomenon which could explain the hydrophobic response and it is related to the formation of '*hydrophobic silica*'. As we mentioned before the silica alone is hydrophilic, but when silica nanoparticles chemically combine with other hydrophobic group like PDMS, it becomes hydrophobic [140]. Ducom *et al*. [141] showed that by leaving PDMS sample in demineralized water for 15 days, they measured some level of degradation of the PDMS. It is thus possible that soluble non-polymerized monomers of the PDMS got bonded to the formed silica nanoparticles due to the hydrolysis of the PDMS in aqueous solutions. This created a hydrophobic surface that we were able to observe through the changing wetting response of the DTI. However, to confirm this observation more surface analysis tools like Energy Dispersive X-Ray Analysis (EDX) is needed to find out the chemical species present at the surface.

## IV.D. Conclusion

In this chapter, we started by introducing the difficulty of using the FDTD 2D model to simulate the echoes response DTI geometry which is complex and required, after investigation, a 3D model. Then we saw the difficulty in exploiting the top surface reflection

coefficient ($r_2$) due to the mix of echoes and the lack of a 3D model to analyze the different echoes in absolute value. However, it served as quantitative parameter in following the wetting kinetics.
In the next part, the acoustic reflection coefficient measurements were performed on four types of DTI wafer with different etch depths (4, 5, 6 and 7 μm) and for each type of DTI sample two micro-channels with different thickness (40 and 80 μm) were used to inject the different liquids. The measurements with the 40 μm micro-channels were performed using different water / ethanol mixtures and it was shown that for the four DTI wafers non-complete and partial wetting behaviors were observed. With the 80 μm micro-channels, a new real-time technique was introduced using the reflection coefficients on the top and bottom echoes. This technique enabled faster data acquisition time and also direct observation (within a delay of some seconds) of the wetting and drying phases. The same measurements using water / ethanol mixtures were performed on the DTI wafers with 80 μm micro-channels and a similar behavior of partial wetting to the one observed using the 40 μm micro-channel was obtained on the four DTI wafers.

Using the 80 μm micro-channel, we did measurements with distilled water and pure ethanol using different flow rates on the DTI 4 μm with 80 μm micro-channel and we saw that there was no effect on the wetting state for the different flow rates (10 $ml.h^{-1}$ – 120 $ml.h^{-1}$).
Next, the measurements with diluted version of SC1 solution (cleaning solution used at STMicroelectronics) were performed on the four DTI wafers. During the drying phase, a wetting transition was observed, with $r_1$ decreasing to 0.87 for the 6 μm DTI wafer which is very close to the complete wetting value (0.86), coupled with the liberation of trapped air inside the trenches. This wetting transition was linked to the presence of oxygen bubbles in the SC1 solution due to the decomposition of $H_2O_2$. Similar observation was also observed using $H_2O_2$ (30%) on a new 6 μm DTI wafer confirming our theory of trapped air pockets inside the trenches which are preventing complete wetting.

Finally, we saw that the wetting response DTI wafers were exposed to modification due to pattern collapse of the DTI pillars and the generation of watermarks on the surface. The pattern collapse is related to the high capillary forces present on the high aspect ratio pillars causing their bending, while the watermarks are related to the presence of oxygen in the drying process, leading to the formation of hydrophobic silicon.

## General Conclusion

This PhD work was done within the framework of the joint STMicroelectronics / IEMN laboratory governed by a CIFRE thesis, between an industrial problem encountered by STMicroelectronics and the potential of an original characterization tool developed at the IEMN.

The context of the problem for STMicroelectronics falls within the application of wet chemical treatments in the processes of etching and cleaning of the constituent patterns of their chips in connection with technologies of imagers, flash memories and 3D integration. The micro / nanometric dimensions of the deep trench isolation (DTI) can then constitute an obstacle to the complete filling of the micro / nanostructures with liquids and the chemical treatment will not be effective. In addition, the drying of these high aspect ratio DTI pose a problem known in industry as pattern collapse which is basically the deformation of the etched structures. The complete wetting and drying of the micro / nanostructures therefore represents an important issue for the manufacture of non-defective products. At IEMN, a high-frequency acoustic reflectometry method had already been developed and used (thesis done by Christophe Virgilio [10] at IEMN) successfully to characterize the wetting of liquid droplets on STMicroelectronics structures done at purely micrometric and nanometric scales. However, to approach the industrial cleaning process used at STMicroelectronics (Single wafer process) which depend on the flow of cleaning liquids, the idea of characterizing the wetting state of the DTI using a system of micro-channel to recreate the flow of liquids was proposed as a transition from the static characterization (droplet) to a dynamic wetting characterization (liquid flow).

The objective of the thesis is then to characterize the dynamic (liquid flow) wetting and investigate the drying process of micro / nanometric DTI structures manufactured by STMicroelectronics by the high frequency acoustic reflectometry method.

The first chapter introduced a reminder of the basics of the physico-chemistry of the wetting of ideal surfaces and surfaces exhibiting texturing in connection with the problems that may be encountered in the microelectronics industry. Different methods of wetting characterization and some results obtained previously with the acoustic reflectometry method were presented along with some basic of flow equations in micro-channels bounded by textured surface. Before approaching the heart of the thesis work, the essential notions of physics (and mathematics) concerning the propagation of acoustic waves were introduced in Chapter II. In addition we presented in Chapter II a state of the art on physical models reflecting the behavior of acoustic waves in micro / nanostructures. It was seen that none of the models presented could be applied directly for the micro / nanostructures of STMicroelectronics. A finite difference model (FDTD) was presented when the wavelength is smaller or comparable to the dimensions texturing which was used to simulate the acoustic wave interactions in the studied DTI structures. The principle of the acoustic reflectometry method was presented in detail in chapter III as well as the different signal processing methods. The experimental conditions of measurement and the entire development process of piezoelectric transducers, from their theoretical design to manufacturing methods, were also presented. In addition, a

new technique involved in modifiying the piezoelectric transducers fabrication in Chapter III in order to generate higher amplitudes of transversal waves was also introduced. However, it was difficult to implement it in our wetting evaluation measurements, but it can open perspectives for other applications. Finally we introduced the PDMS micro-channels dimensioning and fabrication based on hydrodynamic data from the industrial cleaning process at STMicroelectronics as well as the experimental measuring bench. This developed microfluidic system allowed a passage from static to dynamic wetting and drying characterization of the DTI structures.

The final results concerning nanostructures wetting were obtained thanks to our acoustic methods and were provided in chapter IV. We saw that the exploitation of the 2D FDTD model to compare with the experimental results was tedious due to the complexity of the DTI geometry which require a 3D model. The application of the acoustic reflectometry method made it possible to conclude definitively on the state of wetting of the DTI of different etch depths (4, 5, 6 and 7 μm), each one studied with two micro-channels with 40 μm and 80 μm. Thus, it has been shown that all the samples gave partial wetting response with the tested liquids presenting different surface tensions. This behavior was attributed to trapped air pockets inside the nanometric trenches. We were also able to calculated the percentage of wetted surface of the trenches for different ethanol / water mixtures based on the measured acoustic reflection coefficients. A new technique was introduced consisting of monitoring the acoustic reflection coefficients in real-time which enabling us to monitor the wetting transition as well as the drying phases. This new technique authorize us to show that, during the drying phase, a wetting transition from partial wetting to semi or complete wetting of the DTI was possible. This was attributed to pressure changes inside the micro-channel which enabled trapped air pockets to escape from the DTI network as was shown with the SC1, $H_2O_2$ and ethanol solutions. Finally, we discussed the effect of capillary forces during the drying phse in producing pattern collapse on the DTI network. It was shown by multiple SEM images that the deformation occurred on the DTI of 6 μm and 7 μm etch depth due to high aspect ratio of the pillars which ranged from 20 to 23.

The use of the high frequency acoustic reflectometry method coupled with the PDMS micro-channel system therefore made it possible to meet the expectations of STMicroelectronics for the study of the DTI structures.

Concerning the perspectives, we can visualize three major ones: First of all, improving the performance of the piezoelectric transducers in generating higher amplitudes of transverse waves. We saw in Chapter III that the new technique of depositing an inclined ZnO layer enabled us to make the transducers generating both longitudinal and transverse waves. However, the amplitude of the transverse waves was smaller than the longitudinal ones. Also, coupled with the loss of acoustic energy in the diffusive DTI structures, the tranverse signal was difficult to exploit and to use to obtain sufficient precision and without mix of echoes. As it was shown by a simulation done before at the IEMN [10], the transverse waves has the potential of revealing more information about the wetting and the drying state so, the improvement of generation of these waves hold many adavantages in chracterizting micro / nanostructures.

Secondly, It is necessary to develop a 3D FDTD model or another type of 3D model which would provide better theoretical results for the most complex textured surfaces. As we saw in Chapter IV, the 2D FDTD model was not efficient in simulating the acoustic respense of the DTI structures to the their complex geometry. One aspect we can work on to see the acoustic impact of the 7.5 nm silicon dioxide layer in the 2D model. In case the impact of this layer is insignificant, we can ignored it in the 3D model hence, the space step will be higher and corresponding to the 55nm silicon nitride layer thus, reducting the calculation time. A 3D acoustic model would provide much needed information about the acoustic interactions with the nanometric structures as well as the acoustic mode change inside the DTI network which will enable the exploitation and identification of the different reflected echoes.

Finally, it will be advantageous to investigate in more details the drying phenomenon of the DTI. One aspect we encountered during the automatic measurements of the reflection coefficients is the high acquisition time of 12 sec between two consecutive data points, while the drying inside the DTI structures occurrs in shorter times. Decreasing the acquisition times, would provide insights important for STMicroelectronics on the drying times with different liquids. Another aspect is the phenomenon of pattern collapse that occurs due to capillary forces. Finding methods to counter this phenomenon through experimenting drying steps with liquids having lower surface tension and possibly decreasing the drying times through the use of nitrogen gas instead of atmospheric air are couple of examples which could give answers to avoid the pattern collapse which is a major problem still encountered by STMicroelectronics to this day.

# Appendix

## *Appendix A: Laser lithography for micro-channel mold fabrication*

Threre are several steps included in the mold fabrication. These include preparing the design in form of Graphic Design System (GDS) file, deposition of the resists, laser writing and finally development of the resist.

1- ***Preparing the design:***

The GDS file which defines the micro-channel 2D dimensions was preparing using the CleWin layout editor. The dimensions of the micro-channel were chosen so that they cover the area of the DTI matrix (Figure A.1).

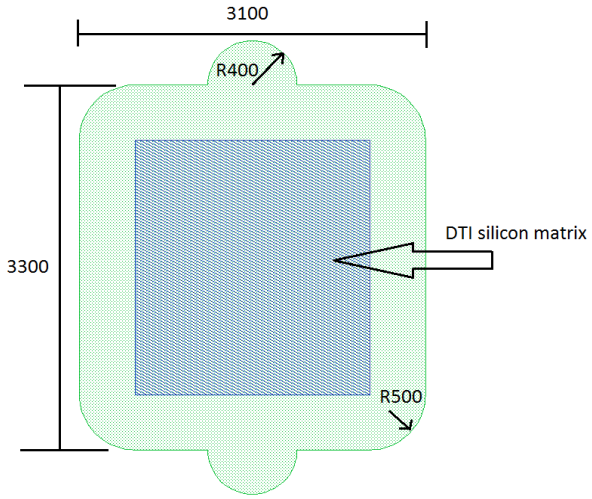


Figure A.1 Schematic illustrating the micro-channel 2D design in the GDS file

2- ***Resist deposition***

Smooth silicon 3 inches in diameter is used as the mold's surface. The process starts with the deposition of SU-2002 (Kayaku advanced materials Inc.) resist layer of 2 µm thickness using a spin coater (Figure A.2).
The parameters inserted to the spin coater are the following using two open cycles: $V_1$ = 500 r.p.m., $t_1$ = 5 s and $A_1$ = 500 r.p.m./s and $V_2$ = 3500 r.p.m., $t_2$ = 30 s and $A_2$ = 1000 r.p.m./s.

Then the wafer is baker on a hot plat at temperature ($T$) = 95$^{O}$C during 2 minutes.

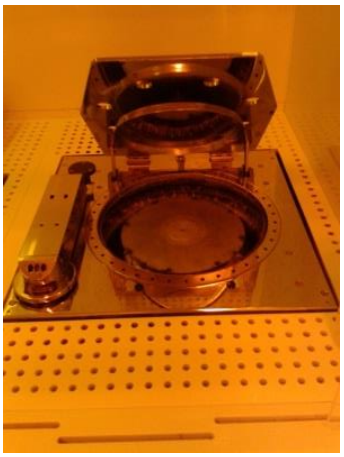

Figure A.2 photo of RC8 Karl Süss spin coater

The SU8 2002 (Kayaku advanced materials Inc.) layer serves as a bonding layer between the silicon surface and the next resist layer that will be deposited.

Depending on the desired thickness of the micro-channel mold (40 μm or 80 μm), one of the two resists SU-8 2035 or SU-8 2075 (Kayaku advanced materials Inc.) is chosen. The two resists differ by viscosity where SU-8 2075 being more viscous.

- 40 μm mold thickness:

The SU-8 2035 is deposited above the SU-8 2002 layer using the following parameters for the spin coater using two open cycles: $V_1$ = 500 r.p.m., $t_1$ = 5 s and $A_1$ = 500 r.p.m./s and $V_2$ = 3500 r.p.m., $t_2$ = 30 s and $A_2$ = 1000 r.p.m./s.

Then a baking process at $T$ = 65$^{O}$C is done during 3 minutes followed directly by another baking at $T$ = 95$^{O}$C for 6 minutes using a hot plate.

- 80 μm mold thickness:

The SU-8 2075 is deposited under the following parameter for the spin coater using two open cycles: $V_1$ = 250 r.p.m., $t_1$ = 10 s and $A_1$ = 250 r.p.m./s and $V_2$ = 2700 r.p.m., $t_2$ = 30 s and $A_2$ = 500 r.p.m./s.

After that a baking process at $T_1$ = 65$^{O}$C is done for 5 minutes followed directly by another baking at $T_2$ = 95$^{O}$C for 20 minutes using a hot plate.

3- ***Laser writing***

After the deposition of the resists, the silicon wafer is moved to the laser writing equipment KLOE Dilase 65 (Figure A.3). The creating GDS file of the micro-channel design is inserted in to the bench and a direct laser pattern the deposited resin with the micro-channel design. The process generally tool between 30 to 45 minutes.

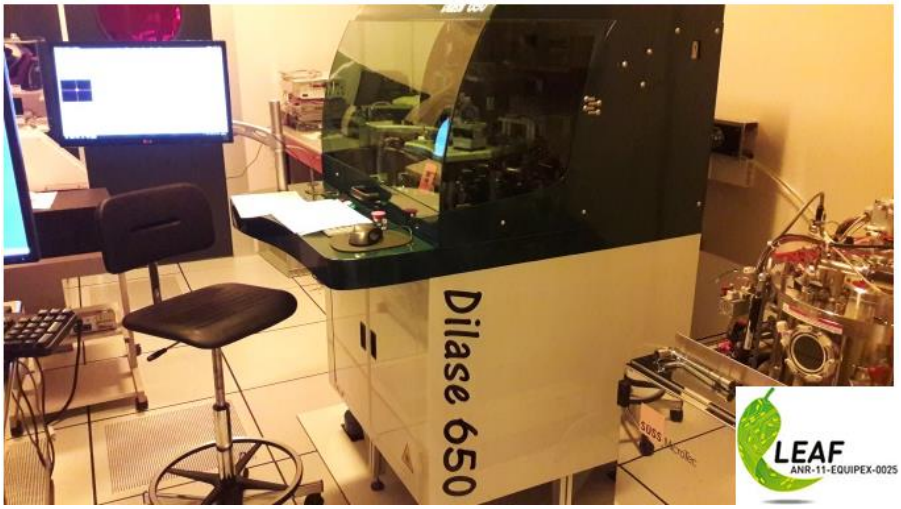


Figure A.3 Photo of the laser writing equipment KLOE Dilase 650

The parameter of the laser writing include writing speed = 30 mm.min$^{-1}$, laser power at 100 % and wavelength equal to 375 nm. These parameters were specifically chosen after multiple testing to avoid cracks in the resist and long operational time (Figure A.4).

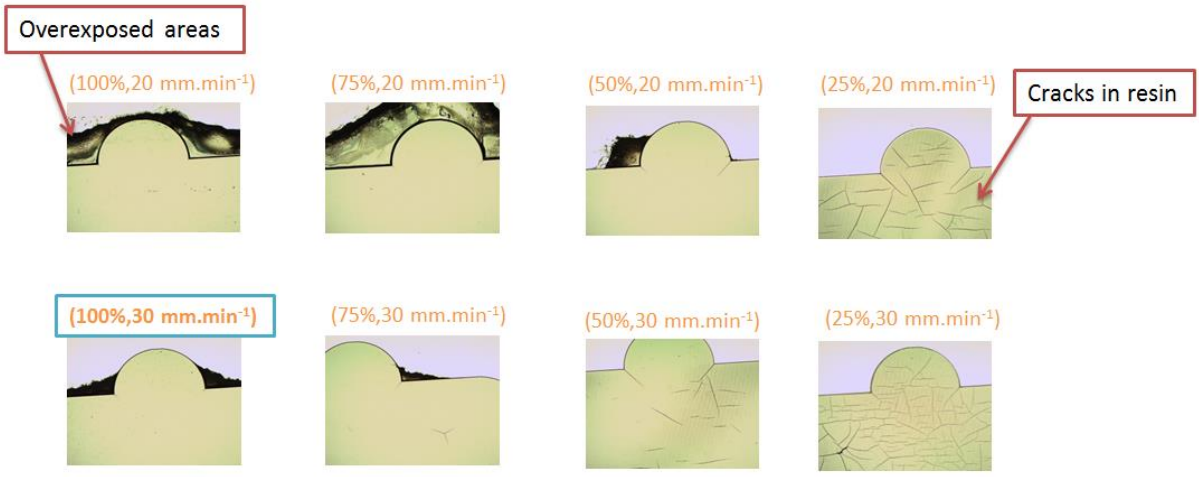


Figure A.4 Photos of different testing done on the mold using different parameters of the laser writing (% power, writing speed). We can observe overexposed areas of resin due to high laser power and formation of cracks on the resist for lower powers. The best configuration (100 %, 30 mm.min$^{-1}$) was chosen.

4- ***Development of resist***

Finally, after exposed the resist layer to laser, the wafer is place on a hot plate as part of the post exposure process. This increase in temperature will make the unexposed areas of the resist soluble in order to be removed in the development solution SU-8 developer (Kayaku advanced materials Inc.).

The temperature and time depend on the resist type and thickness. The parameters are given as:

- SU-8 2035 of 40 µm thickness

$T_1$ = 95$^{O}$C for $t_1$ = 5 minutes using hot plate then placed for $t$ = 5 minutes in the SU-8 developer solution.

- SU-8 2075 of 80 μm thickness

$T_1$ = 65$^{O}$C for $t_1$ = 5 minutes directly followed by another post-baking at $T_2$ = 95$^{O}$C for $t_2$ = 10 minutes at hot plate then placed for $t$ = 8 minutes in the SU-8 developer solution.

At last the developed wafer is rinsed with isopropanol for $t$ > 30 s and dried with nitrogen flow.

## References


[1] Basic, Josip, « Turbulent history of fluid mechanics (brief essay) », 2016.

[2] Mao, Chun & Zhao, Wen-Bo & Luo, Wen-Ping & Liang, Cun & Hou, Xiao & Huang, Xiao-Hua & Liu, Hong-Ke & Xiao, Ying-Hong & Bao, Jian-Chun & Shen, Jian, « Geometric bionics: Lotus effect helps polystyrene nanotube films get good blood compatibility », in *Nature Precedings*, 2009. [En ligne]. Disponible sur: https://doi.org/10.1038/npre.2009.3002.1

[3] Verboven, Pieter & Pedersen, Ole & Ho, Quang Tri & Nicolaï, Bart & Colmer, Timothy, « The mechanism of improved aeration due to gas films on leaves of submerged rice », in *Plant, cell & environment*, vol. 37,10, 2014, p. 2433‑52.

[4] T. Wagner, C. Neinhuis and W. Barthlott, « Wettability and Contaminability of Insect Wings as a Function of Their Surface Sculptures », in *Acta Zoologica*, vol. 77,3, 1996, p. 213‑225.

[5] Chambers LD, Stokes KR, Walsh FC and Wood RJK, « modern approaches to marine antifouling coatings », in *Surface and Coatings Technology*, vol. 201,6, 2006, p. 3642‑3652.

[6] Ogihara H, Xie J, Okagaki J, and Saji T, « Simple Method for Preparing Superhydrophobic Paper: Spray Deposited Hydrophobic Silica Nanoparticle Coatings Exhibit High Water-Repellency and Transparency », in *Langmuir*, vol. 28,10, 2012, p. 4605‑4608.

[7] Moore G.E, « Cramming more Components onto Integrated Circuits », in *Reprinted from Electronics, volume 38, number 8, April 19, 1965, pp.114 ff.," in IEEE Solid-State Circuits Society Newsletter, vol. 11, no. 3, pp. 33-35, Sept. 2006*,

[8] W. Arden, M. Brillouët, P. Cogez, M. Graef, et al., « " More-than-Moore " White Paper », in *The International Technology Roadmap for Semiconductor*, 2010.

[9] Khakifirooz, Marzieh & Fathi, Mahdi & Chien, Chen-Fu, « Modelling and decision support system for intelligent manufacturing: An empirical study for feedforward-feedback learning-based run-to-run controller for semiconductor dry-etching process », in *The International Journal of Industrial Engineering: Theory, Applications and Practice*, vol. 25, 2018, p. 828‑848.

[10] Christophe Virgilio, « Caractérisation du mouillage de surfaces micro/nanostructurées par méthode acoustique haute fréquence : application aux traitements humides dans l'industrie de la microélectronique. Micro et nanotechnologies/Microélectronique », Université de Valenciennes et du Hainaut-Cambresis, 2017.

[11] T. Young, « An essay on the cohesion of fluids », in *Philos. Trans. R. Soc. London*, vol. 61, 1805, p. 65–87.

[12] D. Li, A.W. Neumann, in *Applied Surface Thermodynamics*, J.K. Spelt, A.W. Neumann., Dekker, New York, 1996, p. 109.

[13] R.V. Sedev, J.G. Petrov, A.W. Neumann, « Effect of Swelling of a Polymer Surface on Advancing and Receding Contact Angles », in *Journal of Colloid and Interface Science*, 180 vol., 1996, p. 36‑42.

[14] A.W. Neumann, « Contact angles and their temperature dependence: thermodynamic status, measurement, interpretation and application », in *Advances in Colloid and Interface Science*, vol. 4,2‑3, 1974, p. 105‑191.

[15] R. N. Wenzel, « Resistance of solid surfaces to wetting by water », in *Ind. Eng. Chem.*, vol. 28, n° 8, 1936, p. 988–994.

[16] José Bico, Uwe Thiele, David Quéré, « Wetting of textured surfaces », in *Colloids and Surfaces A: Physicochemical and Engineering Aspects*, vol. 206, Issues 1–3, 2002, p. 41‑46.

[17] A. Marmur, « Wetting on hydrophobic rough surfaces : to be heterogeneous or not to be? », in *Langmuir*, vol. 19, n° 20, 2003, p. 8343–8348.

[18] Gao, Lichao, and Thomas J McCarthy, « How Wenzel and cassie were wrong », in *Langmuir : the ACS journal of surfaces and colloids*, vol. 23,7, 2007, p. Langmuir : the ACS journal of surfaces and colloids.

[19] Kung, Chun Haow (Bryan) & Sow, Pradeep & Zahiri, Beniamin & Mérida, Walter, « Assessment and Interpretation of Surface Wettability Based on Sessile Droplet Contact Angle Measurement: Challenges and Opportunities », vol. 6, 2019.

[20] Marmur, Abraham, « Soft contact: Measurement and interpretation of contact angles. Soft Matter », in *Soft Matter*, vol. 2, 2006, p. 12‑17.
[21] Mchale, Glen, « Cassie and Wenzel: Were They Really So Wrong? », in *Langmuir : the ACS journal of surfaces and colloids*, vol. 23, 2007, p. 8200‑5.
[22] Gershon Wolansky, Abraham Marmur, « Apparent contact angles on rough surfaces: the Wenzel equation revisited », in *Colloids and Surfaces A: Physicochemical and Engineering Aspects*, vol. 156,1‑3, 1999, p. 381‑388.
[23] Yan, Y. Y., Gao, N., & Barthlott, W., « Mimicking natural superhydrophobic surfaces and grasping the wetting process: a review on recent progress in preparing superhydrophobic surfaces. », in *Advances in colloid and interface science*, vol. 169,2, 2011, p. 80‑105.
[24] Marmur, A., & Bittoun, E., « When Wenzel and Cassie are right: reconciling local and global considerations. », in *Langmuir : the ACS journal of surfaces and colloids*, vol. 25,3, 2009, p. 1277‑1281.
[25] Marmur A., « From hygrophilic to superhygrophobic: theoretical conditions for making high-contact-angle surfaces from low-contact-angle materials », in *Langmuir : the ACS journal of surfaces and colloids*, vol. 24,14, 2008, p. 7573–7579.
[26] Ran, C., Ding, G., Liu, W., Deng, Y., & Hou, W., « Wetting on nanoporous alumina surface: transition between Wenzel and Cassie states controlled by surface structure », in *Langmuir : the ACS journal of surfaces and colloids*, vol. 24,18, 2008, p. 9952–9955.
[27] Jung, Y. and B. Bhushan, « Wetting transition of water droplets on superhydrophobic patterned surfaces », in *Scripta Materialia*, vol. 57,12, 2007, p. 1057‑1060.
[28] Koishi, T., Yasuoka, K., Fujikawa, S., Ebisuzaki, T., & Zeng, X. C., « Coexistence and transition between Cassie and Wenzel state on pillared hydrophobic surface », in *Proceedings of the National Academy of Sciences of the United States of America*, vol. 106,21, 2009, p. 8435–8440.
[29] Rothstein, Jonathan, « Slip on Superhydrophobic Surfaces », in *Annu. Rev. Fluid Mech*, vol. 42, 2010, p. 89‑109.
[30] Checco, Antonio and Ocko, Benjamin and Rahman, Atikur and Black, Charles and Tasinkevych, Mykola and Giacomello, Alberto and Dietrich, Siegfried, « Collapse and Reversibility of the Superhydrophobic State on Nanotextured Surfaces », in *Physical Review Letters*, vol. 112,21, 2014, p. 216101.
[31] Shen Y, Xie X, Tao J, Chen H, Cai Z, Liu S, Jiang J., « Mechanical Equilibrium Dynamics Controlling Wetting State Transition at Low-Temperature Superhydrophobic Array-Microstructure Surfaces », in *Coatings*, vol. 11,5, 2021, p. 522.
[32] Fang, Wei & Guo, Hao-Yuan & Li, Bo & Li, Qunyang, « Revisiting the Critical Condition for the Cassie-Wenzel Transition on Micropillar-Structured Surfaces », in *Langmuir*, vol. 34,13, 2018, p. 3838‑3844.
[33] Ling, Hangjian and Katz, Joseph and fu, Matt and Hultmark, Marcus, « Effect of Reynolds number and saturation level on gas diffusion in and out of a superhydrophobic surface », in *Physical Review Fluids*, vol. 2, 2017.
[34] S. Moulinet and D. Bartolo, « Life and death of a fakir droplet: impalement transitions on superhydrophobic surfaces », in *Eur. Phys. J. E*, vol. 24,3, 2007, p. 251–260.
[35] P. Papadopoulos, L. Mammen, X. Deng, D. Vollmer, and H.-J. Butt, « How superhydrophobicity breaks down », in *Proc. Natl. Acad. Sci.*, vol. 110,9, 2013, p. 3254‑3258.
[36] xu, Muchen and Sun, Guangyi and Kim, Chang-Jin, « Infinite Lifetime of Underwater Superhydrophobic States », in *Physical review letters*, vol. 113, 2014, p. 136103.
[37] Kern, W. & Reinhardt, Karen, *Handbook of Silicon Wafer Cleaning Technology: Second Edition.* 2008.
[38] Hattori, T., Osaka, T., Okamoto, A., Saga, K., & Kuniyasu, H., « Contamination Removal by Single-Wafer Spin Cleaning with Repetitive Use of Ozonized Water and Dilute HF », in *Journal of The Electrochemical Society*, vol. 145, 1998, p. 3278‑3284.
[39] Arnaud, Tournier & Leverd, F & Favennec, L & Perrot, C & Pinzelli, L. & Gatefait, M & Cherault, N & Jeanjean, Damien & Carrere, J.-P & Hirigoyen, F. & Grant, Lindsay, « Pixel-to-Pixel isolation by Deep Trench technology: Application to CMOS Image Sensor », 2011.

[40] I. Nakao, H. Umimoto, S. Odanaka, T. Ohzone, and H. Esaki, « A simulation model for wet cleaning of deep trenches », in *J. Electrochem. Soc.*, vol. 137,7, 1990, p. 2303–2305.
[41] H. Lin, A. A. Busnaina, and I. I. Suni, « Physical modeling of rinsing and cleaning of submicron trenches », in *Proc. IEEE 2000 Int.*, 2000, p. 49‑51.
[42] K. Dhane, J. Han, J. Yan, O. Mahdavi, and D. Zamani, « Dynamics of cleaning and rinsing of micro and nano structures in single-wafer cleaning tools », in *IEEE Trans. Semicond. Manuf.*, vol. 24,1, 2011, p. 125‑133.
[43] E. W. Washburn, « The dynamics of capillary flow », in *Phys. Rev.*, vol. 17,3, 1921, p. 273.
[44] D. Zamani, K. Dhane, O. Mahdavi, M. Anthony, J. Yan, and F. Shadman, « surface cleaning of small structures during spin rinsing of patterned substrates », in *Microelectronic engineering*, vol. 108, 2013, p. 57‑65.
[45] J. Haneveld, N. R. Tas, N. Brunets, H. V Jansen, and M. Elwenspoek, « Capillary filling of sub-10 nm nanochannels », in *J. Appl. Phys.*, vol. 104,1, 2008, p. 14309.
[46] F. Chauvet, S. Geoffroy, A. Hamoumi, M. Prat and P. Joseph, « Roles of gas in capillary filling of nanoslits », in *Soft Matter*, vol. 8, 2012, p. 10738–10749.
[47] G. Vereecke, X. Xu, W.-K. Tsai, H. Yang, S. Armini, T. Delande, G. Doumen, F. Kentie, X. Shi, I. Simms, K. Nafus, F. Holsteyns, H. Struyf, and S. De Gendt, « Wetting behavior of aqueous solutions on high aspect ratio nanopillars with hydrophilic surface finish », in *ECS Trans.*, vol. 58,6, 2013, p. 171–182.
[48] Z. Li, J. Wang, Y. Zhang, J. Wang, L. Jiang, and Y. Song, « Closed-air induced composite wetting on hydrophilic ordered nanoporous anodic alumina », in *Appl. Phys. Lett.*, vol. 97, 2015, p. 233107.
[49] M. Ohm, « Liquid-phase processing of hydrophilic features on a silicon wafer », in *J. Electrochem. Soc.*, vol. 144,12, 1997, p. 4331–4335.
[50] H. Namatsu, K. Kurihara, M. Nagase, K. Iwadate, and K. Murase, « Dimensional limitations of silicon nanolines resulting from pattern distortion due to surface tension of rinse water », in *Appl. Phys. Lett.*, vol. 66,20, 1995, p. 2655–2657.
[51] Peter, Daniel, « Pattern Collapse - the Mechanical Stability and Solid Bridging of Semiconductor Nanostructures », 2010.
[52] Rob Legtenberg, Harrie A. C. Tilmans, Job Elders, and Miko Elwenspoek, « Stiction of surface micromachined structures after rinsing and drying: model and investigation of adhesion mechanisms », in *Sensors and Actuators A*, vol. 43, 1994, p. 239.
[53] K. Tanaka, R. Naito, T. Kitada, Y. Kiba, Y. Yamada, M. Kobayashi, and H. Ichikawa, « Improvement of pattern collapse issue by additive added D.I water rinse process », in *Microlithogr. 2003*, 2003, p. 1366–1381.
[54] K. Kim, J. Jung, and H. Kim, « Method of IPA cleaning process on temperature and spin speed for prevent pattern collapse in DRAM capacitor », in *Proc. World Congr. Eng. Comput. Sci.*, vol. 2, 2012, p. 24‑26.
[55] G. H. Kim, S. H. Cho, J. H. Han, Y. B. Lee, C. H. Roh, K. Hong, and S. K. Park, « Effect of drying liquid on stiction of high aspect ratio structures », in *Solid State Phenom.*, vol. 187, 2012, p. 75–78.
[56] J. Ruzyllo, K. Torek, C. Daffron, R. Grant, and R. Novak, « Etching of thermal oxides in low pressure anhydrous HF / CH3OH gas mixture at elevated temperature », in *J. Electrochem. Soc.*, vol. 140,4, 1993, p. 64–66.
[57] X. Xu, N. Vrancken, G. Vereecke, S. Suhard, G. Pourtois, and F. Holsteyns, « Some critical issues in pattern collapse prevention and repair », in *Solid State Phenom.*, vol. 255, 2016, p. 147–151.
[58] Abraham Marmur, « Solid-Surface Characterization by Wetting », in *Annual Review of Materials Research*, vol. 39, 2009, p. 473‑489.
[59] Marmur, Abraham, « A guide to the equilibrium contact angles maze », in *Contact Angle Wettability and Adhesion*, vol. 6, 2009, p. 3‑18.
[60] Pierce, E., Carmona, F. J. & Amirfazli, A, « Understanding of sliding and contact angle results in tilted plate experiments », in *Colloids Surfaces A Physicochem. Eng. Asp.*, vol. 323, 2008, p. 73‑82.

[61] Krasovitski, B. & Marmur, A., « Drops down the hill: Theoretical study of limiting contact angles and the hysteresis range on a tilted plate », in *Langmuir*, vol. 21, 2005, p. 3881–3885.
[62] Chen J, Luo G, Cao W, « The study of layer-by-layer ultrathin films by the dynamic contact angle method. », in *Journal of Colloid and Interface Science*, vol. 238, 2001, p. 62‑69.
[63] Law, K.-Y and Zhao, Hong, *Surface wetting: Characterization, contact angle, and fundamentals*. 2015.
[64] M. Santini, M. Guilizzoni, « 3D X-ray Micro Computed Tomography on Multiphase Drop Interfaces: From Biomimetic to Functional Applications », in *Colloids and Interface Science Communications*, vol. 1, 2014, p. 14‑17.
[65] Kurosaki, Ken et al., « High wettability of liquid caesium iodine with solid uranium dioxide », in *Scientific reports*, vol. 7,1, 2017, p. 11449.
[66] Park, J., Han, HS., Kim, YC. et al., « Direct and accurate measurement of size dependent wetting behaviors for sessile water droplets », in *Sci Rep*, vol. 5, 2015, p. 18150.
[67] K. Rykaczewski, T. Landin, M. L. Walker, J. H. J. Scott, and K. K. Varanasi, « Direct imaging of complex nano- to microscale interfaces involving solid, liquid, and gas phases », in *ACS Nano*, vol. 6,10, 2012, p. 9326–9334.
[68] Noriyuki Inoue, Yoshiko Takashima, Mitsuo Suga, Toshiaki Suzuki, Yoshikazu Nemoto, Osamu Takai, « Observation of wet specimens sensitive to evaporation using scanning electron microscopy », in *Microscopy*, vol. 67,6, 2018, p. 356–366. [En ligne]. Disponible sur: https://doi.org/10.1093/jmicro/dfy041
[69] Jo, H., Hwang, K., Kim, D. et al., « Loss of superhydrophobicity of hydrophobic micro/nano structures during condensation », in *Sci Rep*, vol. 5, 2015, p. 9901.
[70] Chesna, Jacob and Weidmaier, Bob and Wang, Jinlin and Samara, Ayman and Leach, Richard and Her, Tsing-Hua and Smith, Stuart, « Aerial wetting contact angle measurement using confocal microscopy », in *Measurement Science and Technology*, vol. 27, 2016, p. 125202.
[71] Huiling Duan, « Underwater Superhydrophobiciy: Fundamentals and Applications », in *Procedia IUTAM*, vol. 20, 2017, p. 128‑135.
[72] Gerald Wiegand, Thomas Jaworek, Gerhard Wegner, Erich Sackmann, « Studies of Structure and Local Wetting Properties on Heterogeneous, Micropatterned Solid Surfaces by Microinterferometry », in *Journal of Colloid and Interface Science*, vol. 196,2, 1997, p. 299‑312.
[73] A. Elbourne, M.F. Dupont, S. Collett, V. Khanh Truong, X. Xu, N. Vrancken, V. Baulin, E.P. Ivanova, R.J. Crawford, « Imaging the air-water interface: characterising biomimetic and natural hydrophobic surfaces using in situ atomic force microscopy », in *Journal of Colloid and Interface Science*, vol. 536, 2018, p. 363‑371.
[74] A. J. Bard, L. R. Faulkner, *Electrochemical Methods*, John Wiley Sons, Inc., New York. 2001.
[75] Juan C Tuberquia, Nabijan Nizamidin, G Kane Jennings, « Effect of superhydrophobicity on the barrier properties of polymethylene films », in *Langmuir*, vol. 26,17, 2010, p. 14039‑14046.
[76] Juan C. Tuberquia, Nabijan Nizamidin, Robert R. Harl, Jake Albert, Jason Hunter, Bridget R. Rogers, and G. Kane Jennings, « Surface-initiated polymerization of superhydrophobic polymethylene », in *Journal of the American Chemical Society*, vol. 132,16, 2010, p. 5725‑5734.
[77] Zamfir, L.-G.; Puiu, M.; Bala, C., « Advances in Electrochemical Impedance Spectroscopy Detection of Endocrine Disruptors », in *Sensors*, vol. 20, 2020, p. 6443. [En ligne]. Disponible sur: https://doi.org/10.3390/s20226443
[78] Vrancken, N., Li, J., Sergeant, S., Vereecke, G., Doumen, G., Holsteyns, F., Chen, C., Terryn, H., De Gendt, S., & Xu, X., « In-situ ATR-FTIR for dynamic analysis of superhydrophobic breakdown on nanostructured silicon surfaces », in *Scientific reports*, vol. 8,1, 2018, p. 11637.
[79] Reviakine, Ilya and Johannsmann, Diethelm and Richter, Ralf, « Hearing What You Cannot See and Visualizing What You Hear: Interpreting Quartz Crystal Microbalance Data from Solvated Interfaces », in *Analytical chemistry*, vol. 83, 2011, p. 8838‑48.
[80] Wang, Pengtao and Su, Junwei and Shen, Mengyan and Ruths, Marina and Sun, Hongwei, « Detection of liquid penetration into a micropillar surface using quartz crystal microbalance », in *Langmuir*, vol. 33, 2016, p. 638.
[81] Virgilio, C. , Carlier, J. , Campistron, P. , Toubal, M. , Garnier, P. , Broussous, L. , Thomy, V. , Nongaillard, B., « Wetting Characterization of High Aspect Ratio Nanostructures by Gigahertz

Acoustic Reflectometry », in *International Journal of Mechanical and Mechatronics Engineering*, vol. 10,3, 2016, p. 506‑511.
[82] N. Saad, « Caractérisation par ondes acoustiques des surfaces fonctionnalisées », Université de Valenciennes et du Hainaut-Cambresis, 2012.
[83] Christophe Virgilio, L. Broussous, P. Garnier, Julien Carlier, Pierre Campistron, et al., « Deep Trench Isolation and Through Silicon Via Wetting Characterization by High-Frequency Acoustic Reflectometry », in *Solid State Phenomena*, vol. 255, 2016, p. 129‑135.
[84] Chen, Y. , Ren, W. , Mu, X. , Zhang, F. , Xu, Y., « Flow inside Micro-Channel Bounded by Superhydrophobic Surface with Eccentric Micro-Grooves », in *World Academy of Science, Engineering and Technology, Open Science Index 129, International Journal of Mechanical and Mechatronics Engineering*, vol. 11,9, 2017, p. 1579‑1584.
[85] Kim, Tae Jin & Hidrovo, Carlos, « Pressure and partial wetting effects on superhydrophobic friction reduction in microchannel flow », in *Physics of Fluids*, vol. 24,11, 2012.
[86] Yu, K. H. ., Tan, Y. X. ., Abdul Aziz, M. S. ., Teoh, Y. H. ., & Abdullah, M. Z., « The Developing Plane Channel Flow over Water-Repellent Surface Containing Transverse Grooves and Ribs », in *Journal of Advanced Research in Fluid Mechanics and Thermal Sciences*, vol. 45,1, 2018, p. 141‑148.
[87] Lee, Choongyeop and Choi, Chang-Hwan and Kim, Chang-Jin, « Superhydrophobic drag reduction in laminar flows: a critical review », in *Experiments in Fluids*, vol. 57, 2016, p. 176.
[88] Mathieu Foucaud, « Etude de la dégradation de la protection par des résines photosensibles de la grille métallique TiN lors de gravures humides pour la réalisation de transistors de technologies sub-28nm », Micro et nanotechnologies/Microélectronique. Université Grenoble Alpes, 2015. [En ligne]. Disponible sur: HAL Id: tel-01215598
[89] Borg, K., Cregan, V., Fowler, A., McGuinness, M., O'Brien, S., Schwartz, L.W. and Zubkov, V., « Partial Wetting Phenomenon in Superhydrophobic Microchannels », 2009.
[90] D. Royer and E. Dieulesaint, *Ondes élastiques dans les solides Tome 1 Propagation libre et guidée*, Masson. 1996.
[91] Pozzi, Silvia, « High Intensity Focused Ultrasound (HIFU): computing tools for medical applications. », 2015. [En ligne]. Disponible sur: http://dx.doi.org/10.13140/RG.2.1.5098.2166
[92] B. A. Auld, *Acoustic fields and waves in solids*, Wiley., vol. 1. 1973.
[93] L. E. Kinsler et al., *Fundamental of Acoustics*, John Wiley Sons Inc. 2000.
[94] Shtemler, Yuri and Shreiber, Isaac, « Heat transfer in sound propagation and attenuation through gas-liquid polyhedral foams », in *International Communications in Heat and Mass Transfer*, vol. 33, 2007. [En ligne]. Disponible sur: http://dx.doi.org/10.1016/j.icheatmasstransfer.2006.01.003
[95] Pant S, Laliberte J, Martinez M., « Structural health monitoring of composite aerospace structures using Lamb waves », in *Proceedings of the 19th International Conference on Composite Materials (ICCM/19), Montreal*, 2013.
[96] Melzak, K.A.; Martin, F.; Newton, M.I.; McHale, G.; Gizeli, E., « Acoustic Determination of Polymer Molecular Weights and Rotation Times », in *J. Polymer Sci. B*, vol. 40,14, 2002, p. 1490‑1495.
[97] Turton, A.; Bhattacharyya, D.; Wood, D., « Liquid Density Analysis of Sucrose and Alcoholic Beverages using polyimide Guided Love-mode Acoustic Wave Sensors », in *Meas. Sci Technol*, vol. 17, 2006, p. 257‑263.
[98] Corinne Dejous, Dominique Rebiere, Vincent Raimbault, Hamida Hallil, Jean-Luc Lachaud, « Surface Acoustic Wave Devices to Probe Thin Films and Complex Fluids », in *International Conference on Condensed Matter & Applied Physics (ICC-2015)*, 2015. [En ligne]. Disponible sur: https://hal.archives-ouvertes.fr/hal-01169162
[99] H. Tarbague *et al.*, « PDMS (Polydimethylsiloxane) Microfluidic Chip Molding for Love Wave Biosensor », *ECS Trans.*, vol. 23, n° 1, p. 319–325, déc. 2019, doi: 10.1149/1.3183735.
[100] Razan, F.; Rebiere, D.; Dejous, C.; Monin, D.; Joanicot, M.; Conedera, V., « Determination of Menthol Kinetic Constants with Love-Wave Device. », in *Sens. Actuators B*, vol. 118,1‑2, 2006, p. 368‑373.
[101] M. J. S. Lowe, D. N. Alleyne, and P. Cawley, « Defect detection in pipes using guided waves », in *Ultrasonics*, vol. 36,1‑5, 1998, p. 147–154.

[102] Kessler, Seth and Spearing, S., « Damage Detection in Composite Materials Using Lamb Wave Methods », in *Smart Materials and Structures*, vol. 11, 2002, p. 269.
[103] A. Jitsumori, S. Inoue, T. Maekawa, and T. Inari, « Generation of lamb wave using linear array probe and its application for flaw detection », in *Jpn. J. Appl. Phys.*, vol. 25, 1986, p. 200–201.
[104] D. N. Alleyne and P. Cawley, « Optimization of lamb wave inspection techniques », in *NDT E Int.*, vol. 25,1, 1992, p. 11–22.
[105] D. N. Alleyne and P. Cawley, « The Interaction of Lamb Waves with Defects », in *IEEE Trans. Ultrason. Ferroelectr. Freq. Control*, vol. 39,3, 1992, p. 381–397.
[106] Edalati, Kaveh and Kermani, A. and Seiedi, Masoud and Movafeghi, Amir, « Defect detection in thin plates by ultrasonic lamb wave techniques », in *International Journal of Materials and Product Technology*, vol. 27, 2006, p. 156‑172.
[107] Castaings, Michel and Le Clézio, Emmanuel and Hosten, Bernard, « Modal decomposition method for modeling the interaction of Lamb waves with cracks », in *The Journal of the Acoustical Society of America*, vol. 112, 2003, p. 2567‑82. [En ligne]. Disponible sur: http://dx.doi.org/10.1121/1.1500756
[108] L. Pitta Bauermann, L.V. Mesquita, C. Bischoff, M. Drews, O. Fitz, A. Heuer, D. Biro, « Scanning acoustic microscopy as a non-destructive imaging tool to localize defects inside battery cells », in *Journal of Power Sources Advances*, vol. 6, 2021, p. 100035. [En ligne]. Disponible sur: https://doi.org/10.1016/j.powera.2020.100035
[109] Brand, S., Tismer, S., Moe, S.T. et al., « Non-destructive wafer level bond defect identification by scanning acoustic microscopy », in *Microsyst Technol*, vol. 21, 2015, p. 1385–1394. [En ligne]. Disponible sur: https://doi.org/10.1007/s00542-014-2328-z
[110] Meignen, Pierre-Antoine and Le Clézio, Emmanuel and Despaux, Gilles, « High Frequency Acoustic Sensor Dedicated to the High Resolution Measurement of Mechanical Properties », in *Physics Procedia*, vol. 70, 2015, p. 424‑427. [En ligne]. Disponible sur: http://dx.doi.org/10.1016/j.phpro.2015.08.134
[111] Meng, Xiangdi and Lin, Shuyu, « Analysis of a Cascaded Piezoelectric Ultrasonic Transducer with Three Sets of Piezoelectric Ceramic Stacks », in *Sensors*, vol. 19, 2019, p. 580. [En ligne]. Disponible sur: http://dx.doi.org/10.3390/s19030580
[112] Wang, Wenjie and Jiang, Yi and Thomas, Peter, « Structural Design and Physical Mechanism of Axial and Radial Sandwich Resonators with Piezoelectric Ceramics: A Review », in *Sensors*, vol. 21, 2021, p. 1112. [En ligne]. Disponible sur: http://dx.doi.org/10.3390/s21041112
[113] Bertocci, Francesco & Grandoni, Andrea & Djuric-Rissner, Tatjana, « Scanning Acoustic Microscopy (SAM): A Robust Method for Defect Detection during the Manufacturing Process of Ultrasound Probes for Medical Imaging », in *Sensors (Basel, Switzerland)*, vol. 19,22, 2019, p. 4868.
[114] J. Virieux, « P-SV wave propagation in heterogeneous media: Velocity-stress finite-difference method », in *Geophysics*, vol. 51,4, 1986, p. 889–901.
[115] F. E. Fox and G. D. Rock, « Compressional viscosity and sound absorption in water at different temperatures », in *Phys. Rev.*, vol. 70,1‑2, 1946, p. 68.
[116] Pohl, Robert & Liu, Xiao & Thompson, EunJoo, « Low-Temperature Thermal Conductivity and Acoustic Attenuation in Amorphous Solids », in *Reviews of Modern Physics*, vol. 4,220, 2002, p. 991.
[117] Kushwaha, A.K, « Lattice dynamical, elastic properties and sound velocities of γ-Si3N4 », in *Indian Journal of Pure and Applied Physics*, vol. 53,9, 2015, p. 585‑589.
[118] K. Yee, « Numerical solution of initial boundary value problems involving Maxwell's equations in isotropic media », in *IEEE Trans. Antennas Propag.*, vol. 14,3, p. 302–307.
[119] G. Mur, « Absorbing boundary conditions for the finite-difference approximation of the time-domain electromagnetic-field equations », in *IEEE Trans. Electromagn. Compat.*, vol. 4, 1981, p. 377–382.
[120] Campistron, P., Carlier, J., Toubal, M., Dupont, L., Nassar, G., Nongaillard, B., Saad, N., & Gao, G., « High Frequency Ultrasound a Tool for Elastic Properties Measurement of Thin Films Fabricated on Silicon. », in *Trans Tech Publications*, vol. 324, 2011, p. 277‑281.

[121] Carlier, Julien and Toubal, Malika and Li, Sizhe and Campistron, Pierre and Callens-Debavelaere, Dorothée and Thomy, Vincent and Senez, Vincent and Nongaillard, Bertrand, « High Frequency Acoustic Reflectometry for Solid/Liquid Interface Characterization: Application to Droplet Evaporation », in *Physics Procedia*, vol. 70, 2015, p. 459‑462. [En ligne]. Disponible sur: http://dx.doi.org/10.1016/j.phpro.2015.08.285

[122] M. Link, « Study and realization of shear wave mode solidly mounted film bulk acoustic resonators (FBAR) made of c-axis inclined zinc oxide (ZnO) thin films: application as gravimetric sensors in liquid environments », PhD thesis supported at the University of Henri Poincare, Nancy I, 2006.

[123] Dahmani, Hatem and Zaaroura, Ibrahim and Salhab, Abbas and Campistron, Pierre and Carlier, Julien and Toubal, Malika and Harmand, Souad and Thomy, Vincent and Neyens, Marc and Nongaillard, Bertrand, « Fabrication and Optimization of High Frequency ZnO Transducers for Both Longitudinal and Shear Emission: Application of Viscosity Measurement using Ultrasound », in *Advances in Science, Technology and Engineering Systems Journal*, vol. 5, 2020, p. 1428‑1435. [En ligne]. Disponible sur: http://dx.doi.org/10.25046/aj0506173

[124] Yu Hongbin, Zhou Guangya, Chau Fook Siong, Wang Shouhua, Lee Feiwen, « Novel polydimethylsiloxane (PDMS) based microchannel fabrication method for lab-on-a-chip application », in *Sensors and Actuators B: Chemical*, vol. 137,2, 2009, p. 754‑761.

[125] Myeong Chan Jo, Rasim Guldiken, « Effects of polydimethylsiloxane (PDMS) microchannels on surface acoustic wave-based microfluidic devices », in *Microelectronic Engineering*, vol. 113, 2014, p. 98‑104.

[126] T. Bohr, V. Putkaradze, and S. Watanabe, « Averaging theory for the struc- ture of hydraulic jumps and separation in laminar free-surface flows », in *Physical Review Letters*, vol. 79,6, 1997, p. 038‑1041.

[127] Bhatelia, T., Utikar, R., Pareek, V., & Tadé, M., « CHARACTERIZING LIQUID FILM THICKNESS IN SPINNING DISC REACTORS », 2009.

[128] Wehking, Jonathan, « Pressure Losses Experienced By Liquid Flow Through Pdms Microchannels With Abrupt Area Changes », University of Central Florida, 2008.

[129] Craigie, C. and Sheehan, T and Johnson, V. and Burkett, Susan and Moll, Amy and Knowlton, Bill, « Polymer thickness effects on Bosch etch profiles », in *Journal of Vacuum Science & Technology B: Microelectronics and Nanometer Structures*, vol. 20, 2002. [En ligne]. Disponible sur: http://dx.doi.org/10.1116/1.1515910

[130] Perry, Guillaume and Coffinier, Yannick and Thomy, Vincent and Boukherroub, Rabah, « Sliding Droplets on Superomniphobic Zinc Oxide Nanostructures », in *Langmuir : the ACS journal of surfaces and colloids*, vol. 28, 2011, p. 389‑95. [En ligne]. Disponible sur: http://dx.doi.org/10.1021/la2035032

[131] Dufour, Renaud and Perry, Guillaume and Harnois, Maxime and Coffinier, Yannick and Thomy, Vincent and Senez, Vincent and Boukherroub, Rabah, « From micro to nano reentrant structures: Hysteresis on superomniphobic surfaces », in *Colloid and Polymer Science*, vol. 291, 2013, p. 405‑415. [En ligne]. Disponible sur: http://dx.doi.org/10.1007/s00396-012-2750-7

[132] Malviya, Abhigyan & Vrabec, Jadran, « Henry's Law Constant of Nitrogen, Oxygen, and Argon in Ternary Aqueous Alcoholic Solvent Mixtures », in *Journal of Chemical & Engineering Data*, vol. 65,3, 2019, p. 1189–1196.

[133] Battino, Rubin & Rettich, Timothy & Tominaga, Toshihiro, « The Solubility of Nitrogen and Air in Liquids », in *Journal of Physical and Chemical Reference Data*, vol. 13,2, 1984, p. 563‑600.

[134] A. Guha and Debaprasad Panda, « Solubility of some non-polar gases in mixed solvants », in *Int. J. Chem.*, vol. 6,3, 2008, p. 1147‑1167.

[135] Yeh, Wei-Ming, « Pattern collapse in lithographic nanostructures: quantifying photoresist nanostructure behavior and novel methods for collapse mitigation », 2013.

[136] Tamaddon, Amir and Mertens, Paul and Vereecke, Guy and Holsteyns, Frank and Doumen, Geert and De Gendt, Stefan and Heyns, Marc, « Watermark Formation Mechanism by

Evaporation of Ultra-Pure Water: Study the Effect of Ambient », in *ECS Transactions*, vol. 58,6, 2013.

[137] Gale, Glenn and Ohno, H. and Namba, H. and Orii, T. and Takagi, Y. and Yamasaka, M., « Wafer drying defects: Mechanisms and control », in *Proceedings - Electrochemical Society*, 2005, p. 449‑455.

[138] M. Watanabe, M. Hamano, M. Harazono, « The role of atmospheric oxygen and water in the generation of water marks on the silicon surface in cleaning processes », in *Materials Science and Engineering: B*, vol. 4,1-4, 1989, p. 401‑405. [En ligne]. Disponible sur: https://doi.org/10.1016/0921-5107(89)90278-X

[139] Mata, Alvaro and Fleischman, Aaron and Roy, Shuvo, « Characterization of Polydimethylsiloxane (PDMS) Properties for Biomedical Micro/Nanosystems », in *Biomedical microdevices*, vol. 7, 2006, p. 281‑293.

[140] Gong, Xiao and He, Shuang, « Highly Durable Superhydrophobic Polydimethylsiloxane/Silica Nanocomposite Surfaces with Good Self-Cleaning Ability », in *ACS Omega*, vol. 5,8, 2020.

[141] Ducom, Gaëlle and Laubie, Baptiste and Chottier, Claire and Germain, Patrick and Chatain, Vincent, « Hydrolysis of polydimethylsiloxane fluids in controlled aqueous solutions », in *Water science and technology : a journal of the International Association on Water Pollution Research*, vol. 68,4, 2013, p. 813‑820.

# Publications related to the PhD

“Polydimethylsiloxane Micro-Channels Application for the Study of Dynamic Wetting of Nano-Etched Silicon Surfaces Based on Acoustic Characterization Method” A. Salhab, J. Carlier, P. Campistron, M. Neyens, M. Toubal, B. Nongaillard, V. Thomy. The symposium on Ultra Clean processing of Semiconductor Surfaces.

Dahmani, Hatem & Zaaroura, Ibrahim & Salhab, Abbas & Campistron, Pierre & Carlier, Julien & Toubal, Malika & Harmand, Souad & Thomy, Vincent & Neyens, Marc & Nongaillard, Bertrand. (2020). Fabrication and Optimization of High Frequency ZnO Transducers for Both Longitudinal and Shear Emission: Application of Viscosity Measurement using Ultrasound. Advances in Science, Technology and Engineering Systems Journal. 5. 1428-1435. 10.25046/aj0506173.

A. Salhab, J. Carlier, M. Toubal, P. Campistron, M. Neyens, B. Nongaillard, V. Thomy, "Nanostructures wetting evaluation using ultra high frequency ultrasound," Proc. SPIE 12002, Oxide-based Materials and Devices XIII, 120020J (5 March 2022); https://doi.org/10.1117/12.2620992.

# Presentations in international conferences

UCPSS 2021: The Symposium on Ultra Clean Processing of Semiconductor Surfaces, virtual format (April 2021).

SPIE Photonics West On Demand, virtual format (February 2022).

## Abstract

In the semiconductor industry, effective wet cleaning of contamination is a critical factor in ensuring good quality of electronic products. The cycle between the wetting and drying processes can create several problems in the high aspect ratio micro / nanoscale structures. In this thesis work, we present the characterization of the dynamic wetting of fluids within Deep Trench Isolation (DTI) structures used in STMicroelectronics imaging sensors. This characterization uses an original technique of acoustic waves reflectometry at ultra-high frequencies. In order to obtain cleaning conditions as close as possible to those used in the industrial process, dynamic wetting is provided by a microfluidic channel made of PolyDiMethylSiloxane (PDMS) located at the level of the structures to be studied. An analytical numerical model based on 2D finite difference allowed us to simulate the acoustic interactions inside micro / nanostructures to better interpret the experimental results. In addition, the development of a technique for the automatic acquisition of the acoustic reflection coefficient has made it possible to study the rapid wetting processes of DTI structures. Finally, the kinematics of DTI drying was also studied with different liquids. Structural deformation phenomenon, known as "pattern collapse", was analyzed using scanning electron microscopy (SEM) images and correlated with acoustic measurements.



Keywords: Micro and Nano-technology, Wetting, Surface cleaning, Microelectronics, Nondestructive testing, Acoustics, Piezoelectric transducers, Microfluidics, Deep trench isolation.



## Résumé

Dans l'industrie des semi-conducteurs, un nettoyage efficace des contaminations par voie humide est un facteur déterminant pour garantir la bonne qualité des produits électroniques. Le cycle entre les processus de mouillage et de séchage peut alors créer plusieurs problèmes dans les structures micro/nanométriques à rapport d'aspect élevé. Dans ce travail de thèse, nous présentons la caractérisation due mouillage dynamique de fluides au sein de structures "Deep Trench Isolation" (DTI) utilisés dans les capteurs imageurs de STMicroelectronics. Cette caractérisation utilise une technique originale de réflectométrie d'ondes acoustiques à ultra-hautes fréquences. Afin d'obtenir des conditions de nettoyage aussi proches que possible de celles utilisées dans le procédé industriel, le mouillage dynamique est assuré par un canal microfluidique réalisé en PolyDiMethylSiloxane (PDMS) localisé au niveau des structures à étudier. Un modèle numérique analytique basé sur les différences finies 2D nous a permis de simuler les interactions acoustiques à l'intérieur des micro/nanostructures pour interpréter au mieux les résultats expérimentaux. De plus, le développement d'une technique d'acquisition automatique du coefficient de réflexion acoustique a donné la possibilité d'étudier les processus rapides de mouillage des structures DTI. Enfin, la cinématique de séchage des DTI a également été étudiée avec différents liquides. Des phénomènes de déformation des structures ("pattern collapse") ont été analysés à l'aide d'images de microscopie électronique à balayage (MEB) et corrélés avec les mesures acoustiques.



Mots clés: Micro et Nano-technologie, Mouillage, Nettoyage de surface, Microélectronique, Contrôles non destructifs, Acoustique, Transducteurs piézoélectriques, Microfluidique, Deep Trench Isolation.